General Probabilistic Surface Optimization and Log Density Estimation

Dmitry Kopitkov

DIMKAK@TECHNION.AC.IL

Technion Autonomous Systems Program (TASP) Technion - Israel Institute of Technology Haifa 32000, Israel

Vadim Indelman

VADIM.INDELMAN@TECHNION.AC.IL

Department of Aerospace Engineering Technion - Israel Institute of Technology Haifa 32000, Israel

Abstract

Probabilistic inference, such as density estimation and distribution transformation, is a fundamental and highly important problem that needs to be solved in many different domains. Recently, a lot of research was done to solve it using Deep Learning (DL) approaches, including unnormalized and energy models, as well as Generative Adversarial Networks, where DL has shown top approximation performance. In this paper we contribute a novel algorithm family, which generalizes all above, and allows to infer different statistical modalities (e.g. data likelihood and ratio between densities) from data samples. The proposed unsupervised technique, named Probabilistic Surface Optimization (PSO), views a neural network (NN) as a flexible surface which can be pushed according to loss-specific virtual stochastic forces, where a dynamical equilibrium is achieved when the point-wise forces on the surface become equal. Concretely, the surface is pushed up and down at points sampled from two different distributions, with overall up and down forces becoming functions of these two distribution densities and of force intensity magnitudes defined by loss of a particular PSO instance. The eventual force equilibrium upon convergence enforces the NN to be equal to various statistical functions depending on the used magnitude functions, such as data density. Furthermore, this dynamical-statistical equilibrium is extremely intuitive and useful, providing many implications and possible usages in probabilistic inference. Further, we connect PSO to numerous existing statistical works which are also PSO instances, and derive new PSO-based inference methods as demonstration of PSO exceptional usability. Likewise, based on the insights coming from the virtual-force perspective we analyze PSO stability and propose new ways to improve it. Finally, we present new instances of PSO. termed PSO-LDE, for data density estimation on logarithmic scale and also provide a new NN block-diagonal architecture for increased surface flexibility, which significantly improves estimation accuracy. Both PSO-LDE and the new architecture are combined together as a new density estimation technique. In our experiments we demonstrate this technique to be superior over state-of-the-art baselines in density estimation task for multi-modal 20D data.

Keywords: Unnormalized and Energy Models, Unsupervised Learning, Non-parametric Density Estimation, Deep Learning.

DMITRY KOPITKOV AND VADIM INDELMAN

Contents

1	Introduction	5
2 Probabilistic Surface Optimization		
3	Instances of PSO 3.1 Deriving Convergence For PSO Instance	13 13 20
4	PSO, Bregman and "f" Divergencies 4.1 PSO Divergence	22 23 24 25
5	Properties of PSO Estimators 5.1 Consistency and Asymptotic Normality 5.2 Bounded vs Unbounded Magnitude Functions 5.3 Statistics of Surface Change 5.4 Convoluted PSO Balance State 5.5 Model Expressiveness and Smoothness vs Kernel Bandwidth 5.6 Infinite Height Problem and its Solutions	25 26 28 30 30 33
6	Density Estimation via PSO 6.1 DeepPDF	36 37 37 42 44
7	Conditional Density Estimation 7.1 Conditional Density Estimation	45 49
8	NN Architecture 8.1 Block-Diagonal Layers	50 51 53 55 56 57 58
9	Overfitting of PSO 9.1 Problem Illustration	58 59 63

GENERAL PSO AND LOG DENSITY ESTIMATION

10	Additional Applications of PSO	64	
	10.1 Mutual Information Estimation	64	
11	Related work	65	
	11.1 Parametric vs Non-parametric Approaches	65	
	11.2 Unsupervised DL and Thermodynamic Optimization	66	
	11.3 Classification Domain	67	
	11.4 Cross-Entropy as Instance of PSO	68	
	11.5 Other DL-based Density Estimation Techniques	69	
	11.6 Relation to GANs	70	
	11.7 PSO with Unit Magnitudes		
	11.8 Relation to Maximum Likelihood Estimation	73	
12	Experimental evaluation	7 4	
	12.1 Learning Setup	74	
	12.2 Differential approximation	75	
	12.3 PDF Estimation via PSO - Columns Distribution	77	
	12.3.1 PSO Instances Evaluation	79	
	12.3.2 Baselines	85	
	12.3.3 NN Architectures Evaluation	89	
	12.3.4 Batch Size Impact	94	
	12.3.5 Small Training Dataset	96	
	12.4 PDF Estimation via PSO - Transformed Columns Distribution		
	12.5 PDF Estimation via PSO - 3D Image-based Densities	106	
13	Conclusions and Future Work	106	
14	4 Acknowledgments 1		
\mathbf{A}	Proof of Theorem 1	111	
	A.1 Functional $L^{U\cap D}$ over $\mathbb{S}^{U\cap D}$. 111	
	A.2 Functional $L^{U\setminus D}$ over $\mathbb{S}^{U\setminus D}$	113	
	A.3 Functional $L^{D\setminus U}$ over $\mathbb{S}^{D\setminus U}$		
В	Proof of Lemmas 9 and 10	116	
	B.1 Lemma 9	116	
	B.2 Lemma 10	118	
\mathbf{C}	Proof of Theorem 11	120	
	C.1 Lemmata	120	
	C.2 Proof of Theorem		
D	Proof of Theorem 12	123	
${f E}$	Proof of Theorem 13	12 3	

DMITRY KOPITKOV AND VADIM INDELMAN

\mathbf{F}	Proof of Theorem 14	124
	F.1 Lemmata	124
	F.2 Proof of Theorem	127
\mathbf{G}	Proof of Softmax Cross-Entropy being Instance of PSO	128
Н	Proof of Unnormalized Model Family in (Pihlaja et al., 2012) being subgroup of PSO $$)- 132
Ι	Proof of Bregman Divergence Framework in (Gutmann and Hirayama 2012) being subgroup of PSO	ı, 133
J	LSQR Divergence	134
K	Matrix A from definition of $Transformed\ Columns\ Distribution$	135
${f L}$	Weights Uncorrelation and Gradient Similarity Space	135

1. Introduction

Probabilistic inference is the wide domain of extremely important statistical problems including density (ratio) estimation, distribution transformation, density sampling and many more. Solutions to these problems are extensively used in domains of robotics, computer image, economics, and other scientific/industrial data mining cases. Particularly, in robotics we require to manually/automatically infer a measurement model between sensor measurements and the hidden state of the robot. Given such a model we can infer belief over robot state in an on-line scenario. Another example from robotics is the ability to generate/sample measurements that are similar as much as possible to future incoming observations. Such capability is often required in the belief space planning (BSP) problem (Kopitkov and Indelman, 2017), where a robot can reason about the future via prediction of a future observation and act smartly according to it. Considering the above, solutions to probabilistic inference and their applications to real-world problems are highly important for many scientific fields, with emphasis on robust robot operation in stochastic environments.

The universal approximation theory (Hornik, 1991) states that an artificial neural network with fully-connected layers can approximate any continuous function on compact subsets of \mathbb{R}^n , making it a universal approximation tool. Moreover, in the last decade methods based on Deep Learning (DL) provided outstanding performance in areas of computer vision and reinforcement learning. More recently, accurate DL approaches were also developed in the robotics domain, addressing problems such as image-based odometry and localization. Further, distribution transformation techniques, such as Generative Adversarial Networks (GANs), lately demonstrated outstanding results in generating new data samples which can also be used to predict sensor's future observations, as was mentioned above. Furthermore, recently strong frameworks (e.g. TensorFlow; PyTorch; Caffe) were developed that allow fast and sophisticated training of neural networks (NNs) using GPUs.

With this motivation, in this paper we contribute a novel unified paradigm, *Probabilistic* Surface Optimization (PSO), that allows to solve various probabilistic inference problems using DL, where we exploit the approximation power of NNs in full. PSO expresses the problem of probabilistic inference as a virtual physical system where the surface, represented by an NN, is pushed by forces that are outcomes of a Gradient Descent (GD) optimization. We will show that this NN surface is pushed during the optimization to the target surface for which the averaged point-wise forces cancel each other. Further, by using different virtual forces we can enforce our NN surface to converge to different probabilistic functions of data, such as data density, various density ratios, conditional densities and many other useful statistical modalities. Moreover, we will show that many existing probabilistic inference approaches, like unnormalized models, GAN critics, energy models and cross-entropy based methods, already apply such PSO principles implicitly, even though their underlying dynamics were not explored before through the prism of virtual forces. Likewise, many more novel and original methods can be forged in a simple way by following the same fundamental rules of the virtual surface and the force balance. Motivated by usefulness and intuitiveness of the proposed PSO paradigm, we provide herein also its convergence and stability analysis. Furthermore, the entire composition of this paper is focused on statistical inference for continuous multi-dimensional data. Yet, same conclusions and provided techniques can also be applied to the discrete case since PSO principles of force balance will stay exactly the same also there.

Importantly, we emphasize that PSO is not only a new interpretation that allows for simplified and intuitive understanding of statistical learning. Instead, in this paper we show that during the optimization the dynamics that an NN model undergoes are indeed matching the picture of a physical surface with particular forces applied on it. Moreover, such match allowed us to understand the optimization stability of PSO instances (e.g. GAN critics) in more detail and to suggest new ways to improve it.

Further, this paper focuses in more detail on density estimation, which is a fundamental statistical problem essential in many scientific fields and application domains such as probabilistic planning and inference. Today's most statistically robust techniques that work on a wide range of probabilistic distributions are non-parametric where arguably the leading and the most accurate is kernel density estimation (KDE) with its many extensions. Though a large amount of research was done on these techniques, they still are computationally expensive at both estimation and query stages. They require searching for hyper-parameters like bandwidth and kernel type, and their expressiveness in representing the estimated probability density function (pdf) is high but still limited to the selected kernel. On the other hand, NNs applied in this work are known for their high flexibility and ability to approximate any function.

In our previous work (Kopitkov and Indelman, 2018a) we proposed a new DeepPDF method and showed how by using the PSO principles it can perform non-parametric density estimation. As part of this paper, we investigate DL-based methods that estimate data density in logarithmic scale, thereby improving the overall approximation accuracy. For this purpose, we analyze various PSO instances that enforce the NN surface to approximate the log pdf function of a given data. Moreover, we present several new hyper-parametrized families of such PSO instances and verify their performance, both analytically and experimentally. As an example, these approaches contain noise contrastive estimation (NCE) (Smith and Eisner, 2005; Gutmann and Hyvärinen, 2010), widely adapted in language modeling domain, as their member for a particular hyper-parameter choice. Further, we examine several NN architectures for better estimation performance, and propose new block-diagonal layers that led us to significantly improved accuracy. The logarithm scale and new NN architecture allowed us to accurately estimate multi-modal densities of 20D continuous data, with superior precision compared to other state-of-the-art methods, which we demonstrate in our experiments. Additionally, note that in many real-world domains the analyzed data has a lower dimension (e.g. robot poses in robotics have only 6 DoF), making the proposed techniques well-suited for these applications. In future research we shall extend our methods to higher dimensions (e.g. of thousands).

Furthermore, PSO-based density estimation approaches presented in this paper do not enforce any explicit constraint over a total integral of the learned model, allowing it to be totally unnormalized. Yet, the implicit force balance of PSO at convergence produces density approximations that are highly accurate and *almost* normalized, with total integral being very close to 1.

Further, comparable pdf estimation methods that do not produce strictly normalized models, such as NCE and score matching (Hyvärinen, 2007), are typically evaluated on simple distributions of up to 5 dimensions (Gutmann and Hyvärinen, 2010; Pihlaja et al., 2012;

Saremi et al., 2018; Ceylan and Gutmann, 2018), which is not a sufficiently strong evidence of these techniques' true performance. Although in those works additional experiments are performed on high-dimensional data such as image patches, the studies do not report the true error since the real pdf function is analytically unknown for such datasets. Note that a negative log-likelihood of the learned model, averaged on testing dataset, cannot be used here since it is only reliable for perfectly normalized pdf models. Instead, inner parameters of the converged models in (Gutmann and Hyvärinen, 2010; Pihlaja et al., 2012; Saremi et al., 2018; Ceylan and Gutmann, 2018) are investigated and compared with known image feature extractors such as Gabor filters (Fogel and Sagi, 1989). We argue that such feature-based evaluation is not enough to validate consistency of estimated pdf values, which is extremely important to fully demonstrate the reliability of a proposed density estimation approach.

Likewise, in the language modeling domain, the NCE method is applied for density estimation of only low-dimensional discrete data (i.e. language words), which does not yield any information about NCE behavior in a high-dimensional setting. Albeit there is conversion of discrete words into multi-dimensional continuous embeddings, such vector representation can be conceptually seen as output of a middle layer within some bigger neural network that transforms words into appropriate values of a probability mass function (pmf). Therefore, the overall goal of such language modeling remains a low-dimensional and discrete pmf estimation.

Thus, a proper quantitative evaluation of PSO, which contains NCE as a member, in a medium-dimensional setting (dimension higher than 10) is typically not done. However, as we will discuss in this paper, due to curse of dimensionality the higher is the dimension—the more challenging is the inference problem solved by PSO. Certainly, an evaluation in a high-dimensional setting is required to show PSO's real potential and applicability to real world problems.

For this purpose, in our experiments we used datasets sampled from analytically known yet sophisticated highly multi-modal distributions. This allowed us to compare the final pdf estimation with the ground truth and to evaluate the real accuracy error of the produced models. To the best of our knowledge, this is the first time that such **quantitative** medium-dimensional experiments are performed for this class of density inference methods. Furthermore, in this paper we report the substantial estimation consistency evidence for these methods, motivating their usage for a wide range of real world applications.

To summarize, our main contributions in this paper are as follows:

- (a) We develop a *Probabilistic Surface Optimization* (PSO) that enforces any approximator function to converge to a target statistical function which nullifies a point-wise virtual force.
- (b) We show that many existing probabilistic and (un-)supervised learning techniques can be seen as instances of PSO.
- (c) We show how new probabilistic techniques can be derived in a simple way by using PSO principles, and also propose several such new methods.
- (d) We provide analysis of PSO convergence and stability under the model expressiveness limit assumption.

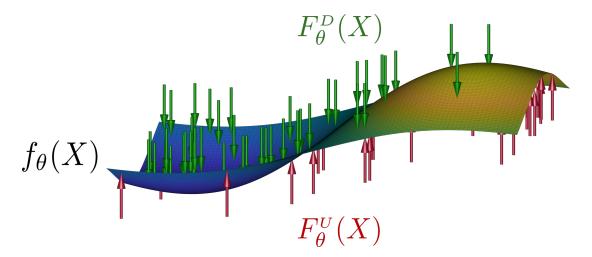


Figure 1: Illustration of PSO principles. Model $f_{\theta}(X) : \mathbb{R}^n \to \mathbb{R}$ (in this paper NN parametrized by θ) represents virtual surface that is pushed in opposite directions - up at points X^U sampled from $\mathbb{P}^U(X)$ and down at points X^D sampled from $\mathbb{P}^D(X)$. Magnitude of each push is amplified by analytical function - $M^U[X, f_{\theta}(X)]$ when pushing at X^U and $M^D[X, f_{\theta}(X)]$ when pushing at X^D , where both functions may have an almost arbitrary form, with only minor restrictions. During optimization via loss gradient in Eq. (1) the up and down forces $F_{\theta}^U(X) = \mathbb{P}^U(X) \cdot M^U[X, f_{\theta}(X)]$ and $F_{\theta}^D(X) = \mathbb{P}^D(X) \cdot M^D[X, f_{\theta}(X)]$, containing both frequency and analytical components, adapt to each other till point-wise balance state $F_{\theta}^U(X) = F_{\theta}^D(X)$ is achieved. Such convergence causes final $f_{\theta}(X)$ to be particular function of $\mathbb{P}^U(X)$ and $\mathbb{P}^D(X)$, and can be used for inferring numerous statistical functions of arbitrary data (see Section 3).

- (e) We use PSO to approximate a logarithm of the target density using a NN, proposing for this purpose several hyper-parametric PSO subgroups and analyzing their properties.
- (f) We present a new NN architecture with block-diagonal layers that allows for lower side-influence (a smaller bandwidth of the corresponding model kernel) between various regions of NN surface support and leads to higher NN flexibility and to more accurate data density estimation.
- (g) We experiment with different continuous 20D densities, and accurately infer all of them using the proposed PSO instances, thus demonstrating these instances' robustness and top performance. Further, we compare our methods with state-of-the-art baselines, showing the superiority of former over latter.

2. Probabilistic Surface Optimization

In previous work (Kopitkov and Indelman, 2018a) we explored a specific instance of *Probabilistic Surface Optimization* (PSO) where we used *pdf loss* for the problem of density estimation. Yet, the PSO can be seen as a much more general family of probabilistic inference algorithms. In this section we will formulate the definition of this family and in Section 3 we will relate it to other existing methods, showing them to be instances of the unifying PSO framework.

Notation	Description
$f_{\theta}(X): \mathbb{R}^n \to \mathbb{R}$	model parametrized by θ (e.g. a neural network), can be viewed
	as a surface with support in \mathbb{R}^n whose height is
	the output of $f_{\theta}(X)$
$ heta \in \mathbb{R}^{ heta }$	model parameters (e.g. neural network weights vector)
$X \in \mathbb{R}^n$	input space of $f_{\theta}(X)$, can be viewed as support of
	model surface in space \mathbb{R}^{n+1}
$X^{\scriptscriptstyle U} \sim \mathbb{P}^{\scriptscriptstyle U}$	<i>n</i> -dimensional random variable with pdf \mathbb{P}^{U} , samples of which
	are the locations where we push the model surface up
$X^{\scriptscriptstyle D} \sim \mathbb{P}^{\scriptscriptstyle D}$	<i>n</i> -dimensional random variable with pdf \mathbb{P}^{D} , samples of which
	are the locations where we push the model surface $down$
$\mathbb{S}^{\scriptscriptstyle U}\subset\mathbb{R}^n$	support of \mathbb{P}^U
$\mathbb{S}^{\scriptscriptstyle D}\subset\mathbb{R}^n$	support of \mathbb{P}^D
$\mathbb{S}^{U\cup D}\subset\mathbb{R}^n$	support union of \mathbb{P}^U and \mathbb{P}^D
$\mathbb{S}^{U\cap D}\subset\mathbb{R}^n$	support intersection of \mathbb{P}^U and \mathbb{P}^D
$\mathbb{S}^{U\setminus D}\subset\mathbb{R}^n$	support of \mathbb{P}^U where $\mathbb{P}^D(X) = 0$
$\mathbb{S}^{\scriptscriptstyle D\setminus U}\subset\mathbb{R}^n$	support of \mathbb{P}^D where $\mathbb{P}^U(X) = 0$
$M^{U}\left[X, f_{\theta}(X)\right] : \mathbb{R}^{n} \times \mathbb{R} \to \mathbb{R}$	force-magnitude function that amplifies an up push force
	which we apply at X^U
$M^{D}\left[X, f_{\theta}(X)\right] : \mathbb{R}^{n} \times \mathbb{R} \to \mathbb{R}$	force-magnitude function that amplifies a $down$ push force
	which we apply at X^D
$F_{\theta}^{U}(X)$ and $F_{\theta}^{D}(X)$	point-wise up and $down$ forces, that are
	applied (on average) at any point $X \in \mathbb{R}^n$
$N^{\scriptscriptstyle U}$ and $N^{\scriptscriptstyle D}$	batch sizes of samples from \mathbb{P}^U and from \mathbb{P}^D , that are used in
	a single optimization iteration
$g_{\theta}(X, X')$	a model kernel that is responsible for generalization and
	interpolation during the GD optimization

Table 1: Paper Main Notations

Formulation Consider an input space $X \in \mathbb{R}^n$ and two densities \mathbb{P}^U and \mathbb{P}^D defined on it, with appropriate pdfs $\mathbb{P}^U(X)$ and $\mathbb{P}^D(X)$ and with supports \mathbb{S}^U and \mathbb{S}^D ; U and D denote the up and down directions of forces under thermodynamical perspective of the optimization (see below). Denote by $\mathbb{S}^{U\cap D}$, $\mathbb{S}^{U\setminus D}$ and $\mathbb{S}^{D\setminus U}$ sets $\{X:X\in\mathbb{S}^U\vee X\in\mathbb{S}^D\}$, $\{X:X\in\mathbb{S}^U\vee X\notin\mathbb{S}^D\}$ and $\{X:X\notin\mathbb{S}^U\vee X\in\mathbb{S}^D\}$ respectively. Further, denote a model $f_{\theta}(X):\mathbb{R}^n\to\mathbb{R}$ parametrized by vector θ (e.g. NN or a function in Reproducing Kernel Hilbert Space, RKHS). Likewise, define two arbitrary functions $M^U(X,s):\mathbb{R}^n\times\mathbb{R}\to\mathbb{R}$ and $M^D(X,s):\mathbb{R}^n\times\mathbb{R}\to\mathbb{R}$, which we name magnitude functions; both functions must be continuous and differentiable $almost\ everywhere\ w.r.t.$ argument s (see also Table 1 for list of main notations). We propose a novel PSO framework for probabilistic inference, that performs a gradient-based iterative optimization $\theta_{t+1}=\theta_t-\delta\cdot d\theta$ with learning rate δ where:

$$d\theta = -\frac{1}{N^{U}} \sum_{i=1}^{N^{U}} M^{U} \left[X_{i}^{U}, f_{\theta}(X_{i}^{U}) \right] \cdot \nabla_{\theta} f_{\theta}(X_{i}^{U}) + \frac{1}{N^{D}} \sum_{i=1}^{N^{D}} M^{D} \left[X_{i}^{D}, f_{\theta}(X_{i}^{D}) \right] \cdot \nabla_{\theta} f_{\theta}(X_{i}^{D}).$$
 (1)

 $\{X_i^U\}_{i=1}^{N^U}$ and $\{X_i^D\}_{i=1}^{N^D}$ are sample batches from \mathbb{P}^U and \mathbb{P}^D respectively. Each PSO instance is defined by a particular choice of $\{\mathbb{P}^U,\mathbb{P}^D,M^U,M^D\}$ that produces a different convergence

```
1 Inputs:
 2 \mathbb{P}^U and \mathbb{P}^D: up and down densities
 3 M^U and M^D: magnitude functions
 4 \theta: initial parameters of model f_{\theta} \in \mathcal{F}
 \delta: learning rate
 6 Outputs: f_{\theta^*}: PSO solution that satisfies balance state in Eq. (2)
 7 begin:
         while Not converged do
 8
              Obtain samples \{X_i^U\}_{i=1}^{N^U} from \mathbb{P}^U Obtain samples \{X_i^D\}_{i=1}^{N^D} from \mathbb{P}^D
 9
10
              Calculate d\theta via Eq. (1)
11
              \theta = \theta - \delta \cdot d\theta
12
         end
13
         \theta^* = \theta
14
15 end
```

Algorithm 1: PSO estimation algorithm. Sample batches can be either identical or different for all iterations, which corresponds to GD and stochastic GD respectively.

of $f_{\theta}(X)$ by approximately satisfying PSO balance state (within a mutual support $\mathbb{S}^{U \cap D}$):

$$\frac{\mathbb{P}^{U}(X)}{\mathbb{P}^{D}(X)} = \frac{M^{D}[X, f_{\theta^{*}}(X)]}{M^{U}[X, f_{\theta^{*}}(X)]}.$$
(2)

Such optimization, outlined in Algorithm 1, will allow us to infer various statistical modalities from available data, making PSO a very useful and general algorithm family.

Derivation Consider *PSO functional* over a twice continuously differentiable function $f: \mathbb{R}^n \to \mathbb{R}$ as:

$$L_{PSO}(f) = - \underset{X \sim \mathbb{P}^U}{\mathbb{E}} \widetilde{M}^U [X, f(X)] + \underset{X \sim \mathbb{P}^D}{\mathbb{E}} \widetilde{M}^D [X, f(X)]$$
 (3)

where we define $\widetilde{M}^U[X,s] \triangleq \int_{s_0}^s M^U(X,t) dt$ and $\widetilde{M}^D[X,s] \triangleq \int_{s_0}^s M^D(X,t) dt$ to be antiderivatives of $M^U(\cdot)$ and $M^D(\cdot)$ respectively; these functions, referred below as impulse functions of PSO, are not necessarily known analytically. The above integral can be separated into several terms related to $\mathbb{S}^{U\cap D}$, $\mathbb{S}^{U\setminus D}$ and $\mathbb{S}^{D\setminus U}$. A minima f^* of $L_{PSO}(f)$ is described below, characterizing f^* within each of these areas.

Theorem 1 (Variational Characterization) Consider densities \mathbb{P}^U and \mathbb{P}^D and magnitudes M^U and M^D . Define $M^{U'}(X,s) \triangleq \frac{\partial M^U(X,s)}{\partial s}$, $M^{D'}(X,s) \triangleq \frac{\partial M^D(X,s)}{\partial s}$ and an arbitrary function $h: \mathbb{S}^{U\setminus D} \to \mathbb{R}$. Then for f^* to be minima of L_{PSO} , it must fulfill the following properties:

1. Mutual support: it is sufficient to satisfy $\forall X \in \mathbb{S}^{U \cap D}$:

$$(a) \ \mathbb{P}^{\scriptscriptstyle U}(X) \cdot M^{\scriptscriptstyle U}\left[X, f^*(X)\right] = \mathbb{P}^{\scriptscriptstyle D}(X) \cdot M^{\scriptscriptstyle D}\left[X, f^*(X)\right].$$

(b)
$$\mathbb{P}^{U}(X) \cdot M^{U'}[X, f^{*}(X)] < \mathbb{P}^{D}(X) \cdot M^{D'}[X, f^{*}(X)].$$

where the first condition, named PSO balance state, is necessary for f^* to be an extrema of L_{PSO} , and the second condition is sufficient for it to be a minima.

- 2. <u>Disjoint support</u>: depending on properties of a function M^U , it is necessary to satisfy $\forall X \in \mathbb{S}^{U \setminus D}$:
 - (a) If $\forall X' \in \mathbb{S}^{U \setminus D}$, $s \in \mathbb{R} : M^U(X', s) > 0$, then $f^*(X) = \infty$.
 - (b) If $\forall X' \in \mathbb{S}^{U \setminus D}$, $s \in \mathbb{R} : M^U(X', s) < 0$, then $f^*(X) = -\infty$.
 - (c) If $\forall X' \in \mathbb{S}^{U \setminus D}$, $s \in \mathbb{R} : M^U(X', s) \equiv 0$, then $f^*(X)$ can be arbitrary.
 - (d) If $\forall X' \in \mathbb{S}^{U \setminus D}, s \in \mathbb{R}$:

$$M^{U}(X',s) = \begin{cases} 0, & s = h(X') \\ > 0, & s < h(X') \\ < 0, & s > h(X') \end{cases}$$

then
$$f^*(X) = h(X)$$
.

(e) Otherwise, additional analysis is required.

The theorem's proof, where the condition 1-a shown to be Euler-Lagrange equation of $L_{PSO}(f)$, as also the analogue of part 2 for $\mathbb{S}^{D\setminus U}$ can be found in the Appendix A. Part 2 helps to understand dynamics in areas outside of mutual support. Yet, below we will mostly rely on part 1, considering the optimization in area $\mathbb{S}^{U\cap D}$. Following from the above, finding a minima of L_{PSO} will produce a function f that satisfies the PSO balance state Eq. (2). Note that the 1-b condition ensures an optimization stability for a specific pair of M^U and M^D , and is satisfied by all PSO instances presented in this paper.

To infer the above f^* , we consider a function space \mathcal{F} , each element f_{θ} of which can be parametrized by θ , and solve the problem $\min_{f_{\theta} \in \mathcal{F}} L_{PSO}(f_{\theta})$. Assuming that \mathcal{F} contains f^* , it will be obtained as a minima of the above minimization. Further, in practice L_{PSO} is optimized via gradient-based optimization where gradient w.r.t. θ is:

$$\nabla_{\theta} L_{PSO}(f_{\theta}) = - \underset{X \sim \mathbb{P}^{U}}{\mathbb{E}} M^{U} \left[X, f_{\theta}(X) \right] \cdot \nabla_{\theta} f_{\theta}(X) + \underset{X \sim \mathbb{P}^{D}}{\mathbb{E}} M^{D} \left[X, f_{\theta}(X) \right] \cdot \nabla_{\theta} f_{\theta}(X) \quad (4)$$

with Eq. (1) being its sampled approximation. Considering a hypothesis class represented by NN and the universal approximation theory (Hornik, 1991), we assume that \mathcal{F} is rich enough to learn the optimal f^* with high accuracy. Furthermore, in our experiments we show that in practice NN-based PSO estimators approximate the PSO balance state in a very accurate manner.

PSO Balance State Given that \mathbb{P}^U and \mathbb{P}^D have the same support, PSO will converge to PSO balance state in Eq. (2), where by ignoring possible singularities (due to assumed identical support) we can see that the converged surface f_{θ^*} will be such that the ratio of frequency components will be opposite-proportional to the ratio of magnitude components. To derive a value of the converged f_{θ^*} for a specific PSO instance, $\{M^U, M^D\}$ of that PSO instance, that typically involve f_{θ} inside them, must be substituted into Eq. (2) and

then it needs to be solved for f_{θ} . Further, this balance state can be used to mechanically recover many existing methods and to easily derive new ones for inference of numerous statistical functions of data; in Section 3 we provide full detail on this point. Likewise, due to the ubiquitousness of PSO principles within various statistical methods the analysis of PSO convergence and numerical stability obtains a very big significance and we present it in Section 5. Furthermore, the above general formulation of PSO is surprisingly simple, considering that it provides a strong intuition about its stability properties as a physical thermodynamical system, as explained below.

Virtual Surface Perspective The main advantage of PSO is in its conceptual simplicity, revealed when viewed via a thermodynamical perspective. Specifically, $f_{\theta}(X)$ can be considered as a virtual surface in \mathbb{R}^{n+1} space, with its support being \mathbb{R}^n , see Figure 1. Further, according to the update rule of a gradient-descent (GD) optimization and Eq. (1), any particular training point X updates θ during a single GD update by $\nabla_{\theta} f_{\theta}(X)$ magnified by the output of a magnitude function $(M^U \text{ or } M^D)$. Furthermore, considering the update of a simple form $\theta_{t+1} = \theta_t - \nabla_{\theta} f_{\theta_t}(X)$, it is easy to show that the height of the surface at any other point X' changes according to a first-order Taylor expansion as:

$$f_{\theta_{t+1}}(X') - f_{\theta_t}(X') \approx \nabla_{\theta} f_{\theta_t}(X')^T \cdot \nabla_{\theta} f_{\theta_t}(X).$$

Hence, by pushing (optimizing) a specific training point X, the surface at other points changes according to the elasticity properties of the model expressed via a gradient similarity kernel $g_{\theta}(X, X') \triangleq \nabla_{\theta} f_{\theta}(X)^T \cdot \nabla_{\theta} f_{\theta}(X')$. When optimizing over RKHS, the above expression turns to be identity and $g_{\theta}(X, X')$ collapses into the reproducing kernel¹. For NNs, this kernel is known as Neural Tangent Kernel (NTK) (Jacot et al., 2018). Moreover, as was empirically observed, NTK has a strong local behavior with its outputs mostly being large only when points X and X' are close by. More insights about NTK can be found in (Jacot et al., 2018; Dou and Liang, 2019; Kopitkov and Indelman, 2019). Further assuming for simplicity that $\forall X \neq X' : g_{\theta}(X, X') \equiv 0$ and that $\{M^U, M^D\}$ are non-negative functions, it follows then that each X_i^U in Eq. (1) pushes the surface at this point up by $g_{\theta}(X_i^U, X_i^U)$ magnified by $M^U[X_i^U, f_{\theta}(X_i^U)]$, whereas each X_i^D is pushing it down in a similar manner.

Further, considering a macro picture of such optimization, $f_{\theta}(X)$ is pushed up at samples from \mathbb{P}^{U} and down at samples from \mathbb{P}^{D} , with the up and down averaged point-wise forces being $F_{\theta}^{U}(X) \triangleq \mathbb{P}^{U}(X) \cdot M^{U}[X, f_{\theta}(X)]$ and $F_{\theta}^{D}(X) \triangleq \mathbb{P}^{D}(X) \cdot M^{D}[X, f_{\theta}(X)]$. Intuitively, such a thermodynamic process converges to a stable state when point-wise forces become equal, $F_{\theta}^{U}(X) = F_{\theta}^{D}(X)$. This is supported mathematically by the condition 1-a of Theorem 1, with such equilibrium being named as PSO balance state. Yet, note that in practice the optimization outcome strongly depends on properties of g_{θ} and on the actual amount of available sample points, which we discuss in Section 5.

Additionally, the actual force direction at samples X_i^U and X_i^D depends on signs of $M^U[X_i^U, f_{\theta}(X_i^U)]$ and $M^D[X_i^U, f_{\theta}(X_i^D)]$, and hence may be different for each instance of PSO. Yet, in most cases the considered *magnitude* functions are non-negative, and thus support the above exposition exactly. Moreover, for negative *magnitudes* the above picture of thermodynamic forces will still stay correct, after swapping between up and down terms.

^{1.} In RKHS defined via a feature map $\phi(X)$ and a reproducing kernel $k(X, X') = \phi(X)^T \cdot \phi(X')$, every function has a form $f_{\theta}(X) = \phi(X)^T \cdot \theta$. Since $\nabla_{\theta} f_{\theta}(X) = \phi(X)$, we obtain $g_{\theta}(X, X') \equiv k(X, X')$.

Furthermore, the thermodynamical equilibrium can also explain dynamics outside of mutual support $\mathbb{S}^{U\cap D}$. Considering the area $\mathbb{S}^{U\setminus D}\subset\mathbb{R}^n$ where only samples X_i^U are located, when M^U has positive outputs, the model surface is pushed indefinitely up, since there is no opposite force required for the equilibrium. Likewise, when M^U 's outputs are negative - it is pushed indefinitely down. Further, when magnitude function is zero, there are no pushes at all and hence the surface can be anything. Finally, if the output of $M^U[X, f_{\theta}(X)]$ is changing signs depending on whether $f_{\theta}(X)$ is higher than h(X), then $f_{\theta}(X)$ must be pushed towards h(X) to balance the forces. Such intuition is supported mathematically by part 2 of Theorem 1. Observe that convergence at infinity actually implies that PSO will not converge to the steady state for any number of iterations. Yet, it can be easily handled by for example limiting range of functions within the considered \mathcal{F} to some set $[a, b] \subset \mathbb{R}$.

3. Instances of PSO

Many statistical methods exist whose loss and gradient have PSO forms depicted in Eq. (3) and Eq. (4) for some choice of densities \mathbb{P}^U and \mathbb{P}^D , and of functions \widetilde{M}^U , \widetilde{M}^D , M^U and M^D , and therefore being instances of the PSO algorithm family. Typically, these methods defined via their loss which involves the pair of impulses $\{\widetilde{M}^U[X,s], \widetilde{M}^D[X,s]\}$. Yet, in practice it is enough to know their derivatives $\{M^U[X,s] = \frac{\partial \widetilde{M}^U(X,s)}{\partial s}, M^D[X,s] = \frac{\partial \widetilde{M}^D(X,s)}{\partial s}\}$ for the gradient-based optimization (see Algorithm 1). Therefore, PSO formulation focuses directly on $\{M^U, M^D\}$, with each PSO instance being defined by a particular choice of this pair.

Moreover, most of the existing PSO instances and subgroups actually require \widetilde{M}^U and \widetilde{M}^D to be analytically known, while PSO composition eliminates such demand. In fact, many pairs $\{M^U, M^D\}$ explored in this paper do not have a closed-form known antiderivatives $\{\widetilde{M}^U, \widetilde{M}^D\}$. Thus, PSO enriches the arsenal of available probabilistic methods.

In Tables 2-6 we show multiple PSO instances. We categorize all losses into two main categories - density estimation losses in Tables 2-3 and ratio density estimation losses in Tables 4-6. In the former class of losses we are interested to infer density \mathbb{P}^U from its available data samples, while \mathbb{P}^D represents some auxiliary distribution with analytically known pdf function $\mathbb{P}^D(X)$ whose samples are used to create the opposite force $F_{\theta}^D(X)$; this force will balance the force $F_{\theta}^U(X)$ from \mathbb{P}^U 's samples. Further, in the latter class we concerned to learn a density ratio, or some function of it, between two unknown densities \mathbb{P}^U and \mathbb{P}^D by using the available samples from both distributions.

In the tables we present the PSO loss of each method, if analytically known, and the corresponding pair $\{M^U, M^D\}$. We also indicate to what the surface $f_{\theta}(X)$ will converge assuming that PSO balance state in Eq. (2) was obtained. Derivation of this convergence appears below. Importantly, it describes the optimal PSO solution only within the area $\mathbb{S}^{U\cap D}\subseteq\mathbb{R}^n$. For X in $\mathbb{S}^{U\setminus D}$ or $\mathbb{S}^{D\setminus U}$, the convergence can be explained via part 2 of Theorem 1. Yet, in most of the paper we will limit the discussion to the convergence within the mutual support, implicitly assuming $\mathbb{S}^U\equiv\mathbb{S}^D$.

3.1 Deriving Convergence For PSO Instance

Given a PSO instance with a particular $\{\mathbb{P}^U, \mathbb{P}^D, M^U, M^D\}$, the convergence within $\mathbb{S}^{U \cap D}$ can be derived by solving PSO balance state $\mathbb{P}^U(X) \cdot M^U[X, f_{\theta}(X)] = \mathbb{P}^D(X) \cdot M^D[X, f_{\theta}(X)]$.

Method	$\underline{\textbf{\textit{F}inal}} \ f_{ heta}(X) \ / \ \underline{\textbf{\textit{R}eferences}} \ / \ \underline{\textbf{\textit{L}oss}} \ / \ M^{ extsup{U}}(\cdot) \ \ extsup{and} \ M^{ extsup{D}}(\cdot)$
DeepPDF	$\underline{\underline{F}}$: $\mathbb{P}^{U}(X)$ $\underline{\underline{R}}$: Baird et al. (2005); Kopitkov and Indelman (2018a)
	$\underline{\mathbf{L}}: -\mathbb{E}_{X \sim \mathbb{P}^U} f_{\theta}(X) \cdot \mathbb{P}^D(X) + \mathbb{E}_{X \sim \mathbb{P}^D} \frac{1}{2} \Big[f_{\theta}(X) \Big]^2$ $M^U, M^D: \mathbb{P}^D(X), f_{\theta}(X)$
PSO-LDE (Log Density Estimators)	
	$M^{U}, M^{D} \colon \frac{\mathbb{P}^{D}(X)}{\left[\left[\exp f_{\theta}(X)\right]^{\alpha} + \left[\mathbb{P}^{D}(X)\right]^{\alpha}\right]^{\frac{1}{\alpha}}}, \frac{\exp f_{\theta}(X)}{\left[\left[\exp f_{\theta}(X)\right]^{\alpha} + \left[\mathbb{P}^{D}(X)\right]^{\alpha}\right]^{\frac{1}{\alpha}}}$
	where α is a hyper-parameter
PSO-MAX	$\underline{\mathbf{F}}$: $\log \mathbb{P}^U(X)$ $\underline{\mathbf{R}}$: This paper, * see Section 12.3.1 $\underline{\mathbf{L}}$: unknown M^U , M^D : $\exp \left[-\max \left[f_{\theta}(X) - \log \mathbb{P}^D(X), 0\right]\right]$,
	$\exp\left[\min\left[f_{\theta}(X) - \log \mathbb{P}^{D}(X), 0\right]\right]$
NCE (Noise Contrastive Estimation)	<u>F</u> : $\log \mathbb{P}^{U}(X)$ <u>R</u> : Smith and Eisner (2005); Gutmann and Hyvärinen (2010); Pihlaja et al. (2012); Mnih and Teh (2012); Mnih and Kavukcuoglu (2013) Gutmann and Hyvärinen (2012)
	$\underline{\mathbf{L}} \colon \mathbb{E}_{X \sim \mathbb{P}^U} \log \frac{\exp[f_{\theta}(X)] + \mathbb{P}^D(X)}{\exp[f_{\theta}(X)]} + \mathbb{E}_{X \sim \mathbb{P}^D} \log \frac{\exp[f_{\theta}(X)] + \mathbb{P}^D(X)}{\mathbb{P}^D(X)}$ $M^U, M^D \colon \frac{\mathbb{P}^D(X)}{\exp[f_{\theta}(X)] + \mathbb{P}^D(X)}, \frac{\exp[f_{\theta}(X)]}{\exp[f_{\theta}(X)] + \mathbb{P}^D(X)}$
IS (Importance Sampling)	$ \begin{array}{l} \underline{\mathbf{F}} \colon \log \mathbb{P}^{U}(X) \\ \underline{\mathbf{F}} \colon \log \mathbb{P}^{U}(X) \\ \underline{\mathbf{R}} \colon \text{ Pihlaja et al. (2012)} \\ \underline{\mathbf{L}} \colon -\mathbb{E}_{X \sim \mathbb{P}^{U}} f_{\theta}(X) + \mathbb{E}_{X \sim \mathbb{P}^{D}} \frac{\exp[f_{\theta}(X)]}{\mathbb{P}^{D}(X)} \\ M^{U}, M^{D} \colon 1, \frac{\exp[f_{\theta}(X)]}{\mathbb{P}^{D}(X)} \end{array} $

Table 2: PSO Instances For Density Estimation, Part 1

Method	$\underline{\textbf{\textit{F}inal}} \ f_{ heta}(X) \ / \ \underline{\textbf{\textit{R}eferences}} \ / \ \underline{\textbf{\textit{L}oss}} \ / \ M^{ extsup{U}}(\cdot) \ \ extbf{\textit{and}} \ M^{ extsup{D}}(\cdot)$
Polynomial	$\underline{\underline{\mathbf{F}}}$: $\log \mathbb{P}^U(X)$
	$\underline{\mathbf{R}}$: Pihlaja et al. (2012)
	$\underline{\mathrm{L}} \colon -\mathbb{E}_{X \sim \mathbb{P}^U} \tfrac{\exp[f_{\theta}(X)]}{\mathbb{P}^D(X)} + \mathbb{E}_{X \sim \mathbb{P}^D} \tfrac{1}{2} \tfrac{\exp[2 \cdot f_{\theta}(X)]}{\mathbb{IP}^D(X)^2}$
	= (-1) = [= (-1)]
	$M^U,\ M^D\colon rac{\exp[f_ heta(X)]}{\mathbb{P}^D(X)},\ rac{\exp[2\cdot f_ heta(X)]}{[\mathbb{P}^D(X)]^2}$
Inverse	$\underline{\mathrm{F}} \colon \log \mathbb{P}^{\scriptscriptstyle U}(X)$
Polynomial	$\underline{\mathbf{R}}$: Pihlaja et al. (2012)
	$-\operatorname{Im}D(\mathbf{v})$ 12 $\operatorname{Im}D(\mathbf{v})$
	$\underline{\mathbf{L}} \colon \mathbb{E}_{X \sim \mathbb{P}^U} \frac{1}{2} \frac{[\mathbb{P}^D(X)]^2}{\exp[2 \cdot f_{\theta}(X)]} - \mathbb{E}_{X \sim \mathbb{P}^D} \frac{\mathbb{P}^D(X)}{\exp[f_{\theta}(X)]}$
	$M^U,\ M^D\colon rac{[\mathbb{P}^D(X)]^2}{\exp[2\cdot f_ heta(X)]}, rac{\mathbb{P}^D(X)}{\exp[f_ heta(X)]}$
Inverse	$\underline{\mathrm{F}} \colon \log \mathbb{P}^{\scriptscriptstyle U}(X)$
Importance	$\underline{\mathbf{R}}$: Pihlaja et al. (2012)
Sampling	$\underline{\mathrm{L}} \colon \mathbb{E}_{X \sim \mathbb{P}^U} rac{\mathbb{P}^D(X)}{\exp[f_{m{ heta}}(X)]} + \mathbb{E}_{X \sim \mathbb{P}^D} f_{m{ heta}}(X)$
	$M^U, M^D : \frac{\mathbb{P}^D(X^U)}{\exp[f_{\theta}(X^U)]}, 1$
	1 [0 \ /]
Root	$\underline{\mathrm{F}}$: $\sqrt[d]{\mathbb{P}^U(X)}$
Density Estimation	$\underline{\mathbf{R}}$: This paper $\underline{\mathbf{L}}$: $-\mathbb{E}_{X \sim \mathbb{P}^U} f_{\theta}(X) \cdot \mathbb{P}^D(X) + \mathbb{E}_{X \sim \mathbb{P}^D} \frac{1}{d+1} \cdot f_{\theta}(X)^{d+1} sign[f_{\theta}(X)]^{d+1}$
	$M^U, M^D \colon \mathbb{P}^D(X) \ , \ f_{ heta}(X)^d \cdot sign[f_{ heta}(X)]^{d+1}$
PDF	$\underline{\mathrm{F}}$: $\log \left[\mathbb{P}^{U}(X) * \mathbb{P}^{v}(X) \right]$, where * is a convolution operator
Convolution	$\underline{\underline{R}}$: This paper
Estimation	$\underline{\mathrm{L}} : -\mathbb{E}_{X \sim \bar{\mathbb{P}}^U} f_{\theta}(X) + \mathbb{E}_{X \sim \mathbb{P}^D} \frac{\exp[f_{\theta}(X)]}{\mathbb{P}^D(X)}$
	$M^U,~M^D\colon 1,~rac{\exp[f_{m{ heta}}(X)]}{\mathbb{P}^D(X)}$
	where $\bar{\mathbb{P}}^U(X) = \mathbb{P}^U(X) * \mathbb{P}^v(X)$ serves as up density,
	whose sample $X \sim \bar{\mathbb{P}}^U$ can be obtained via $X = X^U + v$
	with $X^{U} \sim \mathbb{P}^{U}(X)$ and $v \sim \mathbb{P}^{v}(X)$, see Section 9

Table 3: PSO Instances For Density Estimation, Part 2

Method	$\underline{\textbf{\textit{F}inal}} \ f_{ heta}(X) \ / \ \underline{\textbf{\textit{R}eferences}} \ / \ \underline{\textbf{\textit{L}oss}} \ / \ M^{ extsup{\textit{U}}}(\cdot) \ \ extbf{\textit{and}} \ M^{ extsup{\textit{D}}}(\cdot)$
Simple Loss	<u>F</u> : Kantorovich potential (Villani, 2008), only if the smoothness of $f_{\theta}(X)$ is heavily restricted <u>R</u> : see Section 11.7 <u>L</u> : $-\mathbb{E}_{X \sim \mathbb{P}^U} f_{\theta}(X) + \mathbb{E}_{X \sim \mathbb{P}^D} f_{\theta}(X)$ M^U , M^D : 1, 1
EBGAN Critic	$\underline{\mathbf{F}}: \ f_{\theta}(X) \approx m \ \text{at} \ \{X: \mathbb{P}^{U}(X) < \mathbb{P}^{D}(X)\}, \ \text{and} \ f_{\theta}(X) \approx 0 \ \text{otherwise}$ $\underline{\mathbf{R}}: \ \text{Zhao et al.} \ (2016), \ ^{*} \ \text{see Section 5.6 and } 11.7$ $\underline{\mathbf{L}}: \ \mathbb{E}_{X \sim \mathbb{P}^{U}} \ f_{\theta}(X) + \mathbb{E}_{X \sim \mathbb{P}^{D}} \ \text{max}[m - f_{\theta}(X), 0]$ $M^{U}, \ M^{D}: \ -1, \ -cut_at \ [X, f_{\theta}(X), m]$ $^{*} \ \text{model} \ f_{\theta}(X) \ \text{is constrained to have non-negative outputs}$
uLSIF	$\underline{\mathbf{F}} \colon \frac{\mathbb{P}^{U}(X)}{\mathbb{P}^{D}(X)}$ $\underline{\mathbf{R}} \colon \text{Kanamori et al. (2009); Yamada et al. (2011); Sugiyama et al. (2012b);}$ $\text{Nam and Sugiyama (2015); Uehara et al. (2016)}$ $\underline{\mathbf{L}} \colon -\mathbb{E}_{X \sim \mathbb{P}^{U}} f_{\theta}(X) + \mathbb{E}_{X \sim \mathbb{P}^{D}} \frac{1}{2} \big[f_{\theta}(X) \big]^{2}$ $M^{U}, M^{D} \colon 1, f_{\theta}(X)$
KLIEP	$ \begin{array}{l} \underline{\mathrm{F}} \colon \frac{\mathbb{P}^U(X)}{\mathbb{P}^D(X)} \\ \underline{\mathrm{R}} \colon \mathrm{Sugiyama} \ \mathrm{et} \ \mathrm{al.} \ (2008, 2012\mathrm{a}); \ \mathrm{Uehara} \ \mathrm{et} \ \mathrm{al.} \ (2016) \\ \underline{\mathrm{L}} \colon -\mathbb{E}_{X \sim \mathbb{P}^U} \log f_{\theta}(X) + \mathbb{E}_{X \sim \mathbb{P}^D}[f_{\theta}(X) - 1] \\ M^U, \ M^D \colon \frac{1}{f_{\theta}(X)}, \ 1 \end{array} $
Classical GAN Critic	$ \begin{array}{l} \underline{\mathbf{F}} \colon \frac{\mathbb{P}^U(X)}{\mathbb{P}^U(X) + \mathbb{P}^D(X)} \\ \underline{\mathbf{R}} \colon \operatorname{Goodfellow} \text{ et al. } (2014) \\ \underline{\mathbf{L}} \colon -\mathbb{E}_{X \sim \mathbb{P}^U} \log f_{\theta}(X) - \mathbb{E}_{X \sim \mathbb{P}^D} \log \left[1 - f_{\theta}(X)\right] \\ M^U, \ M^D \colon \frac{1}{f_{\theta}(X)}, \ \frac{1}{1 - f_{\theta}(X)} \\ \ast \text{ for } f_{\theta}(X) = sigmoid(h_{\theta}(X)) \text{ this loss is identical to Logistic Loss in Table 5} \end{array} $
Noise-Data Mixture Ratio	$\begin{array}{l} \underline{\mathrm{F}} \colon \frac{\mathbb{P}^U(X)}{\mathbb{P}^U(X) + \mathbb{P}^D(X)} \\ \underline{\mathrm{R}} \colon \mathrm{This\ paper} \\ \underline{\mathrm{L}} \colon -\mathbb{E}_{X \sim \mathbb{P}^U} f_\theta(X) + \mathbb{E}_{X \sim \mathbb{P}^M} f_\theta(X)^2 \\ M^U, M^D \colon 1, 2f_\theta(X) \\ \mathrm{where} \mathbb{P}^M(X) = \frac{1}{2} \mathbb{P}^U(X) + \frac{1}{2} \mathbb{P}^D(X) \mathrm{serves\ as} down \mathrm{density}, \\ \mathrm{instead\ of\ density} \mathbb{P}^D(X) \end{array}$
Noise-Data Mixture Log-Ratio	$ \begin{array}{l} \underline{\mathrm{F}} \colon \log \frac{\mathbb{P}^U(X)}{\mathbb{P}^U(X) + \mathbb{P}^D(X)} \\ \underline{\mathrm{R}} \colon \mathrm{This \; paper} \\ \underline{\mathrm{L}} \colon -\mathbb{E}_{X \sim \mathbb{P}^U} f_\theta(X) + \mathbb{E}_{X \sim \mathbb{P}^M} 2 \exp[f_\theta(X)] \\ M^U, M^D \colon 1, 2 \exp[f_\theta(X)] \\ \mathrm{where} \mathbb{P}^M(X) = \frac{1}{2} \mathbb{P}^U(X) + \frac{1}{2} \mathbb{P}^D(X) \; \mathrm{serves \; as \; } down \; \mathrm{density}, \\ \mathrm{instead \; of \; density} \; \mathbb{P}^D(X) \end{array} $

Table 4: PSO Instances For Density Ratio Estimation, Part 1

Method	$\underline{\textbf{\textit{F}inal}} \ f_{ heta}(X) \ / \ \underline{\textbf{\textit{R}eferences}} \ / \ \underline{\textbf{\textit{L}oss}} \ / \ M^{\scriptscriptstyle U}(\cdot) \ \ ext{\it and} \ M^{\scriptscriptstyle D}(\cdot)$
Classical	$\underline{\mathrm{F}}$: $\log \frac{\mathbb{P}^U(X)}{\mathbb{P}^U(X) + \mathbb{P}^D(X)}$
GAN Critic	R: This paper
on log-scale	$\underline{\mathbf{L}} \colon \mathbb{E}_{X \sim \mathbb{P}^U} \frac{1}{\exp[f_{\theta}(X)]} - \mathbb{E}_{X \sim \mathbb{P}^D} \log \frac{\exp[f_{\theta}(X)]}{1 - \exp[f_{\theta}(X)]}$
	$\underline{\mathbf{L}} \colon \mathbb{E}_{X \sim \mathbb{P}^U} \frac{1}{\exp[f_{\theta}(X)]} - \mathbb{E}_{X \sim \mathbb{P}^D} \log \frac{\exp[f_{\theta}(X)]}{1 - \exp[f_{\theta}(X)]}$ $M^U, M^D \colon \frac{1}{\exp[f_{\theta}(X)]}, \frac{1}{1 - \exp[f_{\theta}(X)]}$
Power	$\underline{\mathbf{F}}$: $\frac{\mathbb{P}^U(X)}{\mathbb{P}^D(X)}$
Divergence	R: Sugiyama et al. (2012a); Menon and Ong (2016)
Ratio	$\underline{\mathbf{L}}: -\mathbb{E}_{X \sim \mathbb{P}^U} \frac{f_{\theta}(X)^{\alpha}}{\alpha} + \mathbb{E}_{X \sim \mathbb{P}^D} \frac{f_{\theta}(X)^{\alpha+1}}{\alpha+1}$
Estimation	$M^{\scriptscriptstyle U},\ M^{\scriptscriptstyle D}\colon f_{\theta}(X)^{\alpha-1},\ f_{\theta}(X)^{lpha}$
Reversed	$\underline{\mathrm{F}} \colon rac{\mathbb{P}^U(X)}{\mathbb{P}^D(X)}$
KL	<u>R</u> : Uehara et al. (2016)
	$\underline{\mathrm{L}} \colon \mathbb{E}_{X \sim \mathbb{P}^U} \frac{1}{f_{\theta}(X)} + \mathbb{E}_{X \sim \mathbb{P}^D} \log f_{\theta}(X)$
	$M^U,\ M^D\colon rac{1}{[f_ heta(X)]^2},\ rac{1}{f_ heta(X)}$
Balanced	$\underline{\mathrm{F}} \colon rac{\mathbb{P}^U(X)}{\mathbb{P}^D(X)}$
Density	R: This paper
Ratio	$\underline{\mathbf{L}}: -\mathbb{E}_{X \sim \mathbb{P}^U} \log \left[f_{\theta}(X) + 1 \right] + \mathbb{E}_{X \sim \mathbb{P}^D} f_{\theta}(X) - \log \left[f_{\theta}(X) + 1 \right]$
_	$M^U,\ M^D\colon rac{1}{f_ heta(X)+1},\ rac{f_ heta(X)}{f_ heta(X)+1}$
Log-density	$\underline{\mathrm{F}} \colon \log rac{\mathbb{P}^U(X)}{\mathbb{P}^D(X)}$
Ratio	$\underline{\mathbf{R}}$: This paper
	$\underline{\mathbf{L}}: -\mathbb{E}_{X \sim \mathbb{P}^U} f_{\theta}(X) + \mathbb{E}_{X \sim \mathbb{P}^D} \exp[f_{\theta}(X)]$
	$M^{U}, M^{D}: 1, \exp[f_{\theta}(X)]$
Square	$\underline{\mathrm{F}} \colon rac{\mathbb{P}^U(X) - \mathbb{P}^D(X)}{\mathbb{P}^U(X) + \mathbb{P}^D(X)}$
Loss	$\underline{\mathbf{R}}$: Menon and Ong (2016)
	$\underline{\mathbf{L}} \colon \mathbb{E}_{X \sim \mathbb{P}^U} \tfrac{1}{2} [1 - f_{\theta}(X)]^2 + \mathbb{E}_{X \sim \mathbb{P}^D} \tfrac{1}{2} [1 + f_{\theta}(X)]^2$
	$M^{\scriptscriptstyle U}, M^{\scriptscriptstyle D}\!\!: 1-f_{ heta}(X), 1+f_{ heta}(X)$
Logistic	$\underline{\mathrm{F}} \colon \log rac{\mathbb{P}^U(X)}{\mathbb{P}^D(X)}$
Loss	R: Menon and Ong (2016)
	$\underline{\mathbf{L}} \colon \mathbb{E}_{X \sim \mathbb{P}^U} \log \left[1 + \exp[-f_{\theta}(X)] \right] + \mathbb{E}_{X \sim \mathbb{P}^D} \log \left[1 + \exp[f_{\theta}(X)] \right] \\ M^U, \ M^D \colon \frac{1}{\exp[f_{\theta}(X)] + 1}, \ \frac{1}{\exp[-f_{\theta}(X)] + 1}$
	$\exp[j\theta(X)] \pm i \cdot \exp[-j\theta(X)] \pm i$

Table 5: PSO Instances For Density Ratio Estimation, Part 2 $\,$

Method	$\underline{\textbf{\textit{F}}}$ inal $f_{ heta}(X)$ / $\underline{\textbf{\textit{R}}}$ eferences / $\underline{\textbf{\textit{L}}}$ oss / $M^{ extsup{U}}(\cdot)$ and $M^{ extsup{D}}(\cdot)$
Exponential	$\underline{\mathrm{F}} \colon \frac{1}{2} \log \frac{\mathbb{P}^U(X)}{\mathbb{P}^D(X)}$
Loss	$\underline{\mathbf{R}}$: Menon and Ong (2016)
	$\underline{\mathbf{L}} \colon \mathbb{E}_{X \sim \mathbb{P}^U} \exp[-f_{\theta}(X)] + \mathbb{E}_{X \sim \mathbb{P}^D} \exp[f_{\theta}(X)]$ $M^U, M^D \colon \exp[-f_{\theta}(X)], \exp[f_{\theta}(X)]$
LSGAN	$\underline{\mathrm{F}} \colon \ \frac{b \cdot \mathbb{P}^{U}(X) + a \cdot \mathbb{P}^{D}(X)}{\mathbb{P}^{U}(X) + \mathbb{P}^{D}(X)}$
Critic	<u>R</u> : Mao et al. (2017)
	$\underline{\mathbf{L}} \colon \mathbb{E}_{X \sim \mathbb{P}^U} \frac{1}{2} [f_{\theta}(X) - b]^2 + \mathbb{E}_{X \sim \mathbb{P}^D} \frac{1}{2} [f_{\theta}(X) - a]^2$
	$M^{U}, M^{D}: b - f_{\theta}(X), f_{\theta}(X) - a$
	$\underline{\mathbf{F}}$: $1 + \log \frac{\mathbb{P}^U(X)}{\mathbb{P}^D(X)}$
Divergence	R: Nowozin et al. (2016)
	$\underline{\mathbf{L}}: -\mathbb{E}_{X \sim \mathbb{P}^U} f_{\theta}(X) + \mathbb{E}_{X \sim \mathbb{P}^D} \exp[f_{\theta}(X) - 1]$ $M^U, M^D: 1, \exp[f_{\theta}(X) - 1]$
Reverse KL	$\underline{\mathrm{F}}$: $-rac{\mathbb{P}^D(X)}{\mathbb{P}^U(X)}$
Divergence	$\underline{\mathbf{R}}$: Nowozin et al. (2016)
	$\underline{\mathbf{L}}: -\mathbb{E}_{X \sim \mathbb{P}^U} f_{\theta}(X) + \mathbb{E}_{X \sim \mathbb{P}^D} [-1 - \log[-f_{\theta}(X)]] \\ M^U, \ M^D: \ 1, \ \frac{1}{-f_{\theta}(X)}$
Lipschitz	$\underline{\mathbf{F}} \colon \frac{1}{2} \cdot \frac{\mathbb{P}^{U}(X) - \mathbb{P}^{D}(X)}{\sqrt{\mathbb{P}^{U}(X) \cdot \mathbb{P}^{D}(X)}}$
Continuity	$\underline{\mathbf{R}}$: Zhou et al. (2018)
Objective	$\underline{\mathbf{L}} \colon -\mathbb{E}_{X \sim \mathbb{P}^U} \left[f_{\theta}(X) - \sqrt{f_{\theta}(X)^2 + 1} \right] + \mathbb{E}_{X \sim \mathbb{P}^D} \left[f_{\theta}(X) + \sqrt{f_{\theta}(X)^2 + 1} \right]$
	$M^{U}, M^{D}: 1 - \frac{f_{\theta}(X)}{\sqrt{f_{\theta}(X)^{2}+1}}, 1 + \frac{f_{\theta}(X)}{\sqrt{f_{\theta}(X)^{2}+1}}$
Log-density	$\underline{\mathrm{F}}$: $\arctan\log \frac{\mathbb{P}^U(X)}{\mathbb{P}^D(X)}$
Atan-Ratio	R: This paper
	L: unknown
	M^U , M^D : $\frac{1}{\exp[\tan f_{\theta}(X)]+1}$, $\frac{1}{\exp[-\tan f_{\theta}(X)]+1}$ * the range of $f_{\theta}(X)$ should be restricted to $\left[-\frac{\pi}{2}, \frac{\pi}{2}\right]$
Log-density	$\underline{\mathrm{F}}$: $\tanh\log\frac{\mathbb{P}^U(X)}{\mathbb{P}^D(X)}$
Tanh-Ratio	$\underline{\mathbf{R}}$: This paper
	$\underline{\mathrm{L}} \colon \mathbb{E}_{X \sim \mathbb{P}^U} \stackrel{2}{\overset{2}{{_{}}}} \cdot [1 - f_{\theta}(X)]^{\frac{3}{2}} + \mathbb{E}_{X \sim \mathbb{P}^D} \stackrel{2}{\overset{2}{{_{}}}} \cdot [1 + f_{\theta}(X)]^{\frac{3}{2}}$
	$M^{U}, M^{D}: \sqrt{1 - f_{\theta}(X)}, \sqrt{1 + f_{\theta}(X)}$ * the range of $f_{\theta}(X)$ should be restricted to $[-1, 1]$

Table 6: PSO Instances For Density Ratio Estimation, Part 3

Example 1: From Table 2 we can see that IS method has $M^U[X, f_{\theta}(X)] = 1$ and $M^D[X, f_{\theta}(X)] = \frac{\exp[f_{\theta}(X)]}{\mathbb{P}^D(X)}$. Given that samples within the loss have densities $X^U \sim \mathbb{P}^U(X)$ and $X^D \sim \mathbb{P}^D(X)$, we can substitute the sample densities and the *magnitude* functions $\{M^U, M^D\}$ into Eq. (2) to get:

$$\frac{\mathbb{P}^{U}(X)}{\mathbb{P}^{D}(X)} = \frac{\exp[f_{\theta}(X)]/\mathbb{P}^{D}(X)}{1} \quad \Rightarrow \quad f_{\theta}(X) = \log \mathbb{P}^{U}(X),$$

where we use equality between density ratio of the samples and ratio of magnitude functions to derive the final $f_{\theta}(X)$. Thus, in case of Importance Sampling, the surface will converge to the log-density $\log \mathbb{P}^{U}(X)$.

More formally, we can derive PSO convergence according to the below theorem. It requires a definition of inverse functions: for any $h(X,z): \mathbb{R}^n \times \mathbb{R} \to \mathbb{R}$ we define its inverse function $h^{-1}(X,s): \mathbb{R}^n \times \mathbb{R} \to \mathbb{R}$ s.t. $h^{-1}[X,h[X,z]] = z$ and $h[X,h^{-1}[X,s]] = s$.

Theorem 2 (PSO Convergence) Consider a particular $\{\mathbb{P}^U, \mathbb{P}^D, M^U, M^D\}$ and define \mathcal{F} to be a space of functions from \mathbb{R}^n to $\mathbb{A} \subseteq \mathbb{R}$. Define f^* s.t. $\forall X \in \mathbb{S}^{U \cap D} : \mathbb{P}^U(X) \cdot M^U[X, f^*(X)] = \mathbb{P}^D(X) \cdot M^D[X, f^*(X)]$ and assume $f^* \in \mathcal{F}$. Further, assume that:

1.
$$\forall X \in \mathbb{S}^{U \cap D}, s \in \mathbb{A} : \frac{M^D(X,s)}{M^U(X,s)}$$
 is well-defined.

2.
$$\forall X \in \mathbb{S}^{U \cap D}, s_1, s_2 \in \mathbb{A} : \frac{M^D(X, s_1)}{M^U(X, s_1)} = \frac{M^D(X, s_2)}{M^U(X, s_2)} \Leftrightarrow s_1 = s_2.$$

Denote PSO convergence by a transformation $T(X,z): \mathbb{R}^n \times \mathbb{R} \to \mathbb{R}$ s.t. $f^*(X) = T\left[X, \frac{\mathbb{P}^U(X)}{\mathbb{P}^D(X)}\right]$. Then its inverse satisfies:

$$T^{-1}(X,s) \equiv \frac{M^{D}(X,s)}{M^{U}(X,s)},$$

and the transformation T(X,z) can be retrieved by finding an inverse of $T^{-1}(X,s)$ w.r.t. s.

Proof Condition 2 implies that $\frac{M^D(X,s)}{M^U(X,s)}$ is invertible w.r.t. second argument $s \in \mathbb{A}$ for any $X \in \mathbb{S}^{U \cap D}$. It can be seen also as the criteria over $\{M^U, M^D\}$ under which PSO instance has a unique solution when the considered functions have range \mathbb{A} . Observe that $\frac{M^D(X,s)}{M^U(X,s)}$ may be not invertible when considering entire $s \in \mathbb{R}$.

Hence, for any given $X \in \mathbb{S}^{U \cap D}$ the mapping $T^{-1}[X,s] = \frac{M^D(X,s)}{M^U(X,s)}$ has its inverse T[X,z]. From PSO balance state we have $T^{-1}[X,f^*(X)] = \frac{M^D(X,f^*(X))}{M^U(X,f^*(X))} = \frac{\mathbb{P}^U(X)}{\mathbb{P}^D(X)}$. Then applying the inverse T will lead to $T[X,T^{-1}[X,f^*(X)]] = f^*(X)$. Replacing $T^{-1}[X,f^*(X)]$ with $\frac{\mathbb{P}^U(X)}{\mathbb{P}^D(X)}$ will produce $T[X,\frac{\mathbb{P}^U(X)}{\mathbb{P}^D(X)}] = f^*(X)$. Thus, given any ratio of magnitudes $\frac{M^D(X,s)}{M^U(X,s)}$, we can find the PSO convergence T(X,z) as its inverse.

Example 2: Consider the "Polynomial" method in Table 2, with $M^U[X, f_{\theta}(X)] = \frac{\exp[f_{\theta}(X)]}{\mathbb{P}^D(X)}$ and $M^D[X, f_{\theta}(X)] = \frac{\exp[2f_{\theta}(X)]}{\mathbb{P}^D(X)^2}$. Then, according to the above derivation we have $\frac{M^D(X, f_{\theta}(X))}{M^U(X, f_{\theta}(X))} = \frac{\exp[f_{\theta}(X)]}{\mathbb{P}^D(X)}$ and hence $T^{-1}(X, s) = \frac{\exp s}{\mathbb{P}^D(X)}$. Observe that $T^{-1}(X, s)$ is bijective when considering $s \in \mathbb{R}$, and hence there is no need to limit range of a model $f_{\theta}(X)$. Further, T^{-1} has a simple form and its invert is merely $T(X, z) = \log \mathbb{P}^D(X) + \log z$. The above T and T^{-1} are inverse of each other w.r.t. the second argument, which can be easily verified. Next, we can calculate PSO convergence as $f_{\theta}(X) = T\left[X, \frac{\mathbb{P}^U(X)}{\mathbb{P}^D(X)}\right] = \log \mathbb{P}^D(X) + \log \frac{\mathbb{P}^U(X)}{\mathbb{P}^D(X)} = \log \mathbb{P}^U(X)$. Hence, "Polynomial" method converges to $\log \mathbb{P}^U(X)$.

3.2 Deriving New PSO Instance

In order to apply PSO for learning any function of X and $\frac{\mathbb{P}^U(X)}{\mathbb{P}^D(X)}$, the appropriate PSO instance can be derived as following.

Theorem 3 (Ratio Estimation) Denote the required PSO convergence by a transformation $T(X,z): \mathbb{R}^n \times \mathbb{R} \to \mathbb{R}$ s.t. $f_{\theta}(X) = T\left[X, \frac{\mathbb{P}^U(X)}{\mathbb{P}^D(X)}\right]$ is the function we want to learn. Given T(X,z) is one-to-one function w.r.t. z, any pair $\{M^U,M^D\}$ satisfying:

$$\frac{M^{D}(X,s)}{M^{U}(X,s)} = T^{-1}(X,s),$$

will produce the required convergence.

The proof is trivial by noting that:

$$T^{-1}\left[X, f_{\theta}(X)\right] = \frac{M^{D}\left[X, f_{\theta}(X)\right]}{M^{U}\left[X, f_{\theta}(X)\right]} = \frac{\mathbb{P}^{U}(X)}{\mathbb{P}^{D}(X)} \Rightarrow$$

$$\Rightarrow T\left[X, \frac{\mathbb{P}^{U}(X)}{\mathbb{P}^{D}(X)}\right] = T\left[X, T^{-1}\left[X, f_{\theta}(X)\right]\right] = f_{\theta}(X).$$

where we used PSO balance state and properties of inverse functions. Observe that one-to-one property is necessary for existence of T^{-1} .

Hence, to learn any function $T\left[X,\frac{\mathbb{P}^U(X)}{\mathbb{P}^D(X)}\right]$, first we obtain $T^{-1}(X,s)$ by finding an inverse of T(X,z) w.r.t. z. Then any pair of magnitudes satisfying $\frac{M^D(X,s)}{M^U(X,s)} = T^{-1}[X,s]$ will converge at $f_{\theta}(X) = T\left[X,\frac{\mathbb{P}^U(X)}{\mathbb{P}^D(X)}\right]$. For example, we can use a simple choice $M^D[X,s] = T^{-1}[X,s]$ and $M^U[X,s] = 1$ in order to converge to the desired target. Such choice corresponds to minimizing f-divergence (Nguyen et al., 2010; Nowozin et al., 2016), see Section 4 for details. Yet, typically these magnitude functions will be sub-optimal if for example M^D is an unbounded function. When this is the case, we can derive a new pair of bounded magnitude functions by multiplying the old pair by the same factor q[X,s] (see also Section 5.2).

Example 3: Consider a scenario where we would like to infer $f_{\theta}(X) = \frac{\mathbb{P}^{U}(X) - \mathbb{P}^{D}(X)}{\mathbb{P}^{U}(X) + \mathbb{P}^{D}(X)}$, similarly to "Square Loss" method in Table 4. Considering only points $X \in \mathbb{S}^{D}$, we can rewrite our objective as $f_{\theta}(X) = \frac{\mathbb{P}^{U(X)}(X) - 1}{\mathbb{P}^{D(X)}(X) + 1}$ and hence the required PSO convergence is given by $T(X,z) = \frac{z-1}{z+1}$. Further, its inverse function is given by $T^{-1}(X,s) = \frac{1+s}{1-s}$. Therefore, magnitude functions must satisfy $\frac{M^D(X,f_{\theta}(X))}{M^U(X,f_{\theta}(X))} = \frac{1+f_{\theta}(X)}{1-f_{\theta}(X)}$. One choice for such magnitudes is $M^U[X,f_{\theta}(X)] = 1 - f_{\theta}(X)$ and $M^D[X,f_{\theta}(X)] = 1 + f_{\theta}(X)$, just like in the "Square Loss" method (Menon and Ong, 2016), although other variants with the same PSO balance state can be easily constructed. For instance, we can use $M^{U}[X, f_{\theta}(X)] = \frac{1 - f_{\theta}(X)}{D(X, f_{\theta}(X))}$ and $M^{D}[X, f_{\theta}(X)] = \frac{1+f_{\theta}(X)}{D(X, f_{\theta}(X))}$ with $D(X, f_{\theta}(X)) \triangleq |1 - f_{\theta}(X)| + |1 + f_{\theta}(X)|$ instead. Such normalization by function $D(\cdot)$ does not change the convergence, yet it produces bounded magnitude functions that are typically more stable during the optimization. Furthermore, recall that we considered only points within support of $\mathbb{P}^{D}(X)$. Outside of this support, any $X \in \mathbb{S}^{U \setminus D}$ will push the model surface $f_{\theta}(X)$ according to the rules implied by M^{U} ; note also that M^U changes signs at $f_{\theta}(X) = 1$, with force always directed toward the height h(X) = 1. Therefore, at points $\{X \in \mathbb{S}^{U \setminus D}\}$ the convergence will be $f_{\theta}(X) = 1$, which is also the corollary of the condition 2-d in Theorem 1. Finally at points outside of both supports there is no optimization performed, and hence theoretically nothing moves there no constraints are applied on the surface in these areas. Yet, in practice $f_{\theta}(X)$ at $X \notin \mathbb{S}^{U \cup D}$ will be affected by pushes at the training points, according to the elasticity properties of the model expressed via kernel $q_{\theta}(X, X')$.

Likewise, in a similar manner we can also derive a new PSO instances to infer any function of density $T[X, \mathbb{P}^U(X)]$.

Theorem 4 (Density Estimation) Denote the required PSO convergence by a transformation $T(X,z): \mathbb{R}^n \times \mathbb{R} \to \mathbb{R}$ s.t. $f_{\theta}(X) = T[X,\mathbb{P}^U(X)]$ is the function we want to learn. Given T(X,z) is one-to-one function w.r.t. z, any pair $\{M^U,M^D\}$ satisfying:

$$\frac{M^{D}(X,s)}{M^{U}(X,s)} = \frac{T^{-1}(X,s)}{\mathbb{P}^{D}(X)},$$

will produce the required convergence.

The proof is similar to Theorem 3. The above theorem can be used to mechanically recover many existing pdf estimation techniques. In Section 6.2 we will use it to derive new methods for log-density estimation.

Further, density of up and down sample points within PSO loss can be changed from the described above choice \mathbb{P}^U and \mathbb{P}^D , to infer other target functions. For example, in "Noise-Data Mixture Ratio" from Table 4 instead of $\mathbb{P}^D(X)$ we sample $\frac{1}{2}\mathbb{P}^U(X) + \frac{1}{2}\mathbb{P}^D(X)$ to construct training dataset of down points (denoted by $\{X_i^D\}$ in Eq. (1)). That is, the updated down density is mixture of two original densities with equal weights. Then, by substituting sample densities and appropriate magnitude functions $\{M^U[X, f_\theta(X)] = 1, M^D[X, f_\theta(X)] = 2f_\theta(X)\}$ into the balance state equilibrium we will get:

$$\frac{\mathbb{P}^{U}(X)}{\frac{1}{2}\mathbb{P}^{U}(X) + \frac{1}{2}\mathbb{P}^{D}(X)} = \frac{2f_{\theta}(X)}{1} \quad \Rightarrow \quad f_{\theta}(X) = \frac{\mathbb{P}^{U}(X)}{\mathbb{P}^{U}(X) + \mathbb{P}^{D}(X)}.$$

Hence, the "Noise-Data Mixture Ratio" infers the same target function as the Classical GAN Critic loss from Table 4, and can be used as its alternative. Therefore, an additional degree of freedom is acquired by considering different sampling strategies in PSO framework. Similar ideas will allow us to also infer conditional density functions, as shown in Section 7.

In Tables 2-6, we additionally refer to relevant works in case the specific PSO losses were already discovered in previous scientific studies. The previously discovered ones were all based on various sophisticated mathematical laws and theories, yet they all could be also derived in a simple unified way using PSO principles. Additionally, besides the previously discovered methods, in Tables 2-6 we introduce several new losses for inference of different stochastic modalities of the data, as the demonstration of usage and usefulness of the general PSO formulation. Moreover, in Section 4 we reveal that PSO framework has a tight relation with Bregman and "f" divergencies. Furthermore, in Section 11.4 we prove that the cross-entropy losses are also instances of PSO. Likewise, in Section 11.8 we derive Maximum Likelihood Estimation (MLE) from PSO equilibrium.

Finally, notice that in this paper we discuss PSO and its applications in context of only continuous multi-dimensional data. However, in theory the same principles can work also for discrete data. The sampled points X_i^U and X_i^D will be located only at discrete locations of the surface $f_{\theta}(X)$ since the points are in $\mathbb{Z}^n \subset \mathbb{R}^n$. Yet, the balance at each such point will still be governed by the same up and down forces. Thus, we can apply similar PSO methods to also infer statistical properties of discrete data.

Remark 5 From Tables 2-6 it is easy to see that many different PSO instances may have an identical approximated target function. In Sections 5 and 6 we discuss how to choose the most optimal PSO instance from the existing ones, based on the properties of magnitude functions.

4. PSO, Bregman and "f" Divergencies

Below we define PSO divergence and show its connection to Bregman divergence (Bregman, 1967; Gneiting and Raftery, 2007) and f-divergence (Ali and Silvey, 1966), that are associated with many existing statistical methods.

4.1 PSO Divergence

Minimization of $L_{PSO}(f)$ corresponds also to minimization of:

$$D_{PSO}(f^*, f) \triangleq L_{PSO}(f) - L_{PSO}(f^*) = - \underset{X \sim \mathbb{P}^U}{\mathbb{E}} \int_{f^*(X)}^{f(X)} M^U(X, t) dt + \underset{X \sim \mathbb{P}^D}{\mathbb{E}} \int_{f^*(X)}^{f(X)} M^D(X, t) dt$$

$$\tag{5}$$

where f^* is the optimal solution characterized by Theorems 1 and 2. Assuming f^* to be unique and since $L_{PSO}(f) \ge L_{PSO}(f^*)$, we have the following properties: $D_{PSO}(f^*, f) \ge 0$ and $D_{PSO}(f^*, f) = 0 \iff f^* = f$. Thus, D_{PSO} can be used as a "distance" between f and f^* and we name it PSO divergence. Yet, note that D_{PSO} does not measure distance between any two functions; instead it evaluates distance between any f and the optimal solution of specific PSO instance, derived from the corresponding $\{\mathbb{P}^U, \mathbb{P}^D, M^U, M^D\}$ via PSO balance state.

4.2 Bregman Divergence

Define \mathcal{F} to be a convex set of non-negative functions from \mathbb{R}^n to \mathbb{R}_+ . Bregman divergence for every $q, p \in \mathcal{F}$ is defined as $D_{\psi}(q, p) = \psi(q) - \psi(p) + \int \nabla_q \psi(q(X)) \cdot [q(X) - p(X)] dX$, where $\psi(s)$ is a continuously-differentiable, strictly convex functional over $s \in \mathcal{F}$, and ∇_q is the differentiation w.r.t. q. When $\psi(s)$ has a form $\psi(s) = \int \varphi(s(X)) dX$ with a strictly convex function $\varphi : \mathbb{R} \to \mathbb{R}$, the divergence is referred to as U-divergence (Eguchi, 2009) or sometimes as separable Bregman divergence (Grünwald et al., 2004). In such case $D_{\psi}(q, p)$ has the form:

$$D_{\varphi}(q,p) = \int \varphi\left[q(X)\right] - \varphi\left[p(X)\right] + \varphi'\left[p(X)\right] \cdot \left[q(X) - p(X)\right] dX.$$

The above modality is non-negative for all $q, p \in \mathcal{F}$ and is zero if and only if q = p, hence it specifies a "distance" between q and p. For this reason, $D_{\varphi}(q,p)$ is widely used in the optimization $\min_p D_{\varphi}(q,p)$ where q usually represents an unknown density of available i.i.d. samples and p is a model which is optimized to approximate q. For example, when $\varphi(z) = z \cdot \log z$, we obtain the generalized KL divergence $D_{\varphi}(q,p) = \int -q(X) + q(X) \cdot \log p(X) + p(X) dX$ (Uehara et al., 2018). It can be further reduced to MLE objective $-\mathbb{E}_{X \sim q(X)} \log p(X)$ in case p is normalized, as is shown in Section 11.8.

Further, the term $\psi(s) \triangleq \int \varphi\left[s(X)\right] dX$ is called an entropy of s, and $d_{\varphi}(q,p) \triangleq -\psi(p) + \int \varphi'\left[p(X)\right] \cdot \left[q(X) - p(X)\right] dX$ is referred to as a cross-entropy between q and p. Since $D_{\varphi}(q,p) = d_{\varphi}(q,p) - d_{\varphi}(q,q)$, usually the actual optimization being solved is $\min_{p} d_{\varphi}(q,p)$ where the cross-entropy objective is approximated via Monte-Carlo integration.

Claim 6 Consider a strictly convex and twice differentiable function φ and two densities \mathbb{P}^U and \mathbb{P}^D that satisfy $\mathbb{S}^U \subseteq \mathbb{S}^D$. Likewise, define magnitudes $\{M^U[X,t] = \varphi''(t), M^D[X,t] = \frac{t \cdot \varphi''(t)}{\mathbb{P}^D(X)}\}$ and a space of non-negative functions \mathcal{F} . Then PSO functional and PSO divergence are equal to U-cross-entropy (up to an additive constant) and U-divergence defined by φ , respectively:

- 1. $\forall f \in \mathcal{F} : L_{PSO}(f) = d_{\varphi}(\mathbb{P}^{U}, f)$
- 2. $\forall f \in \mathcal{F} : D_{PSO}(\mathbb{P}^U, f) = D_{\varphi}(\mathbb{P}^U, f)$

Proof Impulses corresponding to the above magnitude functions are $\{\widetilde{M}^U[X,t] = \varphi'(t) + c_U, \widetilde{M}^D[X,t] = \frac{[t\cdot\varphi'(t)-\varphi(t)]}{\mathbb{P}^D(X)} + c_D\}$, where c_U and c_D are additive constants. Denote $c \triangleq c_D - c_U$. Introducing above expressions into L_{PSO} defined in Eq. (3) will lead to:

$$\forall f \in \mathcal{F}: \quad L_{PSO}(f) = \int -\varphi \left[f(X) \right] + \varphi' \left[f(X) \right] \cdot \left[f(X) - \mathbb{P}^{U}(X) \right] dX + c = d_{\varphi}(\mathbb{P}^{U}, f) + c.$$

Further, according to Theorem 2 the minimizer f^* of $L_{PSO}(f)$ for a given $\{M^U, M^D\}$ is $\mathbb{P}^U(X)$. Therefore, according to Eq. (5) we have $D_{PSO}(f^*, f) \triangleq L_{PSO}(f) - L_{PSO}(f^*) = d_{\varphi}(\mathbb{P}^U, f) - d_{\varphi}(\mathbb{P}^U, f) - d_{\varphi}(\mathbb{P}^U, f) = D_{\varphi}(\mathbb{P}^U, f)$.

From the above we can conclude that definitions of Bregman and PSO divergencies coincide when the former is limited to U-divergence and the latter is limited to magnitudes

that satisfy $\frac{M^D[X,t]}{M^U[X,t]} = \frac{t}{\mathbb{P}^D(X)}$. Such PSO subgroup has balance state at $f^*(X) = \mathbb{P}^U(X)$, and thus it contains all PSO instances for a density estimation, not including log-density estimation. Further, since $L_{PSO}(f) = d_{\varphi}(\mathbb{P}^U, f)$, a family of algorithms that minimize U-divergence and PSO subgroup of density estimators are equivalent. However, in general PSO divergence is different from Bregman as it can also be used to measure a "distance" between any PSO solution f^* , including even negative functions such as log-density $\log \mathbb{P}^U(X)$ and log-density-ratio $\log \frac{\mathbb{P}^U(X)}{\mathbb{P}^D(X)}$ (see Section 3), and any $f \in \mathcal{F}$ without the non-negative constraint over \mathcal{F} .

4.3 f-Divergence

Define q and p to be probability densities so that q is absolutely continuous w.r.t. p. Then, f-divergence between q and p is defined as $D_{\phi}(q,p) = \int p(X) \cdot \phi(\frac{q(X)}{p(X)}) dX$, where $\phi : \mathbb{R} \to \mathbb{R}$ is a convex and lower semicontinuos function s.t. $\phi(1) = 0$. This divergence family contains many important special cases, such as KL divergence (for $\phi(u) = u \cdot \log u$) and Jensen-Shannon divergence (for $\phi(u) = -(u+1) \cdot \log \frac{1+u}{2} + u \cdot \log u$).

In (Nguyen et al., 2010) authors proved that it is lower-bounded as:

$$D_{\phi}(q, p) \ge \sup_{f \in \mathcal{F}} J(f, q, p), \quad J(f, q, p) \triangleq \underset{X \sim q(X)}{\mathbb{E}} f(X) - \underset{X \sim p(X)}{\mathbb{E}} \phi^{c} \left[f(X) \right],$$

where ϕ^c is the convex conjugate function of ϕ : $\phi^c(v) \triangleq \sup_{u \in \mathbb{R}} \{uv - \phi(u)\}$. The above expression becomes equality when $\phi'(\frac{q(X)}{p(X)})$ belongs to a considered function space \mathcal{F} . In such case, the supremum is obtained via $f(X) = \phi'(\frac{q(X)}{p(X)})$. Therefore, the above lower bound is widely used in the optimization $\max_f J(f,q,p)$ to approximate $D_{\phi}(q,p)$ (Nguyen et al., 2010), and to learn any function of $\frac{q(X)}{p(X)}$ (Nowozin et al., 2016).

Claim 7 Consider a convex and lower semicontinuos function ϕ s.t. $\phi(1) = 0$, its convex conjugate ϕ^c , and two densities \mathbb{P}^U and \mathbb{P}^D that satisfy $\mathbb{S}^U \subseteq \mathbb{S}^D$. Likewise, define PSO impulses $\{\widetilde{M}^U[X,t]=t,\widetilde{M}^D[X,t]=\phi^c(t)\}$ and assume that $\phi'(\frac{\mathbb{P}^U(X)}{\mathbb{P}^D(X)})$ is contained in a function space \mathcal{F} . Then PSO functional and f-divergence have the following connection:

1.
$$\forall f \in \mathcal{F} : L_{PSO}(f) \equiv -J(f, \mathbb{P}^U, \mathbb{P}^D)$$
 and
$$f^* = \arg\min_{f \in \mathcal{F}} L_{PSO}(f) = \arg\max_{f \in \mathcal{F}} J(f, \mathbb{P}^U, \mathbb{P}^D) = \phi'(\frac{\mathbb{P}^U(X)}{\mathbb{P}^D(X)})$$

2.
$$\forall f \in \mathcal{F} : D_{\phi}(\mathbb{P}^U, \mathbb{P}^D) = -L_{PSO}(f^*) \ge -L_{PSO}(f)$$

Proof Introducing the given $\{\widetilde{M}^U, \widetilde{M}^D\}$ into Eq. (3) leads to $L_{PSO}(f) \equiv -J(f, \mathbb{P}^U, \mathbb{P}^D)$. Further, since $\{M^U[X,t] = 1, M^D[X,t] = \phi^{c\prime}(t)\}$ we have $\frac{M^D[X,t]}{M^U[X,t]} = \phi^{c\prime}(t)$. Denote $T^{-1}[X,t] = \frac{M^D[X,t]}{M^U[X,t]} = \phi^{c\prime}(t)$ and observe that its inverse is $T[X,z] = \phi'(z)$ due properties of Legendre-Fenchel transform. Applying Theorem 2, we conclude $f^*(X) = \phi'(\frac{\mathbb{P}^U(X)}{\mathbb{P}^D(X)})$. Finally, since we assumed $f^* \in \mathcal{F}$, we also have $D_{\phi}(\mathbb{P}^U,\mathbb{P}^D) = J(f^*,\mathbb{P}^U,\mathbb{P}^D) = -L_{PSO}(f^*)$.

Hence, in light of the above connection PSO framework can be seen as an estimation of a negative f-divergence between \mathbb{P}^U and \mathbb{P}^D , $-D_{\phi}(\mathbb{P}^U, \mathbb{P}^D)$. Likewise, it is identical to an estimation framework of (Nowozin et al., 2016) when magnitudes are limited to have forms $\{M^U[X,t]=1,M^D[X,t]=\phi^{c'}(t)\}$ for some $\phi^{c'}$. Due to such limitation the algorithm family in (Nowozin et al., 2016) is a strict subgroup of PSO. Furthermore, the formulation of this framework can be generalized as:

$$\min_{f \in \mathcal{F}} - \underset{X \sim q(X)}{\mathbb{E}} G\left[X, f(X)\right] + \underset{X \sim p(X)}{\mathbb{E}} \phi^{c}\left[G\left[X, f(X)\right]\right],\tag{6}$$

where f is replaced by a transformation $G(X,t): \mathbb{R}^n \times \mathbb{R} \to \mathbb{R}$ over the inner model f. Consequently, G can be selected to obtain any required convergence $f^* = G^{-1} \odot \phi' \odot \frac{\mathbb{P}^U}{\mathbb{P}^D}$. Such extension with a given pair $\{\phi, G\}$ becomes identical to PSO instance with a given $\{\widetilde{M}^U, \widetilde{M}^D\}$ via the following connection:

- 1. $\forall G, \phi$ s.t. G[X, f(X)] and $\phi(u)$ are feasible choice in (Nowozin et al., 2016), set $\widetilde{M}^{U}[X, t] = G[X, t]$ and $\widetilde{M}^{D}[X, t] = \phi^{c}[G[X, t]]$.
- 2. $\forall \widetilde{M}^{U}, \widetilde{M}^{D}$ that are feasible PSO choice according to Theorem 1 , set $G\left[X,t\right] = \widetilde{M}^{U}\left[X,t\right]$ and find ϕ s.t. $\widetilde{M}^{D}\left[X,t\right] = \phi^{c}\left[\widetilde{M}^{U}\left[X,t\right]\right]$.

The extension in Eq. (6) requires a remark about novelty of PSO compared to the work in (Nowozin et al., 2016). First, note that the generalization in Eq. (6) was not proposed by any study, to the best of our knowledge, although the original paper was considering a transformation G[f(X)] to control the domain of particular ϕ^c . Further, there are three main points of difference between two estimation procedures. PSO is defined via $\{M^U, M^D\}$, allowing $\{\widetilde{M}^U, \widetilde{M}^D\}$ to not have an analytical form which in turn increases the number of feasible estimators. Further, using G[X, f(X)] instead of G[f(X)] is important to allow more freedom in selecting the required convergence f^* . Finally, PSO allows for a better intuition which is not available for the f-divergence formulation in (Nowozin et al., 2016), and can further be used to analyze convergence outside of the mutual support $\mathbb{S}^{U\cap D}$.

4.4 Divergence Relation Summary

Due to above links PSO loss can be rewritten as $L_{PSO}(f) = D_{PSO}(f^*, f) - D_{\phi}(\mathbb{P}^U, \mathbb{P}^D)$, where PSO divergence $D_{PSO}(f^*, f)$ can be considered as an extension of separable Bregman divergence and where $D_{\phi}(\mathbb{P}^U, \mathbb{P}^D)$ is f-divergence defined via some ϕ . Further, minimization of $L_{PSO}(f)$ is same as the minimization of PSO divergence between f^* and f. Finally, at the convergence f^* , $D_{PSO}(f^*, f^*)$ becomes zero and $L_{PSO}(f^*)$ is equal to $-D_{\phi}(\mathbb{P}^U, \mathbb{P}^D)$.

5. Properties of PSO Estimators

In the above section we saw that PSO principles are omnipresent within many statistical techniques. In this section we will investigate how these principles actually work in practice. Herein we will analyze consistency, convergence and stability of PSO, further emphasizing the extreme similarity between PSO actual dynamics and the thermodynamical illustration in Figure 1. Likewise, we will propose several techniques to improve the practical stability of PSO algorithms.

5.1 Consistency and Asymptotic Normality

PSO solution f_{θ^*} is obtained by solving $\min_{f_{\theta} \in \mathcal{F}} L_{PSO}(f_{\theta})$, and hence PSO belongs to the family of extremum estimators (Amemiya, 1985). Members of this family are known to be consistent and asymptotically normal estimators under appropriate regularity conditions. Below we restate the corresponding theorems.

Herein, we will reduce the scope to PSO instances whose up and down densities have an identical support. This is required to avoid the special PSO cases for which f_{θ^*} has convergence at infinity outside of the mutual support (see part 2 of Theorem 1). Although it is possible to evade such convergence by considering \mathcal{F} whose functions' output is lower and upper bounded (see Section 5.6), we sidestep this by assuming $\mathbb{S}^U \equiv \mathbb{S}^D$, for simplicity.

The empirical PSO loss over N^U samples from \mathbb{P}^U and N^D samples from \mathbb{P}^D has a form:

$$\hat{L}_{PSO}^{N^{U},N^{D}}(f_{ heta}) = -rac{1}{N^{U}}\sum_{i=1}^{N^{U}}\widetilde{M}^{U}\left[X_{i}^{U},f_{ heta}(X_{i}^{U})
ight] + rac{1}{N^{D}}\sum_{i=1}^{N^{D}}\widetilde{M}^{D}\left[X_{i}^{D},f_{ heta}(X_{i}^{D})
ight],$$

with its gradient $\nabla_{\theta} \hat{L}_{PSO}^{N^{U},N^{D}}(f_{\theta})$ being defined in Eq. (1).

Theorem 8 (PSO Consistency) Assume:

- 1. Parameter space Θ is compact set.
- 2. $L_{PSO}(f_{\theta})$ (defined in Eq. (3)) is continuous on $\theta \in \Theta$.
- 3. $\exists !\theta^* \in \Theta, \forall X \in \mathbb{S}^{U \cap D} : \mathbb{P}^U(X) \cdot M^U[X, f_{\theta^*}(X)] = \mathbb{P}^D(X) \cdot M^D[X, f_{\theta^*}(X)].$

4.
$$\sup_{\theta \in \Theta} \left| \hat{L}_{PSO}^{N^U,N^D}(f_{\theta}) - L_{PSO}(f_{\theta}) \right| \stackrel{p}{\to} 0 \text{ along with } \min(N^U,N^D) \to \infty.$$

Define $\hat{\theta}_{N^U,N^D} = \arg\min_{\theta \in \Theta} \hat{L}_{PSO}^{N^U,N^D}(f_{\theta})$. Then $\hat{\theta}_{N^U,N^D}$ converges in probability to θ^* along with $\min(N^U,N^D) \to \infty$, $\hat{\theta}_{N^U,N^D} \stackrel{p}{\to} \theta^*$.

The above assumptions are typically taken by many studies to claim the estimation consistency. Assumption 3 ensures that there is only single vector θ^* for which PSO balance state is satisfied. Hence it ensures that $L_{PSO}(f_{\theta})$ is uniquely minimized at θ^* , according to Theorem 1. Assumption 4 is the uniform convergence of empirical loss towards its population form along with $\min(N^U, N^D) \to \infty$. The above consistency statement and its proof appear as theorem 2.1 in (Newey and McFadden, 1994).

Theorem 8 ensures the estimation consistency of PSO under technical conditions over space Θ . However, some of these conditions (e.g. compactness of Θ) are not satisfied by NNs. Another way, taken by (Nguyen et al., 2010; Kanamori et al., 2012), is to use a complexity metric defined directly over space \mathcal{F} , such as bracketing entropy. We shall leave this more sophisticated consistency derivation for future work.

For asymptotic normality we will apply the following statements where we use notations $\mathcal{I}_{\theta}(X, X') \triangleq \nabla_{\theta} f_{\theta}(X) \cdot \nabla_{\theta} f_{\theta}(X')^{T}$, $N \triangleq N^{U} + N^{D}$ and $\tau \triangleq \frac{N^{U}}{N^{D}}$.

Lemma 9 (PSO Hessian) Assume $\exists \theta^* \in \Theta \text{ s.t. } \forall X \in \mathbb{S}^{U \cap D} : \mathbb{P}^U(X) \cdot M^U[X, f_{\theta^*}(X)] = \mathbb{P}^D(X) \cdot M^D[X, f_{\theta^*}(X)].$ Denote PSO convergence as $f_{\theta^*}(X) = T\left[X, \frac{\mathbb{P}^U(X)}{\mathbb{P}^D(X)}\right] \equiv f^*(X)$, according to Theorem 2. Then the Hessian \mathcal{H} of population PSO loss at θ^* has a form:

$$\mathcal{H} \equiv \nabla_{\theta\theta} L_{PSO}(f_{\theta^*}) = - \underset{X \sim \mathbb{P}^U}{\mathbb{E}} M^{U'}[X, f^*(X)] \cdot \mathcal{I}_{\theta^*}(X, X) + \underset{X \sim \mathbb{P}^D}{\mathbb{E}} M^{D'}[X, f^*(X)] \cdot \mathcal{I}_{\theta^*}(X, X).$$

Lemma 10 (PSO Gradient Variance) Under the same setting, the variance of $\nabla_{\theta} \hat{L}_{PSO}^{N^{U},N^{D}}(f_{\theta})$ at θ^{*} has a form $Var\left[\nabla_{\theta} \hat{L}_{PSO}^{N^{U},N^{D}}(f_{\theta^{*}})\right] = \frac{1}{N}\mathcal{J}$ where:

$$\mathcal{J} = \frac{\tau + 1}{\tau} \underset{X \sim \mathbb{P}^{U}}{\mathbb{E}} \left[M^{U} \left[X, f^{*}(X) \right]^{2} \cdot \mathcal{I}_{\theta^{*}}(X, X) \right] +$$

$$+ (\tau + 1) \underset{X \sim \mathbb{P}^{D}}{\mathbb{E}} \left[M^{D} \left[X, f^{*}(X) \right]^{2} \cdot \mathcal{I}_{\theta^{*}}(X, X) \right] -$$

$$- \frac{(\tau + 1)^{2}}{\tau} \underset{X' \sim \mathbb{P}^{D}}{\mathbb{E}} M^{U} \left[X, f^{*}(X) \right] \cdot M^{D} \left[X', f^{*}(X') \right] \cdot \mathcal{I}_{\theta^{*}}(X, X').$$

 $\mathcal H$ and $\mathcal J$ have several additional forms that appear in Appendix B along with the lemmas' proofs.

Theorem 11 (PSO Asymptotic Normality) Given assumptions and definitions of Theorem 8, assume additionally:

- 1. $\theta^* \in int(\Theta)$.
- 2. $\hat{L}_{PSO}^{N^U,N^D}(f_{\theta})$ is twice continuously differentiable in a neighborhood of θ^* .
- 3. $\nabla_{\theta\theta} L_{PSO}(f_{\theta})$ is continuous in θ .
- 4. Both \mathcal{J} and \mathcal{H} are non-singular matrices.
- 5. Each entry of $\nabla_{\theta\theta}L_{PSO}(f_{\theta})$ and of \mathcal{J} is uniformly bounded by an integrable function.
- 6. $\tau > 0$ is a finite and fixed scalar.

Then
$$\sqrt{N} \cdot \left[\hat{\theta}_{N^U,N^D} - \theta^* \right]$$
 converges in distribution to $\mathcal{N}(0,\mathcal{H}^{-1}\mathcal{J}\mathcal{H}^{-1})$ along with $N \to \infty$.

Proof of the above theorem is in Appendix C. Thus, we can see that for large sample sizes the parametric estimation error $\sqrt{N^U+N^D}\cdot\left[\hat{\theta}_{N^U,N^D}-\theta^*\right]$ is normal with zero mean and covariance matrix $\Sigma=\mathcal{H}^{-1}\mathcal{J}\mathcal{H}^{-1}$. Further, it is possible to simplify an expression for Σ when considering $\{M^U,M^D\}$ of specific PSO instance. Observe also that none of the above theorems and lemmas require the analytical knowledge of $\{\widetilde{M}^U,\widetilde{M}^D\}$.

5.2 Bounded vs Unbounded Magnitude Functions

Any considered functions $\{M^U, M^D\}$ will produce PSO balance state at the convergence, given that they satisfy the condition 1-b of Theorem 1. Further, as was shown in Section 3, there is infinite number of possible magnitudes that will lead to the same convergence. Thus, we need analytical tools to establish the superiority of one magnitude function pair over another. While this is an advanced estimation topic and is beyond this paper's scope, herein we describe one desired property for these functions to have - boundedness.

In Tables 2-6 we can see many choices of $\{M^U, M^D\}$, with both bounded (e.g. NCE in Table 2) and unbounded (e.g. IS in Table 2) outputs. Further, note that IS method has a magnitude function $M^D[X, f_{\theta}(X)] = \frac{\exp(f_{\theta}(X))}{\mathbb{P}^D(X)}$ with outputs that can be extremely high or low, depending on the difference $[f_{\theta}(X) - \log \mathbb{P}^D(X)]$. From Eq. (1) we can see that the optimization gradient of the down term in PSO loss is $M^D[X, f_{\theta}(X)] \cdot \nabla_{\theta} f_{\theta}(X)$. Thus, in case $f_{\theta}(X) \gg \log \mathbb{P}^D(X)$, high values from $M^D(\cdot)$ will produce gradients with large norm. Such large norm causes instability during the optimization, known as exploding gradients problem in DL community. Intuitively, when we make a large step inside θ -space, the consequences can be unpredictable, especially for a highly non-linear models such as modern NNs. Therefore, in practice the loss with bounded gradient is preferred. This conclusion was also empirically supported in context of unnormalized density estimation (Pihlaja et al., 2012). Further, while it is possible to solve this issue by for example gradient clipping and by decreasing the learning rate (Pascanu et al., 2012), such solutions also slow down the entire learning process.

PSO framework allows to achieve the desired gradient boundedness by bounding magnitude functions' outputs. Consider any pair of functions $\{M^U[X,s],M^D[X,s]\}$ with some desired PSO convergence. In case these are unbounded functions, a new pair of bounded functions can be constructed as

$$M_{bounded}^{\scriptscriptstyle U}\left[X,s\right] = \frac{M^{\scriptscriptstyle U}\left[X,s\right]}{\left|M^{\scriptscriptstyle U}\left[X,s\right]\right| + \left|M^{\scriptscriptstyle D}\left[X,s\right]\right|}, \quad M_{bounded}^{\scriptscriptstyle D}\left[X,s\right] = \frac{M^{\scriptscriptstyle D}\left[X,s\right]}{\left|M^{\scriptscriptstyle U}\left[X,s\right]\right| + \left|M^{\scriptscriptstyle D}\left[X,s\right]\right|}.$$

It is clear from their structure that the new functions' outputs are in [-1,1]. Furthermore, their PSO convergence will be identical to the one of the original pair, since the ratio of both old and new pairs is the same - $\frac{M^D[X,s]}{M^U[X,s]} = \frac{M^D_{bounded}[X,s]}{M^U_{bounded}[X,s]}$. In Section 6.2 we will use the above transformation to develop a new family of robust log-pdf estimators.

5.3 Statistics of Surface Change

Herein we will analyze statistical properties of f_{θ} 's evolution during the optimization. To this end, define the differential $df_{\theta_t}(X) \triangleq f_{\theta_{t+1}}(X) - f_{\theta_t}(X)$ as a change of $f_{\theta}(X)$ after t-th GD iteration. Its first-order Taylor approximation is:

$$df_{\theta}(X) \approx -\delta \cdot \nabla_{\theta} f_{\theta}(X)^{T} \cdot \nabla_{\theta} \hat{L}_{PSO}^{N^{U},N^{D}}(f_{\theta}) =$$

$$= \delta \cdot \left[\frac{1}{N^{U}} \sum_{i=1}^{N^{U}} M^{U} \left[X_{i}^{U}, f_{\theta}(X_{i}^{U}) \right] \cdot g_{\theta}(X, X_{i}^{U}) - \frac{1}{N^{D}} \sum_{i=1}^{N^{D}} M^{D} \left[X_{i}^{D}, f_{\theta}(X_{i}^{D}) \right] \cdot g_{\theta}(X, X_{i}^{D}) \right],$$

$$(7)$$

where δ is the learning rate, value of θ is the one before GD iteration, and $\nabla_{\theta} \hat{L}_{PSO}^{N^U,N^D}(f_{\theta})$ is the loss gradient. When the considered model is NN, the above first-order dynamics are typically a very good approximation of the real $df_{\theta}(X)$ (Jacot et al., 2018; Kopitkov and Indelman, 2019). Further, when f_{θ} belongs to RKHS, the above approximation becomes an identity. Therefore, below we will treat Eq. (7) as equality, neglecting the fact that this is only the approximation.

Theorem 12 (Differential Statistics) Denote $F_{\theta}(X) \triangleq \mathbb{P}^{U}(X) \cdot M^{U}[X, f_{\theta}(X)] - \mathbb{P}^{D}(X) \cdot M^{D}[X, f_{\theta}(X)]$ to be a difference of two point-wise forces F_{θ}^{U} and F_{θ}^{D} defined in Section 2. Additionally, define G_{θ} to be the integral operator $[G_{\theta}u](\cdot) = \int g_{\theta}(\cdot, X)u(X)dX$. Then, considering training points as random i.i.d. realizations from the corresponding densities \mathbb{P}^{U} and \mathbb{P}^{D} , the expected value and the covariance of $df_{\theta}(X)$ at any fixed θ are:

$$\mathbb{E}\left[df_{\theta}(X)\right] = \\
= \delta \cdot \left[\mathbb{E}_{X' \sim \mathbb{P}^{U}} \left[M^{U} \left[X', f_{\theta}(X') \right] \cdot g_{\theta}(X, X') \right] - \mathbb{E}_{X' \sim \mathbb{P}^{D}} \left[M^{D} \left[X', f_{\theta}(X') \right] \cdot g_{\theta}(X, X') \right] \right] = \\
= \delta \cdot \int g_{\theta}(X', X) \cdot F_{\theta}(X') dX' = \delta \cdot [G_{\theta}F_{\theta}](X), \quad (8)$$

$$Cov\left[df_{\theta}(X), df_{\theta}(X')\right] = \delta^{2} \cdot \nabla_{\theta} f_{\theta}(X)^{T} \cdot Var\left[\nabla_{\theta} \hat{L}_{PSO}^{N^{U}, N^{D}}(f_{\theta})\right] \cdot \nabla_{\theta} f_{\theta}(X'), \tag{9}$$
with $Var\left[\nabla_{\theta} \hat{L}_{PSO}^{N^{U}, N^{D}}(f_{\theta})\right]$ being proportional to $\frac{1}{N^{U} + N^{D}}$.

Proof of the above theorem together with the explicit form of $\operatorname{Var}\left[\nabla_{\theta}\hat{L}_{PSO}^{N^U,N^D}(f_{\theta})\right]$ is in Appendix D. The theorem provides insights about stochastic dynamics of the surface f_{θ} caused by point-wise forces $F_{\theta}^{U}(X)$ and $F_{\theta}^{D}(X)$. Eq. (8) is an integral transform of the total force $F_{\theta}(X)$, which can also be seen as a point-wise error. That is, on the average $df_{\theta}(X)$ changes proportionally to the convolution of $\left[F_{\theta}^{U}(X') - F_{\theta}^{D}(X')\right]$ w.r.t. the kernel $g_{\theta}(X', X)$. When F_{θ}^{U} is larger than F_{θ}^{D} , after both being convolved via g_{θ} , then on the average $f_{\theta}(X)$ is pushed up, and vice versa. When convolutions of F_{θ}^{U} and F_{θ}^{D} are equal around the point X, $f_{\theta}(X)$ stays constant, again on the average. Further, the variance of $df_{\theta}(X)$ depends on the alignment between $\nabla_{\theta}f_{\theta}(X)$ and the eigenvectors of $\operatorname{Var}\left[\nabla_{\theta}\hat{L}_{PSO}^{N^U,N^D}(f_{\theta})\right]$ that correspond to the largest eigenvalues (the directions in θ -space to which PSO loss mostly propagates), and in addition can be reduced by increasing the size of training datasets.

Considering the differential as the sum $df_{\theta}(X) = \mathbb{E}[df_{\theta}(X)] + \omega_{\theta}(X)$ where ω_{θ} is a zero-mean indexed-by-X stochastic process with the covariance function defined in Eq. (9), $f_{\theta}(X)$ will change on average towards the height where the convoluted PSO equilibrium $G_{\theta}F_{\theta}^{U} = G_{\theta}F_{\theta}^{D}$:

$$\int g_{\theta}(X, X') \cdot F_{\theta}^{U}(X') dX' = \int g_{\theta}(X, X') \cdot F_{\theta}^{D}(X') dX' \tag{10}$$

is satisfied, while ω_{θ} 's variance will cause it to vibrate around such target height. Informally, δ in Eq. (9) has a role of configuration parameter that controls the diapason around the target height where the current estimation $f_{\theta}(X)$ is vibrating. Further, sequential tuning/decaying of the learning rate δ will decrease this vibration amplitude (distance between the target and estimated models).

5.4 Convoluted PSO Balance State

Above we observed that in fact GD optimization will lead to the *convoluted* PSO equilibrium. This can also be derived from the first-order-conditions argument as follows. Assume that at the convergence of PSO algorithm $\nabla_{\theta} \hat{L}_{PSO}^{N^U,N^D}(f_{\theta}) = 0$ is satisfied. Multiplying it by $\nabla_{\theta} f_{\theta}(X)^T$ will lead to:

$$\frac{1}{N^{U}} \sum_{i=1}^{N^{U}} M^{U} \left[X_{i}^{U}, f_{\theta}(X_{i}^{U}) \right] \cdot g_{\theta}(X, X_{i}^{U}) = \frac{1}{N^{D}} \sum_{i=1}^{N^{D}} M^{D} \left[X_{i}^{D}, f_{\theta}(X_{i}^{D}) \right] \cdot g_{\theta}(X, X_{i}^{D}).$$

According to the weak law of large numbers the above equality converges in probability (under appropriate regularity conditions) to Eq. (10) as batch sizes N^U and N^D increase.

Further, considering the asymptotic equilibrium $[G_{\theta}F_{\theta}](\cdot) = 0$, if G_{θ} is injective then we also have $F_{\theta}(\cdot) = 0$ which leads to the variational PSO balance state in Eq. (2). Yet, in general case during the optimization F_{θ} will project into the null-space of G_{θ} . Moreover, even for injective G_{θ} it may take prohibitively many GD iterations in order to obtain the convoluted PSO equilibrium in Eq. (10), depending on the conditional number of G_{θ} (Kopitkov and Indelman, 2019). Hence, at the end of a typical optimization F_{θ} (and thus also F_{θ}^{U} and F_{θ}^{D}) will be located within G_{θ} 's null-space or its low-spectrum space (i.e. a space spanned by G_{θ} 's eigenfunctions related to its lowest eigenvalues).

The above described behavior implicitly introduces a bias into PSO solution. That is, when a function space \mathcal{F} with particular g_{θ} and G_{θ} is chosen, this decision will affect our learning task exactly via the above relation to G_{θ} 's null-space. The deeper analysis is required to answer the following questions. How g_{θ} 's properties effect the PSO solution? What is the rate of converge towards G_{θ} 's null-space? What is the impact of batch sizes N^U and N^D , and what can we say about PSO solution when these batches are finite/small? These advanced questions share their key concepts with the topics of RKHS estimation and Deep Learning theory, and deserve their own avenue. Therefore, we leave most of them out of this paper's scope and shall address them as part of future research. Further, below we analyze a specific property of g_{θ} - its bandwidth.

5.5 Model Expressiveness and Smoothness vs Kernel Bandwidth

The model kernel $g_{\theta}(X, X')$ expresses the impact over $f_{\theta}(X)$ when we optimize at a data point X'. Intuitively, under the thermodynamical perspective (see Section 2) PSO algorithm can be viewed as pushing (up and down) at the training points with some wand whose end's shape is described by the above kernel. Here we will show that the flexibility of the surface f_{θ} strongly depends on $g_{\theta}(X, X')$'s bandwidth (i.e. on flatness of the pushing wand's end).

For this purpose we will define a notion of the model relative kernel:

$$r_{\theta}(X, X') \triangleq \frac{g_{\theta}(X, X')}{g_{\theta}(X, X)},$$
 (11)

which can be interpreted as relative side-influence over $f_{\theta}(X)$ from X', scaled w.r.t. the self-influence $g_{\theta}(X, X)$ of X. Further, assume that the model relative kernel is bounded as:

$$0 < \exp\left[-\frac{d(X, X')}{h_{min}}\right] \le r_{\theta}(X, X') \le \exp\left[-\frac{d(X, X')}{h_{max}}\right] \le 1, \tag{12}$$

where d(X, X') is any function that satisfies the triangle inequality $d(X, X') \leq d(X, X'') + d(X', X'')$ (e.g. metric or pseudometric over \mathbb{R}^n), and where h_{min} and h_{max} can be considered as lower and upper bounds on $r_{\theta}(X, X')$'s bandwidth. Below, we will explore how h_{min} and h_{max} effect the smoothness of f_{θ} . Note, that in case $g_{\theta}(X, X)$ is identical for any X, the below analysis can be performed w.r.t. properties of g_{θ} instead of r_{θ} . However, in case f_{θ} is NN, the NTK g_{θ} can not be bounded as in Eq. (12), yet its normalized version r_{θ} clearly manifests such bounded-bandwidth properties. That is, $r_{\theta}(X, X')$ of NN typically decreases when the distance between X and X' increases (see Section 8), exhibiting some implicit bandwidth induced by a NN architecture. Moreover, while the magnitude of g_{θ} can be quiet different for various NN models and architectures, the normalized r_{θ} is on the same scale, allowing to compare the smoothness properties of particular models. Likewise, Eq. (12) is satisfied by many popular kernels used for RKHS construction, such as Gaussian and Laplacian kernels.

Theorem 13 (Spike Convergence) Assume:

- 1. PSO algorithm converged, with $\nabla_{\theta} \hat{L}_{PSO}^{N^{U},N^{D}}(f_{\theta}) = 0$.
- 2. $\{M^U, M^D\}$ are non-negative functions.
- 3. $M^{U}[X', s]$ is continuous and strictly decreasing w.r.t. s, at $\forall X' \in \mathbb{S}^{U}$.

Denote by $(M^U)^{-1}[X',z]$ the inverse function of M^U w.r.t. second argument. Further, consider any training sample from \mathbb{P}^U and denote it by X. Then the following is satisfied:

1.
$$f_{\theta}(X) \ge (M^{U})^{-1} [X, \alpha]$$
 where $\alpha = \frac{N^{U}}{N^{D}} \sum_{i=1}^{N^{D}} M^{D} [X_{i}^{D}, f_{\theta}(X_{i}^{D})] \cdot \exp \left[-\frac{d(X, X_{i}^{D})}{h_{max}} \right]$.

2.
$$(M^U)^{-1}[X,z]$$
 is strictly decreasing w.r.t. z , with $(M^U)^{-1}[X,\alpha] \to \infty$ when $\alpha \to 0$.

Proof of the above theorem is in Appendix E. From it we can see that for smaller α the surface at any up training point X converges to some very high height, where $f_{\theta}(X)$ can be arbitrary big. This can happen when X is faraway from all down samples $\{X_i^D\}_{i=1}^{N^D}$ (i.e. causing $d(X, X_i^D)$ to have a large output), or when h_{max} is very small (i.e. r_{θ} has a very narrow bandwidth). In these cases we will have up spikes at locations $\{X_i^D\}_{i=1}^{N^D}$. Similarly, when h_{max} is very small, there will be down spikes at locations $\{X_i^D\}_{i=1}^{N^D}$ - the corresponding theorem is symmetric to Theorem 13 and thus is omitted. Hence, the above theorem states that a very narrow bandwidth of r_{θ} will cause at the convergence up and down spikes within the surface f_{θ} , which can be interpreted as overfitting behavior of PSO algorithm (see Section 9 for the empirical demonstration). Note that the theorem's assumptions are not very restrictive, with many PSO instances satisfying them such as PSO-LDE, NCE and logistic loss (see Section 3). Providing a more general theorem with less assumptions (specifically reducing the assumption 3) we shall leave for future work.

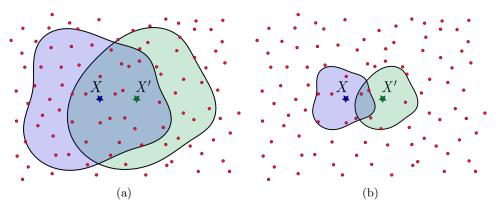


Figure 2: NN flexibility vs influence decay rate (bandwidth) of gradient similarity g_{θ} . Assume for simplicity $\forall X: g_{\theta}(X,X) \equiv \gamma$ for some constant γ . Considering Eq. (7), the differential at X is a weighted average of terms belonging to the training points around X, where $g_{\theta}(X,\cdot)$ serves as a weighting coefficient for each term. Further, consider gradient similarity to have a local-support. Its influence decay can be seen to express an influence area around each point X outside of which the gradient similarity $q_{\theta}(X,\cdot)$ becomes very small and negligible, on average. Above we illustrate two possible scenarios where the *influence* area is (a) large and (b) small. Red points represent training points, from both \mathbb{P}^U and \mathbb{P}^D . Further, blue and green regions around points X and $X' = X + \Delta$ express the neighborhoods around the points where gradient similarity has large values. Note that in context of NNs these regions in general are not centered at X (or X') and are not symmetric, yet exhibit a particular influence decay rate (see Section 8 and Appendix L for the empirical evaluation of q_{θ}). The training points in each such region around some point X can be considered as support training points of X that will influence its surface height. As observed from plots, when the *influence* decay rate is low (i.e. large influence area, see plot (a)) the differentials of X and X' will be very similar since most of the support training points stay the same for both X and X'. In contrast, when the influence decay rate is high (see plot (b)), the differentials at X and X' will be very different since most of the support training points for both X and X' are not the same. Hence, the differential as a function of X changes significantly for a step Δ within the input space when the decay rate is high, and vice versa. Furthermore, when the differential $df_{\theta}(X)$ changes only slightly for different points, the overall update of the surface height at each point is similar/identical to other points. Such surface is pushed up/down as one physical rigid body, making $f_{\theta}(X)$ "inelastic." Moreover, when the *influence* decay rate is significantly high, the point X may have only a single support (up or down) training point and $f_{\theta}(X)$ will be pushed only in a single direction (up or down) yielding the spike near X. Finally, in case the *influence* area of X will not contain any training point, $f_{\theta}(X)$ will stay constant along the entire optimization.

Theorem 14 (Change Difference) For any two points X_1 and X_2 , their change difference is bounded as:

$$|df_{\theta}(X_{1}) - df_{\theta}(X_{2})| \leq \delta \cdot g_{\theta}(X_{1}, X_{1}) \cdot \left[\frac{1}{N^{U}} \sum_{i=1}^{N^{U}} |M^{U}[X_{i}^{U}, f_{\theta}(X_{i}^{U})]| \cdot \nu_{\theta} [X_{1}, X_{2}, X_{i}^{U}] + \frac{1}{N^{D}} \sum_{i=1}^{N^{D}} |M^{D}[X_{i}^{D}, f_{\theta}(X_{i}^{D})]| \cdot \nu_{\theta} [X_{1}, X_{2}, X_{i}^{D}] \right], \quad (13)$$

where

$$u_{\theta}\left[X_{1}, X_{2}, X\right] \triangleq \epsilon\left[X_{1}, X_{2}, X\right] + \frac{|g_{\theta}(X_{1}, X_{1}) - g_{\theta}(X_{2}, X_{2})|}{g_{\theta}(X_{1}, X_{1})},$$

$$\epsilon\left[X_1, X_2, X\right] \triangleq 1 - \exp\left[-\frac{1}{h_{min}}d(X_1, X_2)\right] \cdot \exp\left[-\frac{1}{h_{min}}\max\left[d(X_1, X), d(X_2, X)\right]\right].$$

Proof of the above theorem is in Appendix F. In the above relation we can see that ϵ is smaller for a smaller distance $d(X_1, X_2)$. Likewise, $\epsilon \to 0$ along with $h_{min} \to \infty$. Neglecting the second term in ν_{θ} 's definition $(g_{\theta}(X_1, X_1))$ and $g_{\theta}(X_2, X_2)$ are typically very similar for any two close-by points X_1 and X_2), ν_{θ} has analogous trends. Therefore, the upper bound in Eq. (13) is smaller when two points are nearby or when h_{min} is large. From this we can conclude that $f_{\theta}(X_1)$ and $f_{\theta}(X_2)$ are evolving in similar manner for the above specified setting. Particularly, for $h_{min} \to \infty$ (and if the second term of ν_{θ} is relatively small) the entire surface f_{θ} will change almost identically at each point, intuitively resembling a rigid geometric body that moves u_{θ} and down without changing its internal shape.

To conclude, when we decide which function space \mathcal{F} to use for PSO optimization, this decision is equivalent to choosing the model kernel g_{θ} with the most desired properties. The effect of g_{θ} 's bandwidth on the optimization is described by the above theorems, whose intuitive summary is given in Figure 2. In particular, when a bandwidth of the (relative) kernel is too narrow - there will be spikes at the training points, and when this bandwidth is too wide - the converged surface will be overly smoothed. These two extreme scenarios are also known as overfitting and underfitting, and the kernel bandwidth can be considered as a flexibility parameter of the surface f_{θ} . Furthermore, the above exposition agrees with existing works for RKHS models (Principe, 2010) where the kernel bandwidth is known to affect the bias-variance trade-off of estimation.

5.6 Infinite Height Problem and its Solutions

In this section we study main stability issues encountered due to a mismatch between supports of \mathbb{P}^U and \mathbb{P}^D . From part 2 of Theorem 1 we see that there are settings under which $f_{\theta}(X)$ will go to infinity at X outside of mutual support $\mathbb{S}^{U \cap D}$. In Figure 3 a simple experiment is shown that supports this conclusion empirically, where f_{θ} at $X \notin \mathbb{S}^{U \cap D}$ is increasing during the entire learning process. Observe that while GD optimization obtains the *convoluted* PSO equilibrium in Eq. (10) instead of the variational PSO balance state in Eq. (2), the conclusions of Theorem 1 still remain valid in practice.

Similarly, the above described infinite height problem can happen at $X \in \mathbb{S}^{U \cap D}$ where one of the ratios $\frac{\mathbb{P}^U(X)}{\mathbb{P}^D(X)}$ and $\frac{\mathbb{P}^D(X)}{\mathbb{P}^U(X)}$ is too small, yet is not entirely zero (i.e. $|\log \mathbb{P}^U(X) - \log \mathbb{P}^D(X)|$ is large). Such relative support mismatch can cause instability as following. During the sampling process, at areas where $\mathbb{P}^U(X)$ and $\mathbb{P}^D(X)$ are very different, we can obtain many samples from one density yet almost no samples from the other. Taking Theorem 13 into the account, any training point X that is isolated from samples of the opposite force (i.e. when $d(X, \cdot)$ is large) will enforce a spike at $f_{\theta}(X)$. Moreover, when combined with the narrow kernel bandwidth, such spike behavior will be even more extreme with $f_{\theta}(X)$ being pushed to the infinite height (see Section 9 for the empirical illustration).

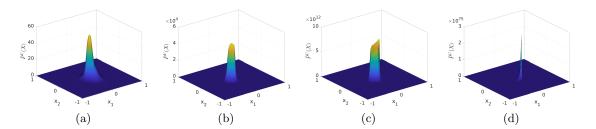


Figure 3: Illustration of PSO behavior in areas outside of the mutual support $\mathbb{S}^{U\cap D}$. We inferred 2D Uniform distribution \mathbb{P}^U via $\bar{\mathbb{P}}^U(X)=\exp f_{\theta}(X)$ by using PSO-LDE with $\alpha=\frac{1}{4}$ (see Table 2 and Section 6.2). The applied NN architecture is block-diagonal with 6 layers, number of blocks $N_B=50$ and block size $S_B=64$ (see Section 8.1). We plot $\bar{\mathbb{P}}^U(X)$ at different optimization times t: (a) t=100, (b) t=200, (c) t=10000 and (d) t=100000. The support \mathbb{S}^U of \mathbb{P}^U is [-1,1] for both dimensions. The chosen down density \mathbb{P}^D is defined with \mathbb{S}^D being identical to \mathbb{S}^U , minus the circle of radius 0.3 around the origin (0,0). In its entire support \mathbb{P}^D is distributed uniformly. Thus, in this setup the zero-centered circle is outside of $\mathbb{S}^{U\cap D}$ - we have samples X_i^U there but no samples X_i^D . For this reason, there is only up force F_{θ}^U present in the circle area, pushing the surface there indefinitely up. This can be observed from how the centered spire rises along the optimization time.

Hence, in both of above cases f_{θ} will go to $\pm \infty$ at various locations. Meaning of this is lack of the optimization convergence. Furthermore, too large f_{θ} outputs may cause arithmetic underflow and overflow instabilities when computing the loss gradient, and hence will lead to the divergence of a learning task.

In case \mathbb{P}^U and \mathbb{P}^D are relatively similar distributions and when g_{θ} 's bandwidth is wide enough, the above problem of *infinite height* will not occur in practice. For other cases, there are two possible strategies to avoid such divergence.

Indicator Magnitudes The above problem can be easily fixed by multiplying any given $magnitude\ M^U$ (or M^D) with the following function:

$$reverse_at [X, f_{\theta}(X), \varphi] = \begin{cases} -1, & \text{if } f_{\theta}(X) > \varphi \quad (\text{or } f_{\theta}(X) < \varphi) \\ 1, & \text{otherwise} \end{cases}$$

The $reverse_at(\cdot)$ will change sign of near magnitude term when $f_{\theta}(X)$ at the training point X passes the threshold height φ . This in turn will change a direction of the force, making it to oscillate the surface $f_{\theta}(X)$ around φ (similarly to part 2-d of Theorem 1). Such behavior will happen only at the "problematic" areas where $f_{\theta}(X)$ got too high/low. In other "safe" areas the function $reverse_at(\cdot)$ will not have any impact. Hence, applying $reverse_at(\cdot)$ next to both M^U and M^D will enforce the surface height at all X to be between some minimal and maximal thresholds, improving in this way the optimization stability.

The alternative to the above function is:

$$cut_at[X, f_{\theta}(X), \varphi] = \begin{cases} 0, & \text{if } f_{\theta}(X) > \varphi \quad (\text{or } f_{\theta}(X) < \varphi) \\ 1, & \text{otherwise} \end{cases}$$
 (14)

In contrast to $reverse_at(\cdot)$, once the surface $f_{\theta}(X)$ at some training point X passed the threshold height φ , the corresponding gradient term of X (either up or down) is withdrawn

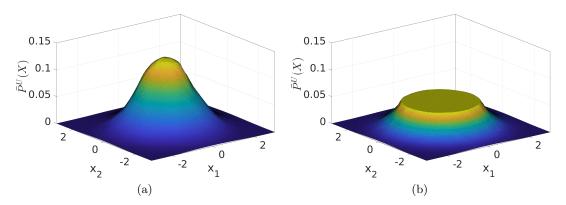


Figure 4: Illustration of impact of function $cut_{-}at[X, f_{\theta}(X), \varphi]$. (a) We inferred 2D Normal distribution via $\bar{\mathbb{P}}^{U}(X) = \exp f_{\theta}(X)$ by using PSO-LDE with $\alpha = \frac{1}{4}$ (see Table 2 and Section 6.2). The applied NN architecture is block-diagonal with 6 layers, number of blocks $N_{B} = 50$ and block size $S_{B} = 64$ (see Section 8.1). (b) We performed the same learning algorithm as in (a), but with modified up magnitude function $\bar{M}^{U}[X, f_{\theta}(X)] = M^{U}[X, f_{\theta}(X)] \cdot cut_{-}at[X, f_{\theta}(X), -3]$, where $cut_{-}at$ is defined in Eq. (14). This function deactivates up pushes for points with $f_{\theta}(X) > -3$ (and $\exp f_{\theta}(X) > 0.0498$), thus the surface $f_{\theta}(X)$ at height above threshold -3 is only pushed by down force and hence is enforced to converge to the threshold. Yet, note that at points where the converged model satisfies $f_{\theta}(X) \leq -3$ the convergence is the same as in (a).

from the total gradient $\nabla_{\theta} \hat{L}_{PSO}^{N^U,N^D}(f_{\theta})$ in Eq. (1), entirely deactivating the influence of X on the learning task. Thus, the surface f_{θ} is not pushed anymore at training points where its height got too high/low. Yet, it is still pushed at samples of the opposite force. Such force composition will constrain the surface height at unbalanced areas to converge to the threshold height φ , similarly to $reverse_at(\cdot)$. Further, unlike $reverse_at(\cdot)$, once any particular training point X got disabled by $cut_at(\cdot)$, it also does not have a side-influence (via $g_{\theta}(X, X')$) on the surface at other points. Likewise, it stops affecting the value of θ , leading to a higher movement freedom within θ -space. Empirically we observed $cut_at(\cdot)$ to result in overall higher approximation accuracy compared to $reverse_at(\cdot)$. The optimization outcome of $cut_at(\cdot)$ usage is illustrated in Figure 4.

The rigorous proof of the above functions' impact on PSO convergence and further analysis of their interplay with properties of the kernel g_{θ} is not the main focus of this paper and therefore is left for future work.

Restriction over Functions' Range Alternatively, we can enforce all functions within the considered function space \mathcal{F} to have any desired range $\mathbb{A} = [H_{min}, H_{max}]$. The constants H_{min} and H_{max} will represents the minimal and maximal surface heights respectively. For example, this can be accomplished by using the model:

$$f_{\theta}(X) = \frac{1}{2} \cdot [H_{max} - H_{min}] \cdot \tanh[h_{\theta}(X)] + \frac{1}{2} \cdot [H_{max} + H_{min}],$$

where h_{θ} represents an inner model that may have unbounded range. Since $\tanh(\cdot)$ is bounded to have values in [-1,1], it is easy to verify that the above model can return only values between H_{min} and H_{max} . Thus, using such model will eliminate the divergence of

the surface to an infinite height. Likewise, other bounded functions can be used instead of $\tanh(\cdot)$ such as $\operatorname{erf}(\cdot)$, $\operatorname{sigmoid}(\cdot)$, $\operatorname{arctan}(\cdot)$ and many others.

6. Density Estimation via PSO

Till now we discussed a general formulation of PSO, where the presented analysis addresses properties of any PSO instance. In this section we focus in more detail on a group of PSO instances that can be applied for the density estimation problem. In particular, in Section 6.1 we shortly describe our previous work on density estimation, while in Section 6.2 we explore new PSO approaches to infer density on a logarithmic scale, with bounded magnitude functions which leads to enhanced optimization performance.

6.1 DeepPDF

In this section we briefly describe the density estimation approach, DeepPDF, introduced in (Kopitkov and Indelman, 2018a), as a particular instance of the PSO paradigm. The density estimation problem involves learning a pdf function $\mathbb{P}^{U}(X)$ from a dataset of i.i.d. samples $\{X_{i}^{U}\}$. For this purpose, the proposed pdf loss was as follows:

$$L_{pdf}(\theta) = - \underset{X \sim \mathbb{P}^U}{\mathbb{E}} f_{\theta}(X) \cdot \mathbb{P}^D(X) + \underset{X \sim \mathbb{P}^D}{\mathbb{E}} \frac{1}{2} \left[f_{\theta}(X) \right]^2, \tag{15}$$

which can be obtained by choosing magnitudes $M^{U}[X, f_{\theta}(X)] = \mathbb{P}^{D}(X)$ and $M^{D}[X, f_{\theta}(X)] = f_{\theta}(X)$. \mathbb{P}^{D} is an arbitrary density with a known pdf function which can be easily sampled.

The above loss is a specific instance of PSO with balance state achieved when the surface $f_{\theta}(X)$ converges to $\mathbb{P}^{U}(X)$ point-wise $\forall X \in \mathbb{S}^{U \cap D}$ (see Theorem 2). Moreover, according to the condition 2-c in Theorem 1 for $X \in \mathbb{S}^{U \setminus D}$ at the convergence $f_{\theta}(X)$ can be arbitrary - M^{U} is zero in area $\mathbb{S}^{U \setminus D}$ and hence the force F_{θ}^{U} is disabled. Due to similar Theorem 32, at $X \in \mathbb{S}^{D \setminus U}$ the optimal solution must satisfy $f_{\theta}(X) = 0$. Therefore, any candidate for \mathbb{P}^{D} with $\mathbb{S}^{U} \subseteq \mathbb{S}^{D}$ will lead to convergence $\forall X \in \mathbb{S}^{U \cup D} : f_{\theta}(X) = \mathbb{P}^{U}(X)$. Outside of the support union $\mathbb{S}^{U \cup D}$ convergence can be arbitrary, depending of the model kernel, which is true for any PSO method.

Concluding from the above, selected \mathbb{P}^D must satisfy $\mathbb{S}^U \subseteq \mathbb{S}^D$. In our experiments we typically use a Uniform distribution for down density \mathbb{P}^D (yet in practice any density can be applied). The minimum and maximum for each dimension of \mathbb{P}^D 's support are assigned to minimum and maximum of the same dimension from the available \mathbb{P}^U 's data points. Thus, the available samples $\{X_i^U\}$ define n-dimensional hyperrectangle in \mathbb{R}^n as support of \mathbb{P}^D , with \mathbb{P}^U 's support being its subset. Inside this hyperrectangle the surface is pushed by F_{θ}^D and F_{θ}^D . Note that for case when the borders of this support hyperrectangle can not be computed a priori (e.g. active learning), the $reverse_at(\cdot)$ and $cut_at(\cdot)$ functions can be used to prevent optimization divergence as described in Section 5.6.

After training is finished, the converged $f_{\theta}(X)$ may have slightly negative values at points $\{X \in \mathbb{S}^{D \setminus U}\}$ being that during optimization the oscillation around height zero is stochastic in nature. Moreover, surface values outside of the *hyperrectangle* may be anything since the $f_{\theta}(X)$ was not optimized there. In order to deal with these possible inconsistencies, we can

use the following proxy function as our estimation of target $\mathbb{P}^{U}(X)$:

$$\bar{f}_{\theta}(X) = \begin{cases} 0, & \text{if } f_{\theta}(X) < 0 \text{ or } \mathbb{P}^{D}(X) = 0 \\ f_{\theta}(X), & \text{otherwise} \end{cases}$$

which produces the desirable convergence $\forall X \in \mathbb{R}^n : \bar{f}_{\theta}(X) = \mathbb{P}^U(X)$.

In (Kopitkov and Indelman, 2018a) we demonstrated that the above DeepPDF method with f_{θ} parametrized by NN outperforms kernel density estimation (KDE) in inference accuracy, and is significantly faster at the query stage when the number of training points is large.

6.2 PSO-LDE - Density Estimation on Logarithmic Scale

Typically, the output from a multidimensional density \mathbb{P}^U will tend to be extra small, where higher data dimension causes smaller pdf values. Representing very small numbers in a computer system may cause underflow and precision-loss problems. To overcome this, in general it is recommended to represent such small numbers in a logarithmic scale. Furthermore, estimation of log-pdf is highly useful. For example, in context of robotics it can represent log-likelihood of sensor measurement and can be directly applied to infer a unobservable state of robot (Kopitkov and Indelman, 2018b). Likewise, once log-pdf is learned its average for data samples approximates the entropy of \mathbb{P}^U , which can further be used for robot planning (Kopitkov and Indelman, 2017).

Here we derive several families of PSO instances that infer logarithm of a pdf, $\log \mathbb{P}^{U}(X)$, as their target function. Although some members of these families were already reported before (e.g. NCE, Gutmann and Hyvärinen (2010)), the general formulation of these families was not considered previously.

6.2.1 Derivation

For our goal we need a PSO instance that pushes the surface $f_{\theta}(X)$ to equilibrium $\log \mathbb{P}^{U}(X)$. Presented below PSO instances with such convergence can be separated into two groups instances with unbounded and bounded magnitude functions $\{M^{U}, M^{D}\}$. As was discussed in Section 5.2 and as will be shown in Section 12, the latter group yields a better optimization stability and also produces a higher accuracy.

We can derive new PSO instance for log-pdf estimation using Theorem 4 as follows. Define \mathbb{P}^D to be arbitrary density with analytically known pdf $\mathbb{P}^D(X)$ that satisfy $\mathbb{S}^U \subseteq \mathbb{S}^D$. Denote the required PSO convergence $f_{\theta}(X) = T[X, \mathbb{P}^U(X)] = \log \mathbb{P}^U(X)$ via the transform $T[X, z] = \log z$. Its inverse w.r.t. second argument is $T^{-1}[X, s] = \exp s$. Then, according to the theorem any pair $\{M^U, M^D\}$ that satisfies:

$$\frac{M^D(X, f_{\theta}(X))}{M^U(X, f_{\theta}(X))} = \frac{\exp f_{\theta}(X)}{\mathbb{P}^D(X)},\tag{16}$$

will produce $f_{\theta}(X) = \log \mathbb{P}^{U}(X)$ at the convergence.

Unbounded *Magnitudes* To produce new PSO instances with the above equilibrium, many choices over $\{M^U, M^D\}$ can be taken. In Table 7 we show several such alternatives.

Loss Version	$\underline{m{L}} m{oss} \ / \ M^{\scriptscriptstyle U}(\cdot) \ \ m{and} \ M^{\scriptscriptstyle D}(\cdot)$
1	$\underline{\mathbf{L}}: -\mathbb{E}_{X \sim \mathbb{P}^U} f_{\theta}(X) \cdot \mathbb{P}^D(X) + \mathbb{E}_{X \sim \mathbb{P}^D} \exp(f_{\theta}(X))$ $M^U, M^D: \mathbb{P}^D(X), \exp(f_{\theta}(X))$
2	$\begin{array}{l} \underline{\mathbf{L}} \colon -\mathbb{E}_{X \sim \mathbb{P}^U} \ f_{\theta}(X) + \mathbb{E}_{X \sim \mathbb{P}^D} \ \frac{\exp(f_{\theta}(X))}{\mathbb{P}^D(X)} \\ M^U, \ M^D \colon 1, \ \frac{\exp(f_{\theta}(X))}{\mathbb{P}^D(X)} \end{array}$
3	$\underline{\mathbf{L}} \colon \mathbb{E}_{X \sim \mathbb{P}^U} \frac{\mathbb{P}^D(X)}{\exp(f_{\theta}(X))} + \mathbb{E}_{X \sim \mathbb{P}^D} f_{\theta}(X)$ $M^U, M^D \colon \frac{\mathbb{P}^D(X)}{\exp(f_{\theta}(X))}, 1$
4	$ \begin{array}{l} \underline{\mathbf{L}} \colon \mathbb{E}_{X \sim \mathbb{P}^U} \ 2 \cdot \exp \left[\frac{1}{2} \cdot \left(\log \mathbb{P}^D(X) - f_{\theta}(X) \right) \right] + \\ + \mathbb{E}_{X \sim \mathbb{P}^D} \ 2 \cdot \exp \left[\frac{1}{2} \cdot \left(f_{\theta}(X) - \log \mathbb{P}^D(X) \right) \right] \\ M^U, \ M^D \colon \exp \left[\frac{1}{2} \cdot \left(\log \mathbb{P}^D(X) - f_{\theta}(X) \right) \right], \\ \exp \left[\frac{1}{2} \cdot \left(f_{\theta}(X) - \log \mathbb{P}^D(X) \right) \right] \end{array} $
5	$\underline{\mathbf{L}}: -\mathbb{E}_{X \sim \mathbb{P}^U} \exp(f_{\theta}(X)) \cdot \mathbb{P}^D(X) + \mathbb{E}_{X \sim \mathbb{P}^D} \frac{1}{2} \cdot \exp(2 \cdot f_{\theta}(X))$ $M^U, M^D: \mathbb{P}^D(X) \cdot \exp(f_{\theta}(X)), \exp(2 \cdot f_{\theta}(X))$

Table 7: Several PSO Instances that converge to $f_{\theta}(X) = \log \mathbb{P}^{U}(X)$

Note that according to PSO we can merely move any term q(X,s) from $M^{U}(X,s)$ into $M^{D}(X,s)$ as $\frac{1}{q(X,s)}$, and vice versa. Such modification will not change the PSO balance state and therefore allows for the exploration of various magnitudes that lead to the same convergence.

Remark 15 Observe that although we can see obvious similarity and relation between magnitudes in Table 7 (they all have the same ratio $M^D(\cdot)/M^U(\cdot)$), the corresponding losses have much smaller resemblance. Without applying PSO rules, it would be hard to deduce that they all approximate the same target function.

The Table 7 with acquired losses serves as a demonstration for simplicity of applying PSO concepts to forge new methods for log-density estimation. However, the produced losses have unbounded magnitude functions, and are not very stable during the real optimization, as will be shown in our experiments. The first loss in Table 7 can lead to precision problems since its M^D is multiplication of (very) small outputs from $\mathbb{P}^D(X)$ and $\exp(f_{\theta}(X))$. Further, M^U of the third loss has devision by output from the current model $\exp(f_{\theta}(X))$ which is time-varying and can produce values arbitrarily close to zero. Likewise, methods 4 and 5 hold similar problems.

Bounded *Magnitudes* Considering the above point, the PSO instances in Table 7 are sub-optimal. Instead, we want to find PSO losses where *magnitude* functions $M^D(\cdot)$ and $M^U(\cdot)$ are bounded. Further, the required relation in Eq. (16) between two *magnitudes* can be seen as:

$$\frac{M^{D}\left[X, f_{\theta}(X)\right]}{M^{U}\left[X, f_{\theta}(X)\right]} = \exp \bar{d}\left[X, f_{\theta}(X)\right],$$

$$\bar{d}[X, f_{\theta}(X)] \triangleq f_{\theta}(X) - \log \mathbb{P}^{D}(X). \tag{17}$$

 $\bar{d}[X, f_{\theta}(X)]$ is a logarithm difference between the model surface and log-pdf of down density, which will play an essential role in magnitude functions below. Considering Section 5.2 and the above relation between $M^{D}(\cdot)$ and $M^{U}(\cdot)$ we can introduce the following family of PSO instances:

$$M^{U}[X, f_{\theta}(X)] = \frac{\mathbb{P}^{D}(X)}{D[X, f_{\theta}(X)]}, \quad M^{D}[X, f_{\theta}(X)] = \frac{\exp f_{\theta}(X)}{D[X, f_{\theta}(X)]},$$
 (18)

where the denominator function $D[X, f_{\theta}(X)]$ takes the responsibility to normalize output of magnitude functions to be in some range $[0, \epsilon]$. Moreover, choice of $D[X, f_{\theta}(X)]$ does not affect the PSO balance state; it is reduced when the above magnitudes are introduced into Eq. (16). Also note that the condition 1-b from Theorem 1 is reduced to $D[X, f_{\theta}(X)] > 0$ for the above family in Eq. (18).

To bound functions $M^D(\cdot)$ and $M^U(\cdot)$ in Eq. (18), $D[X, f_{\theta}(X)]$ can take infinitely many forms. One such form, that was implicitly applied in NCE technique (Smith and Eisner, 2005; Gutmann and Hyvärinen, 2010), is $D[X, f_{\theta}(X)] = \exp f_{\theta}(X) + \mathbb{P}^D(X)$ (see also Table 2). Such choice of normalization function enforces outputs of both magnitude functions in Eq. (18) to be between 0 and 1. Moreover, NCE magnitudes can be seen as functions of a logarithm difference $\bar{d}[X, f_{\theta}(X)]$ in Eq. (17), $M^U(\bar{d}) = sigmoid(-\bar{d}[X, f_{\theta}(X)])$ and $M^U(\bar{d}) = sigmoid(\bar{d}(X, f_{\theta}(X)))$. Thus, an output of magnitude functions at point $X \in \mathbb{R}^n$ entirely depends on this logarithm difference at X. Furthermore, the up magnitude reduces to zero for a large positive \bar{d} and the down magnitude reduces to zero for a large negative \bar{d} (see also Figure 5a).

Such property is highly helpful, as it does not only bound $M^D(\cdot)$ and $M^U(\cdot)$, and stabilize the overall optimization; it also prevents infinite height problem described in Section 5, even when up and down densities are very different and when their support does not match. In neighborhoods where we sample many points X^U but almost no points X^D (ratio $\frac{\mathbb{P}^U(X)}{\mathbb{P}^D(X)}$ is large) the surface is pushed indefinitely up through up term within PSO loss. Yet, as it pushed higher, \bar{d} for these neighborhoods becomes larger and thus the up magnitude $M^U(\bar{d})$ goes quickly to zero. Therefore, when at a specific point X the surface $f_{\theta}(X)$ was pushed up too far from $\log \mathbb{P}^D(X)$, the up magnitude at this point becomes zero thus entirely deactivating the up force $F_{\theta}^U(X)$ at this X. The same logic also applies to down force $F_{\theta}^D(X)$ - in NCE this force is deactivated at points where $f_{\theta}(X)$ was pushed down too far from $\log \mathbb{P}^D(X)$.

Critically, since $f_{\theta}(X)$ approximates $\log \mathbb{P}^U(X)$, $\bar{d}[X, f_{\theta}(X)]$ can also be viewed as an estimation of $\log \frac{\mathbb{P}^U(X)}{\mathbb{P}^D(X)}$. Therefore, the above exposition of NCE dynamics can be also summarized as follows. At points where logarithm difference $\log \mathbb{P}^U(X) - \log \mathbb{P}^D(X)$ is in some dynamical active range [-a,a] for positive a, the up and down forces will be active and will reach equilibrium with $f_{\theta}(X) = \log \mathbb{P}^U(X)$. At points where $[\log \mathbb{P}^U(X) - \log \mathbb{P}^D(X)] > a \Leftrightarrow \frac{\mathbb{P}^U(X)}{\mathbb{P}^D(X)} > \exp a$, the surface will be pushed up to height a. And at points where $[\log \mathbb{P}^U(X) - \log \mathbb{P}^D(X)] < -a \Leftrightarrow \frac{\mathbb{P}^U(X)}{\mathbb{P}^D(X)} < \frac{1}{\exp a}$, the surface will be pushed down to height -a. Once the surface at some point X passes above the height a or below the height -a, the

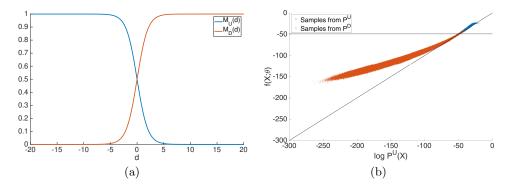


Figure 5: (a) NCE magnitudes as functions of a difference $\bar{d}[X, f_{\theta}(X)] \triangleq f_{\theta}(X) - \log \mathbb{P}^{D}(X)$. (b) Log density estimation via NCE for 20D data, where \mathbb{P}^{U} is standard Normal 20D distribution and \mathbb{P}^D is minimal Uniform 20D distribution that covers all samples from \mathbb{P}^U . Blue points are sampled from \mathbb{P}^U , while red points from \mathbb{P}^D . The x axes represent $\log \mathbb{P}^U(X)$ for each sample, y axes - the surface height $f_{\theta}(X)$ after optimization was finished. Diagonal line represents $f_{\theta}(X) = \log \mathbb{P}^{U}(X)$, where we would see all points in case of *perfect* model inference. The black horizontal line represents $\log \mathbb{P}^{D}(X) = -49$ which is constant for the Uniform density. As can be seen, these two densities have a relative support mismatch - although their pdf values are not zero within the considered point space, the sampled points from both densities are obviously located mostly in different space neighborhoods; this can be concluded from values of $\log \mathbb{P}^{U}(X)$ that are very different for both point populations. Further, points with relatively small $|\bar{d}|$ (around the horizontal line) have a small estimation error since the ratio $\frac{\mathbb{P}^U(X)}{\mathbb{P}^D(X)}$ there is bounded and both points X^U and X^D are sampled from these areas. In contrast, we can see that in areas where $|\bar{d}| > a$ for some positive constant a we have samples from only one of the densities. Further, points with d>0 (above the horizontal line) are pushed up till a some threshold where the surface height is stuck due to up magnitude $M^{U}(\cdot)$ going to zero (see also Figure (a)). Additionally, points with $\bar{d} < 0$ (below the horizontal line) are pushed down till their magnitude $M^{D}(\cdot)$ also becomes zero. Note that below points are pushed further from the horizontal line than the above points. This is because the above points are near the origin (mean of Normal distribution) which is less flexible since it is shaped as Gaussian bell and its slope is restricted from all sides. On opposite, the below points are located far from the origin center on the edges of considered point space, where there is almost no optimization (no points X^U and $M^D(\cdot) \approx 0$) and thus the surface there is much more flexible. Clearly, the PSO estimation task for the above choice of up and down densities can not yield a high accuracy. Yet, we can see that NCE does not push the surface to the infinity at the unbalanced areas.

NCE loss stops pushing it due to (near) zero magnitude component. Yet, the side-influence induced by model kernel $g_{\theta}(X, X')$ from non-zero magnitude areas can still affect the surface height at X. The above NCE behavior is illustrated in Figure 5b where 20D log-density estimation is performed via NCE for Gaussian distribution \mathbb{P}^{U} and Uniform distribution \mathbb{P}^{D} .

Remark 16 Note that the scalar "a" represents a sensitivity threshold, where pushes at points with $|\bar{d}| > a$ have a neglectable effect on the surface due to their small magnitude component. Such sensitivity is different for various functional spaces $f_{\theta} \in \mathcal{F}$; for some spaces a small change of θ can only insignificantly affect the surface $f_{\theta}(X)$, while causing huge impact in others. Hence, the value of "a" depends on specific choice of \mathcal{F} and of magnitude functions $M^{U}(\cdot)$ and $M^{D}(\cdot)$.

The above described relationship between NCE magnitude functions and ratio $\frac{\mathbb{P}^U(X)}{\mathbb{P}^D(X)}$ is very beneficial in the context of density estimation, since it produces high accuracy for points where density ratio is bounded $\frac{1}{\exp a} < \frac{\mathbb{P}^U(X)}{\mathbb{P}^D(X)} < \exp a$ and it is not sensitive to instabilities of areas where $\frac{\mathbb{P}^U(X)}{\mathbb{P}^D(X)} > \exp a$ or $\frac{\mathbb{P}^U(X)}{\mathbb{P}^D(X)} < \frac{1}{\exp a}$. Thus, even for very different densities \mathbb{P}^U and \mathbb{P}^D the optimization process is still very stable (see Figure 5b). Further, in our experiments we observed NCE to be much more accurate than IS due to its better magnitude dynamics.

Yet, such dynamics are not limited only to the loss of NCE, and can actually be enforced also through other PSO variants. Herein, we introduce a novel general algorithm family for PSO log density estimators (PSO-LDE) that takes a normalized form in Eq. (18). The denominator function is defined as $D_{PSO-LDE}^{\alpha}[X, f_{\theta}(X)] \triangleq \left[[\exp f_{\theta}(X)]^{\alpha} + [\mathbb{P}^{D}(X)]^{\alpha} \right]^{\frac{1}{\alpha}}$ with α being family's hyper-parameter. Particularly, each member of PSO-LDE has bounded magnitude functions:

$$M_{\alpha}^{U}(X, f_{\theta}(X)) = \frac{\mathbb{P}^{D}(X)}{\left[\left[\exp f_{\theta}(X)\right]^{\alpha} + \left[\mathbb{P}^{D}(X)\right]^{\alpha}\right]^{\frac{1}{\alpha}}} = \left[\exp\left[\alpha \cdot \bar{d}\left[X, f_{\theta}(X)\right]\right] + 1\right]^{-\frac{1}{\alpha}}, \quad (19)$$

$$M_{\alpha}^{D}(X, f_{\theta}(X)) = \frac{\exp f_{\theta}(X)}{\left[\left[\exp f_{\theta}(X)\right]^{\alpha} + \left[\mathbb{P}^{D}(X)\right]^{\alpha}\right]^{\frac{1}{\alpha}}} = \left[\exp \left[-\alpha \cdot \bar{d}\left[X, f_{\theta}(X)\right]\right] + 1\right]^{-\frac{1}{\alpha}}.$$
 (20)

In Figure 6 the above magnitude functions are plotted w.r.t. logarithm difference \bar{d} , for different values of α . As can be observed, α controls the smoothness and the rate of a magnitude decay to zero. For small values of α the magnitude function turns to zero in a more qentle way, while for bigger values the transformation of magnitude output from 1 to 0 is much sharper. Likewise, this tendency can be viewed as a consideration of some prior knowledge over the difference between $\mathbb{P}^{U}(X)$ and $\mathbb{P}^{D}(X)$. For large α , the magnitudes are very strong even for small value of $|\bar{d}|$, that is even when $\log \mathbb{P}^D(X)$ and $f_{\theta}(X)$ (and hence also $\log \mathbb{P}^U(X)$) are only slightly different from each other. Hence, the strong feedback from magnitudes of such α will "prefer" values of $f_{\theta}(X)$ being closer to $\log \mathbb{P}^{D}(X)$, limiting in this soft way a dynamical range of possible \bar{d} values. In contrast, for small α the magnitudes are increasing much slower when $|\bar{d}|$ grows, hence allowing for a richer dynamical range of \bar{d} values. We argue that these smoother dynamics of smaller α values allow for a more stable optimization and a more accurate convergence, similarly to the robustness of redescending M-estimators (Shevlyakov et al., 2008). Yet, we leave the theoretical analysis of this affect to future work. In Section 12 we will empirically investigate the impact of α on performance of density estimation, where we will show that $\alpha = \frac{1}{4}$ typically has a better performance.

Additionally, the formulation of PSO-LDE in Eqs. (19)-(20) can also be exploited to overcome possible underflow and overflow issues. In a typically used single-precision floating-point format the function $\exp(\cdot)$ can only be computed for an input being in the range [-81,81]. Hence, there is an upper bound for values of $|\bar{d}[X,f_{\theta}(X)]|$ above which $M_{\alpha}^{U}(X,f_{\theta}(X))$ and $M_{\alpha}^{D}(X,f_{\theta}(X))$ can not be computed in practice. Yet, we can set the hyper-parameter α to be small enough to overcome this numerical limitation.

Remark 17 Note that NCE is a member of the above PSO-LDE family for $\alpha = 1$. Further, the analytic loss for magnitudes in Eqs. (19)-(20) is unknown for general α . Yet, the gradient of this loss can be easily calculated.

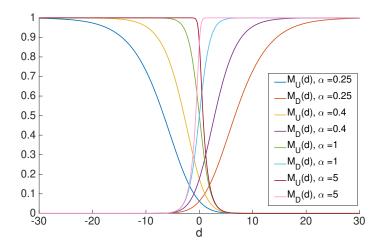


Figure 6: PSO-LDE magnitudes as functions of a difference $\bar{d} \triangleq f_{\theta}(X) - \log \mathbb{P}^{D}(X)$ for different values of hyper-parameter α .

6.2.2 Relation to Curse of Dimensionality

The above relation between optimization dynamics and the density ratio implies that a good candidate density for \mathbb{P}^D must yield a bounded log-density difference $|\log \mathbb{P}^U(X) - \log \mathbb{P}^D(X)| < a$. However, proposing such \mathbb{P}^D requires us to know, at least roughly, the target density $\mathbb{P}^U(X)$. Moreover, even if $\mathbb{P}^U(X)$ is given, finding a good candidate \mathbb{P}^D is still hard since the selected down density must have an analytically known pdf and have a computationally cheap way to be sampled. Further, choosing \mathbb{P}^D is even more difficult in high-dimensional spaces (e.g. thousands of variables), where the log-density difference can become huge even if \mathbb{P}^U and \mathbb{P}^D are only slightly different. For example, consider a scenario where both densities are isometric n-dimensional distributions $\mathbb{P}^U(X) = \prod_{i=1}^n p^U(x_i)$ and $\mathbb{P}^D(X) = \prod_{i=1}^n p^D(x_i)$. Further, assume that $p^U(x)$ and $p^D(x)$ are one-dimensional densities that are very close to each other, with their log-density difference $|\log p^U(x) - \log p^D(x)|$ at a specific point $x \in \mathbb{R}$ being a some small value ϵ . Then, the log-density difference of multivariate distribution $|\log \mathbb{P}^U(X) - \log \mathbb{P}^D(X)|$ at $X = [x, \dots, x]^T \in \mathbb{R}^n$ will be $n \cdot \epsilon$. Hence, in this simple example the log-density difference at point X will grow with dimension n, even if the densities of each dimension, $p^U(x)$ and $p^D(x)$, are almost identical (i.e. ϵ is very small).

Such nature of density ratios and its effect on PSO-LDE's accuracy (and PSO in general) is a direct consequence of the curse of dimensionality, where the space volume (area of the density support in the context of density estimation) grows exponentially with the dimension. As was strongly emphasized in this paper (see Section 5.6 and Figure 3), both \mathbb{P}^U 's and \mathbb{P}^D 's data points should be sampled from the same neighborhoods in \mathbb{R}^n so that the virtual forces at these points can balance each other and converge the surface to the required balance state. Yet, when the overall area is huge, that is when the data dimension is very high, the "same neighborhood" criteria basically implies that \mathbb{P}^U and \mathbb{P}^D must (almost) coincide. When this condition is not satisfied, that is when \mathbb{P}^U and \mathbb{P}^D are not close enough, there will be more areas with the very big log-density difference. Furthermore, these areas will have an arbitrarily big error as was explained above. Thus, we can see that like any other

non-parametric density estimation approach, also PSO-LDE suffers from the *dimensionality* curse. More so, this is also true for any other PSO instance, since the underlying principles of a virtual surface and a force balance at the equilibrium are the same.

To reduce the mismatch between \mathbb{P}^U and \mathbb{P}^D , we can perform rough density estimation of \mathbb{P}^U at the pre-training stage via one of the existing methods. For example, we can approximate every dimension from the available data $\{X_i^U\}$ separately by a Gaussian Mixture Model (GMM) (McLachlan and Basford, 1988). Then, during training we can use this rough estimation as our *down* density \mathbb{P}^D . Such a choice of \mathbb{P}^D will probably be more efficient compared to the typical simple choices like Uniform and Normal distributions. Another alternative is to apply adaptive sampling (Bucher, 1988; Bengio and Senécal, 2008) where \mathbb{P}^D is updated along the optimization to be closer to \mathbb{P}^U . We shall leave the investigation of these directions to future research.

Remark 18 When curse of dimensionality is encountered in the Machine Learning domain, a typical solution is to reduce data dimension, for example by using a (non-linear) principal component analysis (PCA). Such reduction is justified if the high-dimensional target data is actually laying on a manifold of smaller dimension, which is true in many cases. Moreover, recently proposed Progressive Growing of GANs method (Karras et al., 2017) can generate high-resolution images when training the NN in several phases, progressively increasing resolution of the generated data at each training phase. Since the GAN critic is also an instance of PSO, apparently such multi-phase optimization can be used for other PSO instances (e.g. PSO-LDE) as well to overcome the curse of dimensionality. Furthermore, for a general non-image dataset we can perform a similar multi-stage resolution increase by sequentially increasing numerical precision of the applied model. That is, we can go from floating point (FP) 16 representation to FP32 and further to FP64. We shall leave an application of these techniques to PSO-LDE for future research.

Remark 19 Note that the above analysis of PSO-LDE does not involve the side-influence of $g_{\theta}(X', X)$ between different areas of the input space. Yet, when this influence is strong enough, $g_{\theta}(X', X)$ will connect different far away training points and average their mutual force that is applied to the NN surface at each point, as was described in Section 5.5. Further, it can stabilize the up and down forces even at areas where samples of only one density reside. Thus, it also plays a vital role in stability of PSO-LDE family within the unbalanced areas where $\frac{\mathbb{P}^{U}(X)}{\mathbb{P}^{D}(X)}$ is too big/small. We shall leave the analytical investigation of $g_{\theta}(X', X)$'s impact on PSO-LDE convergence for future work.

By replacing pdf loss in Eq. (15) with PSO-LDE we succeeded to increase approximation accuracy of density estimation. We show these results in Section 12. Furthermore, unlike typical density estimators, for both DeepPDF and PSO-LDE cases the total integral of the density estimator is not explicitly constrained to 1, yet was empirically observed to be very close to it. This implies that the proposed herein methods produce an approximately normalized density model. Yet, for many applications such density model is suitable. For example, in the estimation of a measurement likelihood model for Bayesian state inference in robotics (Kopitkov and Indelman, 2018b), the model is required only to be proportional to the real measurement likelihood. Furthermore, upon the optimization completion, the surface $f_{\theta}(X)$ will have consistent outputs only in area $\mathbb{S}^{U \cup D}$, since in the rest of areas we

did not apply any optimization forces. Below, we will describe how to enforce $f_{\theta}(X)$ to have consistent outputs outside of trained areas.

6.2.3 Proxy for Inconsistent Areas

In the above section we saw that the NN surface is optimized only near areas where up and down points were sampled. The rest of the volume of \mathbb{R}^n is literally unoptimized, unless the side-influence $g_{\theta}(X',X)$ is also considered, and can have arbitrarily model outputs by the optimization end. Furthermore, considering only \mathbb{R}^n areas that contain samples, we saw that $f_{\theta}(X)$'s output at unbalanced points with $|\log \mathbb{P}^{U}(X) - \log \mathbb{P}^{D}(X)| > a$ is undefined since the optimization pushes there will eventually have a zero magnitude. Thus, in order to make output of our learned model more reliable, we may want to explicitly assign values in these unoptimized/unbalanced areas.

To that end, we have to detect if a given query point $X \in \mathbb{R}^n$ belongs to any unoptimized/unbalanced area, and if so - explicitly assign a value of $f_{\theta}(X)$ at X to some predefined constant via a proxy function $\bar{f}_{\theta}(X)$ that wraps around $f_{\theta}(X)$ as follows.

First, we consider unoptimized areas of \mathbb{R}^n . Let us define R as a subspace of \mathbb{R}^n which satisfies $R \triangleq \{X : min_i \leq x_i \leq max_i\}$, where x_i represents the i-th coordinate of point X, and where min_i and max_i are minimum and maximum values from available training dataset along dimension i. That is, R represents a minimal n-dimensional hyperrectangle in \mathbb{R}^n that contains all available samples from \mathbb{P}^U . Further, since there were no training up points X^U outside of R, the surface there is unbalanced at areas where points X^D were sampled and unoptimized at areas where no points X^D were sampled. Moreover, for the same reason we can assume that the density of data within a complement subspace $\bar{R} \triangleq \mathbb{R}^n \setminus R$ is zero. Concluding from above, we desire our model to return zero density for a query point $X \in \bar{R}$. We will enforce it via a proxy function $\bar{f}_{\theta}(X)$ below in Eq. (21).

Further, inside the optimized subspace R we may have unbalanced areas, according to the logarithm difference \bar{d} defined in Eq. (17) and according to its connection with the density ratio $\frac{\mathbb{P}^U(X)}{\mathbb{P}^D(X)}$. That is, if at a point $X \in R$ the logarithm difference \bar{d} is very big, above some threshold a_{upper} , then the up magnitude function at this point is zero, $M^U[X, f_{\theta}(X)] \approx 0$. This, in turn, implies that during training there were many points X^U and almost no points X^D around X, which caused the surface go too high till the up magnitude nullified itself. Furthermore, once \bar{d} at a specific point X passed the threshold a_{upper} , the surface height $f_{\theta}(X)$ is only affected by side-forces and does not express accurate density estimation of X. Hence, arguably the most appropriate thing to do at such points $\{X: f_{\theta}(X) > a_{upper}\}$ is to enforce proxy function $\bar{f}_{\theta}(X)$ to return output that satisfies $\bar{d} = a_{upper} \Rightarrow \bar{f}_{\theta}(X) = a_{upper} + \log \mathbb{P}^D(X)$ (see Eq. (21) below).

However, to apply such proxy, we first need to know the sensitivity threshold a_{upper} which is unknown. One way to estimate it is via

$$a_{upper} \approx \max_{X_i^D} \left[f_{\theta}(X_i^D) - \log \mathbb{P}^D(X_i^D), 0 \right] = \max_{X_i^D} \left[\bar{d}(X_i^D; \theta), 0 \right].$$

where $\{X_i^D\}$ are all training points from \mathbb{P}^D . In the above expression we search for the highest point on the logarithm difference $\bar{d}[X, f_{\theta}(X)]$ where we still have training samples from \mathbb{P}^D . That is, the highest surface point where both densities have their samples.

Likewise, if at a point X the logarithm difference \bar{d} is very small, below a some threshold a_{lower} , then the down magnitude function at this point is zero, $M^D[X, f_{\theta}(X)] \approx 0$. Also here, $f_{\theta}(X)$'s output does not express the real point density since the surface at this point is affected mostly by side-forces. Moreover, there are almost no training sample points X^U around such X since the surface was pushed too low. Thus, we can assume that point density $\mathbb{P}^U(X)$ of such X is zero, and enforce our proxy function $\bar{f}_{\theta}(X)$ accordingly. Furthermore, we can estimate a_{lower} in similar way to a_{upper} :

$$a_{lower} \approx \min_{X_i^U} \left[f_{\theta}(X_i^U) - \log \mathbb{P}^D(X_i^U), 0 \right] = \min_{X_i^U} \left[\bar{d}(X_i^U; \theta), 0 \right],$$

where we search for the lowest point on the logarithm difference $\bar{d}[X, f_{\theta}(X)]$ where we still have training samples from \mathbb{P}^{U} . That is, the lowest surface point where both densities have their samples.

Finally, to express the above knowledge and to correct our log-pdf estimator we can use the following proxy function:

$$\bar{f}_{\theta}(X) = \begin{cases}
-\infty, & \text{if } X \notin R \\
a_{upper} + \log \mathbb{P}^{D}(X), & \text{if } [f_{\theta}(X) - \log \mathbb{P}^{D}(X)] > a_{upper} \\
-\infty, & \text{if } [f_{\theta}(X) - \log \mathbb{P}^{D}(X)] < a_{lower} \\
f_{\theta}(X), & \text{otherwise}
\end{cases}$$
(21)

Note that the above proxy heuristic is not required in case both densities \mathbb{P}^U and \mathbb{P}^D are close and if the learned model $f_{\theta}(X)$ is only evaluated at points sampled from one of these two densities. For example, if \mathbb{P}^U and \mathbb{P}^D are properly chosen so that $\frac{1}{\exp a} < \frac{\mathbb{P}^U(X)}{\mathbb{P}^D(X)} < \exp a$ and if a query point X was sampled from \mathbb{P}^U , the calculation of $\bar{f}_{\theta}(X)$ will activate the last case row in Eq. (21), i.e. it will return $f_{\theta}(X)$. Further, in our experiments we do not apply this heuristic since we evaluate trained models only on samples from \mathbb{P}^U and \mathbb{P}^D .

7. Conditional Density Estimation

In this section we show how to utilize PSO balance state to infer conditional (ratio) density functions.

7.1 Conditional Density Estimation

Herein we will focus on problem of conditional density estimation, which specifically requires to infer $\mathbb{P}^{U}_{X|Y}(X|Y)$, and where i.i.d. samples of pairs $\{X_{i}^{U}, Y_{i}^{U}\}$ are given as:

$$\frac{\text{(columns of } X^{U})}{\mathcal{D}} = \begin{pmatrix} X_{1}^{U} & & & & & \\ & X_{2}^{U} & & & & \\ & \vdots & & & \vdots \end{pmatrix}, \text{ where } X_{i}^{U} \in \mathbb{R}^{n_{x}}, Y_{i}^{U} \in \mathbb{R}^{n_{y}}. \tag{22}$$

Notation	Description
$X^{U} \sim \mathbb{P}_{X}^{U}(X)$ $Y^{U} \sim \mathbb{P}_{Y}^{U}(Y)$ $[X^{U}, Y^{U}]$	n_x -dimensional random variable with marginal pdf \mathbb{P}^{U}_X n_y -dimensional random variable with marginal pdf \mathbb{P}^{U}_Y n -dimensional random variable with joint pdf $\mathbb{P}^{U}_{XY}(X,Y)$,
$n = n_x + n_y$ $\mathbb{P}_{X Y}^U(X Y)$ $X^D \sim \mathbb{P}^D$ $[X^D, Y^D]$	at samples of which we push the model surface up joint dimension of random variable $[X^U, Y^U]$ conditional probability density function of $X \equiv X^U$ given $Y \equiv Y^U$ n_x -dimensional random variable with pdf \mathbb{P}^D n -dimensional random variable with joint pdf $\mathbb{P}^D(X) \cdot \mathbb{P}^U_Y(Y)$, at samples of which we push the model surface $down$

Table 8: Main Notations for Conditional Density Estimators

Again, we use U to refer to up force in PSO framework as will be described below. For any dataset \mathcal{D} , the generation process of its samples is governed by the following unknown data densities: $\mathbb{P}^{U}_{XY}(X,Y)$, $\mathbb{P}^{U}_{X}(X)$ and $\mathbb{P}^{U}_{Y}(Y)$. Specifically, in Eq. (22) rows under X^{U} columns will be distributed by marginal pdf $\mathbb{P}^{U}_{X}(X)$, rows under Y^{U} columns - by marginal pdf $\mathbb{P}^{U}_{Y}(Y)$, and entire rows of \mathcal{D} will have the joint density $\mathbb{P}^{U}_{XY}(X,Y)$ (see also Table 8 for list of main notations). Likewise, these densities induce the conditional likelihoods $\mathbb{P}^{U}_{X|Y}(X|Y)$ and $\mathbb{P}^{U}_{Y|X}(Y|X)$, which can be formulated via Bayes theorem:

$$\mathbb{P}_{X|Y}^{U}(X|Y) = \frac{\mathbb{P}_{XY}^{U}(X,Y)}{\mathbb{P}_{Y}^{U}(Y)}, \quad \mathbb{P}_{Y|X}^{U}(Y|X) = \frac{\mathbb{P}_{XY}^{U}(X,Y)}{\mathbb{P}_{X}^{U}(X)}.$$
 (23)

Depending on the task at hand, conditional pdf $\mathbb{P}_{X|Y}^{U}(X|Y)$ can produce valuable information about given data.

The simple way to infer $\mathbb{P}^{U}_{X|Y}(X|Y)$ is by first approximating separately the $\mathbb{P}^{U}_{XY}(X,Y)$ and $\mathbb{P}^{U}_{Y}(Y)$ from data samples (e.g. by using DeepPDF or PSO-LDE), and further applying Bayes theorem in Eq. (23). Yet, such method is not computationally efficient and typically is also not optimal, since approximation errors of both functions can produce even bigger error in the combined function.

A different technique, based on PSO principles, can be performed as follows. Consider a model (PSO surface) $f_{\theta}(X,Y): \mathbb{R}^n \to \mathbb{R}$ with $n=n_x+n_y$, where the concatenated input [X,Y] can be seen as the surface support. Define an arbitrary density \mathbb{P}^D over \mathbb{R}^{n_x} with a known pdf function which can be easily sampled (e.g. Uniform). Density \mathbb{P}^D will serve as a down force to balance samples from \mathbb{P}^U_X , and thus is required to cover the support of \mathbb{P}^U_X . Further, $\mathbb{P}^U_{XY}(X,Y)$ will serve as up density in PSO framework, and its sample batch $\{X_i^U,Y_i^U\}_{i=1}^{N^U}$ will contain all rows from \mathcal{D} . As well, we will use $\mathbb{P}^D(X)\cdot\mathbb{P}^U_Y(Y)$ as down density. Corresponding samples $\{X_i^D,Y_i^D\}_{i=1}^{N^D}$ will be sampled in two steps. $\{Y_i^D\}_{i=1}^{N^D}$ are taken from \mathcal{D} under Y^U columns; $\{X_i^D\}_{i=1}^{N^D}$ are sampled from $\mathbb{P}^D(X)$.

Considering the above setup, we can apply PSO to push $f_{\theta}(X, Y)$ via up and down forces. The optimization gradient will be identical to Eq. (1) where X_i^U and X_i^D are substituted by $\{X_i^U, Y_i^U\}$ and $\{X_i^D, Y_i^D\}$ respectively. For any particular $\{M^U, M^D\}$ the associated PSO

balance state will be:

$$\frac{M^{D}\left[X,Y,f_{\theta}(X,Y)\right]}{M^{U}\left[X,Y,f_{\theta}(X,Y)\right]} = \frac{\mathbb{P}_{XY}^{U}(X,Y)}{\mathbb{P}^{D}(X) \cdot \mathbb{P}_{Y}^{U}(Y)} = \frac{\mathbb{P}_{X|Y}^{U}(X|Y)}{\mathbb{P}^{D}(X)},\tag{24}$$

where we can observe $\mathbb{P}_{X|Y}^{U}(X|Y)$, which we aim to learn. Similarly, to Section 3, below we formulate PSO subgroup for conditional density estimation (or any function of it).

Theorem 20 (Conditional Density Estimation) Denote the required PSO convergence by a transformation $T(X,Y,z): \mathbb{R}^n \times \mathbb{R} \to \mathbb{R}$ s.t. $f_{\theta}(X,Y) = T\left[X,Y,\mathbb{P}_{X|Y}^U(X|Y)\right]$ is the function we want to learn. Given T(X,Y,z) is one-to-one function w.r.t. z, any pair $\{M^U,M^D\}$ satisfying:

$$\frac{M^{D}(X,Y,s)}{M^{U}(X,Y,s)} = \frac{T^{-1}(X,Y,s)}{\mathbb{P}^{D}(X)},$$
(25)

will produce the required convergence.

The proof is trivial by noting that:

$$T^{-1}(X,Y,f_{\theta}(X,Y)) = \mathbb{P}^{D}(X) \cdot \frac{M^{D}(X,Y,f_{\theta}(X,Y))}{M^{U}(X,Y,f_{\theta}(X,Y))} = \mathbb{P}^{D}(X) \cdot \frac{\mathbb{P}^{U}_{X|Y}(X|Y)}{\mathbb{P}^{D}(X)} \Rightarrow T^{-1}(X,Y,f_{\theta}(X,Y)) = \mathbb{P}^{U}_{X|Y}(X|Y)$$

where we used both Eq. (24) and Eq. (25). From properties of inverse functions it follows:

$$T\left[X,Y,\mathbb{P}^{\scriptscriptstyle{U}}_{X|Y}(X|Y)\right]=T\left[X,Y,T^{-1}(X,Y,f_{\theta}(X,Y))\right]=f_{\theta}(X,Y).$$

Observe that one-to-one property is necessary for existence of T^{-1} .

Example 4: Consider a scenario where we would like to infer $f_{\theta}(X,Y) = \mathbb{P}^{U}_{X|Y}(X|Y)$. Thus, the PSO convergence is described by T(X,Y,z) = z. Its inverse is $T^{-1}(X,Y,s) = s$. Hence, magnitude functions must satisfy $\frac{M^{D}(X,Y,f_{\theta}(X,Y))}{M^{U}(X,Y,f_{\theta}(X,Y))} = \frac{f_{\theta}(X,Y)}{\mathbb{P}^{D}(X)}$. One choice for such magnitudes is $M^{U}[X,Y,f_{\theta}(X,Y)] = \mathbb{P}^{D}(X)$ and $M^{D}[X,Y,f_{\theta}(X,Y)] = f_{\theta}(X,Y)$, defined in Table 9 as "Conditional Density Estimation".

Example 5: Consider a scenario where we would like to infer $f_{\theta}(X,Y) = \log \mathbb{P}_{X|Y}^{U}(X|Y)$, which can be essential for high-dimensional data. The PSO convergence is described by $T(X,Y,z) = \log z$, and its inverse is $T^{-1}(X,Y,s) = \exp s$. Hence, magnitude functions must satisfy $\frac{M^{D}(X,Y,f_{\theta}(X,Y))}{M^{U}(X,Y,f_{\theta}(X,Y))} = \frac{\exp f_{\theta}(X,Y)}{\mathbb{P}^{D}(X)}$. One choice for such magnitudes is $M^{U}[X,Y,f_{\theta}(X,Y)] = \frac{\mathbb{P}^{D}(X)}{D(X,Y,f_{\theta}(X,Y))}$ and $M^{D}[X,Y,f_{\theta}(X,Y)] = \frac{\exp f_{\theta}(X,Y)}{D(X,Y,f_{\theta}(X,Y))}$, defined in Table 9 as "PSO-LDE Conditional Form". The denominator $D(X,Y,f_{\theta}(X,Y)) = [[\exp f_{\theta}(X,Y)]^{\alpha} + [\mathbb{P}^{D}(X)]^{\alpha}]^{\frac{1}{\alpha}}$ serves as a normalization to enforce magnitudes to be bounded functions, similarly to PSO-LDE method in Section 6.2.

Conditional	$\underline{\mathbf{F}} : \frac{\mathbb{P}_{X Y}^{U}(X Y)}{\mathbb{P}_{X Y}^{U}(X Y) + \mathbb{P}_{\phi}^{D}(X Y)} ,$
	$\Gamma: \overline{mU} \to \overline{mD} \to \overline{mD} \to \overline{mD}$
GAN Critic	where $\mathbb{P}^{D}_{\phi}(X Y)$ is density of generator parametrized by ϕ
	where $\mathbb{E}_{\phi}(X T)$ is density of generator parametrized by ϕ R: Mirza and Osindero (2014)
	$\underline{\mathbb{L}}: -\mathbb{E}_{[X,Y]\sim \mathbb{P}^{U}_{XY}(X,Y)}\log f_{ heta}(X,Y)-$
	$= \mathbb{E}_{XY}(X, I) \text{of} Y$ $= \mathbb{E}_{XY}(X, I) \text{of} [1 - f_0(X, Y)]$
	$-\mathbb{E}_{[X,Y] \sim \mathbb{P}_{\phi}^{D}(X Y) \cdot \mathbb{P}_{Y}^{U}(Y)} \log \left[1 - f_{\theta}(X,Y)\right]$ $M^{U}, M^{D} : \frac{1}{f_{\theta}(X,Y)}, \frac{1}{1 - f_{\theta}(X,Y)}$

Likelihood-Ratio	$\underline{\mathrm{F}}$: $\log \frac{\mathbb{P}_{X Y}^{\mathcal{V}}(X Y)}{\mathbb{P}_{X}^{\mathcal{V}}(X Y)}$,
with	where $\mathbb{P}^{D}_{\phi}(X Y)$ is density of generator parametrized by ϕ
	$\underline{\mathbf{R}}$: This paper
	$\underline{\mathbf{L}} \colon \mathbb{E}_{[X,Y] \sim \mathbb{P}_{XY}^U(X,Y)} \log \left[1 + \exp[-f_{\theta}(X,Y)] \right] +$
	$+\mathbb{E}_{[X,Y]\sim \mathbb{P}^D_\phi(X Y)\cdot \mathbb{P}^U_Y(Y)}\log\left[1+\exp[f_\theta(X,Y)]\right]$
	M^{U}, M^{D} : $\frac{1}{\exp[f_{\theta}(X,Y)]+1}$, $\frac{1}{\exp[-f_{\theta}(X,Y)]+1}$
Conditional	$\overline{\underline{\mathrm{F}}} \colon \mathbb{P}^{\scriptscriptstyle U}(X Y)$
	$\underline{\mathbf{R}}$: This paper
Estimation	$\underline{\mathbf{L}}: -\mathbb{E}_{[X,Y]\sim \mathbb{P}_{XY}^U(X,Y)} f_{\theta}(X,Y) \cdot \mathbb{P}^D(X) +$
	$+ \operatorname{\mathbb{E}}_{[X,Y] \sim \mathbb{P}^D(X) \cdot \mathbb{P}^U_Y(Y)} rac{1}{2} \Big[f_{ heta}(X,Y) \Big]^2$
	$M^{\scriptscriptstyle U},M^{\scriptscriptstyle D}\colon\mathbb{P}^{\scriptscriptstyle D}(X)\;,f_{\scriptscriptstyle heta}(X,Y)$
Conditional	$\underline{\mathrm{F}}$: $\log \mathbb{P}^{U}(X Y)$
o v	$\underline{\mathbf{R}}$: This paper
Estimation	$\underline{\mathbf{L}} : -\mathbb{E}_{[X,Y] \sim \mathbb{P}_{XY}^U(X,Y)} f_{\theta}(X,Y) + \mathbb{E}_{[X,Y] \sim \mathbb{P}^D(X) \cdot \mathbb{P}_Y^U(Y)} \frac{\exp[f_{\theta}(X,Y)]}{\mathbb{P}^D(X)}$
	$M^U,\ M^D\colon 1,\ rac{\exp[f_ heta(X,Y)]}{\mathbb{P}^D(X)}$
NCE	$\underline{\mathrm{F}} \colon \log \mathbb{P}^U(X Y)$
Conditional	$\underline{\underline{R}}$: Mnih and Teh (2012); Mnih and Kavukcuoglu (2013)
Form	$\underline{\mathbf{L}}$: $\mathbb{E}_{[X,Y] \sim \mathbb{P}_{XY}^U(X,Y)} \log \frac{\exp[f_{\theta}(X,Y)] + \mathbb{P}^D(X)}{\exp[f_{\theta}(X,Y)]} +$
	$+\mathbb{E}_{[X,Y]\sim \mathbb{P}^D(X)\cdot \mathbb{P}^U_Y(Y)}\lograc{\exp[f_{ heta}(X,Y)]+\mathbb{P}^D(X)}{\mathbb{P}^D(X)}$
	$M^{U}, M^{D}: \frac{\mathbb{P}^{D}(X)}{\exp[f_{\theta}(X,Y)] + \mathbb{P}^{D}(X)}, \frac{\exp[f_{\theta}(X,Y)]}{\exp[f_{\theta}(X,Y)] + \mathbb{P}^{D}(X)}$
	$\underline{\mathrm{F}} \colon \log \mathbb{P}^{\scriptscriptstyle U}(X Y)$
	R: This paper
	$\underline{\underline{L}}$: unknown $\mathbb{P}^D(X)$ $\exp f_0(XY)$
	$M^{U}, M^{D}: \frac{\mathbb{P}^{D}(X)}{\left[\left[\exp f_{\theta}(X,Y)\right]^{\alpha} + \left[\mathbb{P}^{D}(X)\right]^{\alpha}\right]^{\frac{1}{\alpha}}}, \frac{\exp f_{\theta}(X,Y)}{\left[\left[\exp f_{\theta}(X,Y)\right]^{\alpha} + \left[\mathbb{P}^{D}(X)\right]^{\alpha}\right]^{\frac{1}{\alpha}}}$
	where $\mathbb{P}_{XY}^{U}(X,Y)$ serves as up density and
	$\mathbb{P}^D(X) \cdot \mathbb{P}^U_Y(Y)$ - as down density

Table 9: PSO Instances For Conditional Density (Ratio) Estimation, see Sections 7.1 and 7.2 for a detailed exposition of conditional PSO $\,$

Thus, we can estimate the conditional density, or any function of it, in a one-step algorithm by applying PSO procedure with up and down densities defined above. This again emphasizes the simplicity and usability of PSO formulation. Further, note that it is also possible to reuse sample Y_i^U as Y_i^D , since within the down term this sample will still be independent of X_i^D and its density is still the marginal $\mathbb{P}_Y^U(Y)$. Such reuse is popular for example in NCE methods (Mnih and Teh, 2012; Mnih and Kavukcuoglu, 2013) in context of language modeling.

The above examples and several other options are listed in Table 9. Similarly to the case of ordinary density estimation, also in the conditional case there are numerous PSO instances with the same target function $\mathbb{P}^U_{X|Y}(X|Y)$ (or $\log \mathbb{P}^U_{X|Y}(X|Y)$). Analyses of these techniques and search for the most "optimal" can be an interesting direction for future research.

7.2 Relation to Conditional GANs

Furthermore, similar idea was also presented in context of GANs, where a conditional generation of data (e.g. images given labels) was explored. Below we show its connection to PSO framework.

Denote the dataset \mathcal{D} as in Eq. (22), where real sample pairs $\{X_i^U, Y_i^U\}$ are distributed according to unknown $\mathbb{P}_{XY}^U(X,Y)$. In Conditional GAN (cGAN) (Mao et al., 2017) the generator produces fake samples from the generator's conditional density $\mathbb{P}_{\phi}^D(X|Y)$, where we again use notations U and D to refer to PSO forces, as is described below. Density $\mathbb{P}_{\phi}^D(X|Y)$ is an implicit distribution of fake samples that are returned by the generator $h_{\phi}(v,Y)$ from the latent space $v \in \mathbb{R}^{n_v}$, where the label Y was a priori sampled from $\mathbb{P}_{Y}^U(Y)$; ϕ is a generator's parametrization. Further, the critic sees pairs [X,Y] coming from \mathcal{D} and from the generator, and tries to decide where the pair is originated from. This is done by estimating a statistical divergence between $\mathbb{P}_{X|Y}^U(X|Y)$ implicitly defined by \mathcal{D} , and between $\mathbb{P}_{\phi}^D(X|Y)$ implicitly defined by ϕ . Moreover, the divergence estimation is typically done by first inferring the ratio $\frac{\mathbb{P}_{X|Y}^U(X|Y)}{\mathbb{P}_{\phi}^D(X|Y)}$ (or some function of this ratio).

The proposed by (Mao et al., 2017) algorithm is identical to PSO procedure, when $\mathbb{P}_{XY}^{U}(X,Y)$ serves as up density, and $\mathbb{P}_{\phi}^{D}(X|Y) \cdot \mathbb{P}_{Y}^{U}(Y)$ - as down density. The up sample batch $\{X_{i}^{U},Y_{i}^{U}\}_{i=1}^{NU}$ will contain all rows from \mathcal{D} . Further, samples $\{X_{i}^{D},Y_{i}^{D}\}_{i=1}^{ND}$ from down density will be sampled in three steps. $\{Y_{i}^{D}\}_{i=1}^{ND}$ are taken from \mathcal{D} under Y^{U} columns; $\{v^{i}\}_{i=1}^{ND}$ are sampled from generator's base distribution; $\{X_{i}^{D}\}_{i=1}^{ND}$ are generator's outputs for inputs $\{Y_{i}^{D},v_{i}\}_{i=1}^{ND}$. Extending the setup of Section 7.1 to the above sampling procedure, any particular $\{M^{U},M^{D}\}$ will produce PSO balance state:

$$\frac{M^{D}\left[X,Y,f_{\theta}(X,Y)\right]}{M^{U}\left[X,Y,f_{\theta}(X,Y)\right]} = \frac{\mathbb{P}_{XY}^{U}(X,Y)}{\mathbb{P}_{\phi}^{D}(X|Y) \cdot \mathbb{P}_{Y}^{U}(Y)} = \frac{\mathbb{P}_{X|Y}^{U}(X|Y)}{\mathbb{P}_{\phi}^{D}(X|Y)},$$

where the conditional ratio shows up. Similarly, to conditional density estimation, below we formulate PSO subgroup for inference of this ratio (or any function of it).

Theorem 21 (Conditional Ratio Estimation) Denote the required PSO convergence by a transformation $T(X,Y,z): \mathbb{R}^{n_x+n_y} \times \mathbb{R} \to \mathbb{R}$ s.t. $f_{\theta}(X,Y) = T\left[X,Y,\frac{\mathbb{P}_{X|Y}^U(X|Y)}{\mathbb{P}_{\phi}^D(X|Y)}\right]$ is

the function we want to learn. Given T(X,Y,z) is one-to-one function w.r.t. z, any pair $\{M^U,M^D\}$ satisfying:

$$\frac{M^{\scriptscriptstyle D}(X,Y,s)}{M^{\scriptscriptstyle U}(X,Y,s)} = T^{-1}(X,Y,s),$$

will produce the required convergence.

The proof is trivial by noting that:

$$T^{-1}(X,Y,f_{\theta}(X,Y)) = \frac{M^{D}(X,Y,f_{\theta}(X,Y))}{M^{U}(X,Y,f_{\theta}(X,Y))} = \frac{\mathbb{P}_{X|Y}^{U}(X|Y)}{\mathbb{P}_{\phi}^{D}(X|Y)} \Rightarrow$$

$$\Rightarrow T^{-1}(X,Y,f_{\theta}(X,Y)) = \frac{\mathbb{P}_{X|Y}^{U}(X|Y)}{\mathbb{P}_{\phi}^{D}(X|Y)}.$$

From properties of inverse functions the Theorem follows.

The cGAN method aimed to infer $\frac{\mathbb{P}_{X|Y}^U(X|Y)}{\mathbb{P}_{X|Y}^U(X|Y) + \mathbb{P}_{\phi}^D(X|Y)}$ to measure Jensen-Shannon divergence between real and fake distributions. This is associated with PSO convergence $T(X,Y,z) = \frac{z}{z+1}$ and the corresponding inverse $T^{-1}(X,Y,s) = \frac{s}{1-s}$. According to Theorem 21 the magnitudes must satisfy:

$$\frac{M^{D}(X, Y, f_{\theta}(X, Y))}{M^{U}(X, Y, f_{\theta}(X, Y))} = \frac{f_{\theta}(X, Y)}{1 - f_{\theta}(X, Y)},$$

with the specific choice $\{M^U(X,Y,f_\theta(X,Y)) = \frac{1}{f_\theta(X,Y)}, M^D(X,Y,f_\theta(X,Y)) = \frac{1}{1-f_\theta(X,Y)}\}$ selected by critic loss in (Mao et al., 2017).

Hence, we can see that cGAN critic loss is a particular instance of PSO, when the sampling procedure of up and down samples is as described above. Further, two main problems of the classical cGAN critic are the not-logarithmic scale of the target function and unboundedness of magnitude functions (for a general model $f_{\theta}(X,Y)$). In Table we propose a "Likelihood-Ratio with Logistic Loss" to learn $\log \frac{\mathbb{P}^{U}_{X|Y}(X|Y)}{\mathbb{P}^{D}_{\phi}(X|Y)}$ whose magnitudes are bounded. We argue such choice to be more stable during the optimization which will lead to a better accuracy. Moreover, for specific case when cGAN critic $f_{\theta}(X,Y)$ is parameterized as $sigmoid(r_{\theta}(X,Y))$ with $r_{\theta}(X,Y)$ being the inner model, cGAN critic loss can be shown to be reduced to the above logistic loss. Thus, with such parametrization the inner NN $r_{\theta}(X,Y)$ within cGAN critic will converge to $\log \frac{\mathbb{P}^{U}_{X|Y}(X|Y)}{\mathbb{P}^{D}_{\phi}(X|Y)}$.

8. NN Architecture

The described above density estimation algorithms, DeepPDF in Section 6.1 and log-density estimators in Section 6.2, typically produce highly accurate density approximations in low dimensional cases. For example, in (Kopitkov and Indelman, 2018a) we showed that DeepPDF produces a better accuracy than KDE methods in 2D and 3D scenarios. This likely can be accounted to the flexibility of NN - its universal ability to approximate any function. As empirically observed, the implicit flexibility parameter of NN, the *influence* decay rate of

 $g_{\theta}(X', X)$ that was discussed in Section 5.5 and which is parallel to the kernel bandwidth, is typically different in various areas of the considered input space. Moreover, $g_{\theta}(X', X)$ of NN is data-dependent and adapts during the optimization to better represent a target function (Kopitkov and Indelman, 2019). This further increases the overall approximation performance. In contrast, KDE methods are typically limited to a specific choice of a kernel and a bandwidth (yet variable-bandwidth KDE methods exist, see Terrell et al. (1992)) that is applied to estimate the entire pdf surface with its many various details.

However, we also observed a considerable underfitting problem of the above PSO instances that grows with the data dimension. That is, even in case where a high-dimensional training dataset is huge, for a typical fully-connected NN architecture the produced estimation is far away from the real data density, and often contains mode-collapses and other prediction inconsistencies. We argue that the reason is the large side-influence of the virtual forces. That is, the bandwidth of $g_{\theta}(X', X)$ is too big which leads to growing of estimation bias. Intuitively, considering the thermodynamic perspective of PSO, the surface height $f_{\theta}(X)$ at any X is changed by pushes at every other training point $X' \in \mathbb{R}^n$ according to the kernel $g_{\theta}(X, X')$, which is typically not entirely zero for any two points. Further, when the bandwidth of $g_{\theta}(X, X')$ is big, $f_{\theta}(X)$ is influenced by many training points. This leads to the smoothness of $f_{\theta}(X)$ w.r.t. X. Hence, as was shown in Section 5.5 the level of side-influence within the NN (e.g. the bandwidth of $g_{\theta}(X, X')$) defines the flexibility of $f_{\theta}(X)$.

As observed empirically, in fully-connected architecture this side-influence is growing considerably with the higher data dimension, thus producing more side interference between the different points and decreasing the overall elasticity of the network. In its turn, this limits the accuracy produced by PSO. In this section we propose a new NN architecture that mitigates the side-influence problem and increases a flexibility of the surface. Further, in Section 12.3.3 we show that such architecture extremely improves the estimation accuracy.

Remark 22 Note that in context of generative adversarial networks (GANs), whose critics are also instances of PSO (see Tables 2-9), the convergence problems (e.g. mode-collapse and non-convergence) were also reported. Typically, these problems are blamed on Nash equilibrium between critic and generator networks which is hard to optimize. Yet, in our work we see that such problems exist even without a two-player optimization. That is, even when only a specific PSO instance (the critic in GAN's context) is trained separately, it is typically underfitting and has mode-collapses within the converged surface $f_{\theta}(X)$ where several separate hills from target $\log \mathbb{P}^{U}(X)$ are represented as one hill inside $f_{\theta}(X)$. Below we present several techniques that allowed us to reduce these convergence problems.

8.1 Block-Diagonal Layers

In (Kopitkov and Indelman, 2018a) we used a simple fully-connected (FC) network to represent a model $f_{\theta}(X)$ of data density $\mathbb{P}^{U}(X)$. While it yielded sophisticated results in 2D and 3D settings, such architecture produces terrible performance for higher dimensions, getting worse with each increase of dimension. In this paper we will experiment with 20D data and show that block-diagonal (BD) layers (see below) provide much better density approximation. In future work we will extend our experiments to higher dimensions (\sim thousands of variables) and further investigate the optimal structure of NN for enhanced surface flexibility.

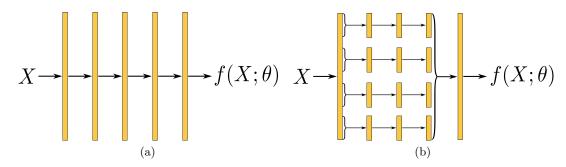


Figure 7: (a) Typical NN architecture used in (Kopitkov and Indelman, 2018a). Yellow blocks are FC layers with non-linearity, except for last layer which is FC layer without activation function. Entire network can be seen as single transformation channel. (b) Proposed NN architecture used in this paper. Block-diagonal layers can be seen as set of independent transformation channels. This independence improves network's flexibility. Output vector of a first FC layer is sliced into N_B separate vectors. Each small vector is used as input to separate channel - FC sub-network. At the end outputs of all channels are concatenated and sent to the final FC layer. All FC layers in this architecture (the yellow blocks) use non-linearity (typically Relu or Leaky-Relu), except for the final FC layer.

A typical FC network (Figure 7a) can be seen as one channel transformation from point X to its surface height $f_{\theta}(X)$. During the optimization, due to such NN structure almost every weight inside θ is updated as a consequence of pushing any point $X \in \mathbb{R}^n$ within PSO loss. Such high sharing of the weights between various regions of \mathbb{R}^n creates a huge side-influence between them, which in its turn decreases the flexibility of NN surface.

The above line of thought guided us to propose an alternative NN architecture where several separate transformation channels are built into one network (see Figure 7b). As we will see below, such architecture is identical to a simple FC network where each layer's weight matrix W_i is block-diagonal.

Specifically, we propose to pass input X through a typical FC layer with output dimension S, and split this output into a set of N_B smaller vectors of size $S_B = S/N_B$. Further, for each S_B -sized vector we construct a channel: a subnetwork with $[N_L - 2]$ FC layers of the same size S_B . Finally, the outputs of all channels are concatenated into vector of size S_B and this vector is sent to the final FC layer (see illustration in Figure 7b). All FC layers within this architecture use non-linearity (typically Relu or Leaky-Relu), except for the last layer.

Exactly the same computational flow will be produced if we use the usual FC network from Figure 7a with inner layers having block-diagonal weight matrices. That is, we can build the same simple network as in Figure 7a, with N_L layers overall, where $[N_L - 2]$ inner FC layers have block-diagonal weight matrices W_i of size $S \times S$. Each W_i in its turn will contain N_B blocks at its diagonal, of $S_B \times S_B$ size each, with rest of the entries being constant zeros.

A straightforward implementation of BD layers by setting off-diagonal entries to be constant zeros can be wasteful w.r.t. memory and computation resources. Instead, we can use multi-dimensional tensors for a more efficient implementation as follows. Consider output of the first FC layer as a tensor \bar{v} with dimensions [B,S], where B is a batch dimension and S is an output dimension of the layer. We can reshape \bar{v} to have dimensions

 $[B, N_B, S_B]$, where the last dimension of \bar{v} will contain small vectors \bar{u}_j of size S_B each, i.e. inputs for independent channels. Further, each inner BD layer can be parametrized by a weight matrix W with dimensions $[N_B, S_B, S_B]$ and bias vector b with dimensions $[N_B, S_B]$. The multiplication between \bar{v} and W, denoted as V, has to be done for each \bar{u}_j with an appropriate slice of weight matrix, W[j,:,:]. Moreover, it should be done for every instance of the batch. This can be done via the following Einstein summation convention:

$$V[i, j, k] = \sum_{m=1}^{S_B} W[j, k, m] \cdot \bar{v}[i, j, m],$$
 (26)

which produces tensor V with size $[B, N_B, S_B]$. Further, bias can be added as:

$$U[i,:,:] = V[i,:,:] + b, (27)$$

where afterwards the tensor U is transformed by point-wise activation function $\sigma(\cdot)$, finally producing the output of BD layer $\hat{U} = \sigma(U)$ of size $[B, N_B, S_B]$.

We construct $[N_L - 2]$ such BD layers that represent N_B independent channels. Further, the output of the last BD layer is reshaped back to have dimensions [B, S], and is sent to the final ordinary FC layer that returns a scalar.

Remark 23 The Einstein summation operation is typically offered by modern DL frameworks, thus implementing the above BD layers is convenient and easy. Yet, the computational efficiency can be improved by a specialized implementation that is specifically optimized on GPU level. We hope that in future versions of DL frameworks such BD layer implementation would be supported. Also, our code for this layer can be found in open source library https://bit.ly/2AMwyJT.

8.1.1 Flexibility of BD vs FC

The above BD architecture allowed us to tremendously improve accuracy of density estimation for high-dimensional data. This was achieved due to the enhanced flexibility of BD architecture vs FC, as we empirically demonstrate below. A more thorough theoretical explanation for such supreme flexibility of BD model, as well as for the analytical relation between $g_{\theta}(X, X')$ and the estimation bias, we shall leave for future work.

To this end, we analyze the side-influence of $g_{\theta}(X, X')$ for each of the architectures. For this, after training was finished we sampled $D = \{X_i\}_{i=1}^{3000}$ testing points from the target density \mathbb{P}^U and calculated their gradients $\nabla_{\theta} f_{\theta}(X_i)$. Further, we calculated Euclidean distance $d(X_i, X_j)$ and gradient similarity $g_{\theta}(X_i, X_j)$ between every two points within D, producing $\frac{3000.3001}{2}$ pairs of distance and similarity values (we consider only unique pairs here). These values are plotted in Figures 8a-8b. As can be seen, $g_{\theta}(X', X)$ values (y axis) of FC network are much higher than these values in BD network. Likewise, there is strong correlation between values of gradient similarity and Euclidean distance. In FC case, for d(X', X) > 0 values of $g_{\theta}(X', X)$ are far away from being zeros, thus implying strong side-influence of optimization pushes on surface $f_{\theta}(X)$ even between far away points. In contrast, for BD case we can see that $g_{\theta}(X', X)$ is centered around zero for d(X', X) > 0, hence side-influence here is less significant and even may be canceled out due to the symmetry of $g_{\theta}(X', X)$ values w.r.t. zero. Furthermore, we stress that similar trends were achieved in all our experiments, for various densities \mathbb{P}^U and \mathbb{P}^D .

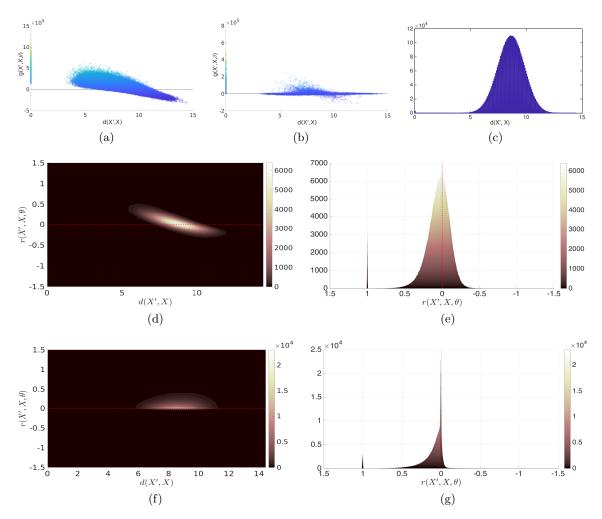


Figure 8: Side-similarity $g_{\theta}(X',X)$ and surface flexibility of FC and BD models. We infer 20D Columns distribution (see Section 12.3) by using PSO-LDE with $\alpha=\frac{1}{4}$ (see Table 2 and Section 6.2). Two networks were trained, FC and BD. The applied FC architecture contains 4 FC layers of size 1024. The applied BD architecture has 6 layers, number of blocks $N_B=50$ and block size $S_B=64$. Values of gradient similarity $g_{\theta}(X',X)$ and values of Euclidean distance d(X',X) are plotted for (a) FC network and (b) BD network. (c) Histogram of d(X',X) calculated between all sample pairs from dataset D. Further, a histogram of obtained $\{r_{\theta}(X_i,X_j)\}$ and $\{d(X_i,X_j)\}$ is plotted for (d) FC model and (f) BD model. Likewise, side views of these histograms are depicted in (e) and (g). See more details in the main text.

Remark 24 Also, note the gap in Figures 8a-8b between points with d(X', X) = 0 and rest of the samples. At d(X', X) = 0 all point pairs are of a form (X_i, X_i) , with overall 3000 such pairs. Rest of the samples are $\{(X_i, X_j) | i \neq j\}$. Furthermore, the histogram of d(X', X) between points in D is illustrated in Figure 8c. As can be observed, d(X', X) is distributed with Gaussian-like density centered around 8.6. Hence, the gap between the points in Figures 8a-8b can be explained by a very low probability of two sampled points to be close to each other when the considered space volume (here the subset of \mathbb{R}^{20}) is huge.

Further, for each sample pair in D we also calculate relative side-influence $r_{\theta}(X_i, X_i)$:

$$r_{\theta}(X, X') \triangleq \frac{g_{\theta}(X, X')}{g_{\theta}(X, X)},$$
 (28)

which represents the side-influence of point X_j on point X_i , normalized by self-influence of point X_i . When this ratio is greater than 1, it implies that point X_j has stronger impact over $f_{\theta}(X_i)$ than the point X_i itself, and vice versa. Hence, for each point X_i the $r_{\theta}(X_i, \cdot)$ can be interpreted as relative side-influence from other areas over $f_{\theta}(X_i)$, scaled w.r.t. the self-influence of X_i . Such normalization allows us to see the actual side-influence impact between two different points, since the value of $g_{\theta}(X, X')$ by itself is meaningless and only achieves significance when compared to the self-similarity $g_{\theta}(X, X)$. Moreover, unlike $g_{\theta}(X, X)$, $r_{\theta}(X, X')$ of different models and NN architectures is on the same scale, allowing to compare the side-influence level between different models.

For $9 \cdot 10^6$ calculated pairs of a relative side-influence $r_{\theta}(X_i, X_j)$ and a Euclidean distance $d(X_i, X_j)$ we constructed a histogram in Figures 8d and 8f for FC and BD networks respectively. Here, we can see the real difference between side-similarities of two models. Within FC network we have a strong relative side-influence even between far away regions. This side-influence interferes with the proper PSO optimization by introducing a bias, as was explained in Section 5.5. In contrast, within BD model the relative side-influence between far away regions stays very close to zero, implying that the surface height $f_{\theta}(X)$ at point X is only pushed by training points that are relatively close to X. Furthermore, this increases the flexibility of the surface, since with a less side-influence (with smaller PSO side-forces) the surface is less constrained and can be pushed at each specific neighborhood more freely.

Hence, we can see empirically that BD surface is much more flexible than FC, which also improves the overall accuracy performance achieved by BD networks (see Section 12.3.3). The mechanism responsible for such difference of the *gradient similarity* is currently unknown and we shall investigate it in future work.

8.1.2 Relation between BD and FC - Additional Perspectives

Another possible explanation for improved performance of BD layers over FC layers is that the Hessian of BD network is closer to a diagonal matrix. Indeed, the model with BD architecture can be shown to be equal to $f_{\theta}(X) = \sum_{i=1}^{N_B} h_{\theta_i}(X) + b$, where $\theta_i \subset \theta$ represents weights of *i*-th channel, $h_{\theta_i}(\cdot)$ represents computational graph of this channel, and where b is a bias of the last FC layer. Thus, the Hessian entries that belong to rows/columns of weights from different independent channels are zeros, $\frac{\partial^2 f_{\theta}(X)}{\partial \theta_i \cdot \partial \theta_j} = 0$, due to this independence. Moreover, in case Hessian is diagonal, the entire optimization can be divided into set of independent optimizations for each weight, where each such weight can be optimized more easily without interference from other weights. Hence, the easier optimization for more sparse Hessian may be seen as a pre-conditioning of the weight space, which may be an additional cause for BD superiority.

Remark 25 The above "sum" formulation of the $f_{\theta}(X)$ has also other benefits. It is indeed possible to optimize each channel independently, by first calculating weight update for θ_i independently of the weight update for θ_i , and further updating entire vector θ with these

updates in single computation. Such procedure can be done in parallel and will be more computationally efficient. Moreover, we may consider to perform second-order optimization on each channel since the size of each θ_i is significantly smaller than entire weights vector θ . As well, we can apply different optimization algorithms for each channel, where potentially such optimization symbiosis may combine different advantages of various optimization techniques together into one single approach. Finally, BD architecture allows for more efficient computation of Fisher Information Matrix and Hessian, both having similar sparsity pattern, which can be used for example to compute model uncertainty (Liao et al., 2018). We shall leave these directions for future research.

Also note, that multi-dimensional tensor implementation of BD layers in Eq. (26-27) allows to significantly reduce size of θ . For example, BD network applied in Figure 8 with 6 layers has less than 10^6 weights ($|\theta| = 902401$), where the straightforward implementation would require above 10^7 weights - 10 times more; the same size that appropriate FC network with 6 layers of size 3200 would take. Further, the size of FC network used in Figure 8 is $|\theta| = 2121729$. Yet, surprisingly the more compact BD network produces better results than the more memory and computation consuming FC network.

Interestingly, BD layers are contained in the hypothesis class of FC layers, thus being instance of the latter. Yet, a typical optimization of FC architecture will not converge weight matrices to be block-diagonal, since the local minima of FC network typically has dense weight matrices. However, in our experiments we will demonstrate that network with BD structure has significantly lower error, comparing to FC structure. This suggests that local minima of FC networks has a much bigger error compared to the error of the global minima for such architecture, since the global minima should be even smaller than the one achieved by BD network. Hence, this implies that common statement about local and global errors of NN being close is not always correct.

8.1.3 Similar Proposed Architectures

The BD network design has a high resemblance to the products of experts (PoE) (Hinton, 1999) where model is constructed as sum (or product) of smaller models. Yet, in typical PoE each expert is trained separately, while herein we represent our block-diagonal model as single computational graph that is trained as whole by the classical backpropagation method.

In addition, we argue that also other DL domains can benefit from a BD architecture, and such investigation can be an interesting future work. In fact, separating network into several independent channels is not new. The family of convolutional Inception models (Szegedy et al., 2015, 2016, 2017) also applied the *split-transform-merge* paradigm, where each network block was separated into a set of independent transformations (channels). These models succeeded to achieve high accuracy at image classification problem. Further, ResNeXt convolutional model in (Xie et al., 2017) generalized this idea to produce NN computational blocks that contain C independent identical transformations, where C is a *cardinality* parameter of NN. The authors showed that increasing *cardinality* instead of width/number of layers can significantly improve the accuracy produced by NN. In context of BD architecture, we have seen a similar trend where increasing number of channels N_B

(which is parallel to C) allows to provide a better approximation of the target pdf density. We demonstrate this in our experiments in Section 12.

Further, a similar architecture was proposed also in (Nesky and Stout, 2018) in the context of the classification, even though it was implemented in a different way. The main motivation of that work was to condense a network size to improve the computational complexity of a NN. The authors showed that by forcing weight matrices to be block-diagonal a significant speedup in time can be achieved with small loss in accuracy. In contrast, in our work we see that such NN structure not only improves runtime and reduces number of weights, but also produces a higher approximation performance.

8.2 NN Pre-Conditioning

It is common practice in Machine Learning to pre-condition a learning algorithm by, for example, whitening and uncorrelating data or performing any other transformation that improves a condition number of the optimization. We also found that such techniques can be valuable for the density estimation task. Specifically, we combine two pre-conditioning methods within our NN $f_{\theta}(X)$: data normalization and NN height bias.

First, we normalize data to have zero mean and unit standard deviation for each dimension i independently, via:

$$\hat{X}_i = \frac{X_i - \mu_i}{\sigma_i},\tag{29}$$

where μ and σ are mean and standard deviation vectors calculated for all available data from target density \mathbb{P}^U .

Second, we bias an initial surface $f_{\theta}(X)$ to coincide with logarithm of the chosen down density $\mathbb{P}^{D}(X)$. We assume that the target surface $\log \mathbb{P}^{U}(X)$ and $\log \mathbb{P}^{D}(X)$ reside on a similar height on average. Thus, to accelerate a convergence we force the initial height of surface $f_{\theta}(X)$ to be identical to log-pdf of \mathbb{P}^{D} . Further, as observed a typical initialization of NN produces the initial surface $f_{\theta}(X) \approx 0$ for all points X. Hence, in order to bias it to the initial height $\log \mathbb{P}^{D}(X)$, we only need to add this log-pdf function to the output of the last layer, $f_{\theta}^{L}(X)$:

$$f_{\theta}(X) = f_{\theta}^{L}(X) + \log \mathbb{P}^{D}(X). \tag{30}$$

Moreover, such NN initialization enforces the logarithm difference $\bar{d}[X, f_{\theta}(X)] \triangleq f_{\theta}(X) - \log \mathbb{P}^{D}(X)$ from Eq. (17) to be zero for all points $X \in \mathbb{R}^{n}$ at beginning of the optimization. Further, considering magnitudes of PSO-LDE in Eqs. (19)-(20), for the above initialization each of $\{M^{U}, M^{D}\}$ will return $2^{-\frac{1}{\alpha}}$ for any point X. Since both $M_{\alpha}^{U}(X, f_{\theta}(X))$ and $M_{\alpha}^{D}(X, f_{\theta}(X))$ have the same value at every point $X \in \mathbb{R}^{n}$, such NN bias produces a properly scaled PSO gradient (see Eq. (1)) at start of the training, which improves the optimization numerical stability. Furthermore, as mentioned above in case the chosen \mathbb{P}^{D} is indeed close to the target \mathbb{P}^{U} , the initial value of the surface $f_{\theta}(X)$ is also close to its final converged form; this in turn increases the convergence rate of PSO-LDE. Further, recently a similar idea was suggested in (Labeau and Allauzen, 2018) specifically for NCE method (PSO-LDE with $\alpha = 1$) in a context of the discrete density estimation for language modeling, where initializing a network according to the noise distribution (parallel to \mathbb{P}^{D} in our work) helped to improve the learned model accuracy.

We perform both techniques inside the computational graph of NN $f_{\theta}(X)$, by adding at the beginning of graph the operation in Eq. (29), and at the end of graph - the operation in Eq. (30).

8.3 Other NN Architecture Aspects

In our experiments we also explored two choices of non-linear activation function to use within NN $f_{\theta}(X)$, Relu and Leaky Relu. We found that both have their advantages and disadvantages. Relu reduces training time by 30% w.r.t. Leaky Relu due to its implicit gradient sparsity, and the converged surface looks more *smooth*. Yet, it often contains mode collapse areas where several modes of \mathbb{P}^U are represented within $f_{\theta}(X)$ by a single hill. On other hand, Leaky-Relu sometimes has artifacts near sharp edges of the target function, that resembles Gibbs phenomenon. Yet, it yields significantly less mode collapses. We argue that these mode collapses are in general caused by the reduced model flexibility, which in case of Relu is induced by more sparse gradients $\nabla_{\theta} f_{\theta}(\cdot)$. The implicit gradient sparsity of Relu, i.e. zero-gradient $\frac{\partial f_{\theta}(X)}{\partial \theta_i} = 0$ for the most part of the weights $\theta_i \in \theta$ at all input points $X \in \mathbb{R}^n$, also reduces number of possible independent gradient vectors at different points, hence in this way increasing the correlation $g_{\theta}(X, X') \triangleq \nabla_{\theta} f_{\theta}(X)^T \cdot \nabla_{\theta} f_{\theta}(X')$ between various (even faraway) points X and X'. This increase can be interpreted as an increase of the kernel bandwidth, which will lead to expressiveness reduction of the model, according to Section 5.5.

Further, residual (skip) connections between different NN layers became very popular in recent NN architectures (He et al., 2016; Szegedy et al., 2017; Xie et al., 2017). Such connections allowed for using deeper neural networks and for the acceleration of learning convergence. Yet, in our work we did not observe any performance improvement from introducing skip connections into NN $f_{\theta}(X)$ with 8 or less layers. Thus, in most part of our experiments we did not employ such shortcuts. The only part where they were used is the Section 12.5 where networks with 14 layers were trained.

Additionally, the Batch Normalization (BN) (Ioffe and Szegedy, 2015) technique was shown in many DL works to stabilize the training process and improve the overall approximation accuracy. However, in our experiments on the density estimation we saw the opposite trend. That is, when BN is combined with PSO density estimators, the outcome is usually worsen than without it.

Finally, dropout (Srivastava et al., 2014) is known to be an useful regularization method to fight the *overfitting*. In our experiment we indeed observed the raise of a side-influence, expressed via values of $g_{\theta}(X, X')$, along with an increase in the dropout probability. Hence, dropout can be considered as a tool to increase side-influence and bias of the estimation, and to reduce its variance. Further, the detailed investigation of dropout affect over $g_{\theta}(X, X')$ is outside of this paper scope.

9. Overfitting of PSO

In this section we will illustrate one of the major challenges involved in training PSO in a small dataset setting - the NN over-flexibility and induced *overfitting*. Likewise, herein we will also discuss possible solutions to overcome this issue.

9.1 Problem Illustration

As was described in (Kopitkov and Indelman, 2018a), the accuracy of the estimated density can be very low for a small dataset setting, since the converged surface can be flat with several peaks at locations of available training data points. This is caused by the fact that apparently we estimate the empirical density of the data which in case of sparse datasets can be represented as a flat surface with several peaks. If the used NN $f_{\theta}(X)$ is overly flexible it can be indeed pushed to such spiky form, as we will demonstrate in this section.

Further, such undesired behavior clearly depends on NN structure and its flexibility, which can be expressed via properties of model kernel $g_{\theta}(X, X')$ such as its influence decay rate. As explained in Section 5.5, $g_{\theta}(X, X')$ acts as a connector of various input space areas, creating the side-influence between these areas which is balancing the overall thermodynamic force at each area. Moreover, as was hypothesized in Section 5.5, with less side-influence various input areas are more independent during the optimization, which in its turn produces a highly flexible NN surface. Below, we will **empirically** observe an evidence supporting this hypothesis.

Furthermore, the size of the available dataset also has its impact, since it is difficult for NN to shape a peak around each training point when there are many such points (yet, it is possible, by using a model with an extreme flexibility where $g_{\theta}(X, X')$ has a very narrow bandwidth). In Figure 9 such overfitting nature of NN surface is illustrated for example where 2D Gaussian distribution is inferred. When the same network is used and the number of samples is decreasing, the outcome is the spiky surface at the end of the optimization.

Onwards, in Figure 10 we can see the experiment where a small dataset of a size 10000 is used for the same pdf inference, and where the number of used layers is decreased. As observed, with less layers the spiky nature of the surface is decreasing due to the reduced NN flexibility/capacity. Similar behavior can also be observed in KDE method in Figure 11 where the bandwidth of Gaussian kernel is increasing. As was proposed in Section 5.5, both KDE and PSO have a similar flexibility behavior, with side-influence level of $g_{\theta}(X, X')$ (e.g. its influence decay rate) and the bandwidth of KDE kernel having the same impact on the converged surface $f_{\theta}(X)$. To stress this point, in Figure 11 we can see that the surface estimated via KDE becomes more and more flexible for a smaller kernel bandwidth, similarly to what we observe in Figure 10.

Moreover, to empirically demonstrate the above point in context of PSO and neural networks, we can analyze the side-influence of $g_{\theta}(X, X')$ for each trained model in Figure 10. For this, we sample $\{X_i\}_{i=1}^{3000}$ testing points from 2D Gaussian and calculate relative side-influence $r_{\theta}(X_i, X_j)$, defined in Eq. (28), for each pair of points. Further, for each pair we also calculate the Euclidean distance $d(X_i, X_j)$.

For $9 \cdot 10^6$ pairs of a relative side-influence $r_{\theta}(X_i, X_j)$ and a Euclidean distance $d(X_i, X_j)$ we construct a histogram in Figure 12. As observed, the relative side-influence is reduced with $d(X_i, X_j)$ - far away points affect each other on much lower level. Further, we can see in left column of Figure 12 a sleeve right from a vertical line d(X', X) = 0 that implies the existence of overall local-support structure of $r_{\theta}(X_i, X_j)$, and existence of some bandwidth of this side-influence. Likewise, we can also see a clear trend between $r_{\theta}(X_i, X_j)$ and the number of NN layers. For shallow networks (see Figures 12g-12h) the relative side-influence is strong even for far away regions. In contrast, in deeper networks (see Figures 12a-12b)

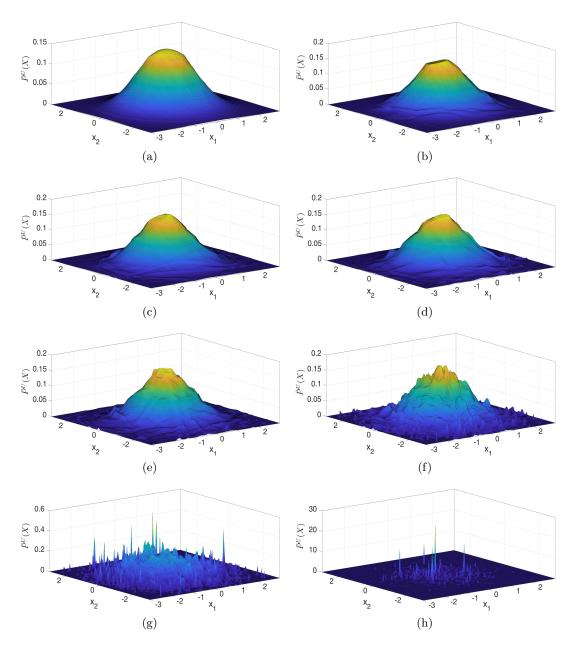


Figure 9: Illustration of PSO overfitting when the training dataset is small. We infer 2D Normal distribution via $\bar{\mathbb{P}}^U(X) = \exp f_{\theta}(X)$ by using PSO-LDE with $\alpha = \frac{1}{4}$ (see Table 2 and Section 6.2). The applied NN architecture is block-diagonal with 6 layers, number of blocks $N_B = 50$ and block size $S_B = 64$ (see Section 8.1). Number of up training points $\{X_i^U\}$ is (a) 10^6 , (b) 10^5 , (c) 80000, (d) 60000, (e) 40000, (f) 20000, (g) 10000 and (h) 1000. As observed, when using the same NN architecture, that is when we do not reduce the flexibility level of the model, the smaller number of training points leads to the spiky approximation. In other words, the converged model will contain a peak around each training sample point.

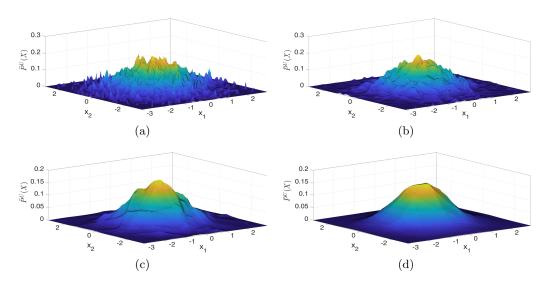


Figure 10: Illustration of decrease in PSO overfitting when the NN flexibility is reduced. We infer 2D Normal distribution via $\bar{\mathbb{P}}^{U}(X) = \exp f_{\theta}(X)$, using only 10000 training samples $\{X_{i}^{U}\}$. The applied loss is PSO-LDE with $\alpha = \frac{1}{4}$ (see Table 2 and Section 6.2). The applied NN architecture is block-diagonal with number of blocks $N_{B} = 20$ and block size $S_{B} = 64$ (see Section 8.1). Number of layers within NN is (a) 5, (b) 4, (c) 3 and (d) 2. As observed, when the number of layers is decreasing, the converged model is more smooth, with less peaks around the training points.

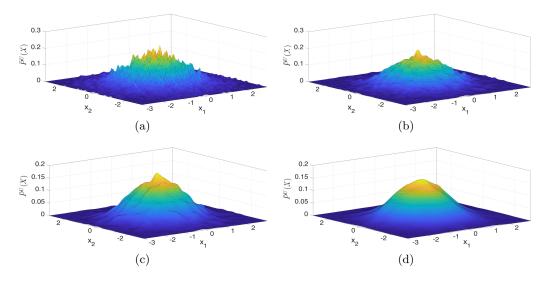


Figure 11: Illustration of decrease in KDE overfitting when the bandwidth h of Gaussian kernel is increased. We infer 2D Normal distribution via KDE, using only 10000 training samples $\{X_i^U\}$. The applied kernel has h equal to (a) 0.04, (b) 0.08, (c) 0.12 and (d) 0.2. As observed, when the bandwidth h is increasing, the converged model is more smooth, with less peaks around the training points. Similar trend is observed for PSO in Figure 10.

 $r_{\theta}(X_i, X_j)$ is centered around zero for pair of far away points, with some close by points having non-zero side-influence. Hence, we can see the obvious relation between the network

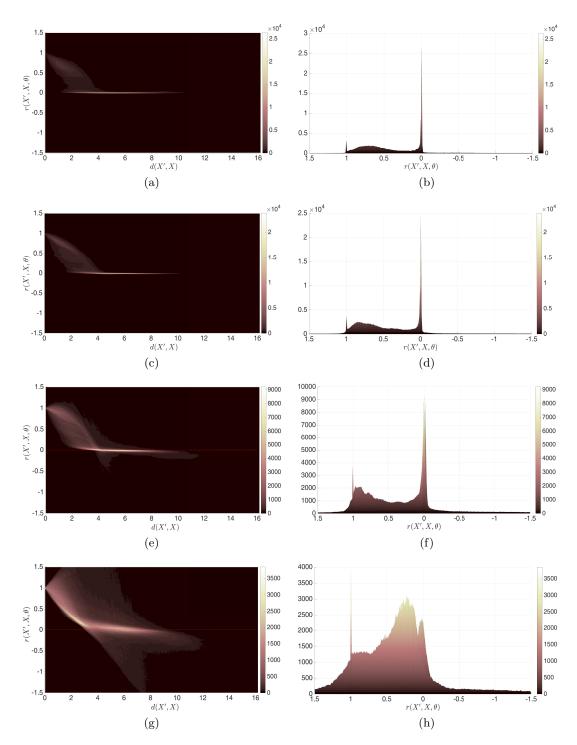


Figure 12: Illustration of NN flexibility and the corresponding side-influence of $g_{\theta}(X, X')$, for each model in Figure 10. We calculate a relative side-influence $r_{\theta}(X_i, X_j)$ and a Euclidean distance $d(X_i, X_j)$ for $9 \cdot 10^6$ point pairs and depict a histogram of obtained $\{r_{\theta}(X_i, X_j)\}$ and $\{d(X_i, X_j)\}$ in left column. Likewise, a side view of this histogram is depicted in right column. Number of layers within NN is (a)-(b) 5, (c)-(d) 4, (e)-(f) 3 and (g)-(h) 2. See more details in the main text.

depth, the bandwidth of gradient similarity and NN flexibility, which supports our current hypothesis that the NN capacity/flexibility is practically defined via the side-influence induced by $g_{\theta}(X, X')$.

Furthermore, optimality of the KDE bandwidth was already investigated in many works (Duong and Hazelton, 2005; Heidenreich et al., 2013; O'Brien et al., 2016; Silverman, 2018) and is known to strongly depend on the number of training data samples. Hence, this implies that the optimal/"desired" influence decay rate of $g_{\theta}(X, X')$ also depends on the size of training dataset, as suggested above and as empirically observed from Figures 9-10.

Remark 26 In Figure 12a we can see that the side-influence between most points is zero, implying that gradients $\nabla_{\theta} f_{\theta}(X_i)$ at different points tend to be orthogonal for a highly flexible model. As observed, there exist some mechanism that enforces this gradient orthogonality during the training (see also Appendix L).

9.2 Possible Solutions

How big the training dataset should be and how to control NN flexibility to achieve the best performance is still an open research question. Some insights can be taken from KDE domain, yet we shall leave it for future investigation. Furthermore, this issue induces a significant challenge for application of PSO density estimators on small datasets, as also other PSO instances. Yet, there are relatively simple regularization methods to reduce such overfitting and to eliminate peaks from the converged surface $f_{\theta}(X)$.

The first method is to introduce a weight regularization term into the loss, such as L2 norm of θ . This will enforce the weight vector to be inside of a ball in the parameter space, thus limiting the flexibility of the NN. Yet, it is unclear what is the exact impact of any specific weight regularization method on the final surface and on properties of $g_{\theta}(X, X')$. Typically, this regularization technique is used in try-and-fail mode, where different norms of θ and term coefficients are applied till a good performance is achieved.

Another arguably more consistent method is data augmentation, which is highly popular in Machine Learning. In context of PSO and its gradient in Eq. (1), we can consider to introduce an additive noise into each sample X^U as:

$$\bar{X}_U = X^U + v$$

where X^U is the original sample from data density $\mathbb{P}^U(X)$ and v is a noise random variable sampled from some density $\mathbb{P}^v(X)$ (e.g. Gaussian distribution). When using \bar{X}_U instead of X^U , we will actually estimate the density of the random variable \bar{X}_U which is the convolution between two densities. Thus, for PSO-LDE the converged surface $f_{\theta}(X)$ will be:

$$f_{\theta^*}(X) = \log \left[\mathbb{P}^{U}(X) * \mathbb{P}^{v}(X) \right],$$

where * defines the convolution operator.

Considering $\mathbb{P}^{v}(X)$ to be Gaussian and recalling that it is a solution of the *heat equation* (Beck et al., 1992), the above equation elucidates the effect of such data augmentation as a simple diffusion of the surface that would be estimated for the original X^{U} . That is, assuming that $f_{\theta}(X)$ would get a spiky form when approximating $\log \mathbb{P}^{U}(X)$, the target density (and thus also the surface approximation) undergoes diffusion in order to yield a

smoother final surface. In case of Gaussian noise, the smoothness depends on its covariance matrix. Yet, the other distributions can be used to perform appropriate convolution and to achieve different diffusion effects. We employ the above technique to improve an inference accuracy under a small training dataset setting in Section 12.3.5.

Remark 27 Additionally, in context of image processing, a typical data augmentation involves image flipping, resizing and introducing various photographic effects (Wong et al., 2016; Perez and Wang, 2017). Such methods produce new samples \bar{X}_U that are still assumed to have the original density $\mathbb{P}^U(X)$, which can be justified by our prior knowledge about the space of all possible images. Given this knowledge is correct, the final estimation is still of $\mathbb{P}^U(X)$ and not of its convolution (or any other operator) with the noise.

10. Additional Applications of PSO

In this section we will demonstrate how the PSO principles can be exploited beyond the (conditional) pdf inference problem. Particularly, we will show how to use PSO for learning mutual information from available data samples.

10.1 Mutual Information Estimation

Mutual information (MI) between two random multi-variable distributions represents correlation between their samples, and is highly useful in the Machine Learning domain (Belghazi et al., 2018). Here we shortly describe possible techniques to learn MI from data, based on PSO principles.

Consider two random variables X and Y with marginal densities \mathbb{P}_X and \mathbb{P}_Y . Additionally, denote by \mathbb{P}_{XY} their joint distribution. The MI between X and Y is defined as:

$$I(X,Y) = \int \int \mathbb{P}_{XY}(X,Y) \cdot R(X,Y) dX dY, \quad R(X,Y) \triangleq \log \frac{\mathbb{P}_{XY}(X,Y)}{\mathbb{P}_{X}(X) \cdot \mathbb{P}_{Y}(Y)}.$$

If ratio R(X,Y) is known/learned in some way, and if we have samples $\{X^i,Y^i\}_{i=1}^N$ from joint density \mathbb{P}_{XY} , we can approximate MI via a sample approximation:

$$I(X,Y) \approx \frac{1}{N} \sum_{i=1}^{N} R(X_i, Y_i).$$

Further, ratio R(X,Y) can be easily learned by one of PSO instances in Tables 2-9 for logarithm density-ratio estimation as follows. Consider a model $f_{\theta}(X,Y): \mathbb{R}^{n_x+n_y} \to \mathbb{R}$. Additionally, we will use $\mathbb{P}_{XY}(X,Y)$ up density in PSO framework, and $\mathbb{P}_{X}(X)\cdot \mathbb{P}_{Y}(Y)$ - as down density. To obtain sample from up density, we can pick random pair from available dataset $\{X^i,Y^i\}_{i=1}^N$, similarly to conditional density estimation in Section 7.1. Further, samples from down density can be acquired by picking X^i and Y^i from dataset independently.

Considering the above sampling procedure, we can apply PSO to push $f_{\theta}(X, Y)$ via up and down forces, using the corresponding magnitude functions. For any particular $\{M^U, M^D\}$ the associated PSO balance state will be:

$$\frac{M^{D}\left[X,Y,f_{\theta}(X,Y)\right]}{M^{U}\left[X,Y,f_{\theta}(X,Y)\right]} = \frac{\mathbb{P}_{XY}(X,Y)}{\mathbb{P}_{X}(X) \cdot \mathbb{P}_{Y}(Y)}.$$

Hence, to produce convergence $f_{\theta}(X,Y) = R(X,Y)$, the appropriate choice of magnitudes must satisfy $\frac{M^D[X,Y,s]}{M^U[X,Y,s]} = \exp s$. For example, $M^U[X,Y,f_{\theta}(X,Y)] = \frac{1}{\exp[f_{\theta}(X,Y)]+1}$ and $M^D[X,Y,f_{\theta}(X,Y)] = \frac{1}{\exp[-f_{\theta}(X,Y)]+1}$ can be used (e.g. variant of logistic loss in Table 5), yet many other alternatives can also be considered. Recently, similar ideas were also presented in (Belghazi et al., 2018).

11. Related work

In this section we consider very different problems all of which involve reasoning about probability density and statistical properties of a given data, which can be also solved by various instances of PSO, as was demonstrated in Section 3. We describe studies done to solve these problems, including both DL and not-DL based methods.

11.1 Parametric vs Non-parametric Approaches

The most traditional probabilistic problem, which is also the main focus of this paper, is density approximation for an arbitrary data. Approaches for statistical density estimation may be divided into two different branches - parametric and non-parametric. Parametric methods assume data to come from a probability distribution of a specific family, and infer parameters of that family, for example via minimizing the negative log-probability of data samples. Non-parametric approaches are distribution-free in the sense that they do not take any assumption over data population a priori. Instead they infer the distribution density totally from data.

The main advantage of the parametric approaches is their statistical efficiency. Given the assumption of a specific distribution family is correct, parametric methods will produce more accurate density estimation for the same number of samples compared to non-parametric techniques. However, in case the assumption is not entirely valid for a given population, the estimation accuracy will be poor, making parametric methods not statistically robust. For example, one of the most flexible distribution families is a Gaussian Mixture Model (GMM) (McLachlan and Basford, 1988). One of its structure parameters is the number of mixtures. Using a high number of mixtures, it can represent multi-modal populations with high accuracy. Yet, in case the real unknown distribution has even higher number of modes, or sometimes even an infinite number, the performance of a GMM will be low.

To handle the problem of unknown number of mixture components in parametric techniques, Bayesian statistics can be applied to model a prior over parameters of the chosen family. Models such as Dirichlet process mixture (DPM) and specifically Dirichlet process Gaussian mixture model (DPGMM) (Antoniak, 1974; Sethuraman and Tiwari, 1982; Görür and Rasmussen, 2010) can represent an uncertainty about the learned distribution parameters and as such can be viewed as infinite mixture models. Although such hierarchical models are more statistically robust (flexible), they still require to manually select a base distribution for DPM, limiting their robustness. Also, Bayesian inference applied in these techniques is more theoretically intricate and computationally expensive (MacEachern and Muller, 1998).

On the other hand, non-parametric approaches can infer distributions of an arbitrary form. Methods such as data histogram and kernel density estimation (KDE) (Scott, 2015;

Silverman, 2018) use frequencies of different points within data samples in order to conclude how a population pdf looks like. In general, these methods require more samples and prone to the curse of dimensionality, but also provide a more robust estimation by not taking any prior assumptions. Observe that "non-parametric" terminology does not implies lack of parametrization. Both histogram and KDE require selection of (hyper) parameters - bin width for histogram and kernel type/bandwidth for KDE which in many cases require the manual parameter search (Silverman, 2018). Although an automatic parameter deduction was proposed in several studies (Duong and Hazelton, 2005; Heidenreich et al., 2013; O'Brien et al., 2016), it is typically computationally expensive and its performance is not always optimal. Moreover, one of the major weaknesses of the KDE technique is its time complexity during the query stage. Even the most efficient KDE methods (e.g. fastKDE, O'Brien et al., 2016) require above linear complexity $(O(m \log m))$ in the number of query points m. In contrast, the PSO methods (DeepPDF and PSO-LDE) are robust non-parametric approaches that can calculate the pdf value of a query point by a single forward pass of a NN. Assuming that such pass is $O(|\theta|)$, query complexity of PSO is $O(m \cdot |\theta|)$, linear in m. When $|\theta| \ll \log m$, PSO methods become much faster alternative when many query points require evaluation. Furthermore, existing KDE implementations do not scale well for data with a high dimension.

11.2 Unsupervised DL and Thermodynamic Optimization

Using NNs for density estimation was studied for several decades (Smolensky, 1986; Bishop, 1994; Bengio and Bengio, 2000; Hinton et al., 2006; Uria et al., 2013). Further, there is a huge amount of work that deals with unsupervised and statistical learning in a similar way to PSO, based on sample frequencies and the optimization energies (forces). Arguably, the first methods were Boltzman machines (BMs) and Restricted Boltzman machines (RBMs) (Ackley et al., 1985; Osborn, 1990; Hinton, 2002). Similarly to PSO, RBMs can learn a distribution over data samples using a thermodynamic equilibrium, and were proved to be very useful for various ML tasks such as dimensionality reduction and feature learning. Yet, they were based on a very basic NN architecture, containing only hidden and visible units, arguably because of over-simplified formulation of the original BM. Moreover, the training procedure of these methods, the contrastive divergence (CD) described in Section 11.7, applies computationally expensive Monte Carlo (MC) sampling. In contrast, PSO-LDE uses samples from an auxiliary distribution \mathbb{P}^D to stabilize pushes from samples of \mathbb{P}^U , which is computationally cheap.

In (Ngiam et al., 2011) authors extended RBMs to Deep Energy Models (DEMs) that contained multiple fully-connected layers, where during training each layer was trained separately via CD. Further, in (Zhai et al., 2016) Deep Structured Energy Based Models were proposed that used fully-connected, convolutional and recurrent NN architectures for an anomaly detection of vector data, image data and time-series data. Moreover, in the latter work authors proposed to train energy based models via a score matching method (Hyvärinen, 2005), which does not require MC sampling. A similar training method was also recently applied in (Saremi et al., 2018) for learning an energy function of data, which is an unnormalized model that is proportional to the real density function. However, the produced by score matching energy function is typically over-smoothed and entirely unnormalized,

with its total integral being arbitrarily far from 1 (see Section 12.3.2). In contrast, PSO-LDE yields a pdf estimation that is almost normalized, with its integral being almost 1 (see Section 12.3.1).

One of the most relevant works to PSO-LDE is noise contrastive estimation (NCE) (Smith and Eisner, 2005; Gutmann and Hyvärinen, 2010), which formulates pdf estimation via binary classification between original data samples and auxiliary noise samples. The derived loss allows for an efficient (conditional) pdf inference and is widely adapted nowadays in the language modeling domain (Mnih and Teh, 2012; Mnih and Kavukcuoglu, 2013; Labeau and Allauzen, 2018). Further, the presented in this paper PSO-LDE can be viewed as a generalization of NCE, where the latter is a specific member of the former for hyper-parameter $\alpha=1$. Yet importantly, both algorithms were derived based on different mathematical principles, and their formulations do not exactly coincide.

Furthermore, the presented herein PSO family is not the first endeavor for unifying different statistical techniques under a single unified framework. In (Pihlaja et al., 2012) authors proposed a family of unnormalized models to infer log-density, which is based on Maximum Likelihood Monte Carlo estimation (Geyer and Thompson, 1992). Their method infers both the energy function of the data and the appropriate normalizing constant. Thus, the produced (log-)pdf estimation is approximately normalized. Further, this work was extended in (Gutmann and Hirayama, 2012) where it was related to the Bregman divergence and where various other statistical methods (e.g. NCE, Gutmann and Hyvärinen, 2010) were shown to be instances of this inference framework. Both of the above frameworks are shown to be strict subsets of PSO, which is proved in Appendices H and I. See also Section 4 for more details about Bregman divergence.

Further, in (Nguyen et al., 2010) and (Nowozin et al., 2016) new techniques were proposed to infer various f-divergences between two densities, based on M-estimation procedure and $Fenchel\ conjugate$ (Hiriart-Urruty and Lemaréchal, 2012). Likewise, the f-GAN framework in (Nowozin et al., 2016) was shown to include many of the already existing GAN methods. In Section 4 we proved it to be also a strict subset of PSO.

The above listed methods, as also the PSO instances in Section 3, are all derived using various math fields, yet they could be easily derived via PSO balance state in Eq. (2). Further, the simplest way to show that PSO is a generalization and not just another perspective that is identical to previous methods is as follows. In most of the above approaches the magnitudes $M^U(\cdot)$ and $M^D(\cdot)$ are equal to the derivative of some other functions, thus they are required to be integrable with a known analytical solution. Whereas in our framework these functions do not have to be integrable at all. Actually, the magnitudes of PSO-LDE in Eq. (19)-(20) do not have a known integral for the general case of any α . Thus, PSO-LDE (and therefore PSO) cannot be viewed as an instance of any previous statistical framework. Moreover, the intuition and simplicity in viewing the optimization as merely point-wise pushes over some virtual surface are very important for investigation of its stability properties and for its applicability in numerous different areas.

11.3 Classification Domain

Considering the image classification domain, convolutional neural networks (CNNs) produce discrete class conditional probabilities (Krizhevsky et al., 2012) for each image. The

typical optimization loss used by classification tasks is a categorical cross entropy of data and label pair, which can also be viewed as an instance of our discovered PSO family (see below). In particular, the classification cross entropy loss can be seen as a variant of the PSO optimization, pushing in parallel multiple virtual surfaces connected by a softmax transformation, that concurrently estimates multiple Bernoulli distributions. These distributions, in their turn, represent one categorical distribution $\mathbb{P}(C|I)$ that models probability of each object class C given a specific image I.

Further, many DL-based methods, such as WaveNet in (Van Den Oord et al., 2016), use such a categorical distribution approach to also model continuous random variables, via discretization of the latter. Yet, there is significant information loss caused by the required data discretization that eventually will limit the approximation accuracy for the continuous target pdf. The proposed herein PSO-LDE and its conditional variant in Section 7.1 solve this problem, providing estimation of any continuous target density, and additionally is conceptually applicable to the discrete setting. Moreover, our presented herein approach infers data distribution in a highly accurate manner without any prior assumption on the target density, and potentially can replace the favored cross-entropy loss.

11.4 Cross-Entropy as Instance of PSO

In this section we will show that the binary cross-entropy loss combined with a sigmoid non-linearity, typical in binary classification problems, is instance of PSO. Further, in Appendix G we extend this setup also to a more general case of softmax cross-entropy. Similarly to a binary sigmoid cross-entropy, a multi-class softmax cross-entropy is shown to be a PSO instance, extended to models with multi-dimensional outputs. Thus, the optimization of multi-class softmax cross-entropy can be seen as pushes of dynamical forces over C different surfaces $\{f_{\theta}(X)_i\}_{i=1}^C$ - the outputs of the model $f_{\theta}(X) \in \mathbb{R}^C$ per each class.

To prove the above point, we derive the binary cross-entropy loss using PSO principles. Define training dataset as set of pairs $\{X_i, Y_i\}_{i=1}^N$ where $X_i \in \mathbb{R}^n$ is data point of arbitrary dimension n (e.g. image) and Y_i is its label - the discrete number that takes values from $\{0, 1\}$. Denote by N_1 and N_0 the number of samples with label 1 and 0 respectively. Further, assume each sample pair to be i.i.d. sampled from an unknown density $\mathbb{P}(X,Y) = \mathbb{P}(X) \cdot \mathbb{P}(Y|X)$. Our task is to enforce the output of $\sigma(f_{\theta}(X))$, the *sigmoid* non-linearity over inner model $f_{\theta}(X)$, to converge to unknown conditional $\mathbb{P}(Y = 1|X)$. Such convergence is equivalent to

$$f_{\theta}(X) = -\log\left[\frac{1}{\mathbb{P}(Y=1|X)} - 1\right] = \log\frac{\mathbb{P}(X,Y=1)}{\mathbb{P}(X,Y=0)} = \log\frac{\mathbb{P}(X|Y=1) \cdot \mathbb{P}(Y=1)}{\mathbb{P}(X|Y=0) \cdot \mathbb{P}(Y=0)}.$$

To apply PSO, we consider $\mathbb{P}(X|Y=1)$ as up density \mathbb{P}^U and $\mathbb{P}(X|Y=0)$ as down density \mathbb{P}^D . Sample batches $\{X_i^U\}_{i=1}^{N_1}$ and $\{X_i^D\}_{i=1}^{N_0}$ from both can be obtained by fetching X_i with appropriate label Y_i . According to Theorem 3 magnitudes must satisfy $\frac{M^D[X,f_{\theta}(X)]}{M^U[X,f_{\theta}(X)]} = \frac{\mathbb{P}(Y=0)\cdot\exp f_{\theta}(X)}{\mathbb{P}(Y=1)}$. One possible choice is:

$$M^{U}[X, f_{\theta}(X)] = \frac{\mathbb{P}(Y=1)}{1 + \exp f_{\theta}(X)}, \quad M^{D}[X, f_{\theta}(X)] = \frac{\mathbb{P}(Y=0) \cdot \exp f_{\theta}(X)}{1 + \exp f_{\theta}(X)}$$
(31)

where the denominator $1+\exp f_{\theta}(X)$ serves as a normalization factor that enforces $\{M^{U}, M^{D}\}$ to be between 0 and 1. Further, above magnitude functions have known antiderivatives:

$$\widetilde{M}^{U}\left[X, f_{\theta}(X)\right] = \mathbb{P}(Y = 1) \cdot \log\left[\sigma(f_{\theta}(X))\right], \ \widetilde{M}^{D}\left[X, f_{\theta}(X)\right] = -\mathbb{P}(Y = 0) \cdot \log\left[1 - \sigma(f_{\theta}(X))\right]$$

that produce the following *PSO functional*:

$$L_{PSO}(f) = - \underset{X \sim \mathbb{P}(X|Y=1)}{\mathbb{E}} \mathbb{P}(Y=1) \cdot \log \left[\sigma(f_{\theta}(X)) \right] - \underset{X \sim \mathbb{P}(X|Y=0)}{\mathbb{E}} \mathbb{P}(Y=0) \cdot \log \left[1 - \sigma(f_{\theta}(X)) \right].$$

Finally, considering $\frac{N_1}{N}$ and $\frac{N_0}{N}$ as estimators of $\mathbb{P}(Y=1)$ and $\mathbb{P}(Y=0)$ respectively, the empirical version of the above loss is:

$$\begin{split} L_{PSO}(f) &\approx -\frac{1}{N_1} \sum_{i=1}^{N_1} \frac{N_1}{N} \cdot \log \left[\sigma(f_{\theta}(X_i^U)) \right] - \frac{1}{N_0} \sum_{i=1}^{N_0} \frac{N_0}{N} \cdot \log \left[1 - \sigma(f_{\theta}(X_i^D)) \right] = \\ &= -\frac{1}{N} \sum_{i=1}^{N} \left[Y_i \cdot \log \left[\sigma(f_{\theta}(X_i)) \right] + \left[1 - Y_i \right] \cdot \log \left[1 - \sigma(f_{\theta}(X_i)) \right] \right], \end{split}$$

where we combine two sums of the first row into a single sum after introducing indicators Y_i and $1 - Y_i$.

The second row is known in Machine Learning community as binary cross-entropy loss. Therefore, we can conclude that PSO instance with magnitudes in Eq. (31) corresponds to cross-entropy when $\mathbb{P}(X|Y=1)$ and $\mathbb{P}(X|Y=0)$ serve as up and down densities respectively. See a similar derivation for multi-class cross-entropy in Appendix G. Therefore, convergence and stability properties of PSO are also applicable for the supervised classification domain which further motivates PSO analysis.

11.5 Other DL-based Density Estimation Techniques

A unique work combining DL and non-parametric inference was done by Baird et al. (Baird et al., 2005). The authors represent a target pdf via Jacobian determinant of a bijective NN that has an implicit property of non-negativity and total integral to be 1. Additionally, their pdf learning algorithm has similarity to our pdf loss described in (Kopitkov and Indelman, 2018a) and which is also shortly presented in Section 6.1. Although the authors did not connect their approach to virtual physical forces that are pushing a model surface, their algorithm can be seen as a simple instance of the more general DeepPDF method that we contributed in our previous work.

Furthermore, the usage of Jacobian determinant and bijective NNs in (Baird et al., 2005) is just one instance of DL algorithm family based on a nonlinear independent components analysis. The methods of this family (Deco and Brauer, 1995; Rippel and Adams, 2013; Dinh et al., 2014, 2016) exploit integration by substitution theorem that provides a mathematical connection between random X's pdf $\mathbb{P}(X)$ and G(X)'s pdf $\mathbb{P}(G(X))$ through Jacobian determinant of the transformation $G(\cdot)$. In case this transformation is done via a NN and given that we know $\mathbb{P}(X)$ of NN's input X, we can calculate in closed form the density of NN's output $\mathbb{P}(G(X))$, which may be required in different applications. However, for the substitution theorem to work the transformation $G(\cdot)$ should be invertible, requiring to

restrict NN architecture of $G(\cdot)$ which significantly limits NN expressiveness. In contrast, the presented PSO-LDE approach does not require any restriction over its NN architecture.

Further, another body of research in DL-based density estimation was explored in (Larochelle and Murray, 2011; Uria et al., 2013; Germain et al., 2015), where the autoregressive property of density functions was employed. The described methods NADE, RNADE and MADE decompose the joint distribution of a multivariate data into a product of simple conditional densities where a specific variable ordering needs to be selected for better performance. Although these approaches provide high statistical robustness, their performance is still very limited since every simple conditional density is approximated by a specific distribution family thus introducing a bias into the estimation. Moreover, the provided solutions are algorithmically complicated. In contrast, in this paper we developed a novel statistically robust and yet conceptually very simple algorithm for density estimation, PSO-LDE.

11.6 Relation to GANs

Recently, Generative Adversarial Networks (GANs) (Goodfellow et al., 2014; Radford et al., 2015; Ledig et al., 2016) became popular methods to generate new data samples (e.g. photorealistic images). GAN learns a generative model of data samples, thus implicitly learning also the data distribution. The main idea behind these methods is to have two NNs, a generator and a critic, competing with each other. The goal of the generator NN is to create new samples statistically similar as much as possible to the given dataset of examples; this is done by transformation G(z) of samples from a predefined prior distribution $z \sim \mathbb{P}^Z$ which is typically a multivariate Gaussian. The responsibility of the critic NN is then to decide which of the samples given to it is the real data example and which is the fake. This is typically done by estimating the ratio between real and fake densities. The latter is performed by minimizing a critic loss, where most popular critic losses (Mohamed and Lakshminarayanan, 2016; Zhao et al., 2016; Mao et al., 2017; Mroueh and Sercu, 2017; Gulrajani et al., 2017; Arjovsky et al., 2017) can be shown to be instances of PSO (see Section 3). Further, both critic and generator NNs are trained in adversarial manner, forcing generator eventually to create very realistic data samples.

Another extension of GAN is Conditional GAN methods (cGANs). These methods use additional labels provided for each example in the training dataset (e.g. ground-truth digit of image from MNIST dataset (LeCun et al., 1998)), to generate new data samples conditioned on these labels. As an outcome, in cGAN methods we can control to some degree the distribution of the generated data, for example by conditioning the generation process on a specific data label (e.g. generate an image of digit "5"). Similarly, we can use such a conditional generative procedure in robotics where we would like to generate future measurements conditioned on old observations/current state belief. Moreover, cGANs are also members of PSO framework as demonstrated in Section 7.1.

Further, it is a known fact that optimizing GANs is very unstable and fragile, though during the years different studies analyzed various instability issues and proposed techniques to handle them (Arjovsky and Bottou, 2017). In (Radford et al., 2015), the authors proposed the DCGAN approach that combines several stabilization techniques such as the batch normalization and Relu non-linearity usage for better GAN convergence. Further

improvement was done in (Salimans et al., 2016) by using a parameter historical average and statistical feature matching. Additionally, in (Arjovsky and Bottou, 2017) it was demonstrated that the main reason for instability in training GANs is the density support difference between the original and generated data. While this insight was supported by very intricate mathematical proofs, we came to the same conclusion in Section 5 by simply applying equilibrium concepts of PSO. As we showed, if there are areas where only one of the densities is positive, the critic's surface is pushed by virtual forces to infinity, causing the optimization instability (see also Figure 3). Moreover, in our analysis we detected another significant cause for optimization instability and inaccuracy - the side-effect produced by gradient similarity $g_{\theta}(X, X')$. In our experiments in Section 12 this side-influence is shown to be one of the biggest factors for a high approximation error of PSO. Moreover, in this paper we show that there is a strong analogy between $q_{\theta}(X, X')$ and the kernel applied in KDE algorithms. Considering KDE, low/high values of kernel bandwidth h can lead to both underfitting and overfitting, depending on the number of training samples. We show the same to be correct also for PSO and the bandwidth of $q_{\theta}(X, X')$. See more details in Sections 9 and 12.

11.7 PSO with Unit Magnitudes

The PSO instance with unit magnitudes $M^U[X, f_{\theta}(X)] = M^D[X, f_{\theta}(X)] = 1$ can be frequently met in Machine Learning (ML) literature. For example, Integral Probability Metrics (IPMs) (Müller, 1997), contrastive divergence (CD) (Hinton, 2002), Maximum Mean Discrepancy (MMD) (Gretton et al., 2007) and critic of the Wasserstein GAN (Arjovsky et al., 2017) all rely on this loss to measure some distance between densities \mathbb{P}^U and \mathbb{P}^D . In this section we will explore this simple loss

$$L_{simple}(f_{\theta}) = - \underset{X \sim \mathbb{P}^{U}}{\mathbb{E}} f_{\theta}(X) + \underset{X \sim \mathbb{P}^{D}}{\mathbb{E}} f_{\theta}(X)$$
(32)

in a context of the derived PSO.

By following the derivation from Section 5, we can see that given a flexible enough surface $f_{\theta}(X)$ (e.g. typical NN) the straight forward optimization via *simple* loss in Eq. (32) will diverge since forces $F_U(X) = \mathbb{P}^U(X)$ and $F_D(X) = \mathbb{P}^D(X)$ are independent of θ and cannot adapt to each other. That is, balance state $F_U(X) = F_D(X)$ can not be achieved by the simple loss. It can be shown that the surface $f_{\theta}(X)$ will be pushed to ∞ at points $\{X : \mathbb{P}^U(X) > \mathbb{P}^D(X)\}$, and to $-\infty$ at $\{X : \mathbb{P}^U(X) < \mathbb{P}^D(X)\}$, up to the surface flexibility. During such optimization, training will eventually fail due to numerical instability that involves too large/small numbers. Furthermore, this point can be easily verified in practice by training NN with loss in Eq. (32).

One way to enforce the convergence of *simple* loss is by adapting/changing density \mathbb{P}^D towards \mathbb{P}^U along the optimization. Indeed, this is the main idea behind the CD method presented in (Hinton, 2002) and further improved in (Ngiam et al., 2011) and (Liu and Wang, 2017). In CD, the model distribution $\hat{\mathbb{P}}^U_{\theta}(X) \triangleq \exp[f_{\theta}(X)]/\int \exp[f_{\theta}(X')]dX'$ is used as *down* density in PSO framework. At each iteration, $\{X_i^D\}_{i=1}^{N^D}$ are sampled from $\hat{\mathbb{P}}^U_{\theta}(X)$ by Gibbs sampling (Hinton, 2002), Monte Carlo with Langevin dynamics (Hyvarinen, 2007), Hybrid Monte Carlo sampling (Ngiam et al., 2011), or Stein Variational Gradient Descent (SVGD) (Liu and Wang, 2017, 2016). Thus, in these methods instead of adapting the

magnitudes $M^U[X, f_{\theta}(X)]$ and $M^D[X, f_{\theta}(X)]$ to each other we constrain down density \mathbb{P}^D to be $\mathbb{P}^D(X) \approx \hat{\mathbb{P}}^U_{\theta}(X)$. The dynamics of such optimization will converge to the equilibrium only when $\mathbb{P}^U(X) = \hat{\mathbb{P}}^U_{\theta}(X)$ which will also lead to $\exp[f(\cdot)] \propto \mathbb{P}^U(X)$. Hence, in CD algorithm the up and down forces are adapted to each other via their frequency components while their analytical components stay constant.

Further, we consider the relation between PSO concepts and Wasserstein GAN (Arjovsky et al., 2017) (WGAN) which has been recently proposed and is considered nowadays to be state-of-the-art. Apparently, the critic's loss in WGAN is exactly Eq. (32). It pushes the surface $f_{\theta}(X)$ up at points sampled from the real data distribution \mathbb{P}^{U} , and pushes down at points sampled from the generator density \mathbb{P}^{D}_{ϕ} , which is an implicit distribution of fake samples that are returned by the generator from the latent space z, with ϕ being a generator parametrization. The critic's loss of WGAN was chosen as proxy to force critic's output to approximate Earth Mover (Wasserstein) distance between \mathbb{P}^{U} and \mathbb{P}^{D}_{ϕ} . Specifically, the simple loss is a dual form of Wasserstein distance under constraint that $f_{\theta}(X)$ is 1-Lipschitz continuous. Intuitively, the critic network will return high values for samples coming from \mathbb{P}^{U}_{ϕ} , and low values for samples coming from \mathbb{P}^{D}_{ϕ} , thus it learns to deduce when its input is sampled from \mathbb{P}^{U} and when it is sampled from \mathbb{P}^{D}_{ϕ} . Once critic's optimization stage ends, the generator of WGAN tries to optimize its weights ϕ in order to increase $f_{\theta}(X)$'s output for samples coming from \mathbb{P}^{D}_{ϕ} via

$$L_{WGAN}^{G}(\phi, X^{D}) = - \mathop{\mathbb{E}}_{X \sim \mathbb{P}_{\phi}^{D}} f_{\theta}(X).$$

The described above "infinity" divergence of simple loss and 1-Lipschitz constraint may explain why the authors needed to clip NN weights to stabilize the approach's learning. In (Arjovsky et al., 2017) after each iteration the NN weights are constrained to be between [-c,c] for some constant c; likely such handling reduces flexibility of surface $f_{\theta}(X)$, thus preventing it from getting too high/low output values. Such conclusion about reduced flexibility is also supported by (Gulrajani et al., 2017). Further, in (Gulrajani et al., 2017) authors prove that 1-Lipschitz constraint of WGAN implies that the surface has gradient (w.r.t. X) with norm at most 1 everywhere, $\left\|\frac{\partial f_{\theta}(X)}{\partial X}|_{\theta=\theta^*}\right\|=1$. Instead weight clipping, they proposed to combine the simple loss with a X-gradient penalty term that forces this gradient norm to be close to 1. The effect of such regularization can be explained as follows. Considering the PSO principles, the optimal surface for the simple loss has areas of $+\infty$ and $-\infty$, thus requiring sharp slopes between these areas. The gradient penalty term constrains these slopes to be around 1, hence it prevents the surface from getting too high/low, solving in this way the "infinity" oscillations. Overall, by using weight clipping and other regularization techniques like gradient penalty (Gulrajani et al., 2017), WGAN is in general highly successful in data generation task. Thus, we can see that basically unstable PSO instance with unit magnitudes can be stabilized by a surface flexibility restriction via appropriate regularization terms within the loss.

Finally, MMD algorithm (Gretton et al., 2007) exploits the simple loss in Eq. (32) to test if two separate datasets are generated from the same distribution. Authors express this loss via RKHS function with a bounded norm, thus implicitly enforcing the model smoothness and eliminating the $infinite\ height$ problem.

Remark 28 Interestingly, as was observed empirically on 20D data, even the prolonged GD optimization via the above simple loss in Eq. (32) leaves the randomly initialized NN surface $f_{\theta}(X)$ almost unchanged for a case when $\mathbb{P}^{U}(X) = \mathbb{P}^{D}(X)$. This is due to the implicit force balance produced by the identical densities. In contrast, when densities are different the optimization diverges very fast, after only a few thousands of iterations. Also, the optimization gradient during these iterations is typically smaller for the same density scenario than for the different densities. Similarly to MMD method, such behavior can be exploited for example to test if samples from two datasets have the same density or not.

Overall, all of the above PSO instances with unit magnitudes, except for CD, handle the instabilities of simple loss by restricting the flexibility of the model $f_{\theta}(X)$. Thus, a typical strategy is to enforce K-Lipschitz constraint. Yet, in context of DL it is still unclear if and how it is possible to enforce a model to be exact K-Lipschitz, even though there are several recently proposed techniques for this (Gulrajani et al., 2017; Petzka et al., 2017; Miyato et al., 2018; Zhou et al., 2018).

11.8 Relation to Maximum Likelihood Estimation

Finally, since most of density estimation algorithm rely on MLE, below we establish the relation between MLE and PSO procedures. Particularly, we derive MLE approach from principles of PSO. In this setting we have a batch of i.i.d. samples $\{X_i^U\}_{i=1}^{N^U}$ sampled from density \mathbb{P}^U , whose pdf we aim to estimate. Consider an auxiliary distribution \mathbb{P}^D with analytically known pdf $\mathbb{P}^D(X)$ that satisfies $\mathbb{S}^U \subseteq \mathbb{S}^D$, and define PSO functional as:

$$L_{PSO}(f) = - \underset{X \sim \mathbb{P}^U}{\mathbb{E}} \left[1 + \log f(X) \right] + \underset{X \sim \mathbb{P}^D}{\mathbb{E}} \frac{f(X)}{\mathbb{P}^D(X)}$$

whose *magnitude* functions are:

$$M^{U}[X, f(X)] = \frac{1}{f(X)}, \quad M^{D}[X, f(X)] = \frac{1}{\mathbb{P}^{D}(X)}.$$
 (33)

Define the hypothesis class \mathcal{F} with functions that are positive on \mathbb{S}^U so that $\log f(X)$ is properly defined for all $f \in \mathcal{F}$ and $X \in \mathbb{S}^U$. Then, the optimal $f^* = \arg \min_{f \in \mathcal{F}} L_{PSO}(f)$ will satisfy PSO balance state in Eq. (2) which yields $f^*(X) = \mathbb{P}^U(X)$.

Furthermore, in case \mathcal{F} is a space of positive functions whose total integral is equal to 1 (i.e. probability measure space), the above loss can be reduced to:

$$L_{PSO}(f) = \int -\mathbb{P}^{U}(X) \cdot [1 + \log f(X)] + f(X)dX = -\underset{X \sim \mathbb{P}^{U}}{\mathbb{E}} \log f(X), \tag{34}$$

where we apply an equality $\int \mathbb{P}^U(X)dX = \int f(X)dX$ since f is normalized. Note that limiting \mathcal{F} to be a probability measure space does not affect the *balance state* of PSO since the optimal solution f^* is also a probability measure. Further, considering the thermodynamical perspective of PSO such choice of \mathcal{F} has an implicit regularization affect, removing a need for the *down* force F_{θ}^D in order to achieve a force equilibrium over the surface f(X).

The loss in Eq. (34) and its empirical variant $L_{PSO}(f) \approx -\frac{1}{N^U} \sum_{i=1}^{N^U} \log f(X_i^U)$ define the standard MLE estimation. Therefore, we can conclude that PSO with magnitudes defined

in Eq. (33) corresponds to MLE when the auxiliary distribution \mathbb{P}^U is absolutely continuous w.r.t. \mathbb{P}^D and when each $f \in \mathcal{F}$ is a normalized function. Likewise, such relation can also be explained by the connection between PSO and Kullback-Leibler (KL) divergencies shown in Section 4.

12. Experimental evaluation

Below we report several experimental scenarios that demonstrate the efficiency of the proposed PSO algorithm family, and also show empirical validity of the assumptions taken during the PSO derivation/analysis. Concretely, in Section 12.2 we show that the first-order Taylor approximation of the surface differential is actually very accurate in practice. Further, in Section 12.3 we apply PSO to infer a pdf of 20D Columns distribution, where in sub-section 12.3.1 we compare between various PSO instances; in 12.3.2 we experiment with state-of-the-art baselines and compare their accuracy with PSO-LDE; in 12.3.3 we evaluate the pdf inference performance for different NN architectures; in 12.3.4 we investigate the impact of a batch size on PSO performance; and in 12.3.5 we show how different sizes of training dataset affect inference accuracy and explore different techniques to overcome difficulties of a sparse dataset setting. Furthermore, in Section 12.4 we perform pdf inference over the more challenging distribution Transformed Columns and in Section 12.5 we apply our pdf estimation approach over 3D densities generated from pixel landscape of RGB images.

Importantly, our main focus in this paper is to introduce a novel paradigm for inferring various statistics of an arbitrary data in a highly accurate and consistent manner. To this end and concretely in context of density estimation, we are required to demonstrate **quantitatively** that the converged approximation $\bar{\mathbb{P}}_{\theta}(X)$ of the pdf function $\mathbb{P}(X)$ is indeed very close to its target. Therefore, we avoid experiments on real datasets (e.g. MNIST, LeCun et al. (1998)) since they lack information about the true pdf values of the samples. Instead, we generate datasets for our experiments from analytically known pdf functions, which allows us to evaluate the *ground truth* error between $\bar{\mathbb{P}}_{\theta}(X)$ and $\mathbb{P}(X)$. However, all selected pdf functions are highly multi-modal and therefore are very challenging to infer.

Likewise, in this work we purposely consider vector datasets instead of image data, to decouple our main approach from complexities coming with images and CNN networks. Our main goal is to solve general unsupervised learning, and we do not want it to be biased towards spatial data. Moreover, vector data is mostly neglected in modern research and our method together with the new BD architecture addresses this gap.

12.1 Learning Setup

All the pdf inference experiments were done using Adam optimizer (Kingma and Ba, 2014) since it showed better convergence rate compared to stochastic GD. Note that replacing GD with Adam does not change the target function approximated by PSO estimation. The used Adam hyper-parameters are $\beta_1 = 0.75$, $\beta_2 = 0.999$ and $\epsilon = 10^{-10}$. Each experiment optimization is performed for 300000 iterations, which typically takes about one hour to run on a GeForce GTX 1080 Ti GPU card. The batch size is $N^U = N^D = 1000$. During each iteration next batch of up points $\{X_i^U\}_{i=1}^{1000}$ is retrieved from the training dataset, and next batch of down points $\{X_i^D\}_{i=1}^{1000}$ is sampled from down density \mathbb{P}^D . For Columns distribution

in Section 12.3 we use a Uniform distribution as \mathbb{P}^D . Next, the optimizer updates the weights vector θ according Eq. (1), where the magnitude functions are specified according to a specific PSO instance. The applied learning rate is 0.0035. We keep it constant for first 40000 iterations and then exponentially decay it down to a minimum learning rate of $3 \cdot 10^{-9}$. Further, in all our models we use Leaky-Relu as a non-linearity activation function. Additionally, weights are initialized via popular Xavier initialization (Glorot and Bengio, 2010). Each model is learned 5 times; we report its mean accuracy and the standard deviation. Further, PSO implementation, based on TensorFlow framework, can be accessed via open source library https://bit.ly/2AMwyJT.

To evaluate performance and consistency of each learned model, we calculate three different errors over testing dataset $\{X_i^U\}_{i=1}^N$, where each point was sampled from \mathbb{P}^U and N is 10^5 . First one is pdf squared error $PSQR = \frac{1}{N} \sum_{i=1}^N \left[\mathbb{P}^U(X_i^U) - \bar{\mathbb{P}}_{\theta}(X_i^U) \right]^2$, with $\bar{\mathbb{P}}_{\theta}(\cdot)$ being the pdf estimator produced by a specific model after an optimization convergence. Further, since we deal with high-dimensional data, PSQR involves operations with very small numbers. To prevent inaccuracies caused by the computer precision limit, the second used error is \log -pdf squared error $LSQR = \frac{1}{N} \sum_{i=1}^{N} \left[\log \mathbb{P}^U(X_i^U) - \log \bar{\mathbb{P}}_{\theta}(X_i^U) \right]^2$. Since in this paper we target $\log \mathbb{P}(\cdot)$ in the first place, the LSQR error expresses a distance between the data log-pdf and the learned NN surface $f_{\theta}(\cdot)$. Moreover, LSQR is related to statistical divergence between \mathbb{P}^U and $\bar{\mathbb{P}}_{\theta}$ (see more details in Appendix J).

Further, the above two errors require to know ground truth for their evaluation. Yet, in real applications such ground truth is not available. To overcome this problem and to measure model performance in real applications, we propose to use the loss of Importance Sampling from Table 2, $IS = -\frac{1}{N} \sum_{i=1}^{N} f_{\theta}(X_{i}^{U}) + \frac{1}{N} \sum_{i=1}^{N} \frac{\exp[f_{\theta}(X_{i}^{D})]}{\mathbb{P}^{D}(X_{i}^{D})}$, where $\{X_{i}^{D}\}_{i=1}^{N}$ are i.i.d. samples from \mathbb{P}^{D} . As we will see, while IS is less accurate than the ground truth errors, it still a reliable indicator for choosing the best member from a set of learned models. Additionally, during the optimization IS is correlated with the real error and if required can be used to monitor current convergence and to allow an early stop evaluation.

Remark 29 Note that unlike typical density estimator evaluation, herein we do not use information-theoretic performance metrics such as perplexity (Jelinek et al., 1977) and various kinds of f-divergences, or negative-likelihood scores. This is because the PSO-learned models are only approximately normalized, while information-theoretic metrics typically require strictly normalized models for their metric consistency. Still, both PSQR and LSQR are mean squared errors between target and approximation functions, and are similar to other performance metrics that are widely applied in regression problems of Machine Learning domain.

12.2 Differential approximation

In this section we will empirically justify our approximation in Eq. (7), where we assumed that surface differential, caused by GD update of weights θ , can be approximated via its first-order Taylor expansion.

For this purpose we performed a single iteration of GD optimization and measured the real and the estimated differentials at train and test points as following. First, points $D = \{X^i\}_{i=1}^{2000}$ were sampled from \mathbb{P}^U density, which is Columns distribution from Section

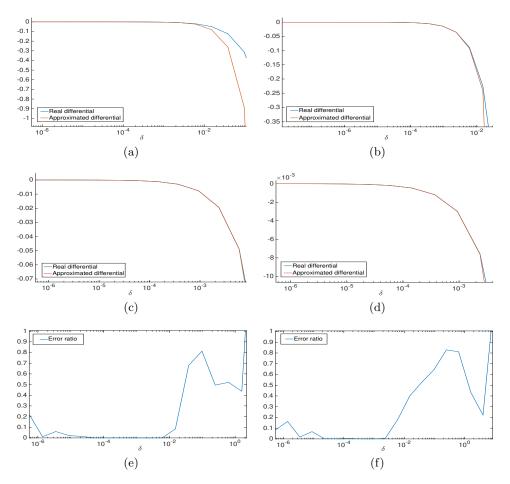


Figure 13: Real and approximated differentials for training point X_{train} (a)-(c)-(e) and testing point X_{test} (b)-(d)-(f). (a)-(b) Real differential (blue line) vs approximated differential (red line), as a function of the learning rate δ ; (c)-(d) Zoom-in of (a)-(b); (e)-(f) Error ratio, defined in Eq. (36).

12.3, where $X^i \in \mathbb{R}^n$ with n = 20. Further, we performed a single GD iteration of the following loss:

$$L(\theta, D) = -\frac{1}{1000} \sum_{i=1}^{1000} f_{\theta}(X^{i}) + \frac{1}{1000} \sum_{i=1001}^{2000} f_{\theta}(X^{i}),$$

where $f_{\theta}(X)$ is a FC network depicted in Figure 7a, with overall 4 layers of size 1024 each. Next, we measured the surface height $f_{\theta}(X)$ at two points X_{train} and X_{test} before and after GD update, where $X_{train} \in D$ and $X_{test} \notin D$. We performed this procedure for a range of learning rate values and thus obtained the real differential $df_{\theta}(X)$ at X_{train} and X_{test} as a function of δ (see Figure 13).

Next, we calculated the approximated differential $\bar{d}f(X)$ at X_{train} and X_{test} using first-order Taylor expansion as:

$$\bar{d}f(X) = \frac{\delta}{1000} \cdot \frac{\partial f_{\theta}(X)}{\partial \theta}^{T} \cdot \left[\sum_{i=1}^{1000} \frac{\partial f_{\theta}(X^{i})}{\partial \theta} - \sum_{i=1001}^{2000} \frac{\partial f_{\theta}(X^{i})}{\partial \theta} \right] =
= \frac{\delta}{1000} \cdot \left[\sum_{i=1}^{1000} g(X, X^{i}, \theta) - \sum_{i=1001}^{2000} g(X, X^{i}, \theta) \right], \quad (35)$$

where θ is taken at time before GD update.

In Figures 13a and 13b we can see the calculated differentials for both X_{train} and X_{test} , respectively. In both figures the real differential (blue line) and the estimated differential (red line) become very close to each other for $\delta < 0.01$. Recall that for the most part of the typical optimization process this condition stays true.

Further, in Figures 13e (for X_{train}) and 13f (for X_{test}) we can see the ratio:

$$ratio = \left| df_{\theta}(X) - \bar{d}f(X) \right| / \left| df_{\theta}(X) \right|, \tag{36}$$

which expresses an error $|df_{\theta}(X) - \bar{d}f(X)|$ as the percentage from the real differential. As can be seen, for both X_{train} and X_{test} the error ratio is very low for $\delta < 0.01$ (under 10% for most part). Additionally, the error ratio slightly increases for a very small δ (around 10^{-6}). We speculate this to be a precision artifact, since calculation of approximated differential in Eq. (35) was done in a single-precision floating-point format (float32) and involved multiplication by a very small number δ .

Additionally, we calculated the real and approximated differentials along the entire GD optimization process of PSO-LDE, where the same NN architecture was used as in the first experiment, and where the pdf inference was applied to Columns distribution from Section 12.3. Particularly, we trained a NN for 300000 iterations, while during each iteration we computed the real and the approximated differentials for a specific test point X. We performed such simulation twice, for two different points and plotted their differentials in Figure 14. In the left column, the blue line is the absolute value of the real differential, $|df_{\theta}(X)|$, and the red line is error $|df_{\theta}(X) - \bar{d}f(X)|$, both smoothed via moving mean with window size 300. The right column shows the ratio between smoothed $|df_{\theta}(X) - \bar{d}f(X)|$ and smoothed $|df_{\theta}(X)|$, $|df_{\theta}(X) - \bar{d}f(X)| / |df_{\theta}(X)|$, which can be seen as the error percentage from the real differential. As shown in Figures 14b and 14d, this error percentage is less than 15% and for most part of the training is even lower. This trend is the same for both verified points, suggesting that the real differential indeed can be approximated very closely by the first-order Taylor expansion.

In overall, above we showed that most of the surface change can be explained by the gradient similarity $g_{\theta}(X, X')$ in Eq. (7).

12.3 PDF Estimation via PSO - Columns Distribution

In this Section we will infer a 20D Columns distribution from its sampled points, using various PSO instances and network architectures. The target pdf here is $\mathbb{P}^{U}(X) = \mathbb{P}^{Clmns}(X)$

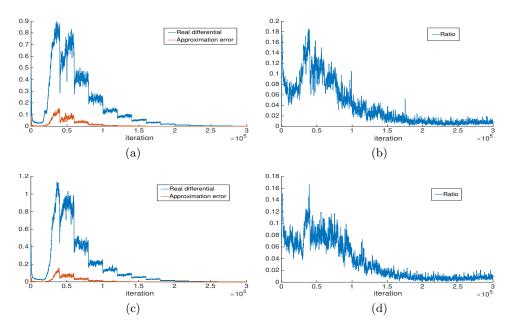


Figure 14: The real differential and the approximation error during the training of PSO-LDE for two different testing points X_1 and X_2 . (a)-(b) Results for X_1 . (c)-(d) Results for X_2 . (a)-(c) Blue line is an absolute value of real differential at specific point for each iteration time, smoothed via moving mean with window size 300; red line is absolute value of difference between real differential and the approximated one, smoothed via moving mean of the same window size. (b)-(d) Ratio between two lines in (a)-(c), can be seen as moving mean version of Eq. (36) - an error as the percentage of the real differential.

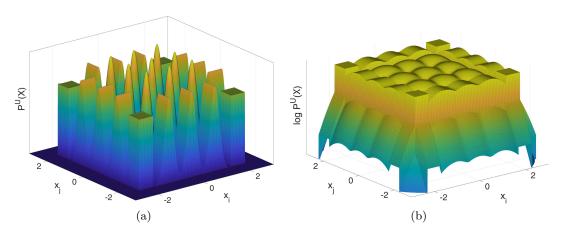


Figure 15: (a) Illustration of *Columns* distribution. Every slice of its pdf function $\mathbb{P}(x_i, x_j) = \mathbb{P}^U(0, \dots, 0, x_i, 0, \dots, 0, x_j, 0, \dots, 0)$ in Eq. (37) contains 25 modes of different shape. Overall, this distribution has 5^{20} modes. (b) Logarithm of pdf slice in (a) that will be learned via NN surface.

and is defined as:

$$\mathbb{P}^{Clmns}(x_1, \dots, x_{20}) = \prod_{i=1}^{20} p(x_i), \tag{37}$$

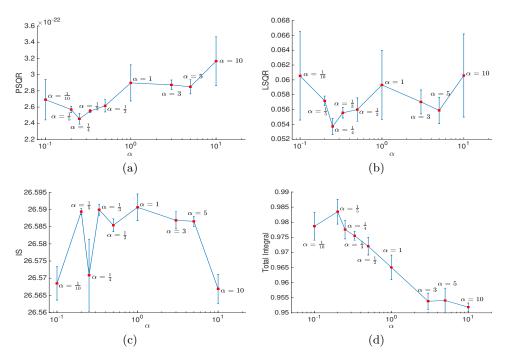


Figure 16: Evaluation of PSO-LDE for estimation of Columns distribution, where NN architecture is block-diagonal with 6 layers, number of blocks $N_B = 50$ and block size $S_B = 64$ (see Section 8.1). For different values of hyper-parameter α , (a) PSQR, (b) LSQR and (c) IS are reported, along with their empirical standard deviation. Here, IS is less correlated with ground truth errors since all models are very close to each other, providing highly accurate estimation. (d) Estimators of total integral $TI = \int \bar{\mathbb{P}}_{\theta}(X) dX$ of learned models for each value of α . For a specific learned model $\bar{\mathbb{P}}_{\theta}(X)$ this integral is estimated through importance sampling as $\overline{TI} = \sum_{i=1}^{N} \frac{\bar{\mathbb{P}}_{\theta}(X_i^D)}{\mathbb{P}^D(X_i^D)}$ over $N = 10^8$ samples from down density \mathbb{P}^D . Note that such estimator is consistent, with $TI = \overline{TI}$ for $N \to \infty$.

where $p(\cdot)$ is a 1D mixture distribution with 5 components $\{Uniform(-2.3, -1.7), \mathcal{N}(-1.0, std = 0.2), \mathcal{N}(0.0, std = 0.2), \mathcal{N}(1.0, std = 0.2), Uniform(1.7, 2.3)\}$; each component has weight 0.2. This distribution has overall $5^{20} \approx 9.5 \cdot 10^{13}$ modes, making the structure of its entire pdf surface very challenging to learn. For the illustration see Figure 15a.

First, we evaluate the proposed density estimation methods under the setting of infinite training dataset, with number of training points being 10⁸. Later, in Section 12.3.5 we will investigate how a smaller dataset size affects the estimation accuracy, and propose various techniques to overcome issues of sparse data scenario.

12.3.1 PSO Instances Evaluation

Here we perform pdf learning using different PSO instances, and compare their performance. The applied NN architecture is block-diagonal from Section 8.1, with 6 layers, number of blocks $N_B = 50$ and block size $S_B = 64$.

PSO-LDE and α First, we apply the PSO-LDE instances from Section 6.2, where we try various values for the hyper-parameter α . In Figure 16 we can see all three errors for

different α . All models produce highly accurate pdf estimation, with average LSQR being around 0.057. That is, the learned NN surface $f_{\theta}(X)$ is highly close to the target $\log \mathbb{P}^{U}(X)$. Further, we can see that some α values (e.g. $\alpha = \frac{1}{4}$) produce slightly better accuracy than others. This can be explained by smoother magnitude dynamics with respect to logarithm difference \bar{d} from Eq. (17), that small values of α yield (see also Section 6.2). Note that here IS error is not very correlative with ground truth errors PSQR and LSQR since the accuracy of all models is very similar and IS is not sensitive enough to capture the difference.

Further, we also estimate the total integral $TI = \int \bar{\mathbb{P}}_{\theta}(X) dX$ for each learned model via importance sampling. In Figure 16d we can see that the learned models are indeed very close to be *normalized*, with estimated total integral being on average 0.97 - very close to the proper value 1. Note that in our experiments the model normalization was not enforced in any explicit way, and PSO-LDE achieved it via its implicit normalization objective.

Furthermore, in Figure 16d it is also shown that smaller values of α are more properly normalized, which also correlates with the approximation error. That is, in Figure 16a the same models with smaller α are shown to have a lower error. We argue that further approximation improvement (e.g. via better NN architecture) will also increase the normalization quality of the produced models.

Moreover, in Figure 17a we can see a slice of the learned $\exp f_{\theta}(X)$ for the first two dimensions, where the applied PSO instance was PSO-LDE with $\alpha = \frac{1}{4}$. As observed, it is highly close to the real pdf slice from Figure 15a. In particular, all modes and their shapes (within this slice) were recovered during learning. Further, in Figure 17b we can observe the learned surface height $f_{\theta}(X)$ and ground truth height $\log \mathbb{P}^{U}(X)$ for sample points from \mathbb{P}^{U} and \mathbb{P}^{D} . As shown, there are approximation errors at both X^{U} and X^{D} , with down points having bigger error than up points. As we will see below, these errors are related to the norm of θ gradient at each point.

Additionally, in Figure 17b we can see an asymmetry of error w.r.t. horizontal line $\log \mathbb{P}^D(X) = -30.5$, where points above this line (mostly blue points) have a NN height $f_{\theta}(X)$ slightly lower than a target $\log \mathbb{P}^U(X)$, and points below this line (mostly red points) have a NN height $f_{\theta}(X)$ slightly higher than target $\log \mathbb{P}^U(X)$. This trend was observed in all our experiments. Importantly, this error has to be related to an estimation bias (and not an variance), since the considered herein setting is of infinite dataset setting where an estimation variance is in theory insignificant.

Further, we speculate that the reason for such bias can be explained as follows. The points above this horizontal line have a positive logarithm difference $\bar{d} = f_{\theta}(X) + 30.5$ defined in Eq. (17), $\bar{d} \geq 0$, whereas points below this line have a negative $\bar{d} \leq 0$. From the relation between \bar{d} and magnitude functions, discussed in Section 6.2, we know that within "above" points the up magnitude $M^{U}(\cdot)$ is on average smaller than down magnitude $M^{D}(\cdot)$. The opposite trend can be observed within "below" points. There $M^{D}(\cdot)$ has smaller values relatively to $M^{U}(\cdot)$. Thus, the surface parts above this horizontal line have large down magnitudes, while parts below the line have large up magnitudes, which in its turn creates a global side-influence forces that come from these two regions. Finally, these global side influences generate this asymmetric error with $\log \mathbb{P}^{D}(X) = -30.5$ being the center of the pressure. Likewise, we argue that this asymmetric tendency can be reduced by selecting \mathbb{P}^{U} and \mathbb{P}^{D} densities that are closer to each other, as also enhancing NN architecture to be more flexible, with side-influence between far away regions being reduced to zero. In fact, we

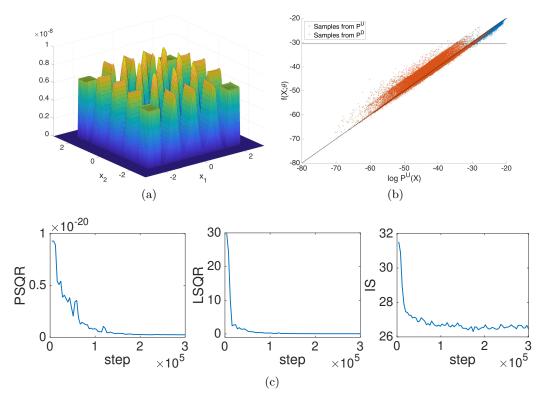


Figure 17: Learned pdf function of Columns distribution by PSO-LDE with $\alpha = \frac{1}{4}$, where NN architecture is block-diagonal with 6 layers, number of blocks $N_B=50$ and block size $S_B=50$ 64 (see Section 8.1). (a) Illustration of learned pdf function. The depicted slice is $\mathbb{P}(x_1, x_2) =$ $\mathbb{P}^U(x_1, x_2, 0, \dots, 0)$, with x_1 and x_2 forming grid of points in first two dimensions of the density's support. As can be seen, all modes (within first two dimensions) and their appropriate shapes are recovered. (b) Illustration of the learned surface $f_{\theta}(X)$. Blue points are sampled from \mathbb{P}^{U} , while red points - from \mathbb{P}^D , minimal 20D Uniform distribution that covers all samples from \mathbb{P}^U . The x axis represents $\log \mathbb{P}^{U}(X)$ for each sample, y axis represents the surface height $f_{\theta}(X)$ after the optimization was finished. The diagonal line represents $f_{\theta}(X) = \log \mathbb{P}^{U}(X)$, where we would see all points in case of perfect model inference. The black horizontal line represents $\log \mathbb{P}^D(X) = -30.5$ which is a constant for the Uniform density. As can be seen, these two densities have a relative support mismatch - although their pdf values are not zero within the considered point space, the sampled points from both densities are obviously located mostly in different space neighborhoods. This can be concluded from values of $\log \mathbb{P}^{U}(X)$ that are different for both point populations. Further, we can see that there are errors at both X^{U} and X^{D} locations, possibly due to high bias of the surface estimator $f_{\theta}(X)$ caused by a large norm of θ gradient (see also Figure 18). (c) Testing errors as function of the optimization iteration. All three errors can be used to monitor the learning convergence. Further, IS error can be calculated without knowing the ground truth.

empirically observed that NN architectures with bigger side-influence (e.g. FC networks) have a greater error asymmetry, where the angle between point cloud and line $f_{\theta}(X) = \log \mathbb{P}^{U}(X)$ in Figure 17b is bigger for a bigger overall side-influence within the applied model (see also Figure 23b). We leave a more thorough investigation of this asymmetry nature for future research.

Further, the above asymmetry also clears out why all learned models in Figure 16d had total integral less than 1. Since total integral is calculated by taking exponential over the learned $f_{\theta}(X)$, red points in Figure 17b almost do not have any impact on it, compared with the blue points (red points' exponential is much lower than exponential of blue points). Yet, blue points have smaller $\exp f_{\theta}(X)$ than their real pdf values $\mathbb{P}^{U}(X)$. Therefore, the total integral comes out to be slightly smaller than 1.

Also, in Figure 17c we can see all three errors along the optimization time; the IS is shown to monotonically decrease, similarly to ground truth errors. Hence, in theory it can be used in real applications where no ground truth is available, to monitor the optimization convergence.

Point-wise Error Furthermore, we empirically observe a direct connection between point-wise ground truth error and self gradient similarity $g_{\theta}(X, X)$ (squared norm of gradient $\frac{\partial f_{\theta}(X)}{\partial \theta}$ at the point). To demonstrate this, we define two inverse-gradient-norm empirical metrics as follows. First, after training was finished we sample 1000 points $D = \{X_i\}$, where 500 are sampled from \mathbb{P}^U and 500 - from \mathbb{P}^D , and calculate their gradients $\frac{\partial f_{\theta}(X_i)}{\partial \theta}$. Next, we compute the Gramian matrix G that contains all gradient similarities among the samples, with $G_{ij} = g_{\theta}(X_i, X_j)$. Then, the first empirical metric C_1 for sample X_i is calculated as

$$C_1(X_i) = \frac{1}{G_{ii}} = \frac{1}{g(X_i, X_i, \theta)}.$$

The above $C_1(X_i)$ is bigger if $g_{\theta}(X, X)$ is smaller, and vice versa. The second metric C_2 is defined as

$$C_2(X_i) = \left[G^{-1} \right]_{ii}.$$

Since matrix G is almost diagonal (see Figure 18g), both C_1 and C_2 usually have a similar trend.

In Figure 18 we can see that the above metrics $C_1(X_i)$ and $C_2(X_i)$ are highly correlated with point-wise $LSQR(X_i) = \left[\log \mathbb{P}^U(X_i) - \log \bar{\mathbb{P}}(X_i;\theta)\right]^2$. That is, points with a bigger norm of the gradient $\frac{\partial f_{\theta}(X)}{\partial \theta}$ (bigger $g_{\theta}(X,X)$) have a bigger approximation error. One possible explanation for this trend is that there exists an estimation bias, which caused by side-influence forces, and which is amplified by a bigger gradient norm at the point. Moreover, this hypothesis is consistent with the strong relation between bias and $g_{\theta}(X,X')$, empirically observed along this paper. Further investigation is required to clarify this aspect. Concluding, we empirically demonstrate that in the infinite data setting we can measure model uncertainty (error) at query point X via a norm of its gradient. For a smaller dataset size the connection between the gradient norm and the approximation error is less obvious, probably because there we have another/additional factors that increase the approximation error (e.g. an estimation variance). Also, note that herein we use metrics C_1 and C_2 that are opposite-proportional to the gradient norm instead of using the gradient norm directly since the *inverse* relation is visually much more substantial.

Additionally, in Figure 18 it is visible that on average samples from \mathbb{P}^D have a bigger gradient norm than samples from \mathbb{P}^U . This can explain why in Figure 17b we have higher error at samples from down density.

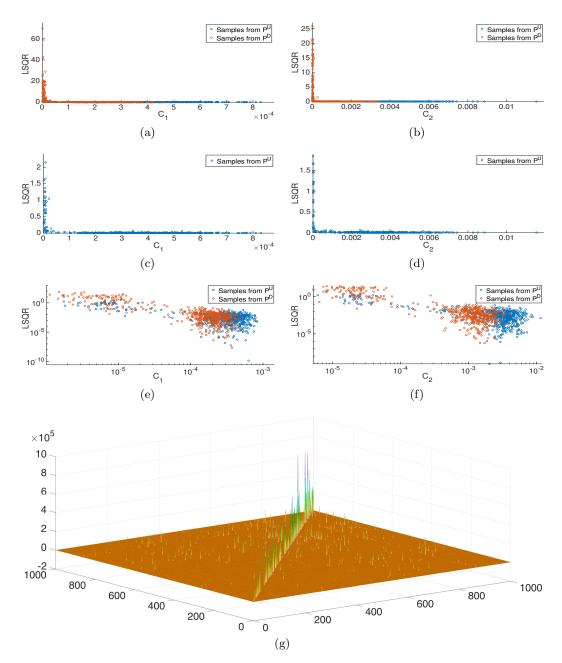


Figure 18: Relation between point-wise error and gradient norm. The pdf function of *Columns* distribution is learned by PSO-LDE with $\alpha = \frac{1}{4}$, where NN architecture is block-diagonal with 6 layers, number of blocks $N_B = 50$ and block size $S_B = 64$ (see Section 8.1). (a)-(b) Relation between inverse-gradient-norm metrics C_1 and C_2 and point-wise error LSQR. As can be seen, points with smaller inverse-gradient-norm (that is, with a bigger norm of θ gradient) have a greater approximation error. See details in the main text. (c)-(d) Plots of (a)-(b) with only samples from \mathbb{P}^U density. (e)-(f) Plots of (a)-(b) with both x and y axes scaled logarithmically. (g) Matrix G, with $G_{ij} = g_{\theta}(X_i, X_j)$.

Method	PSQR	LSQR	IS
PSO-LDE, averaged over all α	$2.7 \cdot 10^{-22} \pm 2.58 \cdot 10^{-23}$	0.057 ± 0.004	26.58 ± 0.01
IS	$1.79 \cdot 10^{-21} \pm 5 \cdot 10^{-22}$	0.46 ± 0.14	26.84 ± 0.07
PSO-MAX	$3.04 \cdot 10^{-22} \pm 1.55 \cdot 10^{-23}$	0.058 ± 0.002	26.57 ± 0.001

Table 10: Performance comparison between various PSO instances

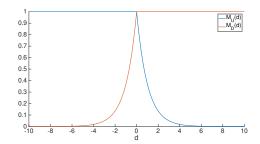


Figure 19: PSO-MAX magnitudes as functions of a difference $\bar{d}[X, f_{\theta}(X)] = f_{\theta}(X) - \log \mathbb{P}^{D}(X)$.

Other PSO Instances Further, several other PSO instances were executed to compare with PSO-LDE. First is the Importance Sampling (IS) method from Table 2. As was discussed in Section 6.2.1, its magnitude functions are unbounded which may cause instability during the optimization. In Table 10 we can see that indeed its performance is much inferior to PSO-LDE with bounded magnitudes.

Additionally, we used an instance of a normalized family defined in Eq. (18), which we name PSO-MAX, with the following *magnitude* functions:

$$M^{U}\left[X, f_{\theta}(X)\right] = \frac{\mathbb{P}^{D}(X)}{\max\left[\mathbb{P}^{D}(X), \exp f_{\theta}(X)\right]} = \exp\left[-\max\left[\bar{d}\left[X, f_{\theta}(X)\right], 0\right]\right], \quad (38)$$

$$M^{D}\left[X, f_{\theta}(X)\right] = \frac{\exp f_{\theta}(X)}{\max\left[\mathbb{P}^{D}(X), \exp f_{\theta}(X)\right]} = \exp\left[\min\left[\bar{d}\left[X, f_{\theta}(X)\right], 0\right]\right]. \tag{39}$$

In Figure 19 the above magnitudes are depicted as functions of a logarithm difference \bar{d} where we can see them to be also bounded. In fact, PSO-MAX is also an instance of PSO-LDE for a limit $\alpha \to \infty$. Similarly to other instances of PSO-LDE, the bounded magnitudes of PSO-MAX allow to achieve a high approximation accuracy, which gets very close to the performance of PSO-LDE for finite values of α (see Table 10). Yet, PSO-MAX is slightly worse, suggesting that very high values of α are sub-optimal for the task of pdf inference.

In overall, our experiments show that PSO instances with bounded magnitudes have superior performance at pdf inference task. Further, PSO-LDE with $\alpha = \frac{1}{4}$ has better accuracy w.r.t. other values of α . Note that this implies PSO-LDE with $\alpha = \frac{1}{4}$ is being superior to NCE (Smith and Eisner, 2005; Gutmann and Hyvärinen, 2010), which is PSO-LDE with $\alpha = 1$. Finally, in an infinite dataset setting and when using BD network

architecture, we can measure model uncertainty of a specific query point X via self gradient similarity $g_{\theta}(X, X)$.

12.3.2 Baselines

In the above section we showed that particular instances of PSO-LDE perform better than the NCE method (i.e. PSO-LDE with $\alpha=1$). Likewise, in our previous work (Kopitkov and Indelman, 2018a) we showed on 2D and 3D data that PSO-based methods are much more accurate than kernel density estimation (KDE) approach. Unfortunately, the KDE method does not scale well with higher dimensions, with very few implementations handling data of arbitrary dimension. Instead, below we evaluate score matching (Hyvärinen, 2005, 2007; Zhai et al., 2016; Saremi et al., 2018), Masked Auto-encoder for Distribution Estimation (MADE) (Germain et al., 2015) and Masked Autoregressive Flow (MAF) (Papamakarios et al., 2017) as state-of-the-art baselines in the context of density estimation.

Score Matching The originally introduced score matching approach (Hyvärinen, 2005) employed the following loss over samples $\{X^i\}_{i=1}^N$ from the target density:

$$L_{SM}(\theta, \{X^i\}_{i=1}^N) = \frac{1}{N} \sum_{i=1}^N \sum_{j=1}^n \left[-\frac{\partial^2 f_{\theta}(X_i)}{\partial X_{ij}^2} + \frac{1}{2} \left(\frac{\partial f_{\theta}(X_i)}{\partial X_{ij}} \right)^2 \right], \tag{40}$$

where $\frac{\partial f_{\theta}(X_i)}{\partial X_{ij}}$ and $\frac{\partial^2 f_{\theta}(X_i)}{\partial X_{ij}^2}$ are first and second derivatives of $f_{\theta}(X_i)$ w.r.t. j-th entry of the n-dimensional sample X_i . Intuitively, we can see that this loss tries to construct a surface $f_{\theta}(X)$ where each sample point will be a local minima - its first derivative is "softly" enforced to be zero via the minimization of a term $\left(\frac{\partial f_{\theta}(X_i)}{\partial X_{ij}}\right)^2$, whereas the second one is "softly" optimized to be positive via maximization of $\frac{\partial^2 f_{\theta}(X_i)}{\partial X_{ij}^2}$. The inferred $f_{\theta}(X)$ of such optimization converges to the data energy function, which is proportional to the real negative log-pdf with some unknown partition constant, $\exp\left[-f_{\theta}(X)\right] \sim \mathbb{P}^U(X)$. Further, note that to optimize an NN model via $L_{SM}(\cdot)$, the typical GD-based back-propagation process will require to compute a third derivative of $f_{\theta}(X)$, which is typically computationally unfeasible for large NN models.

Due to the last point, in (Zhai et al., 2016; Saremi et al., 2018) it was proposed to use the following loss as a proxy:

$$L_{SM}(\theta, \{X^i\}_{i=1}^N) = \frac{1}{N} \sum_{i=1}^N \left\| -v_i + \sigma^2 \cdot \frac{\partial f_{\theta}(X)}{\partial X} |_{X = X_i + v_i} \right\|_2^2, \tag{41}$$

where v_i is zero-centered i.i.d. noise that is typically sampled from $\sim \mathcal{N}(0, \sigma^2 \cdot I)$. This "denoising" loss was shown in (Vincent, 2011) to converge to the same target of the score matching loss in Eq. (40).

Furthermore, the above loss enforces $f_{\theta}(X)$ to converge to the data energy function. However, in this paper we are interested to estimate the data pdf, which is proportional to the negative data energy function. To infer the latter via score matching, we employ the

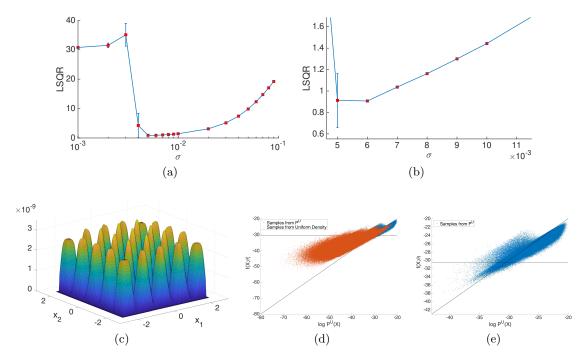


Figure 20: Learned pdf function of Columns distribution by score matching, where NN architecture is block-diagonal with 6 layers, number of blocks $N_B = 50$ and block size $S_B = 64$ (see Section 8.1). The employed activation function is tanh(). (a) LSQR error (mean and standard deviation) for various values of a scaling hyper-parameter σ ; (b) Zoom of (a); (c) Illustration of learned pdf function for best model with $\sigma = 0.006$. The depicted slice is $\mathbb{P}(x_1, x_2) = \overline{\mathbb{P}}^U(x_1, x_2, 0, \dots, 0)$, with x_1 and x_2 forming grid of points in first two dimensions of density's support. As can be seen, the estimated pdf is over-smoothed w.r.t. real pdf in Figure 15a. In contrast, PSO-LDE estimation in Figure 17a does not have this over-smoothing nature. (d) Illustration of the learned surface $f_{\theta}(X)$. Blue points are sampled from \mathbb{P}^U , while red points - from \mathbb{P}^D , minimal 20D Uniform distribution that covers all samples from \mathbb{P}^U . The x axis represents $\log \mathbb{P}^U(X)$ for each sample, y axis represents the surface "normalized" height $\bar{f}_{\theta}(X) = f_{\theta}(X) - \log(\overline{TI}) = \log \bar{\mathbb{P}}_{\theta}(X)$ after optimization was finished. The diagonal line represents $\bar{f}_{\theta}(X) = \log \mathbb{P}^U(X)$, where we would see all points in case of perfect model inference. (e) Plot from (d) with only samples from \mathbb{P}^U . We can see that the produced surface is significantly less accurate than the one produced by PSO-LDE in Figures 17a-17b.

following sign change of the noise term:

$$L_{SM}(\theta, \{X^i\}_{i=1}^N) = \frac{1}{N} \sum_{i=1}^N \left\| v_i + \sigma^2 \cdot \frac{\partial f_{\theta}(X)}{\partial X} |_{X = X_i + v_i} \right\|_2^2, \tag{42}$$

which has the same equilibrium as the loss in Eq. (41), yet with the negative sign. That is, at convergence $f_{\theta}(X)$ will satisfy $\exp[f_{\theta}(X)] \sim \mathbb{P}^{U}(X)$. In our experiments we used this version of score matching loss for density estimation of 20D *Columns* distribution.

The employed learning setup of score matching is identical to PSO-LDE, with the loss in Eq. (42) being applied in a mini-batch mode, where at each optimization iteration a batch of samples $\{X^i\}_{i=1}^N$ was fetched from the training dataset and the new noise batch $\{v^i\}_{i=1}^N$ was generated. The learning rate of Adam optimizer was 0.003. Note that this

method infers $\exp[f_{\theta}(X)]$ which is only proportional to the real pdf with some unknown partition constant. Therefore, in order to compute LSQR of such model we also calculated its partition via importance sampling. Specifically, for each learned model $\exp[f_{\theta}(X)]$ its integral was estimated through $\overline{TI} = \sum_{i=1}^{N^D} \frac{\exp[f_{\theta}(X_i^D)]}{\mathbb{P}^D(X_i^D)}$ over $N^D = 10^8$ samples from density \mathbb{P}^D , which is the minimal 20D Uniform distribution that covers all samples from \mathbb{P}^U . Further, we used $\bar{\mathbb{P}}_{\theta}(X) = \exp[f_{\theta}(X) - \log(\overline{TI})]$ as the final estimation of data pdf.

Furthermore, we trained the score matching model for a range of σ values. After the explicit normalization of each trained model, in Figures 20a-20b we can see the LSQR error for each value of hyper-parameter σ . Particularly, for $\sigma=0.006$ we got the smaller error $LSQR=0.907\pm0.0075$, which is still much inferior to the accuracy obtained by PSO-LDE. Moreover, in Figure 20c we can see that estimated surface is over-smoothed and does not accurately approximate the sharp edges of the target pdf. In contrast, PSO-LDE produces a very close pdf estimation of an arbitrary shape, as was shown in Section 12.3.1. Likewise, comparing Figures 20d and 17b we can see again that PSO-LDE yields a much better accuracy.

Masked Auto-encoder for Distribution Estimation This technique is based on the autoregressive property of density functions, $\mathbb{P}(x_1,\ldots,x_n)=\prod_{i=1}^n\mathbb{P}(x_i|x_1,\ldots,x_{i-1})$, where each conditional $\mathbb{P}(x_i|x_1,\ldots,x_{i-1})$ is parameterized by NN's output. MADE constructs a network with sequential FC layers, where the autoregressive property is preserved via masks applied on activations of each layer (Germain et al., 2015). Likewise, each conditional can be modeled as 1D density of any known distribution family, with a typical choice being Gaussian or Mixture of Gaussians (MoG).

In our experiments we used MoG with k components to model each conditional, due to the highly multi-modal nature of Columns distribution. Moreover, we evaluated MADE for a range of various k, to see how the components number affects technique's performance. Furthermore, the learning setup was similar to the other experiments, with the only difference that the applied NN architecture was FC, with 4 layers of size 1024 each, and the exploited non-linearity was Relu.

In Figures 21a-21b the LSQR error is shown for each value of k. We can clearly see that with higher number of components the accuracy improves, where the best performance was achieved by k=512 with $LSQR=0.2\pm0.0141$. Furthermore, in Figure 21c we can see an estimated surface for the best learned model. As observed, most of the MoG components are spent to represent flat peaks of the target density. Such outcome is natural since for MoG to approximate flat areas the value of k has to go to infinity. Moreover, this again demonstrates the difference between parametric and non-parametric techniques. Due to an explicit parametrization of each conditional, MADE can be considered as a member of the former family, while PSO-LDE is definitely a member of the latter. Further, non-parametric approaches are known to be more robust/flexible in general. In overall, we can see that PSO-LDE outperforms MADE even for a large number of mixture components.

Masked Autoregressive Flow This technique combines an NN architecture of the previous method, MADE, with the idea of a normalizing flow (Rezende and Mohamed, 2015) where a bijective transformation $h(\cdot)$ is applied to transform a priori chosen base density into the target density. Such bijective transformation allows to re-express the density of target

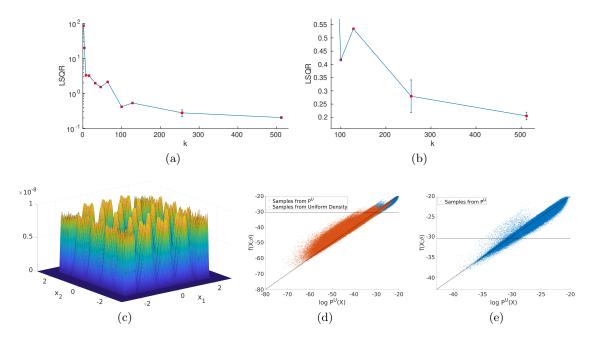


Figure 21: Learned pdf function of *Columns* distribution by MADE, where NN architecture is fully-connected with 4 layers of size 1024. The employed activation function is Relu. (a) LSQR error (mean and standard deviation) for various values of a k - a number of mixture components; (b) Zoom of (a); (c) Illustration of learned pdf function for the best model with k = 512. The depicted slice is $\mathbb{P}(x_1, x_2) = \bar{\mathbb{P}}^U(x_1, x_2, 0, \dots, 0)$, with x_1 and x_2 forming grid of points in first two dimensions of density's support. As can be seen, the estimated pdf is over-spiky in areas where the real pdf in Figure 15a is flat. This is due to an inability of MoG model to represent flat non-zero surfaces. In contrast, PSO-LDE estimation in Figure 17a does not have this issue. (d) Illustration of the estimated pdf $\bar{\mathbb{P}}_{\theta}(X)$. Blue points are sampled from \mathbb{P}^U , while red points - from \mathbb{P}^D , minimal 20D Uniform distribution that covers all samples from \mathbb{P}^U . The x axis represents $\log \mathbb{P}^U(X)$ for each sample, y axis represents $\bar{f}_{\theta}(X) \triangleq \log \bar{\mathbb{P}}_{\theta}(X)$ after optimization was finished. The diagonal line represents $\bar{f}_{\theta}(X) = \log \mathbb{P}^U(X)$, where we would see all points in case of perfect model inference. (e) Plot from (d) with only samples from \mathbb{P}^U .

data via an inverse of $h(\cdot)$ and via the known pdf of a base density, and further to infer target pdf via a standard MLE loss. Moreover, the architecture of MADE can be seen as such bijective transformation, which is specifically exploited by MAF method (Papamakarios et al., 2017). Particularly, several MADE transformations are stuck together into one large bijective transformation, which allows for richer representation of the inferred pdf. In our experiments we evaluated MAF method with 5 inner MADE bijections.

Furthermore, the original paper proposed two MAF types. First one, referred as MAF(·) in the paper, uses multivariate normal distribution as a base density. During the evaluation this type did not succeed to infer 20D *Columns* distribution at all, probably because of its inability to handle distribution with 5^{20} modes.

The second MAF type, referred as MAF $MoG(\cdot)$ in the paper, uses MADE MoG as a base density in addition to the MADE-based bijective transformation. This type showed better performance w.r.t. first type, and we used it as an another baseline. Likewise, note

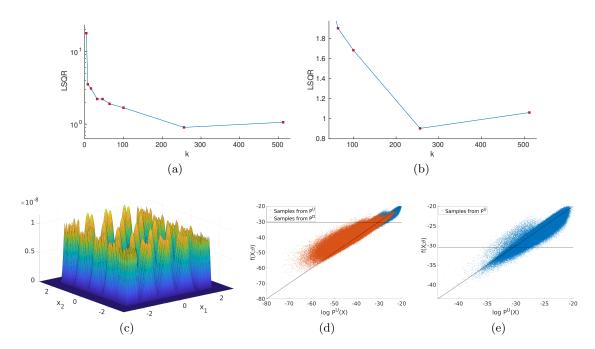


Figure 22: Learned pdf function of *Columns* distribution by MAF, with 5 inner MADE bijections and MADE MoG as a base density. (a) LSQR error (mean and standard deviation) for various values of a k - a number of mixture components; (b) Zoom of (a); (c) Illustration of learned pdf function for the best model with k = 256. The depicted slice is $\mathbb{P}(x_1, x_2) = \bar{\mathbb{P}}^U(x_1, x_2, 0, \dots, 0)$, with x_1 and x_2 forming grid of points in first two dimensions of density's support. The same over-spiky behavior can be observed as in Figure 21c. (d) Illustration of the estimated pdf $\bar{\mathbb{P}}_{\theta}(X)$ for the best model, constructed similarly to Figure 21d. (e) Plot from (d) with only samples from \mathbb{P}^U .

that also in the original paper (Papamakarios et al., 2017) this type was shown on average to be superior between the two.

Like in MADE experiments, also here we tested MAF MoG for different values of k-mixture components number of the base density, parametrized by a separate MADE MoG model. In Figures 22a-22b the LSQR error is shown for each value of k. As in MADE case, also here accuracy improves with higher number of components. The top accuracy was achieved by k=256 with $LSQR=0.9\pm0.009$. On average, MAF MoG showed the same trends as MADE method, yet with some higher LSQR error. Moreover, during the experiments it was observed as a highly unstable technique, with thorough hyper-parameter tuning needed to overcome numerical issues of this approach.

In overall, we observed that non-parametric PSO-LDE is superior to other state-of-the-art baselines when dealing with highly multi-modal *Columns* distribution.

12.3.3 NN ARCHITECTURES EVALUATION

Here we compare performance of various NN architectures for the pdf estimation task.

FC Architecture We start with applying PSO-LDE with different values of α where the used NN architecture is now fully-connected (FC), with 4 layers of size 1024. In Figure 23a

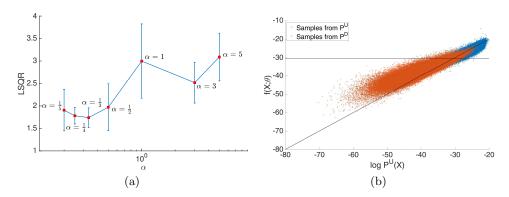


Figure 23: Evaluation of PSO-LDE for estimation of Columns distribution, where NN architecture is fully-connected with 4 layers of size 1024 (see Section 8.1). (a) For different values of hyper-parameter α , LSQR error is reported, along with its empirical standard deviation. (b) Illustration of the learned surface $f_{\theta}(X)$. Blue points are sampled from \mathbb{P}^{U} , while red points from \mathbb{P}^{D} . The x axes represent $\log \mathbb{P}^{U}(X)$ for each sample, y axes - the surface height $f_{\theta}(X)$ after optimization was finished. Diagonal line represents $f_{\theta}(X) = \log \mathbb{P}^{U}(X)$, where we would see all points in case of perfect model inference. The black horizontal line represents $\log \mathbb{P}^{D}(X) = -30.5$ which is constant for the Uniform density. As can be seen, there are high approximation errors at both X^{U} and X^{D} locations. Compared with BD architecture in Figure 17b, on average the error is much higher for FC network.

we show LSQR for different α , where again we can see that $\alpha = \frac{1}{4}$ (and now also $\alpha = \frac{1}{3}$) performs better than other values of α . On average, LSQR error is around 2.5 which is significantly higher than 0.057 for BD architecture. Note also that BD network, used in Section 12.3.1, is twice smaller than FC network, containing only 902401 weights in BD vs 2121729 in FC, yet it produced a significantly better performance.

Further, in Figure 23b we illustrated the learned surface $f_{\theta}(X)$ for a single FC model with $\alpha = \frac{1}{4}$. Compared with Figure 17b, we can see that FC architecture produces a much less accurate NN surface. We address it to the fact that in BD network the gradient similarity $g_{\theta}(X, X')$ has much smaller overall side-influence and the induced bias compared to the FC network, as was demonstrated in Section 8.1. Hence, BD models are more flexible than FC and can be pushed closer to the target function $\log \mathbb{P}^{U}(X)$, producing more accurate estimations.

Additionally, note the error asymmetry in Figure 23b which was already observed in Figure 17b. Also here we can see that the entire cloud of points is rotated from zero error line $f_{\theta}(X) = \log \mathbb{P}^{U}(X)$ by some angle where the rotation axis is also around horizontal line $\log \mathbb{P}^{D}(X) = -30.5$. As explained in Section 12.3.1, according to our current hypotheses there are global up and down side-influence forces that are responsible for this angle.

Further, to ensure that FC architecture can not produce any better results for the given inference task, we also evaluate it for different values of N_L and S - number of layers and size of each layer respectively. In Figure 24 we see that $N_L = 4$ and S = 1408 achieve best results for FC NN. Yet, the achieved performance is only LSQR = 1.17, which is still nowhere near the accuracy of BD architecture.

BD Architecture Further, we performed learning with a BD architecture, but with increasing number of blocks N_B . For N_B taking values between 20 and 200, in Figure 25 we

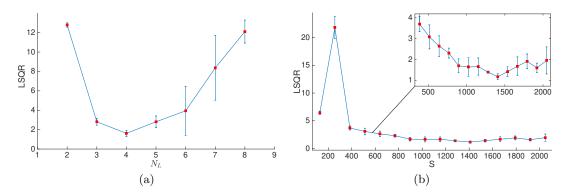


Figure 24: Evaluation of PSO-LDE for estimation of *Columns* distribution, where NN architecture is fully-connected (see Section 8.1). The applied loss is PSO-LDE with $\alpha = \frac{1}{4}$. (a) For different number of layers N_L , LSQR error is reported, where a size of each layer is S = 1024. (b) For different values of layer size S, LSQR error is reported, where a number of layers is $N_L = 4$.

can see that with bigger N_B there is improvement in approximation accuracy. This can be explained by the fact that bigger N_B produces bigger number of independent transformation channels inside NN; with more such channels there is less parameter sharing and side-influence between far away input regions - different regions on average rely on different transformation channels. As a result, the NN becomes highly flexible. Further, in the setting of infinite dataset such high NN flexibility is desirable, and leads to a higher approximation accuracy. In contrast, in Section 12.3.5 below we will see that for a smaller dataset size the relation between NN flexibility and the accuracy is very different.

Likewise, we experiment with number of layers N_L to see how the network depth of a BD architecture affects the accuracy of pdf inference. In Figure 26 we see that deeper networks allow us to further decrease LSQR error to around 0.03. Also, we can see that at some point increasing N_L causes only a slight error improvement. Thus, increasing N_L beyond that point is not beneficial, since for very small error reduction we will pay with higher computational cost due to increasing size of θ .

Furthermore, in Figure 27 we evaluate BD performance for different sizes of blocks S_B . Here we don't see anymore a monotonic error decrease that we observed above for N_B and N_L . The error is big for S_B below 32 or above 160. This probably can be explained as follows. For a small block size S_B each independent channel has too narrow width that is not enough to properly transfer the required signal from NN input to output. Yet, surprisingly it still can achieve a very good approximation, yielding LSQR error of 0.075 for $S_B = 16$ with only 72001 weights, which is very impressive for such small network. Further, for a large block size S_B each independent channel becomes too wide, with information from too many various regions in \mathbb{R}^n passing through it. This in turn causes interference (side-influence) between different regions and reduces overall NN flexibility, similarly to what is going on inside a regular FC network.

NN Pre-conditioning Finally, we verified efficiency of pre-conditioning techniques proposed in Section 8.2, namely the data normalization in Eq. (29) and the height bias in Eq. (30). In Table 11 we see that both methods improve the estimation accuracy. Further,

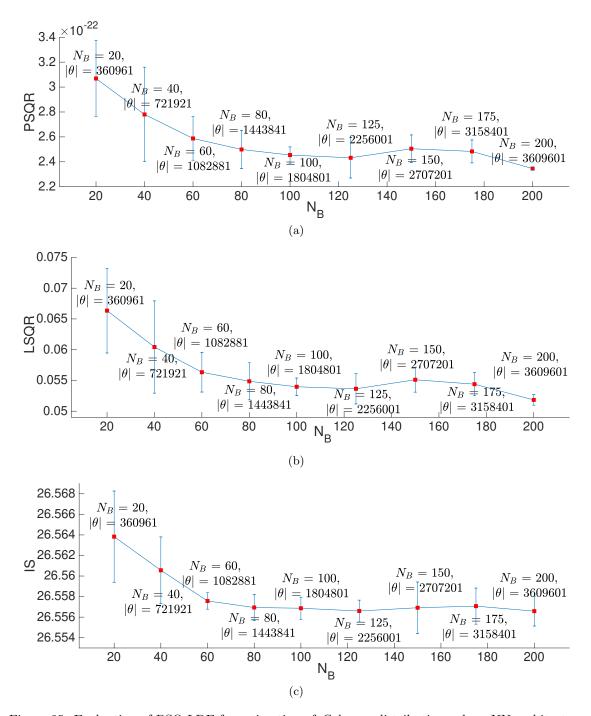


Figure 25: Evaluation of PSO-LDE for estimation of *Columns* distribution, where NN architecture is block-diagonal with 6 layers and block size $S_B=64$ (see Section 8.1). The number of blocks N_B is changing. The applied loss is PSO-LDE with $\alpha=\frac{1}{4}$. For different values of N_B , (a) PSQR (b) LSQR and (c) IS are reported. As observed, the bigger number of blocks (e.g. independent channels) N_B improves the pdf inference.

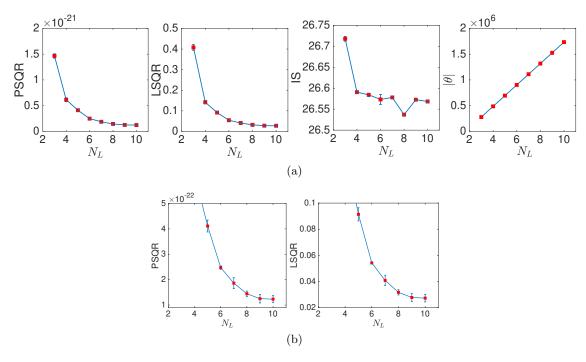


Figure 26: Evaluation of PSO-LDE for estimation of Columns distribution, where NN architecture is block-diagonal with number of blocks $N_B = 50$ and block size $S_B = 64$ (see Section 8.1). The number of layers N_L is changing from 3 to 10. The applied loss is PSO-LDE with $\alpha = \frac{1}{4}$. (a) For different values of N_L we report PSQR, LSQR and IS, and their empirical standard deviation. Additionally, in last column we depict the size of θ for each value of N_L . (b) Zoom of (a).

Method	PSQR	LSQR	IS
BD, ✓ DT, ✓ HB BD, X DT, ✓ HB BD, ✓ DT, X HB BD, X DT, X HB	$2.48 \cdot 10^{-22} \pm 6.63 \cdot 10^{-24}$ $2.49 \cdot 10^{-22} \pm 9.8 \cdot 10^{-24}$ $2.51 \cdot 10^{-22} \pm 1.1 \cdot 10^{-23}$ $3 \cdot 10^{-22} \pm 4.79 \cdot 10^{-23}$	$\begin{aligned} 0.054 &\pm 0.0009 \\ 0.055 &\pm 0.0021 \\ 0.056 &\pm 0.0026 \\ 0.066 &\pm 0.011 \end{aligned}$	26.57 ± 0.01 26.57 ± 0.002 26.57 ± 0.002 26.57 ± 0.005
FC, ✓ DT, ✓ HB FC, ✗ DT, ✓ HB FC, ✓ DT, ✗ HB FC, ✗ DT, ✗ HB	$5.56 \cdot 10^{-18} \pm 1.02 \cdot 10^{-17}$ $1.2 \cdot 10^{-16} \pm 2.67 \cdot 10^{-16}$ $7.9 \cdot 10^{-21} \pm 2.37 \cdot 10^{-21}$ $1.36 \cdot 10^{-12} \pm 3 \cdot 10^{-12}$	1.78 ± 0.18 1.35 ± 0.058 2.38 ± 0.3 2.5 ± 0.23	27.29 ± 0.05 27.157 ± 0.029 27.52 ± 0.08 27.54 ± 0.08

Table 11: Performance comparison between various NN pre-conditioning ways. The pdf function of *Columns* distribution is learned by PSO-LDE with $\alpha = \frac{1}{4}$. The applied models are fully-connected (FC) with 4 layers of size 1024, and block-diagonal (BD) with 6 layers, number of blocks $N_B = 50$ and block size $S_B = 64$ (see Section 8.1). The evaluated pre-conditioning techniques are the data normalization in Eq. (29) (DT), and the height bias in Eq. (30) (HB).

in case the used model is FC, the LSQR error improvement produced by the height bias is much more significant. Yet, for FC architecture it is unclear if the data normalization indeed helps.

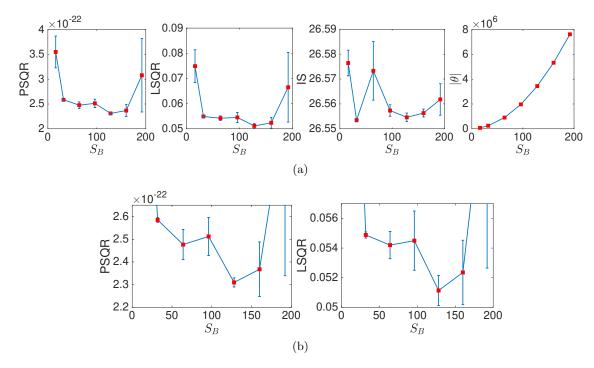


Figure 27: Evaluation of PSO-LDE for estimation of *Columns* distribution, where NN architecture is block-diagonal with 6 layers and number of blocks $N_B = 50$ (see Section 8.1). The block size S_B is taking values $\{16, 32, 64, 96, 128, 160, 192\}$. The applied loss is PSO-LDE with $\alpha = \frac{1}{4}$. (a) For different values of S_B we report PSQR, LSQR and IS, and their empirical standard deviation. Additionally, in the last column we depict the size of θ for each value of S_B . (b) Zoom of (a).

Overall, our experiments **combined** with observations from Section 8.1.1 show that BD architecture has a smaller side-influence (small values of $g_{\theta}(X, X')$ for $X \neq X'$) and a higher flexibility than FC architecture. This in turn yields superior accuracy for BD vs FC networks. Moreover, in an infinite dataset setting we can see that further increase of NN flexibility by increasing N_B or N_L yields even better approximation accuracy. The block size S_B around 64 produces better performance in general. Yet, its small values are very attractive since they yield a network of small size with appropriate computational benefits, with a relatively small error increase.

12.3.4 BATCH SIZE IMPACT

Herein we investigate the relation between PSO approximation error and a batch size of training points. In particular, in PSO loss we have two terms, the up term which is sum over batch points $\{X_i^U\}_{i=1}^{N^U}$ and the down term which is sum over batch points $\{X_i^D\}_{i=1}^{N^D}$. We will see how values of N^U and N^D affect PSO performance.

Increasing both N^U and N^D First, we run a scenario where both batch sizes are the same, $N^U = N^D = N$. We infer *Columns* distribution with different values of N, ranging from 10 to 6000. In Figures 28a-28b we can observe that LSQR error is decreasing for bigger N, which is expected since then the stochastic forces at each point $X \in \mathbb{R}^n$ are getting closer

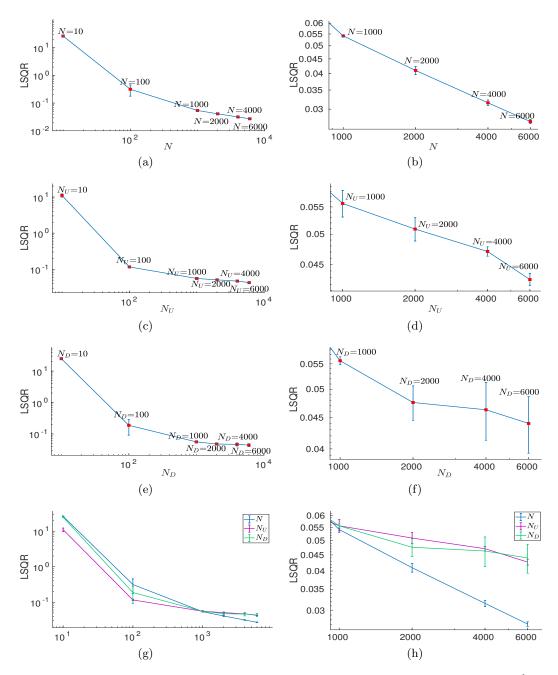


Figure 28: Batch size evaluation. Columns distribution is estimated via PSO-LDE with $\alpha=\frac{1}{4}$, where NN architecture is block-diagonal with 6 layers, number of blocks $N_B=50$ and block size $S_B=64$ (see Section 8.1). (a)-(b) For different values of batch size $N=N^U=N^D$ we report LSQR and its empirical standard deviation. Both up batch size N^U and down batch size N^D are kept the same. (c)-(d) The N^U receives different values while N^D is 1000. (e)-(f) The N^D receives different values while N^U is 1000. (g)-(h) All scenarios are plotted together in the same graph. Note that both x and y axes are log-scaled. Right column is zoom-in of left column.

to the averaged forces $F_{\theta}^{U}(X) = \mathbb{P}^{U}(X) \cdot M^{U}[X, f_{\theta}(X)]$ and $F_{\theta}^{D}(X) = \mathbb{P}^{D}(X) \cdot M^{D}[X, f_{\theta}(X)]$. In other words, the sampled approximation of PSO gradient in Eq. (4) becomes more accurate.

Moreover, we can observe that for the smaller batch size the actual PSO-LDE performance is very poor, with LSQR being around 26.3 for N=10 and decreasing to 0.31 for N=100. The high accuracy, in range 0.03-0.05, is only achieved when we increase the number of batch points to be above 1000. This implies that to reach a higher accuracy, PSO will require a higher demand over the memory/computation resources. Therefore, the higher available resources, expected from future GPU cards, will lead to higher PSO accuracy.

Increasing only N^U Further, we experiment with increasing/decreasing only one of the batch sizes while the other stays constant. In Figures 28c-28d a scenario is depicted where N^U is changing while N^D is 1000. Its error for small values of N^U is smaller than in the previous scenario, with LSQR being around 11 for $N^U = 10$ and decreasing to 0.11 for $N^U = 100$. Comparing with the previous experiment, we can see that even if N^U is small, a high value of N^D (1000) improves the optimization performance.

Increasing only N^D Furthermore, in Figures 28e-28f we depict the opposite scenario where N^D is changing while N^U is 1000. Unlike the experiment in Figures 28c-28d, here the improvement of error for small values of N^D w.r.t. first experiment is not that significant. For $N^D = 10$ the error is 24.8 and for $N^D = 100$ it is 0.19. Hence, the bigger number of up points $(N^U = 1000)$ does not lead to a much higher accuracy if a number of down points N^D is too small.

Finally, in Figures 28g-28h we plot all three experiments together. Note that all lines cross at the same point, where all experiments were configured to have $N^U = N^D = 1000$. We can see that in case our resource budget is low (smaller values of x in Figure 28g), it is more efficient to spend them to increase N^D . Yet, for a high overall resource budget (higher values of x in Figure 28g) both N^U and N^D affect the error similarly, and it is better to keep them equal and increase them as much as possible.

12.3.5 Small Training Dataset

In this section we will learn a 20D *Columns* distribution using only 100000 training sample points. As we will see below, the density inference task via non-parametric PSO becomes much more challenging when the size of the training dataset is limited.

Various Sizes of Dataset To infer the data pdf, here we applied PSO-LDE with $\alpha = \frac{1}{4}$. Further, we use BD NN architecture since it has superior approximation performance over FC architecture. First, we perform the inference task using the same BD network as in Section 12.3.1, with 6 layers, $N_B = 50$ and $S_B = 64$, where the size of the entire weights vector is $|\theta| = 902401$. The Columns pdf is inferred using a various number N_{DT} of overall training points $\{X_i^U\}_{i=1}^{N_{DT}}$. In Figure 29a it is shown how LSQR error increases for smaller size N_{DT} of the training dataset. From error 0.05 for $N_{DT} = 10^8$ it gets to 0.062 for $N_{DT} = 10^7$, 0.67 for $N_{DT} = 10^6$, 91.2 for $N_{DT} = 10^5$ and 8907 for $N_{DT} = 10^4$. As we will see below and as was also discussed in Section 9, one of the main reasons for such large errors is a too flexible NN model, which in a small dataset setting can significantly damage performance of PSO-LDE, and PSO in general.

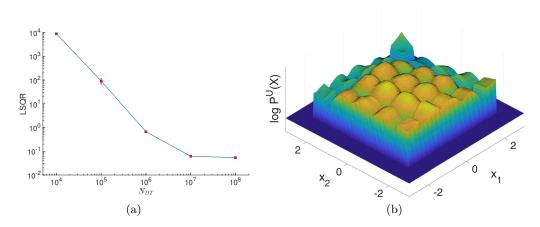


Figure 29: Evaluation of PSO-LDE for estimation of Columns distribution with different sizes N_{DT} of training dataset. Used NN architecture is block-diagonal with 6 layers, number of blocks $N_B = 50$ and block size $S_B = 64$ (see Section 8.1). Number of weights is $|\theta| = 902401$. Applied PSO instance is PSO-LDE with $\alpha = \frac{1}{4}$. (a) LSQR error as function of training dataset size N_{DT} , where both x and y axes are log-scaled. (b) Illustration of the learned log-pdf surface $f_{\theta}(X)$ for dataset size $N_{DT} = 10^5$. The depicted slice is $\log \mathbb{P}(x_1, x_2) \triangleq f([x_1, x_2, 0, \dots, 0]; \theta)$, with x_1 and x_2 forming grid of points in first two dimensions of density's support. Note the resemblance similarity between this plot and the target surface in Figure 15b. Even though LSQR error of this model in (a) is very high (≈ 91.2), the local structure within the converged surface is close to the local structure of the target function. Unfortunately, its global structure is inconsistent and far away from the target.

Interestingly, although LSQR error is high for models with $N_{DT}=10^5$, in Figure 29b we can see that the converged surface $f_{\theta}(X)$ highly resembles visually the real target log-pdf in Figure 15b. We can see that main lines and forms of the target surface were learned by $f_{\theta}(X)$, yet the overall global shape of NN surface is far away from the target. Furthermore, if we calculate $\exp f_{\theta}(X)$, we will get a surface that is very far from its target $\mathbb{P}^{U}(X)$ since the exponential will amplify small errors into large.

Further, in Figure 30 we can observe the error curves for models learned in Figure 29a. Both train and test errors are reported for all three error types, per different dataset size N_{DT} . Train and test errors are very similar for big N_{DT} in Figures 30a-30b. Moreover, in Figure 30b we can see according to the LSQR error (middle column) that at the beginning error decreases but after 10^5 steps it starts increasing, which suggests a possible overfitting to the training dataset at $N_{DT} = 10^6$. Further, in Figures 30c-30d we can see that train and test errors are more distinct from each other. Likewise, here PSQR and LSQR, both train and test, are increasing almost from the start of the optimization. In contrast, in Figures 30c-30d in case of IS the train and test errors have different trends compared with each other. While the test IS is increasing, the train IS is decreasing. This is a typical behavior of optimization error that indicates strong overfitting of the model, here for $N_{DT} = 10^5$ and $N_{DT} = 10^4$. In turn, this means that we apply a too rich model family - over-flexible NN which can be pushed to form peaks around the training points, as was demonstrated in Section 9. Further, we can detect such overfitting using IS error, which does not depend on ground truth.

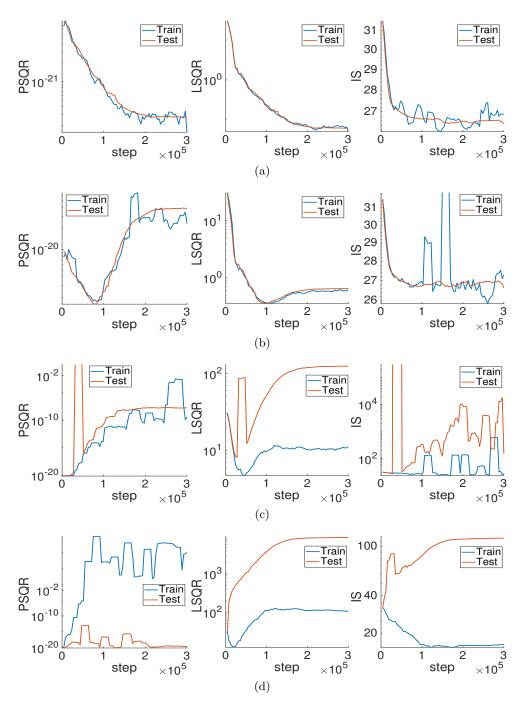


Figure 30: Error curves for models learned in Figure 29a, where various dataset sizes N_{DT} were evaluated. The error is reported for (a) $N_{DT}=10^7$, (b) $N_{DT}=10^6$, (c) $N_{DT}=10^5$ and (d) $N_{DT}=10^4$. In each row we report: PSQR - first column; LSQR - middle column; IS - last column. Each plot contains both train and test errors; the former is evaluated over 10^3 up points from training dataset chosen as a batch for a specific optimization iteration, whereas the latter over 10^5 up points from testing dataset.

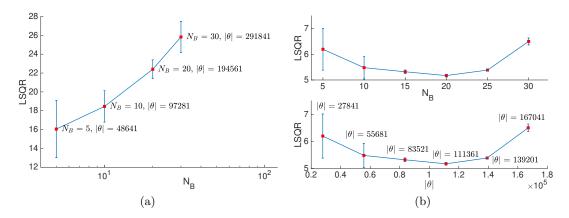


Figure 31: Evaluation of PSO-LDE for estimation of Columns distribution with only 10^5 training samples. Used NN architecture is block-diagonal with block size $S_B = 64$ (see Section 8.1). Applied PSO instance is PSO-LDE with $\alpha = \frac{1}{4}$. (a) LSQR error for models with 4 layers and various values of blocks number N_B . Size of weights vector θ is depicted for each model. (b) LSQR error for models with 3 layers and various values of blocks number N_B . Top - LSQR is shown as function of N_B ; bottom - LSQR is shown as function of size $|\theta|$. As can be seen, too big and too small number of parameters, $|\theta|$, produces a very inaccurate pdf approximation in the small dataset setting.

Note that train and test errors of PSQR/LSQR have the same trend herein, unlike IS, since these errors express a real ground truth distance between NN surface and the target function, whereas IS error is only a some rough estimation of it.

Reduction of NN Flexibility to Tackle Overfitting Next, we perform the inference task using BD network with only 4 layers, on the training dataset of size $N_{DT} = 10^5$. We learn models for various numbers of blocks N_B inside our network, being between 5 and 30. In Figure 31a we can see that LSQR error is still very high compared to the results of an infinite dataset setting in Section 12.3.1: ≈ 20 vs ≈ 0.05 . Yet, it is smaller than in Figure 29a, where we used 6 layers instead of 4 and $N_B = 50$. Moreover, we can see in Figure 31a that error is reducing with smaller number of blocks N_B and smaller number of NN parameters $|\theta|$.

Further, we perform the same experiment where BD architecture has only 3 layers (first and last are FC layers and in the middle there is BD layer). In Figure 31b we can see that for too small/large value of N_B the LSQR is higher. That is, for too big/small number of weights in θ we have worse pdf approximation. This can be explained as follows. Small size $|\theta|$ implies NN with low flexibility which is not enough to closely approximate a target surface $\log \mathbb{P}^U(X)$, thus producing underfitting. We observed similar results also in an infinite dataset setting in Section 12.3.3, where bigger size of θ yielded an even smaller error. Furthermore, when $|\theta|$ is too big, the NN surface becomes too flexible and causes overfitting. Such over-flexibility is not appropriate for small dataset setting, since it allows to closely approximate a peak around each training sample X^U (or X^D), where the produced spiky surface $f_{\theta}(X)$ will obviously have a high approximation error, as was demonstrated in Section 9. In other words, in contrast to common regression learning, in case of unsupervised PSO approaches the size (and the flexibility) of NN should be adjusted according to the

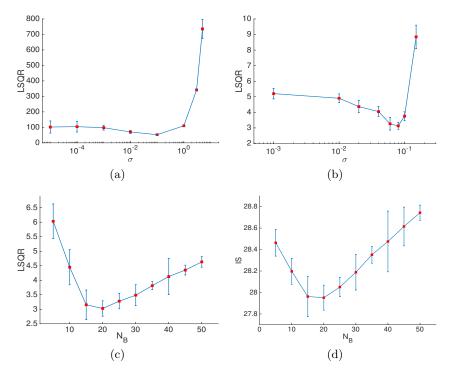


Figure 32: Evaluation of PSO-LDE for estimation of Columns distribution with only 10⁵ training samples, using a data augmentation noise. The used NN architecture is block-diagonal with block size $S_B = 64$ (see Section 8.1). Applied PSO instance is PSO-LDE with $\alpha = \frac{1}{4}$. Each up training point X^U is sampled from data density \mathbb{P}^U . Further, an additive 20D noise $v \sim \mathcal{N}(0, \sigma^2 \cdot I)$ is sampled and added to X^U . The PSO-LDE loss is applied on $\bar{X}_U = X^U + v$ instead of the original X^U . Number of overall \mathbb{P}^U 's samples is 10^5 ; new samples of noise v are sampled at each optimization iteration. We learn models using various values of σ . (a) LSQR error as a function of σ , for models with 6 layers and blocks number $N_B = 50$. (b) LSQR error as function of σ , for models with 3 layers and blocks number $N_B = 0.08$. As can be seen, smaller size (up to some threshold) of NN produces much higher accuracy in a limited training dataset setting. Also, the additive noise can yield an accuracy improvement.

number of available training points, otherwise the produced approximation error will be enormous. In contrast, in common DL-based regression methods such over-flexible NN may cause *overfitting* to training samples which increases testing error, yet it will not affect the overall approximation performance as destructively as in PSO.

Interestingly, the optimal size $|\theta|$ in Figure 31b-bottom is around 100000 - the number of available training points. It would be an important investigatory direction to find the exact mathematical relation between the dataset size and properties of NN (e.g. its size, architecture and gradient similarity) for the optimal inference. We shall leave it for future research.

Data Augmentation to Tackle Overfitting Additionally, we also apply the augmentation data technique to smooth the converged surface $f_{\theta}(X)$, as was described in Section 9. Concretely, we use samples of r.v. $\bar{X}_U = X^U + v$ as our up points, where we push the

NN surface up. The X^U is sampled from data density \mathbb{P}^U , while the additive 20D noise v is sampled from $\sim \mathcal{N}(0, \sigma^2 \cdot I)$. At each optimization iteration the next batch of $\{X_i^U\}_{i=1}^{N^U}$ is fetched from a priori prepared training dataset of size 10^5 , and new noise instances $\{v^i\}_{i=1}^{N^U}$ are generated. Further, $\{\bar{X}_U^i\}_{i=1}^{N^U}$ is used as the batch of up points within PSO-LDE loss, where $\bar{X}_U^i = X_i^U + v^i$. Such a method allows us to push the $f_{\theta}(X)$ up not only at the limited number of training points X_i^U , but also at other points in some ball neighborhood around each X_i^U , thus implicitly changing the approximated function to be smoother and less spiky. Another perspective to look over it is that we apply Gaussian diffusion over our NN surface, since adding Gaussian noise is identical to replacing the target pdf $\mathbb{P}^U(X)$ with the convolution $\mathbb{P}^U(X) * \mathcal{N}(0, \sigma^2 \cdot I)$.

In Figure 32a we can see results of such data augmentation for BD network with 6 layers and 50 blocks, with $S_B = 64$. In such case, where the used model is over-flexible with too many degrees of freedom, the data augmentation is not helpful, with an overall error being similar to the one obtained in Figure 29a. Yet, when model size (and its flexibility) is reduced to only 3 layers and 20 blocks, the performance trend is different. In Figure 32b we can see that for particular values of noise s.t.d. σ (e.g. 0.08) the data augmentation technique reduces LSQR error from 5.17 (see Figure 31b) to only 3.13.

Further, in Figures 32c-32d we can see again that there is an optimal NN size/flexibility that produces the best performance, where smaller NN suffers from *underfitting* and larger NN suffers from *overfitting*. Moreover, in Figure 32d we can see again that the empirical error IS is correlated with the ground truth error LSQR, although the former is less accurate than the latter. Hence, IS can be used in practice to select the best learned model.

Overall, in our experiments we observed both underfitting and overfitting cases of PSO optimization. The first typically happens for large dataset size when NN is not flexible enough to represent all the information contained within training samples. In contrast, the second typically happens for small datasets when NN is over-flexible so that it can be pushed to have spikes around the training points. Further, overfitting can be detected via IS test error. Finally, the data augmentation reduces effect of overfitting.

12.4 PDF Estimation via PSO - Transformed Columns Distribution

In this section we will show that PSO is not limited only to isotropic densities (e.g. Columns distribution from Section 12.3) where there is no correlation among different data dimensions, and can be actually applied also over data with a complicated correlation structure between various dimensions. Specifically, herein we infer a 20D Transformed Columns distribution, $\mathbb{P}^{U}(X) = \mathbb{P}^{TrClmns}(X)$, which is produced from isotropic Columns by multiplying a random variable $X \sim \mathbb{P}^{Clmns}$ (defined in Eq. (37)) with a dense invertible matrix A which enforces correlation between different dimensions. Its pdf can be written as:

$$\mathbb{P}^{TrClmns}(X) = \frac{1}{abs \left[\det A \right]} \mathbb{P}^{Clmns}(A^{-1} \cdot X),$$

where A appears in Appendix K. As we will see below, the obtained results for this more sophisticated distribution have similar trends to results of *Columns*. Additionally, we will also show how important is the choice of \mathbb{P}^D .

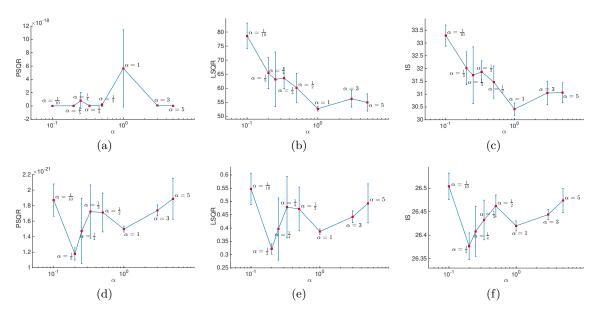


Figure 33: Evaluation of PSO-LDE for estimation of Transformed Columns distribution, where NN architecture is block-diagonal with 6 layers, number of blocks $N_B = 50$ and block size $S_B = 64$ (see Section 8.1). The down density \mathbb{P}^D is Uniform in top row (a)-(b)-(c), and Gaussian in bottom row (d)-(e)-(f). For different values of hyper-parameter α , (a)-(d) PSQR, (b)-(e) LSQR and (c)-(f) IS are reported, along with their empirical standard deviation. As observed, when \mathbb{P}^D is Uniform, PSO-LDE fails to learn data density due to large relative support mismatch. On other hand, when \mathbb{P}^D is Gaussian, the target surface is accurately approximated.

Uniform \mathbb{P}^D First, we evaluate PSO-LDE for different values of α on the density inference task. The applied model is BD with 6 layers, number of blocks $N_B = 50$ and block size $S_B = 64$. The dataset size is 10^8 and \mathbb{P}^D is Uniform. In Figures 33a-33b-33c we can see the appropriate errors of the learned models. The errors are huge, implying that inference task failed. The reason for this is the relative support mismatch between Uniform and Transformed Columns densities. After transformation by matrix A the samples from $\mathbb{P}^{TrClmns}$ are more widely spread out within the space \mathbb{R}^{20} . The range of samples along each dimension is now around [-10, 10] instead of appropriate range [-2.3, 2.3] in Columns distribution. Yet, the samples are mostly located in a small subspace of hyperrectangle $R = [-10, 10]^{20}$. When we choose \mathbb{P}^D to be Uniform with R as its support, most of the samples X^U and X^D are located in different areas of this huge hyperrectangle and cannot balance each other to reach PSO equilibrium. Such relative support mismatch prevents proper learning of the data density function.

Gaussian \mathbb{P}^D Next, instead of Uniform we used Gaussian distribution $\sim \mathcal{N}(\mu, \Sigma)$ as our down density \mathbb{P}^D . The mean vector μ is equal to the mean of samples from \mathbb{P}^U ; the Σ is a diagonal matrix whose non-zero values are empirical variances for each dimension of available up samples. In Figures 33d-33e-33f we can observe that overall achieved accuracy is high, yet it is worse than the results for Columns distribution. Such difference can be again explained by a mismatch between \mathbb{P}^U and \mathbb{P}^D densities. While Columns and Uniform densities in Section 12.3 are relatively aligned to each other, the Transformed Columns and

Method	PSQR	LSQR	IS
PSO-LDE, averaged over all α	$1.6 \cdot 10^{-21} \pm 3.17 \cdot 10^{-22}$	0.442 ± 0.095	26.44 ± 0.05
IS	$9.3 \cdot 10^{-21} \pm 3.4 \cdot 10^{-24}$	26.63 ± 0.86	31.3 ± 0.04
PSO-MAX	$2.1 \cdot 10^{-21} \pm 2.96 \cdot 10^{-22}$	0.54 ± 0.088	26.52 ± 0.03

Table 12: Performance comparison between various PSO instances for Transformed Columns density

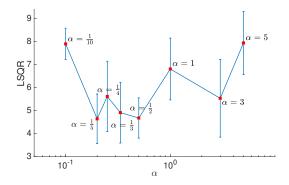


Figure 34: Evaluation of PSO-LDE for estimation of *Transformed Columns* distribution, where NN architecture is fully-connected with 4 layers of size 1024 (see Section 8.1). For different values of hyper-parameter α , LSQR error is reported, along with its empirical standard deviation. Again, the small values of α (around $\frac{1}{4}$) have lower error.

Gaussian distributions have a bounded ratio $\frac{\mathbb{P}^U(X)}{\mathbb{P}^D(X)}$ only around their mean point μ . In far away regions such ratio becomes too big/small, causing PSO inaccuracies. Hence, we argue that a better choice of \mathbb{P}^D would yield better accuracy.

Further, we can also see that in case of $Transformed\ Columns\ PSO-LDE$ with $\alpha=\frac{1}{5}$ achieves the smallest error, with its LSQR being 0.32 ± 0.02 . Additionally, we evaluated the Importance Sampling (IS) method from Table 2 and PSO-MAX defined in Eq. (38)-(39). In Table 12 we see that performance of PSO-MAX is slightly worse than PSO-LDE, similarly to what was observed for Columns. Moreover, the IS fails entirely, producing a very large error. Furthermore, in order to stabilize its learning process we were required to reduce the learning rate from 0.0035 to 0.0001. Hence, here we can see again the superiority of bounded magnitude functions over not bounded.

Various NN Architectures Additionally, we evaluated several different NN architectures for Transformed Columns distribution, with \mathbb{P}^D being Gaussian. In Figure 34 we report performance for FC networks. As can be observed, the FC architecture has higher error w.r.t. BD architecture in Figure 33e. Likewise, PSO-LDE with α around $\frac{1}{4}$ performs better.

Further, in Figure 35 we experiment with BD architecture for different values of block size S_B . Similarly to what was observed in Section 12.3.3 for *Columns* distribution, also here too small/large block size has worsen accuracy.

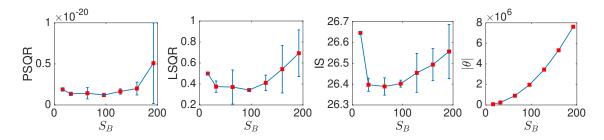


Figure 35: Evaluation of PSO-LDE for estimation of *Transformed Columns* distribution, where NN architecture is block-diagonal with 6 layers and number of blocks $N_B = 50$ (see Section 8.1). The block size S_B is taking values $\{16, 32, 64, 96, 128, 160, 192\}$. The applied loss is PSO-LDE with $\alpha = \frac{1}{5}$. For different values of S_B we report PSQR, LSQR and IS, and their empirical standard deviation. Additionally, in the last column we depict the size of θ for each value of S_B .

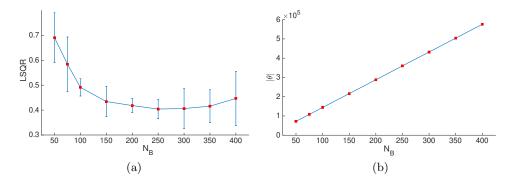


Figure 36: Evaluation of PSO-LDE for estimation of *Transformed Columns* distribution, where NN architecture is block-diagonal with 6 layers and block size $S_B = 16$ (see Section 8.1). The number of blocks N_B is changing. The applied loss is PSO-LDE with $\alpha = \frac{1}{5}$. For different values of N_B , (a) LSQR error and (b) number of weights $|\theta|$ are reported.

We also perform additional experiments for BD architecture where this time we use small blocks, with $S_B = 16$. In Figure 36 we see that for such networks the bigger number of blocks per layer N_B , that is bigger number of transformation channels, yields better performance. However, we also can observe the drop in an accuracy when the number of these channels grows considerably (above 250). Furthermore, no matter how big is the number of blocks N_B , the models with small blocks ($S_B = 16$) in Figure 36 produced inferior results w.r.t. model with big blocks ($S_B = 64$, see Figure 33e for $\alpha = \frac{1}{5}$).

Further, we evaluated the same small block network for a different number of layers N_L . In Figure 37 we can see that when N_L grows from 1 to 6, the overall performance is getting better. Yet, for larger number of layers the performance trend is inconsistent. When N_L is between 7 and 11, some values of N_L are better than the other, with no evident improvement pattern for large N_L . Moreover, for $N_L = 12$ the error grows significantly. More so, we empirically observed that 2 out of 5 runs of this setting didn't succeed to learn at all due to zero gradient. Thus, the most likely conclusion for this setting is that for a too deep networks the signal from input fails to reach its end, which is a known issue in DL

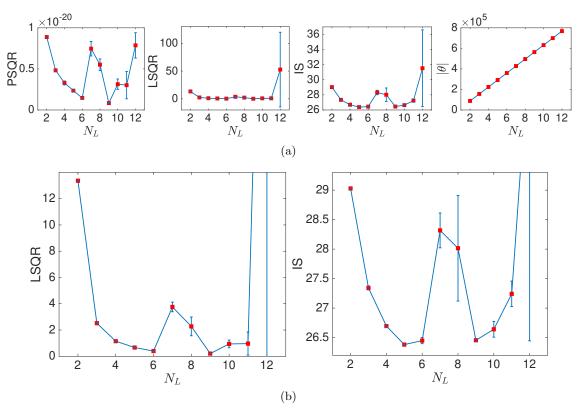


Figure 37: Evaluation of PSO-LDE for estimation of Columns distribution, where NN architecture is block-diagonal with number of blocks $N_B = 50$ and block size $S_B = 64$ (see Section 8.1). The number of layers N_L is changing from 3 to 10. The applied loss is PSO-LDE with $\alpha = \frac{1}{5}$. (a) For different values of N_L we report PSQR, LSQR and IS, and their empirical standard deviation. Additionally, in last column we depict size of θ for each value of N_L . (b) Zoom of (a).

domain. Also, from our experiments it follows that learning still can succeed, depending on the initialization of network weights.

Furthermore, along with the above inconsistency that can occur for too deep networks, for $N_L = 9$ in Figure 37 we still received our best results for *Transformed Columns*, with averaged LSQR being 0.204. That is, even when BD network uses blocks of a small size $(S_B = 16)$, it still can produce a superior performance if it is deep enough. Besides, the zero-gradient issue may be tackled by adding shortcut connections between various layers. We shall leave it as a direction for future research.

Overall, in our experiments we saw that when \mathbb{P}^U and \mathbb{P}^D are not properly aligned (i.e. far from each other), PSO fails entirely. Further, PSO-LDE with values of α around $\frac{1}{5}$ was observed to perform better, which is an another superiority evidence for small values of α . Moreover, IS with unbounded magnitude functions could not be applied at all for far away densities. BD architecture showed again significantly higher accuracy over FC networks. Block size $S_B = 96$ produced better inference. Finally, for BD networks with small blocks $(S_B = 16)$ the bigger number of blocks N_B and the bigger number of layers N_L perform better. However, at some point the increase in both can cause a drop in an accuracy.

12.5 PDF Estimation via PSO - 3D Image-based Densities

In order to further evaluate the presented herein density estimation approach, namely PSO-LDE, we use intricate 3D densities that are based on image surfaces. More specifically, we consider a given RGB image I as a function F(x, y, c) from \mathbb{R}^3 to \mathbb{R} where x, y and c represent width, height and color channel of I respectively. For simplicity we define the range for each input scalar variable from [x, y, c] to be [0, 1], with $F : [0, 1]^3 \to [0, 1]$. We use grid of values from image I to appropriately interpolate outputs of function F at any input point $X \in [0, 1]^3 \subseteq \mathbb{R}^3$. In our experiments we used a linear interpolation.

Further, we use F as pdf function which we sample to create a dataset for our PSO-LDE experiments. Yet, the function F, interpolated from image I, is not a valid pdf function since its integral can be any positive number. Thus, we normalize it by its total integral to get a normalized function \bar{F} which we use as an intricate 3D pdf function for further density estimation evaluation. Next, we sample the density \bar{F} via rejection sampling method and gather a dataset of size 10^7 per each image-based density. Furthermore, we approximate the target surface $\log \bar{F}(X)$ via PSO-LDE only from these sampled points.

Note that $\log \bar{F}$ has a very sophisticated structure since the used images have a very high contrast and nearby pixels typically have significantly different values. This makes $\log \bar{F}$ a highly non-linear function, which cannot be easily approximated by typical parametric density estimation techniques. Yet, as we will see below, due to the approximation power of DL, which is exploited in full by PSO, and due to a high flexibility of the proposed BD architecture, the non-parametric PSO-LDE allows us to accurately estimate even such complex distributions. Importantly, we emphasize that the evaluated distributions in this section have their support in \mathbb{R}^3 , and are **not** some very high-dimensional densities over image data that can be often encountered in DL domain.

We use the sampled dataset in order to infer the target $\log \bar{F}$ via PSO-LDE with $\alpha = \frac{1}{4}$. The applied NN architecture is block-diagonal with a number of blocks $N_B = 15$, a block size $S_B = 64$ and a number of layers $N_L = 14$ (see Section 8.1). In order to tackle the problem of vanishing gradients in such a deep model, we introduced shortcut connections into our network, where each layer has a form $u_i = h_i(u_{i-1}; \theta_i) + u_{i-1}$ with u_i and $h_i(\cdot; \theta_i)$ being respectively the output and the applied transformation function of *i*-th BD layer within the BD network. Note that in this paper we use such shortcuts only for the experiments of this section. Furthermore, after training is finished, we convert the inferred \bar{F} back into an image format, producing an inferred image I'.

In Figures 38 and 39 we show inferred images for several input images. As can be seen, there is high resemblance between both input I and inferred I'. That is, PSO-LDE succeeded to accurately infer densities even with a very complicated surface. Note that each image-based density was inferred by using identical hyper-parameters, that are the same as in the rest of our experiments (except for NN structure where shortcuts were applied). Additional parameter-tuning per specific input image will most probably improve the produced herein results.

13. Conclusions and Future Work

In this paper we contributed a new algorithm family, *Probabilistic Surface Optimization* (PSO), that allows to learn numerous different statistical functions of given data, including

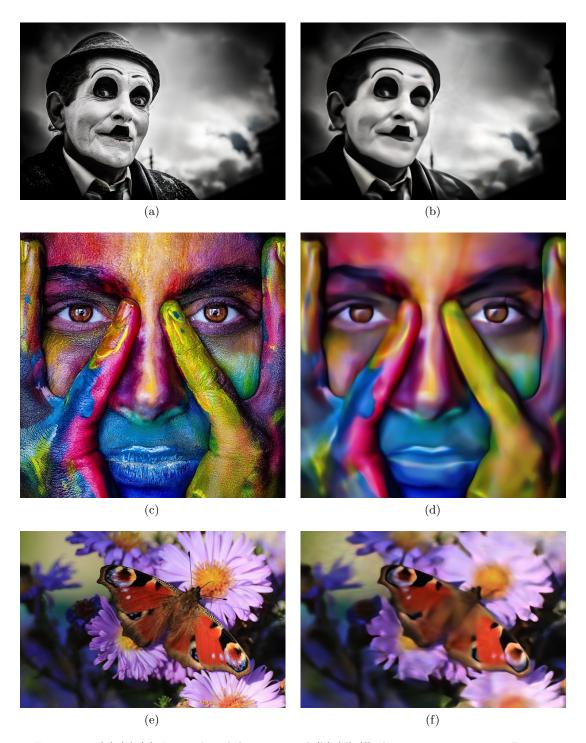


Figure 38: (a),(c),(e) Image-based densities and (b),(d),(f) their approximations - Part 1.

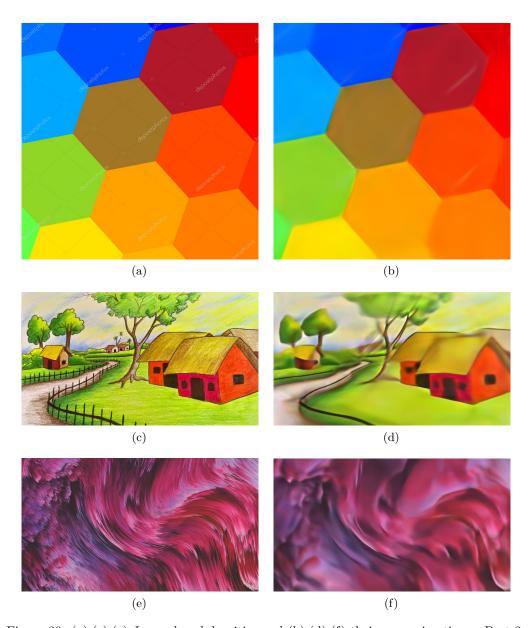


Figure 39: (a),(c),(e) Image-based densities and (b),(d),(f) their approximations - Part 2.

(conditional) density estimation and ratios between two unknown pdfs of two given datasets. In our work we found a new perspective to view a model as a representation of a virtual physical surface, which is pushed by the PSO algorithm up and down via gradient descent (GD) optimization updates. Further, the equilibrium at each point, that is, when up and down forces are point-wise equal, ensures that the converged surface satisfies PSO balance state, where the ratio of the frequency components is equal to the opposite ratio of the analytical components. In Section 3 we saw that such formulation generalizes many existing works, like energy and unnormalized models as also critics of GAN approaches. Likewise, we saw that the cross entropy loss from the image classification domain is also an instance of PSO, which applies the same thermodynamical forces over several NN surfaces in parallel.

Moreover, the **main** goal behind this work is to introduce a novel universal way in forging new statistical techniques and appropriate losses. Due to simplicity and intuitiveness of the presented PSO principles, this new framework allows for easy derivation of new statistical approaches, which, in turn, is highly useful in many different domains. Depending on the target function required by a specific application, a data analyst can select suitable *magnitude* functions according to the PSO *balance state*, and simply employ them inside the general PSO loss. Along this paper we demonstrated a step-by-step derivation of several such new approaches.

Likewise, herein we investigated the reason for such high resemblance between optimization of neural networks and thermodynamics over virtual surfaces. We found that during the optimization, a change of network output at any point (the height change of the virtual surface at the point) is equal to gradient similarity between this point and the optimized training point. Furthermore, following from this, the surface changes only at points where the gradients have similar direction to a gradient of the optimized point. Additionally, in our experiments we show that gradient similarity has an approximately local support, with its values decreasing for far away points. This, in turn, has a strong analogy to bandwidth of KDE method - both KDE bandwidth and gradient similarity of NN may be viewed as model hyper-parameters that control the bias-variance tradeoff. Moreover, the side-influence of gradient similarity is directly related to generalization properties of neural networks, explaining how each training point changes NN output at any given testing point along the optimization.

Also, we analyzed convergence and stability of PSO under the *expressiveness* limit assumption. Specifically, we considered a model whose gradients at various training points are orthogonal to each other, which cancels out the side-*influence* between the points and leads to an infinite effective representation capacity of a NN. Under such setting we showed that during the optimization an NN undergoes an adaptation that matches exactly the above described virtual surface thermodynamics. Furthermore, in our experiments we demonstrated that the gradients at different points indeed tend to be *approximately* orthogonal to each other, thus justifying the *expressiveness* assumption.

Further, we showed **empirically** that in practice PSO performance strongly depends on the actual gradient similarity of the neural network, and proposed an explanation behind this relation. Viewing the gradient similarity as a kernel-like function with a local support, a large radius of this support will lead to the high interference between different surface areas. In our experiments we showed that large values of such local support "radius" are correlated with a sub-optimal optimization performance in case of a large training dataset. Moreover, if this

side-influence "radius" is too small and in case of a small training dataset, the surface will converge to peaks around the training points and also produce a poor target approximation. Thus, similarly to the optimal bandwidth of KDE method, the desired amount of overall influence produced by gradient similarity depends on the number of available training points. Furthermore, the above influence "radius" of the gradient similarity can be interpreted also as a flexibility setting of a NN surface. That is, less side-influence between different areas yields a more flexible NN.

Further, we applied PSO to learn data log-density via non-parametric estimation, proposing several new PSO instances for this purpose, including PSO log density estimators (PSO-LDE). Moreover, we analyzed optimization stability of the new approaches, emphasized their weak points, and also provided some techniques to overcome them. Additionally, we empirically investigated both underfitting and overfitting scenarios that can occur in PSO, and discussed their relation to the surface (neural network) flexibility. Furthermore, we presented a new NN block-diagonal architecture that allowed us to significantly reduce the side-influence between far away points (the gradient similarity between distant points within input space) and to extremely increase an approximation accuracy. In our experiments we showed how the above methods can be used to perform precise pdf inference of multi-modal 20D data, getting a superior accuracy over other state-of-the-art baselines. Importantly, in an infinite dataset setting we also empirically revealed a connection between the point-wise error and gradient norm at the point, which in theory can be used for measuring model uncertainty.

Along this paper we remarked many possible research directions to further enhance PSO density estimation techniques. The current solution is still very new and many of its aspects require additional attention and further study. First of all, it is important to understand the real relation between bias and variance of PSO estimators and various properties of the *gradient similarity* function, and to perform proper mathematical analysis in contrast to the empirical investigation taken in this paper. This can lead to a better explanation of the PSO convergence properties, and may guide us to better NN architectures and new methods to control the bias-variance tradeoff, as also new techniques for quantifying model uncertainty in a small dataset setting.

Further, selection of down density should be done in a smarter way, since without it we cannot handle high-dimensional data due to relative support mismatch. Likewise, currently in a small dataset setting PSO yields a sub-optimal solution, which we argue can be significantly improved once we understand the exact relation between NN flexibility and the number of available training points, and how to control properties of the gradient similarity. Hence, this investigation avenue is also very crucial for PSO applicability in practice, e.g. in the robotics domain.

Moreover, in the context of PSO-LDE, it is still unclear how to pick value of the hyperparameter α for better accuracy, without learning multiple models for many different values and selecting the one with the highest performance metric. It is important to understand the exact connection between α and the produced log-pdf estimation, and also to provide a more intelligent way to choose α based on properties of the given data. Furthermore, since PSO framework allows us to generate a huge number of various PSO instances to approximate a specific target function, a more thorough exploration of all PSO instances for log-pdf inference is required. Herein, the goal is to categorize different instances by their performance properties and to find more optimal PSO losses.

We plan to address all of the above in our future work.

14. Acknowledgments

This work was supported in part by the Israel Ministry of Science & Technology (MOST) and Intel Corporation. We gratefully acknowledge the support of NVIDIA Corporation with the donation of the Titan Xp GPU, which, among other GPUs, was used for this research.

Appendix A. Proof of Theorem 1

Consider definitions in Table 1. Further, define *PSO functional*:

$$\begin{split} L_{PSO}(f) &= -\mathop{\mathbb{E}}_{X \sim \mathbb{P}^U} \widetilde{M}^U \left[X, f(X) \right] + \mathop{\mathbb{E}}_{X \sim \mathbb{P}^D} \widetilde{M}^D \left[X, f(X) \right] = \\ &= \int -\mathbb{P}^U(X) \cdot \widetilde{M}^U \left[X, f(X) \right] + \mathbb{P}^D(X) \cdot \widetilde{M}^D \left[X, f(X) \right] dX = \\ &= L^{U \cap D}(f) + L^{U \setminus D}(f) + L^{D \setminus U}(f), \end{split}$$

$$\begin{split} L^{U\cap D}(f) &\triangleq \int_{\mathbb{S}^{U\cap D}} -\mathbb{P}^{U}(X) \cdot \widetilde{M}^{U}\left[X, f(X)\right] + \mathbb{P}^{D}(X) \cdot \widetilde{M}^{D}\left[X, f(X)\right] dX \\ L^{U\setminus D}(f) &\triangleq -\int_{\mathbb{S}^{U\setminus D}} \mathbb{P}^{U}(X) \cdot \widetilde{M}^{U}\left[X, f(X)\right] dX \\ L^{D\setminus U}(f) &\triangleq \int_{\mathbb{S}^{D\setminus U}} \mathbb{P}^{D}(X) \cdot \widetilde{M}^{D}\left[X, f(X)\right] dX, \end{split}$$

where we define $\widetilde{M}^{U}[X,s] \triangleq \int_{s_0}^{s} M^{U}(X,t)dt$ and $\widetilde{M}^{D}[X,s] \triangleq \int_{s_0}^{s} M^{D}(X,t)dt$ to be antiderivatives of $M^{U}(\cdot)$ and $M^{D}(\cdot)$ respectively, not necessarily known analytically.

Furthermore, in case \mathbb{P}^U and \mathbb{P}^D have an identical support, then we have $L_{PSO}(f) = L^{U \cap D}(f)$. Such a setting is the one discussed in most of the paper, and its variational minima is proven below in Section A.1. Additionally, afterwards in Sections A.2 and A.3 we continue to derive a minima of functionals $L^{U \setminus D}(f)$ and $L^{D \setminus U}(f)$ as a proof of part 2 in Theorem 1.

A.1 Functional $L^{U\cap D}$ over $\mathbb{S}^{U\cap D}$

Consider the following minimization:

$$f^* \in \underset{f \in C^2(\mathbb{S}^{U \cap D})}{\operatorname{arg inf}} L^{U \cap D}(f) \tag{43}$$

where f is a twice continuously differentiable function with a support in $\mathbb{S}^{U\cap D}$. Further, we will characterize f^* in Eq. (43) using calculus of variations and the appropriate Euler-Lagrange equation of the functional $L^{U\cap D}$.

Remark 30 Importantly, the below variational-based proof is only valid when considering specific function space for which the fundamental lemma of calculus of variations is proven.

Therefore, herein we are limiting our proof to the case where $f^* \in C^2(\mathbb{S}^{U \cap D})$. Furthermore, this assumption can be weakened to a class of square integrable functions (Jost et al., 1998), but the proof becomes more difficult and hence we shall leave it for future work. Likewise, we assume here that all regularity conditions, including functions M^U and M^D being continuous almost everywhere, also hold; eliminating these assumptions and providing a more general case is out of this paper scope.

Next, consider an arbitrary differentiable function $\eta : \mathbb{R}^n \to \mathbb{R}$ and a small number ϵ , with $\epsilon \cdot \eta(X)$ being a variation of the function f(X), and define the following objective $J(\epsilon)$:

$$\begin{split} J(\epsilon) &= L^{U\cap D}\left[f(X) + \epsilon \cdot \eta(X)\right] = \\ &= \int_{\mathbb{S}^{U\cap D}} -\mathbb{P}^{U}(X) \cdot \widetilde{M}^{U}\left[X, f(X) + \epsilon \cdot \eta(X)\right] + \mathbb{P}^{D}(X) \cdot \widetilde{M}^{D}\left[X, f(X) + \epsilon \cdot \eta(X)\right] dX. \end{split}$$

From calculus of variations it follows that a specific f is a minima of $L^{U\cap D}(f)$ iff $\epsilon=0$ is a minima of $J(\epsilon)$ for this f and for any $\eta(X)$ (Courant and Hilbert, 1953). Hence, we can find the solution of Eq. (43) by finding f that satisfies:

$$0 = \arg\min_{\epsilon} J(\epsilon).$$

To this end, we consider the second derivative test for $\epsilon = 0$ to be a minima of $J(\epsilon)$:

$$\frac{dJ(\epsilon)}{d\epsilon}\big|_{\epsilon=0} = 0, \quad \frac{d^2J(\epsilon)}{d\epsilon^2}\big|_{\epsilon=0} > 0 \tag{44}$$

and find f that satisfies these conditions for any differentiable $\eta(X)$. Note that the second condition is sufficient but is not necessary and can be replaced by more general conditions from the *higher-order derivative test*. Yet, in practice it is good enough since it is satisfied by most of PSO instances, as is mentioned below.

The first derivative of the objective $J(\epsilon)$ is:

$$\begin{split} \frac{dJ(\epsilon)}{d\epsilon} &= \int_{\mathbb{S}^{U\cap D}} \left[-\mathbb{P}^{U}(X) \cdot \frac{\partial \widetilde{M}^{U}(X,s)}{\partial s} \bigg|_{s=f(X)+\epsilon \cdot \eta(X)} + \\ &+ \mathbb{P}^{D}(X) \cdot \frac{\partial \widetilde{M}^{D}(X,s)}{\partial s} \bigg|_{s=f(X)+\epsilon \cdot \eta(X)} \right] \cdot \eta(X) dX = \\ &= \int_{\mathbb{S}^{U\cap D}} \left[-\mathbb{P}^{U}(X) \cdot M^{U} \left[X, f(X) + \epsilon \cdot \eta(X) \right] + \\ &+ \mathbb{P}^{D}(X) \cdot M^{D} \left[X, f(X) + \epsilon \cdot \eta(X) \right] \right] \cdot \eta(X) dX. \end{split}$$

Further, we apply the first condition from Eq. (44):

$$\frac{dJ(\epsilon)}{d\epsilon}\Big|_{\epsilon=0} = \int_{\mathbb{S}^{U\cap D}} \left[-\mathbb{P}^U(X)\cdot M^U\left[X,f(X)\right] + \mathbb{P}^D(X)\cdot M^D\left[X,f(X)\right] \right] \cdot \eta(X)dX = 0.$$

According to the fundamental lemma of calculus of variations, from the above expression it follows that:

$$-\mathbb{P}^{\scriptscriptstyle U}(X)\cdot M^{\scriptscriptstyle U}\left[X,f(X)\right]+\mathbb{P}^{\scriptscriptstyle D}(X)\cdot M^{\scriptscriptstyle D}\left[X,f(X)\right]=0,$$

which is the Euler-Lagrange equation of the functional $L^{U\cap D}(f)$. Further, we can rewrite it as:

$$\mathbb{P}^{U}(X) \cdot M^{U}\left[X, f(X)\right] = \mathbb{P}^{D}(X) \cdot M^{D}\left[X, f(X)\right], \tag{45}$$

with this form being referred in the main paper as PSO balance state.

The second derivative of the objective $J(\epsilon)$ is:

$$\begin{split} \frac{d^2 J(\epsilon)}{d\epsilon^2} &= \int_{\mathbb{S}^{U \cap D}} \left[-\mathbb{P}^U(X) \cdot M^{U'} \left[X, f(X) + \epsilon \cdot \eta(X) \right] + \right. \\ &\left. + \mathbb{P}^D(X) \cdot M^{D'} \left[X, f(X) + \epsilon \cdot \eta(X) \right] \right] \cdot \eta^2(X) dX, \end{split}$$

where $M^{U\prime}(X,s) \triangleq \frac{\partial M^U(X,s)}{\partial s}$ and $M^{D\prime}(X,s) \triangleq \frac{\partial M^D(X,s)}{\partial s}$. Further, we apply the second condition from Eq. (44):

$$\frac{d^2 J(\epsilon)}{d\epsilon^2}\Big|_{\epsilon=0} = \int_{\mathbb{Q}U\cap\mathcal{D}} \left[-\mathbb{P}^U(X) \cdot M^{U'}[X, f(X)] + \mathbb{P}^D(X) \cdot M^{D'}[X, f(X)] \right] \cdot \eta^2(X) dX.$$

For the above expression to be positive for any $\eta(X)$, $\frac{d^2 J(\epsilon)}{d\epsilon^2}\Big|_{\epsilon=0} > 0$, it is sufficient to satisfy the following condition at any $X \in \mathbb{S}^{U \cap D}$:

$$\left[-\mathbb{P}^{U}(X) \cdot M^{U'}[X, f(X)] + \mathbb{P}^{D}(X) \cdot M^{D'}[X, f(X)] \right] > 0,$$

or

$$\mathbb{P}^{U}(X) \cdot M^{U'}[X, f(X)] < \mathbb{P}^{D}(X) \cdot M^{D'}[X, f(X)]. \tag{46}$$

To conclude, for $f^* \in C^2(\mathbb{S}^{U \cap D})$ to be a minima of $L^{U \cap D}(f)$ it is necessary to satisfy Eq. (45) and it is sufficient to satisfy Eq. (46). These conditions have to be examined w.r.t. a particular pair of magnitude functions $\{M^U, M^D\}$ to verify that a solution f^* of Eq. (45) is also satisfying Eq. (46). If Eq. (46) holds then f^* is a minima. Further, if the condition in Eq. (46) is not satisfied, the higher derivatives of $J(\epsilon)$ must be tested according to the higher-order derivative test. However, in practice it is typically not required since most of the PSO instances satisfy Eq. (46) at f^* (see examples in main paper).

A.2 Functional $L^{U \setminus D}$ **over** $\mathbb{S}^{U \setminus D}$

Herein we prove part 2 of Theorem 1 from the paper, considering the input space outside of the mutual support $\mathbb{S}^{U\cap D}$. Specifically, consider the following minimization:

$$f^* \in \operatorname*{arg\,inf} L^{U \setminus D}(f) = - \int_{\mathbb{S}^{U \setminus D}} \mathbb{P}^U(X) \cdot \widetilde{M}^U\left[X, f(X)\right] dX$$

where f is an arbitrary function with a support in $\mathbb{S}^{U\setminus D}$, for which the above integral is well-defined. We are going to prove the following Theorem (identical to part 2 of Theorem 1).

Theorem 31 Define an arbitrary function $h: \mathbb{S}^{U \setminus D} \to \mathbb{R}$. Then, depending on properties of a function M^U , for f^* to be minima of $L^{U\setminus D}$ it must satisfy:

- 1. If $\forall X \in \mathbb{S}^{U \setminus D}$, $t \in \mathbb{R} : M^U(X,t) > 0$, then $f^*(X) = \infty$.
- 2. If $\forall X \in \mathbb{S}^{U \setminus D}$, $t \in \mathbb{R} : M^U(X,t) < 0$, then $f^*(X) = -\infty$.
- 3. If $\forall X \in \mathbb{S}^{U \setminus D}$, $t \in \mathbb{R} : M^U(X,t) \equiv 0$, then $f^*(X)$ can be arbitrary.
- 4. If $\forall X \in \mathbb{S}^{U \setminus D}, t \in \mathbb{R}$:

$$M^{U}(X,t) = \begin{cases} 0, & t = h(X) \\ > 0, & t < h(X) \\ < 0, & t > h(X) \end{cases}$$

then $f^*(X) = h(X)$.

5. Otherwise, additional analysis is required.

The motivation behind Theorem 31, proved below, is that in many PSO instances M^U satisfies one of its conditions. In such case this Theorem can be applied to understand the PSO convergence behavior in the region $\mathbb{S}^{U\setminus D}$. Moreover, Theorem further supports the PSO framework's perspective, where virtual forces are pushing NN surface towards a thermodynamical equilibrium.

Proof

Define a new function $f_a(X) \triangleq f(X) + a$ for some scalar a and for some function f. Due to the definition of \widetilde{M}^U , for any a and for any f we have:

$$\Delta_a L \triangleq L^{U \setminus D}(f) - L^{U \setminus D}(f_a) = \int_{\mathbb{S}^{U \setminus D}} \mathbb{P}^U(X) \cdot \left[\int_{f(X)}^{f(X) + a} M^U(X, t) dt \right] dX. \tag{47}$$

Further, from Eq. (47) we can conclude that if M^U is a strictly positive function, $\forall X \in \mathbb{S}^{U \setminus D}, t \in \mathbb{R} : M^U(X,t) > 0$, then any a > 0 satisfies $\Delta_a L > 0$. Thus, in such a case $L^{U \setminus D}(f_a)$ is smaller than $L^{U \setminus D}(f)$ and hence f(X) can not be a minima of $L^{U \setminus D}$ unless $\forall X \in \mathbb{S}^{U \setminus D} : f(X) = \infty$.

Due to similar arguments, in case $\forall X \in \mathbb{S}^{U \setminus D}, t \in \mathbb{R} : M^U(X, t) < 0$, any a < 0 satisfies $\Delta_a L > 0$. Hence, the minima of $L^{U \setminus D}$ in this case must satisfy $\forall X \in \mathbb{S}^{U \setminus D} : f(X) = -\infty$.

Furthermore, if $\forall X \in \mathbb{S}^{U \setminus D}, t \in \mathbb{R} : M^U(X,t) \equiv 0$, then for any a we have $\Delta_a L = 0$. Moreover, in such a case we also have $\forall X \in \mathbb{S}^{U \setminus D}, t \in \mathbb{R} : \widetilde{M}^U(X,t) \equiv 0$ and $\forall f : L^{U \setminus D}(f) \equiv 0$. Therefore, f(X) can have an arbitrary outputs at $X \in \mathbb{S}^{U \setminus D}$, since the functional $L^{U \setminus D}$ does not depend on it. In practice this means that the optimization does not enforce any constraint over a learned model within a region $\mathbb{S}^{U \setminus D}$ where up magnitude function M^U is zero.

Finally, we will prove the forth property of the Theorem. Consider an arbitrary function h(X) and define M^U as:

$$M^{U}(X,t) = \begin{cases} 0, & t = h(X) \\ > 0, & t < h(X) \\ < 0, & t > h(X) \end{cases}$$
(48)

Next, define the performance difference between f and h as:

$$\Delta_{f,h}L \triangleq L^{U \setminus D}(f) - L^{U \setminus D}(h) =$$

$$= \int_{\mathbb{S}^{U \setminus D}} \mathbb{P}^{U}(X) \cdot \left[\widetilde{M}^{U}[X, h(X)] - \widetilde{M}^{U}[X, f(X)]\right] dX = \int_{\mathbb{S}^{U \setminus D}} \mathbb{P}^{U}(X) \cdot D_{f,h}(X) dX,$$

where

$$\begin{split} D_{f,h}(X) & \triangleq \widetilde{M}^{\scriptscriptstyle U}\left[X,h(X)\right] - \widetilde{M}^{\scriptscriptstyle U}\left[X,f(X)\right] = \int_{s_0}^{h(X)} M^{\scriptscriptstyle U}(X,t)dt - \int_{s_0}^{f(X)} M^{\scriptscriptstyle U}(X,t)dt = \\ & = \begin{cases} 0, & f(X) = h(X) \\ \int_{f(X)}^{h(X)} M^{\scriptscriptstyle U}(X,t)dt, & f(X) < h(X) \\ - \int_{h(X)}^{f(X)} M^{\scriptscriptstyle U}(X,t)dt, & f(X) > h(X) \end{cases}. \end{split}$$

Using the properties of M^U in Eq. (48), we can conclude that:

$$D_{f,h}(X) = \begin{cases} 0, & f(X) = h(X) \\ > 0, & \text{otherwise} \end{cases}$$

and therefore also

$$\Delta_{f,h}L = \begin{cases} 0, & \forall X \in \mathbb{S}^{U \setminus D} : f(X) = h(X) \\ > 0, & \text{otherwise} \end{cases}.$$

Thus, we can conclude that if M^U is defined as in Eq. (48), then f(X) can not be a minima of $L^{U\setminus D}$ unless $\forall X\in\mathbb{S}^{U\setminus D}:f(X)=h(X)$.

Otherwise, if $M^{U}(X,t)$ does not satisfy any of the Theorem properties (1)-(4), a further analysis of this particular magnitude function in the context of $L^{U \setminus D}$ needs to be done.

A.3 Functional $L^{D\setminus U}$ over $\mathbb{S}^{D\setminus U}$

Consider the following minimization:

$$f^* \in \operatorname*{arg\,inf} L^{D \setminus U}(f) = \int_{\mathbb{S}^{D \setminus U}} \mathbb{P}^D(X) \cdot \widetilde{M}^D\left[X, f(X)\right] dX$$

where f is an arbitrary function with a support in $\mathbb{S}^{D\setminus U}$, for which the above integral is well-defined. The PSO convergence behavior in the region $\mathbb{S}^{D\setminus U}$ can be summarized via the following Theorem.

Theorem 32 Define an arbitrary function $h: \mathbb{S}^{D \setminus U} \to \mathbb{R}$. Then, depending on properties of a function M^D , for f^* to be minima of $L^{D \setminus U}$ it must satisfy:

1. If
$$\forall X \in \mathbb{S}^{D \setminus U}$$
, $t \in \mathbb{R} : M^D(X, t) > 0$, then $f^*(X) = -\infty$.

- 2. If $\forall X \in \mathbb{S}^{D \setminus U}$, $t \in \mathbb{R} : M^D(X,t) < 0$, then $f^*(X) = \infty$.
- 3. If $\forall X \in \mathbb{S}^{D \setminus U}$, $t \in \mathbb{R} : M^D(X, t) \equiv 0$, then $f^*(X)$ can be arbitrary.
- 4. If $\forall X \in \mathbb{S}^{D \setminus U}, t \in \mathbb{R}$:

$$M^{D}(X,t) = \begin{cases} 0, & t = h(X) \\ > 0, & t > h(X) \\ < 0, & t < h(X) \end{cases}$$

then $f^*(X) = h(X)$.

5. Otherwise, additional analysis is required.

The proof of Theorem 32 is symmetric to the proof of Theorem 31 and hence omitted.

Appendix B. Proof of Lemmas 9 and 10

B.1 Lemma 9

Consider the setting of Section 5.1. Further, notate the model Hessian as $\mathcal{H}_{\theta}(X) \equiv \nabla_{\theta\theta} f_{\theta}(X)$. Using the gradient of $L_{PSO}(f_{\theta})$ defined in Eq. (4), the second derivative of $L_{PSO}(f_{\theta})$ w.r.t. θ is:

$$\nabla_{\theta\theta}L_{PSO}(f_{\theta}) = -\underset{X \sim \mathbb{P}^{U}}{\mathbb{E}} \left[M^{U'}[X, f_{\theta}(X)] \cdot \mathcal{I}_{\theta}(X, X) + M^{U}[X, f_{\theta}(X)] \cdot \mathcal{H}_{\theta}(X) \right] + \\ + \underset{X \sim \mathbb{P}^{D}}{\mathbb{E}} \left[M^{D'}[X, f_{\theta}(X)] \cdot \mathcal{I}_{\theta}(X, X) + M^{D}[X, f_{\theta}(X)] \cdot \mathcal{H}_{\theta}(X) \right] = \\ = -\underset{X \sim \mathbb{P}^{U}}{\mathbb{E}} M^{U'}[X, f_{\theta}(X)] \cdot \mathcal{I}_{\theta}(X, X) - \underset{X \sim \mathbb{P}^{U}}{\mathbb{E}} M^{U}[X, f_{\theta}(X)] \cdot \mathcal{H}_{\theta}(X) + \\ + \underset{X \sim \mathbb{P}^{D}}{\mathbb{E}} M^{D'}[X, f_{\theta}(X)] \cdot \mathcal{I}_{\theta}(X, X) + \underset{X \sim \mathbb{P}^{D}}{\mathbb{E}} M^{D}[X, f_{\theta}(X)] \cdot \mathcal{H}_{\theta}(X).$$

Likewise, at θ^* we also have:

$$- \underset{X \sim \mathbb{P}^{U}}{\mathbb{E}} M^{U} [X, f_{\theta^{*}}(X)] \cdot \mathcal{H}_{\theta^{*}}(X) + \underset{X \sim \mathbb{P}^{D}}{\mathbb{E}} M^{D} [X, f_{\theta^{*}}(X)] \cdot \mathcal{H}_{\theta^{*}}(X) =$$

$$= - \underset{X \sim \mathbb{P}^{U}}{\mathbb{E}} M^{U} [X, f^{*}(X)] \cdot \mathcal{H}_{\theta^{*}}(X) + \underset{X \sim \mathbb{P}^{D}}{\mathbb{E}} M^{D} [X, f^{*}(X)] \cdot \mathcal{H}_{\theta^{*}}(X) =$$

$$= \int [-\mathbb{P}^{U}(X) \cdot M^{U} [X, f^{*}(X)] + \mathbb{P}^{D}(X) \cdot M^{D} [X, f^{*}(X)]] \cdot \mathcal{H}_{\theta^{*}}(X) dX = 0,$$

where the last row is true because f^* satisfies PSO balance state.

Therefore, we have

$$\mathcal{H} \equiv \nabla_{\theta\theta} L_{PSO}(f_{\theta^*}) =$$

$$= - \underset{X \sim \mathbb{P}^U}{\mathbb{E}} M^{U'}[X, f_{\theta^*}(X)] \cdot \mathcal{I}_{\theta^*}(X, X) + \underset{X \sim \mathbb{P}^D}{\mathbb{E}} M^{D'}[X, f_{\theta^*}(X)] \cdot \mathcal{I}_{\theta^*}(X, X) =$$

$$= - \underset{X \sim \mathbb{P}^U}{\mathbb{E}} M^{U'}[X, f^*(X)] \cdot \mathcal{I}_{\theta^*}(X, X) + \underset{X \sim \mathbb{P}^D}{\mathbb{E}} M^{D'}[X, f^*(X)] \cdot \mathcal{I}_{\theta^*}(X, X). \quad (49)$$

Observe also that only \mathcal{I}_{θ^*} terms depend on the parameter vector θ^* .

Additionally, \mathcal{H} has an another form:

$$\mathcal{H} = \underset{X \sim \mathbb{P}^D}{\mathbb{E}} \frac{M^U \left[X, f^*(X) \right]}{T' \left[X, \frac{\mathbb{P}^U(X)}{\mathbb{P}^D(X)} \right]} \cdot \mathcal{I}_{\theta^*}(X, X), \tag{50}$$

where $T'(X,z) \triangleq \frac{\partial T(X,z)}{\partial z}$ is a first derivative of the considered PSO convergence T(X,z). This can be derived as follows.

First, since T and $T^{-1} \equiv \frac{M^D}{M^U}$ are inverse functions, derivative of T^{-1} can be computed via derivative of T as:

$$\frac{\partial T^{-1}(X,s)}{\partial s} = \frac{1}{T'(X,T^{-1}(X,s))}.$$

Observe that due to PSO balance state we have

$$\left. \frac{\partial T^{-1}(X,s)}{\partial s} \right|_{s=f^*(X)} = \frac{1}{T'(X,T^{-1}(X,f^*(X)))} = \frac{1}{T'(X,\frac{\mathbb{P}^U(X)}{\mathbb{P}^D(X)})}.$$

Next, the expression inside integral of Eq. (49) is:

$$\begin{split} & - \mathbb{P}^{\boldsymbol{U}}(X) \cdot \boldsymbol{M}^{\boldsymbol{U}'}[X, f^*(X)] + \mathbb{P}^{\boldsymbol{D}}(X) \cdot \boldsymbol{M}^{\boldsymbol{D}'}[X, f^*(X)] = \\ & = \mathbb{P}^{\boldsymbol{D}}(X) \cdot \boldsymbol{M}^{\boldsymbol{U}'}[X, f^*(X)] \cdot \left[- \frac{\mathbb{P}^{\boldsymbol{U}}(X)}{\mathbb{P}^{\boldsymbol{D}}(X)} + \frac{\boldsymbol{M}^{\boldsymbol{D}'}[X, f^*(X)]}{\boldsymbol{M}^{\boldsymbol{U}'}[X, f^*(X)]} \right] = \\ & = \mathbb{P}^{\boldsymbol{D}}(X) \cdot \boldsymbol{M}^{\boldsymbol{U}'}[X, f^*(X)] \cdot \left[- \frac{\boldsymbol{M}^{\boldsymbol{D}}[X, f^*(X)]}{\boldsymbol{M}^{\boldsymbol{U}}[X, f^*(X)]} + \frac{\boldsymbol{M}^{\boldsymbol{D}'}[X, f^*(X)]}{\boldsymbol{M}^{\boldsymbol{U}'}[X, f^*(X)]} \right] = \\ & = \mathbb{P}^{\boldsymbol{D}}(X) \cdot \boldsymbol{M}^{\boldsymbol{U}}[X, f^*(X)] \cdot \frac{\boldsymbol{M}^{\boldsymbol{D}'}[X, f^*(X)] \cdot \boldsymbol{M}^{\boldsymbol{U}}[X, f^*(X)]^2}{\boldsymbol{M}^{\boldsymbol{U}}[X, f^*(X)]} = \\ & = \mathbb{P}^{\boldsymbol{D}}(X) \cdot \boldsymbol{M}^{\boldsymbol{U}}[X, f^*(X)] \cdot \frac{\partial \underline{\boldsymbol{M}^{\boldsymbol{D}}(X, s)}}{\partial s}|_{s = f^*(X)} = \\ & = \mathbb{P}^{\boldsymbol{D}}(X) \cdot \boldsymbol{M}^{\boldsymbol{U}}[X, f^*(X)] \cdot \frac{\partial T^{-1}(X, s)}{\partial s}|_{s = f^*(X)} = \frac{\mathbb{P}^{\boldsymbol{D}}(X) \cdot \boldsymbol{M}^{\boldsymbol{U}}[X, f^*(X)]}{T'(X, \frac{\mathbb{P}^{\boldsymbol{U}}(X)}{\mathbb{P}^{\boldsymbol{D}}(X)})}. \end{split}$$

Hence:

$$\mathcal{H} = \int \frac{\mathbb{P}^{D}(X) \cdot M^{U}[X, f^{*}(X)]}{T'(X, \frac{\mathbb{P}^{U}(X)}{\mathbb{P}^{D}(X)})} \cdot \mathcal{I}_{\theta^{*}}(X, X) dX,$$

from which Eq. (50) follows.

B.2 Lemma 10

Consider the empirical PSO gradient $\nabla_{\theta} \hat{L}_{PSO}^{N^U,N^D}(f_{\theta})$ as defined in Eq. (1). Its uncentered variance is then:

$$\mathbb{E}\left[\nabla_{\theta}\hat{L}_{PSO}^{NU,N^{D}}(f_{\theta}) \cdot \nabla_{\theta}\hat{L}_{PSO}^{NU,N^{D}}(f_{\theta})^{T}\right] = \\
= \frac{1}{(N^{U})^{2}} \sum_{i,j=1}^{N^{U}} \mathbb{E}\left[M^{U}\left[X_{i}^{U}, f_{\theta}(X_{i}^{U})\right] \cdot M^{U}\left[X_{j}^{U}, f_{\theta}(X_{j}^{U})\right] \cdot \mathcal{I}_{\theta}(X_{i}^{U}, X_{j}^{U})\right] + \\
+ \frac{1}{(N^{D})^{2}} \sum_{i,j=1}^{N^{D}} \mathbb{E}\left[M^{D}\left[X_{i}^{D}, f_{\theta}(X_{i}^{D})\right] \cdot M^{D}\left[X_{j}^{D}, f_{\theta}(X_{j}^{D})\right] \cdot \mathcal{I}_{\theta}(X_{i}^{U}, X_{j}^{D})\right] - \\
- \frac{1}{N^{U}N^{D}} \sum_{i=1}^{N^{U}} \sum_{j=1}^{N^{D}} \mathbb{E}\left[M^{U}\left[X_{i}^{U}, f_{\theta}(X_{i}^{U})\right] \cdot M^{D}\left[X_{j}^{D}, f_{\theta}(X_{j}^{D})\right] \cdot \mathcal{I}_{\theta}(X_{i}^{U}, X_{j}^{D})\right] - \\
- \frac{1}{N^{U}N^{D}} \sum_{i=1}^{N^{U}} \sum_{j=1}^{N^{D}} \mathbb{E}\left[M^{U}\left[X_{i}^{U}, f_{\theta}(X_{i}^{U})\right] \cdot M^{D}\left[X_{j}^{D}, f_{\theta}(X_{j}^{D})\right] \cdot \mathcal{I}_{\theta}(X_{j}^{D}, X_{i}^{U})\right] = \\
= \frac{1}{(N^{U})^{2}} \sum_{i=1}^{N^{U}} \mathbb{E}\left[M^{U}\left[X_{i}^{U}, f_{\theta}(X_{i}^{U})\right] \cdot M^{U}\left[X_{i}^{U}, f_{\theta}(X_{i}^{U})\right] \cdot \mathcal{I}_{\theta}(X_{i}^{U}, X_{i}^{U})\right] + \\
+ \frac{1}{(N^{D})^{2}} \sum_{i,j=1}^{N^{D}} \mathbb{E}\left[M^{D}\left[X_{i}^{D}, f_{\theta}(X_{i}^{D})\right] \cdot M^{D}\left[X_{j}^{D}, f_{\theta}(X_{j}^{U})\right] \cdot \mathcal{I}_{\theta}(X_{i}^{U}, X_{j}^{U})\right] + \\
+ \frac{1}{(N^{D})^{2}} \sum_{i,j=1}^{N^{D}} \mathbb{E}\left[M^{U}\left[X_{i}^{U}, f_{\theta}(X_{i}^{U})\right] \cdot M^{D}\left[X_{j}^{D}, f_{\theta}(X_{j}^{D})\right] \cdot \mathcal{I}_{\theta}(X_{i}^{U}, X_{j}^{D})\right] - \\
- \frac{1}{N^{U}N^{D}} \sum_{i=1}^{N^{D}} \sum_{j=1}^{N^{D}} \mathbb{E}\left[M^{U}\left[X_{i}^{U}, f_{\theta}(X_{i}^{U})\right] \cdot M^{D}\left[X_{j}^{D}, f_{\theta}(X_{j}^{D})\right] \cdot \mathcal{I}_{\theta}(X_{i}^{U}, X_{j}^{D})\right] - \\
- \frac{1}{N^{U}N^{D}} \sum_{i=1}^{N^{D}} \sum_{i=1}^{N^{D}} \mathbb{E}\left[M^{U}\left[X_{i}^{U}, f_{\theta}(X_{i}^{U})\right] \cdot M^{D}\left[X_{j}^{D}, f_{\theta}(X_{j}^{D})\right] \cdot \mathcal{I}_{\theta}(X_{i}^{U}, X_{j}^{D})\right] - \\
- \frac{1}{N^{U}N^{D}} \sum_{i=1}^{N^{D}} \sum_{i=1}^{N^{D}} \mathbb{E}\left[M^{U}\left[X_{i}^{U}, f_{\theta}(X_{i}^{U})\right] \cdot M^{D}\left[X_{j}^{D}, f_{\theta}(X_{j}^{D})\right] \cdot \mathcal{I}_{\theta}(X_{i}^{U}, X_{j}^{D})\right] - \\
- \frac{1}{N^{U}N^{D}} \sum_{i=1}^{N^{D}} \sum_{i=1}^{N^{D}} \mathbb{E}\left[M^{U}\left[X_{i}^{U}, f_{\theta}(X_{i}^{U})\right] \cdot M^{D}\left[X_{j}^{D}, f_{\theta}(X_{j}^{D})\right] \cdot \mathcal{I}_{\theta}(X_{i}^{U}, X_{j}^{D})\right]. (51)$$

Denote:

$$\bar{\mu}_{\theta}^{U} \triangleq \underset{X \sim \mathbb{P}^{U}}{\mathbb{E}} M^{U} [X, f_{\theta}(X)] \cdot \nabla_{\theta} f_{\theta}(X), \quad \bar{\mu}_{\theta}^{D} \triangleq \underset{X \sim \mathbb{P}^{D}}{\mathbb{E}} M^{D} [X, f_{\theta}(X)] \cdot \nabla_{\theta} f_{\theta}(X). \tag{52}$$

According to Eq. (51), we have:

$$\begin{split} \mathbb{E}\left[\nabla_{\theta}\hat{L}_{PSO}^{N^{U},N^{D}}(f_{\theta})\cdot\nabla_{\theta}\hat{L}_{PSO}^{N^{U},N^{D}}(f_{\theta})^{T}\right] = \\ &= \frac{1}{N^{U}}\sum_{X\sim\mathbb{P}^{U}}\left[M^{U}\left[X,f_{\theta}(X)\right]^{2}\cdot\mathcal{I}_{\theta}(X,X)\right] + \frac{1}{N^{D}}\sum_{X\sim\mathbb{P}^{D}}\left[M^{D}\left[X,f_{\theta}(X)\right]^{2}\cdot\mathcal{I}_{\theta}(X,X)\right] + \\ &+ \frac{N^{U}-1}{N^{U}}\bar{\mu}_{\theta}^{U}\cdot(\bar{\mu}_{\theta}^{U})^{T} + \frac{N^{D}-1}{N^{D}}\bar{\mu}_{\theta}^{D}\cdot(\bar{\mu}_{\theta}^{D})^{T} - \bar{\mu}_{\theta}^{U}\cdot(\bar{\mu}_{\theta}^{D})^{T} - \bar{\mu}_{\theta}^{D}\cdot(\bar{\mu}_{\theta}^{U})^{T} = \\ &= \frac{1}{N^{U}}\left[\sum_{X\sim\mathbb{P}^{U}}\left[M^{U}\left[X,f_{\theta}(X)\right]^{2}\cdot\mathcal{I}_{\theta}(X,X)\right] - \bar{\mu}_{\theta}^{U}\cdot(\bar{\mu}_{\theta}^{U})^{T}\right] + \\ &+ \frac{1}{N^{D}}\left[\sum_{X\sim\mathbb{P}^{D}}\left[M^{D}\left[X,f_{\theta}(X)\right]^{2}\cdot\mathcal{I}_{\theta}(X,X)\right] - \bar{\mu}_{\theta}^{D}\cdot(\bar{\mu}_{\theta}^{D})^{T} - \bar{\mu}_{\theta}^{D}\cdot(\bar{\mu}_{\theta}^{U})^{T}\right] + \\ &+ \bar{\mu}_{\theta}^{U}\cdot(\bar{\mu}_{\theta}^{U})^{T} + \bar{\mu}_{\theta}^{D}\cdot(\bar{\mu}_{\theta}^{D})^{T} - \bar{\mu}_{\theta}^{U}\cdot(\bar{\mu}_{\theta}^{D})^{T} - \bar{\mu}_{\theta}^{D}\cdot(\bar{\mu}_{\theta}^{U})^{T}. \end{split}$$

Further, the outer product of $\nabla_{\theta} \hat{L}_{PSO}^{N^U,N^D}(f_{\theta})$'s expected value $\mathbb{E}\left[\nabla_{\theta} \hat{L}_{PSO}^{N^U,N^D}(f_{\theta})\right] = -\bar{\mu}_{\theta}^U + \bar{\mu}_{\theta}^D$ is:

$$\mathbb{E}\left[\nabla_{\theta}\hat{L}_{PSO}^{N^U,N^D}(f_{\theta})\right] \cdot \mathbb{E}\left[\nabla_{\theta}\hat{L}_{PSO}^{N^U,N^D}(f_{\theta})\right]^T = \bar{\mu}_{\theta}^U \cdot (\bar{\mu}_{\theta}^U)^T + \bar{\mu}_{\theta}^D \cdot (\bar{\mu}_{\theta}^D)^T - \bar{\mu}_{\theta}^U \cdot (\bar{\mu}_{\theta}^D)^T - \bar{\mu}_{\theta}^D \cdot (\bar{\mu}_{\theta}^U)^T,$$

and hence:

$$\operatorname{Var}\left[\nabla_{\theta} \hat{L}_{PSO}^{N^{U},N^{D}}(f_{\theta})\right] = \frac{1}{N^{U}} \left[\underset{X \sim \mathbb{P}^{U}}{\mathbb{E}} \left[M^{U} \left[X, f_{\theta}(X) \right]^{2} \cdot \mathcal{I}_{\theta}(X,X) \right] - \bar{\mu}_{\theta}^{U} \cdot (\bar{\mu}_{\theta}^{U})^{T} \right] + \frac{1}{N^{D}} \left[\underset{X \sim \mathbb{P}^{D}}{\mathbb{E}} \left[M^{D} \left[X, f_{\theta}(X) \right]^{2} \cdot \mathcal{I}_{\theta}(X,X) \right] - \bar{\mu}_{\theta}^{D} \cdot (\bar{\mu}_{\theta}^{D})^{T} \right].$$

Next, using relations $N^U = \frac{\tau}{\tau+1}N$ and $N^D = \frac{1}{\tau+1}N$, we can write the above variance as:

$$\operatorname{Var}\left[\nabla_{\theta}\hat{L}_{PSO}^{N^{U},N^{D}}(f_{\theta})\right] = \frac{1}{N} \left[\frac{\tau+1}{\tau} \underset{X \sim \mathbb{P}^{U}}{\mathbb{E}} \left[M^{U}\left[X, f_{\theta}(X)\right]^{2} \cdot \mathcal{I}_{\theta}(X, X)\right] + \left[\tau+1\right] \underset{X \sim \mathbb{P}^{D}}{\mathbb{E}} \left[M^{D}\left[X, f_{\theta}(X)\right]^{2} \cdot \mathcal{I}_{\theta}(X, X)\right] - \frac{\tau+1}{\tau} \bar{\mu}_{\theta}^{U} \cdot (\bar{\mu}_{\theta}^{U})^{T} - \left[\tau+1\right] \bar{\mu}_{\theta}^{D} \cdot (\bar{\mu}_{\theta}^{D})^{T}\right]. \tag{53}$$

Further, due to the identical support assumption $\mathbb{S}^U \equiv \mathbb{S}^D$ we also have $\bar{\mu}^U_{\theta^*} = \bar{\mu}^D_{\theta^*}$:

$$\mathbb{E}\left[\nabla_{\theta}\hat{L}_{PSO}^{N^{U},N^{D}}(f_{\theta^{*}})\right] = -\bar{\mu}_{\theta^{*}}^{U} + \bar{\mu}_{\theta^{*}}^{D} =$$

$$= -\mathbb{E}_{X \sim \mathbb{P}^{U}} M^{U}\left[X, f^{*}(X)\right] \cdot \nabla_{\theta} f_{\theta^{*}}(X) + \mathbb{E}_{X \sim \mathbb{P}^{D}} M^{D}\left[X, f^{*}(X)\right] \cdot \nabla_{\theta} f_{\theta^{*}}(X) =$$

$$= \int \left[-\mathbb{P}^{U}(X) \cdot M^{U}\left[X, f^{*}(X)\right] + \mathbb{P}^{D}(X) \cdot M^{D}\left[X, f^{*}(X)\right]\right] \cdot \nabla_{\theta} f_{\theta^{*}}(X) dX = 0, \quad (54)$$

where the last row is true because f^* satisfies PSO balance state. Hence, the following is also true:

$$\bar{\mu}_{\theta^*}^U \cdot (\bar{\mu}_{\theta^*}^U)^T = \bar{\mu}_{\theta^*}^D \cdot (\bar{\mu}_{\theta^*}^D)^T = \bar{\mu}_{\theta^*}^U \cdot (\bar{\mu}_{\theta^*}^D)^T = \bar{\mu}_{\theta^*}^D \cdot (\bar{\mu}_{\theta^*}^U)^T.$$
 (55)

Therefore,
$$\operatorname{Var}\left[\nabla_{\theta}\hat{L}_{PSO}^{N^{U},N^{D}}(f_{\theta})\right]$$
 (Eq. (53)) at θ^{*} is $\operatorname{Var}\left[\nabla_{\theta}\hat{L}_{PSO}^{N^{U},N^{D}}(f_{\theta^{*}})\right] = \frac{1}{N}\mathcal{J}$ with:

$$\mathcal{J} = \frac{\tau + 1}{\tau} \underset{X \sim \mathbb{P}^{U}}{\mathbb{E}} \left[M^{U} \left[X, f^{*}(X) \right]^{2} \cdot \mathcal{I}_{\theta^{*}}(X, X) \right] +$$

$$+ (\tau + 1) \underset{X \sim \mathbb{P}^{D}}{\mathbb{E}} \left[M^{D} \left[X, f^{*}(X) \right]^{2} \cdot \mathcal{I}_{\theta^{*}}(X, X) \right] -$$

$$- \frac{(\tau + 1)^{2}}{\tau} \underset{X' \sim \mathbb{P}^{D}}{\mathbb{E}} M^{U} \left[X, f^{*}(X) \right] \cdot M^{D} \left[X', f^{*}(X') \right] \cdot \mathcal{I}_{\theta^{*}}(X, X'),$$

where we applied identity from Eq. (55). Observe that only \mathcal{I}_{θ^*} terms depend on the parameter vector θ^* . Likewise, the term next to $\frac{(\tau+1)^2}{\tau}$ is actually $\bar{\mu}_{\theta^*}^U \cdot (\bar{\mu}_{\theta^*}^D)^T$, and it can be substituted by either of $\{\bar{\mu}_{\theta^*}^U \cdot (\bar{\mu}_{\theta^*}^U)^T; \bar{\mu}_{\theta^*}^D \cdot (\bar{\mu}_{\theta^*}^D)^T; \bar{\mu}_{\theta^*}^D \cdot (\bar{\mu}_{\theta^*}^U)^T\}$.

Appendix C. Proof of Theorem 11

First, we prove the stepping stone lemmas.

C.1 Lemmata

Lemma 33 Denote $N \triangleq N^U + N^D$ and $\tau \triangleq \frac{N^U}{N^D}$, and assume τ to be a strictly positive, finite and constant scalar. Then $\sqrt{N} \cdot \nabla_{\theta} \hat{L}_{PSO}^{N^U,N^D}(f_{\theta^*}) \stackrel{d}{\to} \mathcal{N}(0,\mathcal{J})$, convergence in distribution along with $N \to \infty$ with \mathcal{J} being defined by Lemma 10.

Proof

Define:

$$\Sigma_{\theta}^{U} \triangleq \underset{X \sim \mathbb{P}^{U}}{\operatorname{Var}} M^{U}\left[X, f_{\theta}(X)\right] \cdot \nabla_{\theta} f_{\theta}(X) = \underset{X \sim \mathbb{P}^{U}}{\mathbb{E}} \left[M^{U}\left[X, f_{\theta}(X)\right]^{2} \cdot \mathcal{I}_{\theta}(X, X)\right] - \bar{\mu}_{\theta}^{U} \cdot (\bar{\mu}_{\theta}^{U})^{T},$$

$$\Sigma_{\theta}^{D} \triangleq \underset{X \sim \mathbb{P}^{D}}{\operatorname{Var}} M^{D} \left[X, f_{\theta}(X) \right] \cdot \nabla_{\theta} f_{\theta}(X) = \underset{X \sim \mathbb{P}^{D}}{\mathbb{E}} \left[M^{D} \left[X, f_{\theta}(X) \right]^{2} \cdot \mathcal{I}_{\theta}(X, X) \right] - \bar{\mu}_{\theta}^{D} \cdot (\bar{\mu}_{\theta}^{D})^{T},$$

where $\bar{\mu}_{\theta}^{U}$ and $\bar{\mu}_{\theta}^{D}$ are defined in Eq. (52).

Consider the average $\frac{1}{N^U} \sum_{i=1}^{N^U} M^U \left[X_i^U, f_{\theta^*}(X_i^U) \right] \cdot \nabla_{\theta} f_{\theta^*}(X_i^U)$. It contains i.i.d. random vectors with mean $\bar{\mu}_{\theta^*}^U$ and variance $\Sigma_{\theta^*}^U$. Using a multivariate Central Limit Theorem (CLT) on the considered average, we have:

$$\bar{a} \equiv \sqrt{N^U} \left[\frac{1}{N^U} \sum_{i=1}^{N^U} M^U \left[X_i^U, f_{\theta^*}(X_i^U) \right] \cdot \nabla_{\theta} f_{\theta^*}(X_i^U) - \bar{\mu}_{\theta^*}^U \right] \xrightarrow{d} \mathcal{N}(0, \Sigma_{\theta^*}^U).$$

In similar manner, we also have:

$$\bar{b} \equiv \sqrt{N^D} \left[\frac{1}{N^D} \sum_{i=1}^{N^D} M^D \left[X_i^D, f_{\theta^*}(X_i^D) \right] \cdot \nabla_{\theta} f_{\theta^*}(X_i^D) - \bar{\mu}_{\theta^*}^D \right] \xrightarrow{d} \mathcal{N}(0, \Sigma_{\theta^*}^D).$$

Therefore, the linear combination also has a convergence in distribution:

$$-\sqrt{\frac{\tau+1}{\tau}} \cdot \bar{a} + \sqrt{\tau+1} \cdot \bar{b} \xrightarrow{d} \mathcal{N}(0, \Sigma), \quad \Sigma \triangleq \frac{\tau+1}{\tau} \cdot \Sigma_{\theta^*}^U + (\tau+1) \cdot \Sigma_{\theta^*}^D,$$

where $\sqrt{\frac{\tau+1}{\tau}}$ and $\sqrt{\tau+1}$ are finite constant scalars, and where the convergence happens along with $N^U \to \infty$ and $N^D \to \infty$. Note that this implies the convergence in $N \to \infty$, since the latter leads to $\{N^U \to \infty, N^D \to \infty, \min(N^U, N^D) \to \infty\}$ due to τ being fixed and finite.

Further, using relations $N^U = \frac{\tau}{\tau+1}N$ and $N^D = \frac{1}{\tau+1}N$, the above linear combination is equal to:

$$\begin{split} -\sqrt{\frac{\tau+1}{\tau}} \cdot \bar{a} + \sqrt{\tau+1} \cdot \bar{b} &= \sqrt{N} \Big[-\frac{1}{N^U} \sum_{i=1}^{N^U} M^U \left[X_i^U, f_{\theta^*}(X_i^U) \right] \cdot \nabla_{\theta} f_{\theta^*}(X_i^U) + \bar{\mu}_{\theta^*}^U + \\ &+ \frac{1}{N^D} \sum_{i=1}^{N^D} M^D \left[X_i^D, f_{\theta^*}(X_i^D) \right] \cdot \nabla_{\theta} f_{\theta^*}(X_i^D) - \bar{\mu}_{\theta^*}^D \Big] = \sqrt{N} \cdot \nabla_{\theta} \hat{L}_{PSO}^{N^U, N^D}(f_{\theta^*}), \end{split}$$

where we used $\bar{\mu}_{\theta^*}^U = \bar{\mu}_{\theta^*}^D$ from Eq. (54). Thus, we have $\sqrt{N} \cdot \nabla_{\theta} \hat{L}_{PSO}^{N^U,N^D}(f_{\theta^*}) \stackrel{d}{\to} \mathcal{N}(0,\Sigma)$. Finally, we have:

$$\Sigma = \frac{\tau + 1}{\tau} \cdot \left[\underset{X \sim \mathbb{P}^U}{\mathbb{E}} \left[M^U \left[X, f_{\theta^*}(X) \right]^2 \cdot \mathcal{I}_{\theta^*}(X, X) \right] - \bar{\mu}_{\theta^*}^U \cdot (\bar{\mu}_{\theta^*}^U)^T \right] +$$

$$+ (\tau + 1) \cdot \left[\underset{X \sim \mathbb{P}^D}{\mathbb{E}} \left[M^D \left[X, f_{\theta^*}(X) \right]^2 \cdot \mathcal{I}_{\theta^*}(X, X) \right] - \bar{\mu}_{\theta^*}^D \cdot (\bar{\mu}_{\theta^*}^D)^T \right].$$

Using Eq. (55) we conclude $\mathcal{J} \equiv \Sigma$.

C.2 Proof of Theorem

Define $\hat{\theta}_{N^U,N^D} = \arg\min_{\theta \in \Theta} \hat{L}_{PSO}^{N^U,N^D}(f_{\theta})$ and $\theta^* = \arg\min_{\theta \in \Theta} L_{PSO}(f_{\theta})$. Since assumptions of Theorem 8 are also the assumptions of Theorem 11, f_{θ^*} satisfies PSO balance state and that $\hat{\theta}_{N^U,N^D} \stackrel{p}{\to} \theta^*$ when $\min(N^U,N^D) \to \infty$.

Further, note that first order conditions (FOCs) are also satisfied $\nabla_{\theta} \hat{L}_{PSO}^{N^U,N^D}(f_{\hat{\theta}_{N^U,N^D}}) = 0$. Assuming that $\hat{L}_{PSO}^{N^U,N^D}(f_{\theta})$ is continuously differentiable w.r.t. θ , we can apply mean-value theorem on FOCs:

$$\nabla_{\theta} \hat{L}_{PSO}^{N^{U},N^{D}}(f_{\hat{\theta}_{N^{U},N^{D}}}) = \nabla_{\theta} \hat{L}_{PSO}^{N^{U},N^{D}}(f_{\theta^{*}}) + \nabla_{\theta\theta} \hat{L}_{PSO}^{N^{U},N^{D}}(f_{\bar{\theta}}) \cdot \left[\hat{\theta}_{N^{U},N^{D}} - \theta^{*}\right] = 0, \quad (56)$$

where $\bar{\theta}$ is located on a line segment between $\hat{\theta}_{N^U,N^D}$ and θ^* . Given the estimation consistency $\hat{\theta}_{N^U,N^D} \stackrel{p}{\to} \theta^*$, the definition of $\bar{\theta}$ implies $\bar{\theta} \stackrel{p}{\to} \theta^*$.

The identity in Eq. (56) can be rewritten as:

$$\sqrt{N} \cdot \left[\hat{\theta}_{N^U,N^D} - \theta^* \right] = - \left[\nabla_{\theta\theta} \hat{L}_{PSO}^{N^U,N^D}(f_{\bar{\theta}}) \right]^{-1} \cdot \sqrt{N} \cdot \nabla_{\theta} \hat{L}_{PSO}^{N^U,N^D}(f_{\theta^*}),$$

where we used a notation $N \triangleq N^U + N^D$. Using CLT in Lemma 33 we have:

$$\sqrt{N} \cdot \nabla_{\theta} \hat{L}_{PSO}^{N^{U}, N^{D}}(f_{\theta^{*}}) \xrightarrow{d} \mathcal{N}(0, \mathcal{J}). \tag{57}$$

Next, $\nabla_{\theta\theta} \hat{L}_{PSO}^{N^U,N^D}(f_{\bar{\theta}})$ has a form:

$$\nabla_{\theta\theta} \hat{L}_{PSO}^{N^U,N^D}(f_{\bar{\theta}}) = -\frac{1}{N^U} \sum_{i=1}^{N^U} \nabla_{\theta\theta} \widetilde{M}^U \left[X_i^U, f_{\bar{\theta}}(X_i^U) \right] + \frac{1}{N^D} \sum_{i=1}^{N^D} \nabla_{\theta\theta} \widetilde{M}^D \left[X_i^D, f_{\bar{\theta}}(X_i^D) \right].$$

Using the uniform law of large numbers (LLN) and $\bar{\theta} \stackrel{p}{\to} \theta^*$, we get:

$$\frac{1}{N^{U}} \sum_{i=1}^{N^{U}} \nabla_{\theta\theta} \widetilde{M}^{U} \left[X_{i}^{U}, f_{\bar{\theta}}(X_{i}^{U}) \right] \stackrel{p}{\to} \underset{X \sim \mathbb{P}^{U}}{\mathbb{E}} \nabla_{\theta\theta} \widetilde{M}^{U} \left[X, f_{\theta^{*}}(X) \right],$$

$$\frac{1}{N^{D}} \sum_{i=1}^{N^{D}} \nabla_{\theta\theta} \widetilde{M}^{D} \left[X_{i}^{D}, f_{\bar{\theta}}(X_{i}^{D}) \right] \xrightarrow{p} \underset{X \sim \mathbb{P}^{D}}{\mathbb{E}} \nabla_{\theta\theta} \widetilde{M}^{D} \left[X, f_{\theta^{*}}(X) \right],$$

and hence

$$\nabla_{\theta\theta} \hat{L}_{PSO}^{N^{U},N^{D}}(f_{\bar{\theta}}) \stackrel{p}{\to} - \underset{X \sim \mathbb{P}^{U}}{\mathbb{E}} \nabla_{\theta\theta} \widetilde{M}^{U} [X, f_{\theta^{*}}(X)] + \underset{X \sim \mathbb{P}^{D}}{\mathbb{E}} \nabla_{\theta\theta} \widetilde{M}^{D} [X, f_{\theta^{*}}(X)] =$$

$$= \nabla_{\theta\theta} \left[- \underset{X \sim \mathbb{P}^{U}}{\mathbb{E}} \widetilde{M}^{U} [X, f_{\theta^{*}}(X)] + \underset{X \sim \mathbb{P}^{D}}{\mathbb{E}} \widetilde{M}^{D} [X, f_{\theta^{*}}(X)] \right] = \nabla_{\theta\theta} L_{PSO}(f_{\theta^{*}}) = \mathcal{H},$$

with \mathcal{H} being defined by Lemma 9. Applying the Continuous Mapping Theorem, we get:

$$\left[\nabla_{\theta\theta}\hat{L}_{PSO}^{N^{U},N^{D}}(f_{\bar{\theta}})\right]^{-1} \xrightarrow{p} \mathcal{H}^{-1}.$$
 (58)

Further, we apply Slutzky theorem on Eqs. (57)-(58) to get:

$$-\left[\nabla_{\theta\theta}\hat{L}_{PSO}^{N^U,N^D}(f_{\bar{\theta}})\right]^{-1}\cdot\sqrt{N}\cdot\nabla_{\theta}\hat{L}_{PSO}^{N^U,N^D}(f_{\theta^*})\xrightarrow{d}-\mathcal{H}^{-1}\mathcal{N}(0,\mathcal{J})=\mathcal{N}(0,\mathcal{H}^{-1}\mathcal{J}\mathcal{H}^{-1}).$$

Note that $\min(N^U, N^D) \to \infty$ is required for the convergence (see Lemma 33). This limit is identical to $N \to \infty$ due to assumption that τ is fixed and constant.

Therefore, we get:

$$\sqrt{N} \cdot \left[\hat{\theta}_{N^U,N^D} - \theta^* \right] \stackrel{d}{\to} \mathcal{N}(0,\mathcal{H}^{-1}\mathcal{J}\mathcal{H}^{-1}),$$

where the convergence in distribution is achieved along with $N \to \infty$. Further, all the regulatory assumptions of the theorem are required for application of CLT, LLN, and satisfaction of FOCs. See theorem 3.1 in (Newey and McFadden, 1994) for the more technical exposition.

Appendix D. Proof of Theorem 12

The proof for $df_{\theta}(X)$'s expected value is trivial. Its covariance is derived as following:

$$\mathbb{E}\left[df_{\theta}(X) \cdot df_{\theta}(X')\right] = \delta^{2} \cdot \mathbb{E}\left[\nabla_{\theta} f_{\theta}(X)^{T} \cdot \nabla_{\theta} \hat{L}_{PSO}^{N^{U},N^{D}}(f_{\theta}) \cdot \nabla_{\theta} \hat{L}_{PSO}^{N^{U},N^{D}}(f_{\theta})^{T} \cdot \nabla_{\theta} f_{\theta}(X')\right] =$$

$$= \delta^{2} \cdot \nabla_{\theta} f_{\theta}(X)^{T} \cdot \mathbb{E}\left[\nabla_{\theta} \hat{L}_{PSO}^{N^{U},N^{D}}(f_{\theta}) \cdot \nabla_{\theta} \hat{L}_{PSO}^{N^{U},N^{D}}(f_{\theta})^{T}\right] \cdot \nabla_{\theta} f_{\theta}(X'),$$

$$\mathbb{E}\left[df_{\theta}(X)\right] = -\delta \cdot \nabla_{\theta} f_{\theta}(X)^T \cdot \mathbb{E}\left[\nabla_{\theta} \hat{L}_{PSO}^{N^U,N^D}(f_{\theta})\right],$$

$$\operatorname{Cov}\left[df_{\theta}(X), df_{\theta}(X')\right] = \mathbb{E}\left[df_{\theta}(X) \cdot df_{\theta}(X')\right] - \mathbb{E}\left[df_{\theta}(X)\right] \cdot \mathbb{E}\left[df_{\theta}(X')\right] =$$

$$= \delta^{2} \cdot \nabla_{\theta} f_{\theta}(X)^{T} \cdot \mathbb{E}\left[\nabla_{\theta} \hat{L}_{PSO}^{N^{U}, N^{D}}(f_{\theta}) \cdot \nabla_{\theta} \hat{L}_{PSO}^{N^{U}, N^{D}}(f_{\theta})^{T}\right] \cdot \nabla_{\theta} f_{\theta}(X') -$$

$$- \delta^{2} \cdot \nabla_{\theta} f_{\theta}(X)^{T} \cdot \mathbb{E}\left[\nabla_{\theta} \hat{L}_{PSO}^{N^{U}, N^{D}}(f_{\theta})\right] \cdot \mathbb{E}\left[\nabla_{\theta} \hat{L}_{PSO}^{N^{U}, N^{D}}(f_{\theta})\right]^{T} \cdot \nabla_{\theta} f_{\theta}(X') =$$

$$= \delta^{2} \cdot \nabla_{\theta} f_{\theta}(X)^{T} \cdot \left[\mathbb{E}\left[\nabla_{\theta} \hat{L}_{PSO}^{N^{U}, N^{D}}(f_{\theta}) \cdot \nabla_{\theta} \hat{L}_{PSO}^{N^{U}, N^{D}}(f_{\theta})^{T}\right] -$$

$$- \mathbb{E}\left[\nabla_{\theta} \hat{L}_{PSO}^{N^{U}, N^{D}}(f_{\theta})\right] \cdot \mathbb{E}\left[\nabla_{\theta} \hat{L}_{PSO}^{N^{U}, N^{D}}(f_{\theta})\right]^{T} \cdot \nabla_{\theta} f_{\theta}(X') =$$

$$= \delta^{2} \cdot \nabla_{\theta} f_{\theta}(X)^{T} \cdot \operatorname{Var}\left[\nabla_{\theta} \hat{L}_{PSO}^{N^{U}, N^{D}}(f_{\theta})\right] \cdot \nabla_{\theta} f_{\theta}(X'),$$

where $\operatorname{Var}\left[\nabla_{\theta}\hat{L}_{PSO}^{N^{U},N^{D}}(f_{\theta})\right]$ was proven to have a form in Eq. (53). Observe that it is proportional to $\frac{1}{N}$ where $N=N^{U}+N^{D}$.

Appendix E. Proof of Theorem 13

Assume that first order conditions (FOCs) were satisfied, $\nabla_{\theta} \hat{L}_{PSO}^{N^U,N^D}(f_{\theta}) = 0$. Then we have:

$$\frac{1}{N^U}\sum_{i=1}^{N^U}M^U\left[X_i^U,f_{\theta}(X_i^U)\right]\cdot\nabla_{\theta}f_{\theta}(X_i^U) = \frac{1}{N^D}\sum_{i=1}^{N^D}M^D\left[X_i^D,f_{\theta}(X_i^D)\right]\cdot\nabla_{\theta}f_{\theta}(X_i^D).$$

Consider a specific \mathbb{P}^U 's training sample $X \equiv X_j^U$ with $j \in \{1, \dots, N^U\}$. Multiplying the above expression by $\nabla_{\theta} f_{\theta}(X)^T$, we get

$$\begin{split} M^{U}\left[X, f_{\theta}(X)\right] \cdot g_{\theta}(X, X) + \sum_{i, i \neq j}^{N^{U}} M^{U}\left[X_{i}^{U}, f_{\theta}(X_{i}^{U})\right] \cdot g_{\theta}(X, X_{i}^{U}) = \\ &= \frac{N^{U}}{N^{D}} \sum_{i=1}^{N^{D}} M^{D}\left[X_{i}^{D}, f_{\theta}(X_{i}^{D})\right] \cdot g_{\theta}(X, X_{i}^{D}). \end{split}$$

Since both M^U and g_θ are assumed to be non-negative, we obtain an inequality:

$$M^{\scriptscriptstyle U}\left[X,f_{\theta}(X)\right]\cdot g_{\theta}(X,X) \leq \frac{N^{\scriptscriptstyle U}}{N^{\scriptscriptstyle D}}\sum_{i=1}^{N^{\scriptscriptstyle D}}M^{\scriptscriptstyle D}\left[X_i^{\scriptscriptstyle D},f_{\theta}(X_i^{\scriptscriptstyle D})\right]\cdot g_{\theta}(X,X_i^{\scriptscriptstyle D}).$$

Next, we divide by $g_{\theta}(X, X)$:

$$M^{U}[X, f_{\theta}(X)] \leq \frac{N^{U}}{N^{D}} \sum_{i=1}^{N^{D}} M^{D}[X_{i}^{D}, f_{\theta}(X_{i}^{D})] \cdot r_{\theta}(X, X_{i}^{D}) \leq$$

$$\leq \frac{N^{U}}{N^{D}} \sum_{i=1}^{N^{D}} M^{D}[X_{i}^{D}, f_{\theta}(X_{i}^{D})] \cdot \exp\left[-\frac{d(X, X_{i}^{D})}{h_{max}}\right] \equiv \alpha, \quad (59)$$

where in the last part we applied the assumed bounds over r_{θ} .

Denote the inverse function of $M^U[X,s]$ by $(M^U)^{-1}[X,z]$. Since M^U is assumed to be strictly decreasing, then so is its inverse $(M^U)^{-1}$. Further, apply $(M^U)^{-1}$ on both sides of Eq. (59):

$$(M^{U})^{-1}[X, M^{U}[X, f_{\theta}(X)]] = f_{\theta}(X) \ge (M^{U})^{-1}[X, \alpha],$$

where we reversed the inequality since the applied function is strictly decreasing.

Next, observe that $0 \le \alpha \le \infty$ due to the assumed non-negativity of M^D . Further, for $h_{max} \to 0$ we also have $\alpha \to 0$ - for zero bandwidth α goes also to zero. Moreover, due to its properties $(M^U)^{-1}[X,\alpha]$ is strictly decreasing for $\alpha \in [0,\infty]$. Hence, $(M^U)^{-1}[X,\alpha] \to \max_{\alpha' \in [0,\infty]} (M^U)^{-1}[X,\alpha']$ along with $\alpha \to 0$.

Further note that the range of $(M^U)^{-1}$ is the subset of values within \mathbb{R} that $f_{\theta}(X)$ can have. That is, $(M^U)^{-1}$ and f_{θ} share their range. Assuming that this range is entire \mathbb{R} or its positive part \mathbb{R}_+ , extended to contain ∞ , we will have $\max_{\alpha' \in [0,\infty]} (M^U)^{-1} [X,\alpha'] = \infty$.

To conclude, we have that $f_{\theta}(X) \geq (M^{U})^{-1}[X, \alpha]$, where for $\alpha \to 0$ this lower bound behaves as $(M^{U})^{-1}[X, \alpha] \to \infty$.

Appendix F. Proof of Theorem 14

First, we prove the stepping stone lemmas.

F.1 Lemmata

Lemma 34 Consider the relative model kernel r_{θ} defined in Eq. (11), and assume it to be bounded as in Eq. (12). Then $|r_{\theta}(X_1, X) - r_{\theta}(X_2, X)| \le \epsilon [X_1, X_2, X]$ with $\epsilon [X_1, X_2, X] \triangleq 1 - \exp\left[-\frac{1}{h_{min}}d(X_1, X_2)\right] \cdot \exp\left[-\frac{1}{h_{min}}\max\left[d(X_1, X), d(X_2, X)\right]\right]$.

Proof

Consider two scenarios: $r_{\theta}(X_1, X) \ge r_{\theta}(X_2, X)$ and $r_{\theta}(X_1, X) < r_{\theta}(X_2, X)$. In the first case we have:

$$|r_{\theta}(X_{1}, X) - r_{\theta}(X_{2}, X)| = r_{\theta}(X_{1}, X) - r_{\theta}(X_{2}, X) \le 1 - \exp\left[-\frac{1}{h_{min}}d(X_{2}, X)\right] \le$$

$$\le 1 - \exp\left[-\frac{1}{h_{min}}d(X_{1}, X_{2})\right] \cdot \exp\left[-\frac{1}{h_{min}}d(X_{1}, X)\right] \triangleq c_{1},$$

where in the second row we used a triangle inequality $d(X_2, X) \leq d(X_1, X_2) + d(X_1, X)$. Similarly, in the second case $r_{\theta}(X_1, X) < r_{\theta}(X_2, X)$ we will obtain:

$$\begin{split} |r_{\theta}(X_1,X) - r_{\theta}(X_2,X)| &= r_{\theta}(X_2,X) - r_{\theta}(X_1,X) \leq \\ &\leq 1 - \exp\left[-\frac{1}{h_{min}}d(X_1,X_2)\right] \cdot \exp\left[-\frac{1}{h_{min}}d(X_2,X)\right] \triangleq c_2. \end{split}$$

Next, we combine the two cases:

$$|r_{\theta}(X_1, X) - r_{\theta}(X_2, X)| \le \max(c_1, c_2) =$$

$$= 1 - \exp\left[-\frac{1}{h_{min}} d(X_1, X_2)\right] \cdot \exp\left[-\frac{1}{h_{min}} \max\left[d(X_1, X), d(X_2, X)\right]\right].$$

Lemma 35 Consider the relative model kernel r_{θ} defined in Eq. (11), and assume it to be bounded as in Eq. (12). Then $\left|\frac{df_{\theta}(X_1)}{g_{\theta}(X_1,X_1)} - \frac{df_{\theta}(X_2)}{g_{\theta}(X_2,X_2)}\right| \leq \varepsilon_1(X_1,X_2)$ with:

$$\varepsilon_{1}(X_{1}, X_{2}) = \delta \cdot \left[\frac{1}{N^{U}} \sum_{i=1}^{N^{U}} |M^{U}[X_{i}^{U}, f_{\theta}(X_{i}^{U})]| \cdot \epsilon [X_{1}, X_{2}, X_{i}^{U}] + \frac{1}{N^{D}} \sum_{i=1}^{N^{D}} |M^{D}[X_{i}^{D}, f_{\theta}(X_{i}^{D})]| \cdot \epsilon [X_{1}, X_{2}, X_{i}^{D}] \right].$$

Proof

According to Eq. (7) we have:

$$\begin{split} \left| \frac{df_{\theta}(X_{1})}{g_{\theta}(X_{1}, X_{1})} - \frac{df_{\theta}(X_{2})}{g_{\theta}(X_{2}, X_{2})} \right| &= \delta \cdot \left| \frac{1}{N^{U}} \sum_{i=1}^{N^{U}} M^{U} \left[X_{i}^{U}, f_{\theta}(X_{i}^{U}) \right] \cdot \left[r_{\theta}(X_{1}, X_{i}^{U}) - r_{\theta}(X_{2}, X_{i}^{U}) \right] - \\ &- \frac{1}{N^{D}} \sum_{i=1}^{N^{D}} M^{D} \left[X_{i}^{D}, f_{\theta}(X_{i}^{D}) \right] \cdot \left[r_{\theta}(X_{1}, X_{i}^{D}) - r_{\theta}(X_{2}, X_{i}^{D}) \right] \right| \leq \\ &\leq \delta \cdot \frac{1}{N^{U}} \sum_{i=1}^{N^{U}} \left| M^{U} \left[X_{i}^{U}, f_{\theta}(X_{i}^{U}) \right] \right| \cdot \left| r_{\theta}(X_{1}, X_{i}^{U}) - r_{\theta}(X_{2}, X_{i}^{U}) \right| + \\ &+ \delta \cdot \frac{1}{N^{D}} \sum_{i=1}^{N^{D}} \left| M^{D} \left[X_{i}^{D}, f_{\theta}(X_{i}^{D}) \right] \right| \cdot \left| r_{\theta}(X_{1}, X_{i}^{D}) - r_{\theta}(X_{2}, X_{i}^{D}) \right| \leq \\ &\leq \delta \cdot \frac{1}{N^{U}} \sum_{i=1}^{N^{U}} \left| M^{U} \left[X_{i}^{U}, f_{\theta}(X_{i}^{U}) \right] \right| \cdot \epsilon \left[X_{1}, X_{2}, X_{i}^{U} \right] + \\ &+ \delta \cdot \frac{1}{N^{D}} \sum_{i=1}^{N^{D}} \left| M^{D} \left[X_{i}^{D}, f_{\theta}(X_{i}^{U}) \right] \right| \cdot \epsilon \left[X_{1}, X_{2}, X_{i}^{D} \right] \right| \cdot \epsilon \left[X_{1}, X_{2}, X_{i}^{D} \right], \end{split}$$

where in the last part we applied Lemma 34.

Lemma 36 Consider the relative model kernel r_{θ} defined in Eq. (11), and assume it to be bounded as in Eq. (12). Then $\left|\frac{df_{\theta}(X)}{g_{\theta}(X,X)}\right| \leq \varepsilon_2$ with:

$$\varepsilon_2 = \delta \cdot \left[\frac{1}{N^U} \sum_{i=1}^{N^U} \left| M^U\left[X_i^U, f_{\theta}(X_i^U)\right] \right| + \frac{1}{N^D} \sum_{i=1}^{N^D} \left| M^D\left[X_i^D, f_{\theta}(X_i^D)\right] \right| \right].$$

Proof

$$\begin{split} \left| \frac{df_{\theta}(X)}{g_{\theta}(X,X)} \right| &= \\ &= \delta \cdot \left| \frac{1}{N^{U}} \sum_{i=1}^{N^{U}} M^{U} \left[X_{i}^{U}, f_{\theta}(X_{i}^{U}) \right] \cdot r_{\theta}(X, X_{i}^{U}) - \frac{1}{N^{D}} \sum_{i=1}^{N^{D}} M^{D} \left[X_{i}^{D}, f_{\theta}(X_{i}^{D}) \right] \cdot r_{\theta}(X, X_{i}^{D}) \right| \leq \\ &\leq \delta \cdot \frac{1}{N^{U}} \sum_{i=1}^{N^{U}} \left| M^{U} \left[X_{i}^{U}, f_{\theta}(X_{i}^{U}) \right] \right| \cdot r_{\theta}(X, X_{i}^{U}) + \delta \cdot \frac{1}{N^{D}} \sum_{i=1}^{N^{D}} \left| M^{D} \left[X_{i}^{D}, f_{\theta}(X_{i}^{D}) \right] \right| \cdot r_{\theta}(X, X_{i}^{D}) \leq \\ &\leq \delta \cdot \frac{1}{N^{U}} \sum_{i=1}^{N^{U}} \left| M^{U} \left[X_{i}^{U}, f_{\theta}(X_{i}^{U}) \right] \right| + \delta \cdot \frac{1}{N^{D}} \sum_{i=1}^{N^{D}} \left| M^{D} \left[X_{i}^{D}, f_{\theta}(X_{i}^{D}) \right] \right|, \end{split}$$

where in the last part we used $r_{\theta}(X, X') \leq 1$.

F.2 Proof of Theorem

Observe that:

$$\left| \frac{df_{\theta}(X_1)}{g_{\theta}(X_1, X_1)} - \frac{df_{\theta}(X_2)}{g_{\theta}(X_2, X_2)} \right| =$$

$$= \frac{1}{g_{\theta}(X_1, X_1)} \cdot \left| df_{\theta}(X_1) - df_{\theta}(X_2) - \frac{g_{\theta}(X_1, X_1) - g_{\theta}(X_2, X_2)}{g_{\theta}(X_2, X_2)} \cdot df_{\theta}(X_2) \right|.$$

Applying Lemma 35, we have:

$$\left| df_{\theta}(X_1) - df_{\theta}(X_2) - \frac{g_{\theta}(X_1, X_1) - g_{\theta}(X_2, X_2)}{g_{\theta}(X_2, X_2)} \cdot df_{\theta}(X_2) \right| \le g_{\theta}(X_1, X_1) \cdot \varepsilon_1(X_1, X_2).$$

Using the reverse triangle inequality $||x| - |y|| \le |x - y|$ on left part of the above equation, we get:

$$\left| |df_{\theta}(X_1) - df_{\theta}(X_2)| - \left| \frac{g_{\theta}(X_1, X_1) - g_{\theta}(X_2, X_2)}{g_{\theta}(X_2, X_2)} \cdot df_{\theta}(X_2) \right| \right| \le g_{\theta}(X_1, X_1) \cdot \varepsilon_1(X_1, X_2).$$

Next, we check the above inequality under two possible scenarios:

1)
$$|df_{\theta}(X_1) - df_{\theta}(X_2)| \ge \left| \frac{g_{\theta}(X_1, X_1) - g_{\theta}(X_2, X_2)}{g_{\theta}(X_2, X_2)} \cdot df_{\theta}(X_2) \right|$$
: Here we have:

$$|df_{\theta}(X_1) - df_{\theta}(X_2)| \le g_{\theta}(X_1, X_1) \cdot \varepsilon_1(X_1, X_2) + \left| \frac{g_{\theta}(X_1, X_1) - g_{\theta}(X_2, X_2)}{g_{\theta}(X_2, X_2)} \cdot df_{\theta}(X_2) \right|.$$
(60)

2) $|df_{\theta}(X_1) - df_{\theta}(X_2)| < \left| \frac{g_{\theta}(X_1, X_1) - g_{\theta}(X_2, X_2)}{g_{\theta}(X_2, X_2)} \cdot df_{\theta}(X_2) \right|$: In such case Eq. (60) is trivially satisfied.

Hence, Eq. (60) is satisfied always and therefore:

$$|df_{\theta}(X_{1}) - df_{\theta}(X_{2})| \leq g_{\theta}(X_{1}, X_{1}) \cdot \varepsilon_{1}(X_{1}, X_{2}) + |g_{\theta}(X_{1}, X_{1}) - g_{\theta}(X_{2}, X_{2})| \cdot \left| \frac{df_{\theta}(X_{2})}{g_{\theta}(X_{2}, X_{2})} \right| \leq g_{\theta}(X_{1}, X_{1}) \cdot \varepsilon_{1}(X_{1}, X_{2}) + |g_{\theta}(X_{1}, X_{1}) - g_{\theta}(X_{2}, X_{2})| \cdot \varepsilon_{2} \equiv \varepsilon_{3}(X_{1}, X_{2}), \quad (61)$$

where we applied Lemma 36.

Further, using definitions of ε_1 and ε_2 we get:

$$\varepsilon_{3}(X_{1}, X_{2}) = g_{\theta}(X_{1}, X_{1}) \cdot \delta \cdot \left[\frac{1}{N^{U}} \sum_{i=1}^{N^{U}} |M^{U}[X_{i}^{U}, f_{\theta}(X_{i}^{U})]| \cdot \epsilon [X_{1}, X_{2}, X_{i}^{U}] + \frac{1}{N^{D}} \sum_{i=1}^{N^{D}} |M^{D}[X_{i}^{D}, f_{\theta}(X_{i}^{D})]| \cdot \epsilon [X_{1}, X_{2}, X_{i}^{D}] \right] + \\
+ |g_{\theta}(X_{1}, X_{1}) - g_{\theta}(X_{2}, X_{2})| \cdot \delta \cdot \left[\frac{1}{N^{U}} \sum_{i=1}^{N^{U}} |M^{U}[X_{i}^{U}, f_{\theta}(X_{i}^{U})]| + \frac{1}{N^{D}} \sum_{i=1}^{N^{D}} |M^{D}[X_{i}^{D}, f_{\theta}(X_{i}^{D})]| \right] = \\
= \delta \cdot g_{\theta}(X_{1}, X_{1}) \cdot \left[\frac{1}{N^{U}} \sum_{i=1}^{N^{U}} |M^{U}[X_{i}^{U}, f_{\theta}(X_{i}^{U})]| \cdot \left[\epsilon [X_{1}, X_{2}, X_{i}^{U}] + \frac{|g_{\theta}(X_{1}, X_{1}) - g_{\theta}(X_{2}, X_{2})|}{g_{\theta}(X_{1}, X_{1})} \right] + \\
+ \frac{1}{N^{D}} \sum_{i=1}^{N^{D}} |M^{D}[X_{i}^{D}, f_{\theta}(X_{i}^{D})]| \cdot \left[\epsilon [X_{1}, X_{2}, X_{i}^{D}] + \frac{|g_{\theta}(X_{1}, X_{1}) - g_{\theta}(X_{2}, X_{2})|}{g_{\theta}(X_{1}, X_{1})} \right] \right]. (62)$$

Define $\nu_{\theta}(X_1, X_2, X) \triangleq \epsilon[X_1, X_2, X] + \frac{|g_{\theta}(X_1, X_1) - g_{\theta}(X_2, X_2)|}{g_{\theta}(X_1, X_1)}$. Then, the combination of Eq. (61) and Eq. (62) will lead to:

$$\begin{aligned} |df_{\theta}(X_{1}) - df_{\theta}(X_{2})| &\leq \delta \cdot g_{\theta}(X_{1}, X_{1}) \cdot \left[\frac{1}{N^{U}} \sum_{i=1}^{N^{U}} |M^{U}[X_{i}^{U}, f_{\theta}(X_{i}^{U})]| \cdot \nu_{\theta}(X_{1}, X_{2}, X_{i}^{U}) + \right. \\ &\left. + \frac{1}{N^{D}} \sum_{i=1}^{N^{D}} |M^{D}[X_{i}^{D}, f_{\theta}(X_{i}^{D})]| \cdot \nu_{\theta}(X_{1}, X_{2}, X_{i}^{D}) \right]. \end{aligned}$$

Appendix G. Proof of Softmax Cross-Entropy being Instance of PSO

Here we will derive the cross-entropy loss combined with a Softmax layer, typically used in the image classification domain, via PSO principles, showing it to be another instance of PSO. For this we define our training dataset as a set of pairs $\{X_i, Y_i\}_{i=1}^N$ where $X_i \in \mathbb{R}^n$ is a data point of an arbitrary dimension n (e.g. image) and Y_i is its label - a discrete number that takes values from $\{1, \ldots, C\}$ with C being the number of classes. Number of samples for each class is denoted by $\{N_1, \ldots, N_C\}$, with $\sum_{j=1}^C N_j = N$. For the classification task we assume that each sample pair is i.i.d. sampled from an unknown density $\mathbb{P}(X,Y) = \mathbb{P}(X) \cdot \mathbb{P}(Y|X)$. Our task is to enforce the output of Softmax layer to converge to the unknown conditional $\mathbb{P}(Y|X)$. To this end, define a model f_θ that returns C dimensional output $f_\theta(X) \in \mathbb{R}^C$, with its j-th entry denoted by $f_{\theta,j}(X)$. Further, Softmax transformation $h_{\theta}(X)$ is defined as:

$$h_{\theta,j}(X) = \frac{\exp f_{\theta,j}(X)}{\sum_{k=1}^{C} \exp f_{\theta,k}(X)} = \frac{\exp f_{\theta,j}(X)}{\|\exp f_{\theta}(X)\|_{1}},$$

which yields properties $h_{\theta,j}(X) \ge 0$ and $\sum_k h_{\theta,k}(X) = 1$. We aim for $h_{\theta,j}(X)$ to converge to $\mathbb{P}(Y = j|X)$ - the probability of X's label to be j. Each $f_{\theta,j}(X)$ will be considered as an

independent surface in PSO framework, which we will push to converge to the state where

$$\frac{\exp f_{\theta,j}(X)}{\|\exp f_{\theta}(X)\|_{1}} = \mathbb{P}(Y=j|X),\tag{63}$$

by optimizing the corresponding loss $L_{PSO}(f_{\theta,j})$, with total minimized loss being defined as $L_{PSO}(f_{\theta}) = \sum_{j=1}^{C} L_{PSO}(f_{\theta,j})$. That is, the described below minimization of $L_{PSO}(f_{\theta})$ will consist of solving C PSO problems in parallel.

PSO over $f_{\theta,j}(X)$ **via** $L_{PSO}(f_{\theta,j})$: Consider a typical PSO estimation, where $\mathbb{P}(X|Y=j)$ serves as up density \mathbb{P}^U and $\mathbb{P}(X|Y\neq j)$ - as down density \mathbb{P}^D . Sample batch from $\mathbb{P}(X|Y=j)$ is obtained by fetching samples with label Y=j; data points from $\mathbb{P}(X|Y\neq j)$ will be the rest of samples. Note also that the identity $\frac{\mathbb{P}(X|Y=j)}{\mathbb{P}(X|Y\neq j)} = \frac{\mathbb{P}(Y\neq j)}{\mathbb{P}(Y=j)} \cdot \frac{\mathbb{P}(Y=j|X)}{1-\mathbb{P}(Y=j|X)}$ holds, due to below derivation:

$$\frac{\mathbb{P}(X|Y\neq j)}{\mathbb{P}(X|Y=j)} = \frac{\mathbb{P}(X,Y\neq j)\cdot\mathbb{P}(Y=j)}{\mathbb{P}(X,Y=j)\cdot\mathbb{P}(Y\neq j)} = \frac{\mathbb{P}(Y=j)}{\mathbb{P}(Y\neq j)} \cdot \frac{\sum_{k\neq j}\mathbb{P}(X,Y=k)}{\mathbb{P}(X,Y=j)} = \\
= \frac{\mathbb{P}(Y=j)}{\mathbb{P}(Y\neq j)} \cdot \frac{\left[\sum_{k=1}^{C}\mathbb{P}(X,Y=k)\right] - \mathbb{P}(X,Y=j)}{\mathbb{P}(X,Y=j)} = \frac{\mathbb{P}(Y=j)}{\mathbb{P}(Y\neq j)} \cdot \left[\frac{\mathbb{P}(X)}{\mathbb{P}(X,Y=j)} - 1\right] = \\
= \frac{\mathbb{P}(Y=j)}{\mathbb{P}(Y\neq j)} \cdot \frac{1 - \mathbb{P}(Y=j|X)}{\mathbb{P}(Y=j|X)}. \quad (64)$$

Considering PSO balance state, we are looking for a pair of magnitudes $\{M_j^U, M_j^D\}$ that for the below system:

$$\frac{M_{j}^{D}\left[X, f_{\theta}(X)\right]}{M_{i}^{U}\left[X, f_{\theta}(X)\right]} = \frac{\mathbb{P}(X|Y=j)}{\mathbb{P}(X|Y\neq j)},$$

will produce a solution at Eq. (63). That is, denoting $\frac{M_j^D[X,s]}{M_j^U[X,s]}$ by $R(X,s): \mathbb{R}^n \times \mathbb{R}^C \to \mathbb{R}$ and using the identity in Eq. (64), we are looking for the transformation R s.t. the solution of:

$$R[X, f_{\theta}(X)] = \frac{\mathbb{P}(Y \neq j)}{\mathbb{P}(Y = j)} \cdot \frac{\mathbb{P}(Y = j|X)}{1 - \mathbb{P}(Y = j|X)},$$

will lead to Eq. (63). Assuming that R has a form $R[X, f_{\theta}(X)] = \bar{R}\left[\frac{\exp f_{\theta,j}(X)}{\|\exp f_{\theta}(X)\|_1}\right], \bar{R}(s)$: $\mathbb{R} \to \mathbb{R}$ can be identified as $\bar{R}(s) = \frac{\mathbb{P}(Y \neq j)}{\mathbb{P}(Y = j)} \cdot \frac{s}{1-s}$. From this we conclude that $R[X, f_{\theta}(X)] = \frac{\mathbb{P}(Y \neq j)}{\mathbb{P}(Y = j)} \cdot \frac{\exp f_{\theta,j}(X)}{\|\exp f_{\theta}(X)\|_1 - \exp f_{\theta,j}(X)}$ and that magnitudes must satisfy:

$$\frac{M_j^D\left[X, f_{\theta}(X)\right]}{M_i^U\left[X, f_{\theta}(X)\right]} = \frac{\mathbb{P}(Y \neq j)}{\mathbb{P}(Y = j)} \cdot \frac{\exp f_{\theta, j}(X)}{\|\exp f_{\theta}(X)\|_1 - \exp f_{\theta, j}(X)}.$$

Specifically, we will choose them to be:

$$M_{j}^{U}[X, f_{\theta}(X)] = \mathbb{P}(Y = j) \cdot \frac{\|\exp f_{\theta}(X)\|_{1} - \exp f_{\theta, j}(X)}{\|\exp f_{\theta}(X)\|_{1}} = \mathbb{P}(Y = j) \cdot \frac{\sum_{k=1, k \neq j}^{C} \exp f_{\theta, k}(X)}{\|\exp f_{\theta}(X)\|_{1}},$$
(65)

$$M_j^D[X, f_{\theta}(X)] = \mathbb{P}(Y \neq j) \cdot \frac{\exp f_{\theta, j}(X)}{\|\exp f_{\theta}(X)\|_1}$$
 (66)

where the denominator $\|\exp f_{\theta}(X)\|_1$ serves as a normalization factor that enforces $\{M_j^U, M_j^D\}$ to be between 0 and 1. Such normalization is only one from many possible, yet this choice will eventually yield the popular softmax cross-entropy loss.

Using the above setting to define $L_{PSO}(f_{\theta,i})$, its gradient can be written as

$$\nabla_{\theta} L_{PSO}(f_{\theta,j}) = - \underset{X \sim \mathbb{P}(X|Y=j)}{\mathbb{E}} M_j^U [X, f_{\theta}(X)] \cdot \nabla_{\theta} f_{\theta,j}(X) + \\ + \underset{X \sim \mathbb{P}(X|Y\neq j)}{\mathbb{E}} M_j^D [X, f_{\theta}(X)] \cdot \nabla_{\theta} f_{\theta,j}(X).$$

Gradient-based optimization via the above expression will lead to Eq. (63). Also, in practice $\mathbb{P}(Y=j)$ inside M_j^U can be approximated as $\frac{N_j}{N}$, and $\mathbb{P}(Y\neq j)$ inside M_j^D - as $\frac{N-N_j}{N}$.

PSO over multiple surfaces via $L_{PSO}(f_{\theta})$: Further, combining all losses together into $L_{PSO}(f_{\theta}) = \sum_{j=1}^{C} L_{PSO}(f_{\theta,j})$ will produce $\nabla_{\theta} L_{PSO}(f_{\theta}) = \sum_{j=1}^{C} \nabla_{\theta} L_{PSO}(f_{\theta,j})$:

$$\nabla_{\theta} L_{PSO}(f_{\theta}) = \sum_{j=1}^{C} \left[- \underset{X \sim \mathbb{P}(X|Y=j)}{\mathbb{E}} M_{j}^{U} \left[X, f_{\theta}(X) \right] \cdot \nabla_{\theta} f_{\theta,j}(X) + \right. \\ \left. + \underset{X \sim \mathbb{P}(X|Y\neq j)}{\mathbb{E}} M_{j}^{D} \left[X, f_{\theta}(X) \right] \cdot \nabla_{\theta} f_{\theta,j}(X) \right].$$

The above expression is also the gradient of softmax cross-entropy, which can be shown as follows. First, note that the second term can be rewritten as:

$$\mathbb{E}_{X \sim \mathbb{P}(X|Y \neq j)} M_j^D [X, f_{\theta}(X)] \cdot \nabla_{\theta} f_{\theta,j}(X) =$$

$$= \int \mathbb{P}(X, Y \neq j) \cdot \frac{\exp f_{\theta,j}(X)}{\|\exp f_{\theta}(X)\|_1} \cdot \nabla_{\theta} f_{\theta,j}(X) dX =$$

$$= \int \left[\sum_{k=1, k \neq j}^C \mathbb{P}(X, Y = k) \right] \cdot \frac{\exp f_{\theta,j}(X)}{\|\exp f_{\theta}(X)\|_1} \cdot \nabla_{\theta} f_{\theta,j}(X) dX =$$

$$= \sum_{k=1, k \neq j}^C \mathbb{P}(Y = k) \cdot \mathbb{E}_{X \sim \mathbb{P}(X|Y = k)} \frac{\exp f_{\theta,j}(X)}{\|\exp f_{\theta}(X)\|_1} \cdot \nabla_{\theta} f_{\theta,j}(X).$$

Then, $\nabla_{\theta} L_{PSO}(f_{\theta})$ is equal to:

$$\nabla_{\theta} L_{PSO}(f_{\theta}) = \sum_{j=1}^{C} \left[-\mathbb{P}(Y=j) \cdot \underset{X \sim \mathbb{P}(X|Y=j)}{\mathbb{E}} \frac{\sum_{k=1, k \neq j}^{C} \exp f_{\theta,k}(X)}{\|\exp f_{\theta}(X)\|_{1}} \cdot \nabla_{\theta} f_{\theta,j}(X) + \right.$$

$$+ \sum_{k=1, k \neq j}^{C} \mathbb{P}(Y=k) \cdot \underset{X \sim \mathbb{P}(X|Y=k)}{\mathbb{E}} \frac{\exp f_{\theta,j}(X)}{\|\exp f_{\theta}(X)\|_{1}} \cdot \nabla_{\theta} f_{\theta,j}(X) \right] =$$

$$= -\sum_{j=1}^{C} \mathbb{P}(Y=j) \cdot \underset{X \sim \mathbb{P}(X|Y=j)}{\mathbb{E}} \frac{\sum_{k=1, k \neq j}^{C} \exp f_{\theta,k}(X)}{\|\exp f_{\theta}(X)\|_{1}} \cdot \nabla_{\theta} f_{\theta,j}(X) +$$

$$+ \sum_{j=1}^{C} \mathbb{P}(Y=j) \cdot \underset{X \sim \mathbb{P}(X|Y=j)}{\mathbb{E}} \sum_{k=1, k \neq j}^{C} \frac{\exp f_{\theta,k}(X)}{\|\exp f_{\theta}(X)\|_{1}} \cdot \nabla_{\theta} f_{\theta,k}(X),$$

where the second equality can be verified by examining coefficients of each $\nabla_{\theta} f_{\theta,j}(X)$ before and after "=". Further:

$$\nabla_{\theta} L_{PSO}(f_{\theta}) = -\sum_{j=1}^{C} \mathbb{P}(Y=j) \cdot \underset{X \sim \mathbb{P}(X|Y=j)}{\mathbb{E}} \left[\frac{\|\exp f_{\theta}(X)\|_{1} - \exp f_{\theta,j}(X)}{\|\exp f_{\theta}(X)\|_{1}} \cdot \nabla_{\theta} f_{\theta,j}(X) - \sum_{k=1, k \neq j}^{C} \frac{\exp f_{\theta,k}(X)}{\|\exp f_{\theta}(X)\|_{1}} \cdot \nabla_{\theta} f_{\theta,k}(X) \right],$$

with the expression in brackets being derivative of $\log \frac{\exp f_{\theta,j}(X)}{\|\exp f_{\theta}(X)\|_1}$ w.r.t. θ . Concluding from above, $L_{PSO}(f_{\theta})$ with the above gradient can be written as:

$$L_{PSO}(f_{\theta}) = -\sum_{j=1}^{C} \mathbb{P}(Y=j) \cdot \underset{X \sim \mathbb{P}(X|Y=j)}{\mathbb{E}} \log \frac{\exp f_{\theta,j}(X)}{\|\exp f_{\theta}(X)\|_{1}} =$$

$$= -\int \sum_{j=1}^{C} \left[\mathbb{P}(X,Y=j) \cdot \log \frac{\exp f_{\theta,j}(X)}{\|\exp f_{\theta}(X)\|_{1}} \right] dX =$$

$$= -\underset{X,Y \sim \mathbb{P}(X,Y)}{\mathbb{E}} \log \frac{\exp f_{\theta,Y}(X)}{\|\exp f_{\theta}(X)\|_{1}}$$

with its empirical version being:

$$L_{PSO}(f_{\theta}) \approx -\frac{1}{N} \sum_{i=1}^{N} \log \frac{\exp f_{\theta, Y_i}(X_i)}{\|\exp f_{\theta}(X_i)\|_1}.$$

The above loss is known in Machine Learning community as softmax cross-entropy loss. Therefore, we can conclude that PSO over multiple surfaces $\{f_{\theta,j}(X)\}_{j=1}^{C}$ with magnitudes in Eqs. (65)-(66) corresponds to cross-entropy when $\mathbb{P}(X|Y=j)$ and $\mathbb{P}(X|Y\neq j)$ serve as up and down densities respectively. Yet, according to the PSO principles the magnitudes in Eqs. (65)-(66) are not the only choice for such convergence. In fact, we can play with

the norm within the denominator of $M^{U}(\cdot)$ and $M^{D}(\cdot)$, and change it to be any L-p norm, since the denominator term is eventually canceled out and since its actual role is to bound outputs of magnitude functions. Similarly to what we observed in our experiments about the PSO-LDE (see Sections 6.2 and 12), different norms (the α value in context of PSO-LDE) can have smoother dynamics and produce a smaller approximation error. There are many possibilities to infer $\mathbb{P}(Y|X)$ when considering principles of PSO, and it would be interesting to explore these directions to see if any of them can yield any advantage over the standard cross-entropy loss. We shall leave it for future research.

Appendix H. Proof of Unnormalized Model Family in (Pihlaja et al., 2012) being subgroup of PSO

The family of estimators in Pihlaja et al. (2012) is defined by the objective function:

$$L(\theta, \{X_i^U\}, \{X_i^D\}) = -\frac{1}{N^U} \sum_{i=1}^{N^U} g_1 \left[\frac{\exp(f_{\theta}(X_i^U))}{\mathbb{P}^D(X_i^U)} \right] + \frac{1}{N^D} \sum_{i=1}^{N^D} g_2 \left[\frac{\exp(f_{\theta}(X_i^D))}{\mathbb{P}^D(X_i^D)} \right], \tag{67}$$

where points X_i^U and X_i^D are sampled from approximated data density \mathbb{P}^U and auxiliary distribution \mathbb{P}^D respectively. Further, $f_{\theta}(X)$ is an estimated model parametrized by weight vector θ . The $g_1[\cdot]$ and $g_2[\cdot]$ are nonlinear functions such that

$$\frac{g_2'[q]}{g_1'[q]} = q. (68)$$

When the above condition holds, the model approximates target log density $f_{\theta}(X) = \log \mathbb{P}^{U}(X)$.

Comparing Eq. (67) with the *empirical* PSO loss in Eq. (1), we can conclude that the above algorithm family from Pihlaja et al. (2012) is contained inside PSO family for *magnitude* functions defined as

$$M^{U}(X,s) = \frac{\partial g_{1}\left[r(X,s)\right]}{\partial r(X,s)} \cdot \frac{\exp(s)}{\mathbb{P}^{D}(X)} = g'_{1}[r(X,s)] \cdot r(X,s),$$

$$M^{D}(X,s) = \frac{\partial g_{2}\left[r(X,s)\right]}{\partial r(X,s)} \cdot \frac{\exp(s)}{\mathbb{P}^{D}(X)} = g'_{2}[r(X,s)] \cdot r(X,s),$$

$$r(X,s) \triangleq \frac{\exp(s)}{\mathbb{P}^{D}(X)}.$$
(69)

The opposite relation, PSO being contained in algorithm family Pihlaja et al. (2012), does not hold since PSO instances are not limited to estimate only $\log \mathbb{P}^{U}(X)$ (see Section 3).

Further, by applying PSO principles to the the above *magnitude* functions we can see that PSO *balance state* is achieved when:

$$\frac{\mathbb{P}^{U}(X)}{\mathbb{P}^{D}(X)} = \frac{M^{D}[X, f_{\theta}(X)]}{M^{U}[X, f_{\theta}(X)]} = \frac{g'_{1}[r(X, f_{\theta}(X))]}{g'_{2}[r(X, f_{\theta}(X))]} = r(X, f_{\theta}(X)) = \frac{\exp(f_{\theta}(X))}{\mathbb{P}^{D}(X)}$$

$$\Rightarrow f_{\theta}(X) = \log \mathbb{P}^{U}(X),$$

where we used identities from Eq. (68) and Eq. (69). Thus, the *balance state* of PSO agrees with conclusions made in Pihlaja et al. (2012).

Appendix I. Proof of Bregman Divergence Framework in (Gutmann and Hirayama, 2012) being subgroup of PSO

The family of estimators in (Gutmann and Hirayama, 2012) is defined by the objective functional:

$$L(f) = \int \left[-\Psi(f(X)) + \Psi'(f(X)) \cdot f(X) - \Psi'(f(X)) \cdot h(X) \right] d\mu, \tag{70}$$

which minimizes separable Bregman divergence between the target function h(X) and the approximation model f(X), and where $\Psi : \mathbb{R} \to \mathbb{R}$ is twice-differentiable and strictly convex function:

$$\Psi''(s) > 0. \tag{71}$$

Further, μ is a nondecreasing weighting function.

In order to prove that the above framework is a subgroup of PSO, we will reformulate the functional in Eq. (70) as an instance of the more general *PSO functional* in Eq. (3). To this end, we will find the appropriate *magnitude* functions of the loss in Eq. (70). Assuming for simplicity that μ is a constant weighting function, we can rewrite the above loss as:

$$\begin{split} L(f) &= \int \left[-\Psi(f(X)) + \Psi'(f(X)) \cdot f(X) - \Psi'(f(X)) \cdot h(X) \right] dX = \\ &= \int -\mathbb{P}^{\scriptscriptstyle U}(X) \cdot \frac{\Psi'(f(X)) \cdot h(X)}{\mathbb{P}^{\scriptscriptstyle U}(X)} + \mathbb{P}^{\scriptscriptstyle D}(X) \cdot \frac{-\Psi(f(X)) + \Psi'(f(X)) \cdot f(X)}{\mathbb{P}^{\scriptscriptstyle D}(X)} dX = \\ &= \int -\mathbb{P}^{\scriptscriptstyle U}(X) \cdot \widetilde{M}^{\scriptscriptstyle U}\left[X, f(X)\right] + \mathbb{P}^{\scriptscriptstyle D}(X) \cdot \widetilde{M}^{\scriptscriptstyle D}\left[X, f(X)\right] dX, \\ \widetilde{M}^{\scriptscriptstyle U}\left[X, s\right] &\triangleq \frac{\Psi'(s) \cdot h(X)}{\mathbb{P}^{\scriptscriptstyle U}(X)}, \quad \widetilde{M}^{\scriptscriptstyle D}\left[X, s\right] \triangleq \frac{-\Psi(s) + \Psi'(s) \cdot s}{\mathbb{P}^{\scriptscriptstyle D}(X)}, \end{split}$$

where we divided various terms into two groups, belonging to densities $\mathbb{P}^{U}(X)$ and $\mathbb{P}^{D}(X)$. Such separation was also done in the original paper (see Eq. (9) in (Gutmann and Hirayama, 2012)), where $\mathbb{P}^{U}(X)$ typically represented density of the analyzed data and $\mathbb{P}^{D}(X)$ - an auxiliary (noise) distribution.

The above loss is identical to PSO functional in Eq. (3) and hence corresponds to PSO instance with magnitude functions:

$$M^{U}(X,s) = \frac{\partial \widetilde{M}^{U}(X,s)}{\partial s} = \Psi''(s) \cdot \frac{h(X)}{\mathbb{P}^{U}(X)}, \tag{72}$$

$$M^{D}(X,s) = \frac{\partial \widetilde{M}^{D}(X,s)}{\partial s} = \Psi''(s) \cdot \frac{s}{\mathbb{P}^{D}(X)}.$$
 (73)

Further, note that the above $M^{U}(\cdot)$ in Eq. (72) contains $\mathbb{P}^{U}(X)$ and h(x) that typically are unknown a priori. Yet, in a usual setting these terms are canceling each other out.

From the above we can see that the estimation family in (Gutmann and Hirayama, 2012) is sub-family of PSO for magnitude functions defined in Eq. (72-73) that depends on an arbitrary strictly positive function $\Psi''(s) > 0$. The opposite relation, PSO being contained in the framework (Gutmann and Hirayama, 2012), does not hold since not all PSO instances can be expressed via Eq. (72-73). For example, the magnitudes from Square Loss in Table 5 can not be expressed as Eq. (72-73) for any $\Psi''(s)$. This is true also for other PSO instances.

Furthermore, additional attention needs to be given to the conditions required by both Bergman and PSO frameworks over feasible pairs of *magnitude* functions. In (Gutmann and Hirayama, 2012) the main requirement is the strict positiveness in Eq. (71) while PSO requirement is summarized as the condition 1-b of Theorem 1:

$$\mathbb{P}^{U}(X) \cdot M^{U'}[X, f^{*}(X)] < \mathbb{P}^{D}(X) \cdot M^{D'}[X, f^{*}(X)]. \tag{74}$$

For M^U and M^D defined as in Eq. (72-73) both requirements are identical. This can be shown by deriving Eq. (71) from Eq. (74) as follows. First, the derivatives of Eq. (72-73) are:

$$M^{U'}(X,s) = \frac{\partial M^{U}(X,s)}{\partial s} = \Psi'''(s) \cdot \frac{h(X)}{\mathbb{P}^{U}(X)},$$

$$M^{D'}(X,s) = \frac{\partial M^{D}(X,s)}{\partial s} = \frac{1}{\mathbb{P}^{D}(X)} \left[\Psi'''(s) \cdot s + \Psi''(s) \right].$$

Further, introducing these identities into Eq. (74) will lead to:

$$\mathbb{P}^{\scriptscriptstyle U}(X) \cdot \Psi^{\prime\prime\prime}\left[f^*(X)\right] \cdot \frac{h(X)}{\mathbb{P}^{\scriptscriptstyle U}(X)} < \mathbb{P}^{\scriptscriptstyle D}(X) \cdot \frac{1}{\mathbb{P}^{\scriptscriptstyle D}(X)} \left[\Psi^{\prime\prime\prime}\left[f^*(X)\right] \cdot f^*(X) + \Psi^{\prime\prime}\left[f^*(X)\right]\right],$$

$$\Psi^{\prime\prime\prime}\left[f^{*}(X)\right]\cdot h(X)<\Psi^{\prime\prime\prime}\left[f^{*}(X)\right]\cdot f^{*}(X)+\Psi^{\prime\prime}\left[f^{*}(X)\right],$$

$$\Psi'''[f^*(X)] \cdot [h(X) - f^*(X)] < \Psi''[f^*(X)].$$

Since $f^*(X) = h(X)$, we will get:

$$\Psi''[f^*(X)] > 0,$$

which leads to Eq. (71). Likewise, it is possible to derive Eq. (74) from Eq. (71) by following the above deduction in the backward order.

To summarize, the algorithm family in (Gutmann and Hirayama, 2012) is a strict subset of more general PSO. Furthermore, PSO formulation is more flexible and is much more intuitive.

Appendix J. LSQR Divergence

Here we will prove that LSQR evaluation metric, considered in this paper, is an actual statistical divergence. First, log-pdf squared error (LSQR) divergence is defined as:

$$LSQR(\mathbb{P}, \mathbb{Q}) = \int \mathbb{P}(X) \cdot \left[\log \mathbb{P}(X) - \log \mathbb{Q}(X)\right]^2 dX, \tag{75}$$

where \mathbb{P} is pdf over compact support $\Omega \in \mathbb{R}^n$; \mathbb{Q} is normalized or unnormalized model whose support is also Ω .

According to definition of the statistical divergence, LSQR must satisfy $\forall \mathbb{P}, \mathbb{Q} : LSQR(\mathbb{P}, \mathbb{Q}) \geq 0$ and $LSQR(\mathbb{P}, \mathbb{Q}) = 0 \Leftrightarrow \mathbb{P} = \mathbb{Q}$. Obviously, these two conditions are satisfied by Eq. (75). Hence, $LSQR(\mathbb{P}, \mathbb{Q})$ is statistical divergence.

Importantly, we emphasize that $LSQR(\mathbb{P}, \mathbb{Q})$ measures discrepancy between pdf \mathbb{P} and model \mathbb{Q} where the latter must not be normalized. Therefore, it can be used to evaluate PSO-based methods since they are only approximately normalized. However, such evaluation is only possible when \mathbb{P} is known analytically.

Further, in this paper LSQR is measured between the target density, defined as \mathbb{P}^U in the paper, and the pdf estimator $\bar{\mathbb{P}}_{\theta}$ produced by some method in the following way:

$$LSQR(\mathbb{P}^{\scriptscriptstyle U}, \bar{\mathbb{P}}_{\theta}) = rac{1}{N} \sum_{i=1}^N \left[\log \mathbb{P}^{\scriptscriptstyle U}(X_i^{\scriptscriptstyle U}) - \log \bar{\mathbb{P}}_{\theta}(X_i^{\scriptscriptstyle U})
ight]^2,$$

where $\{X_i^U\}_{i=1}^N$ are testing points, sampled from \mathbb{P}^U , that were not involved in estimation of $\mathbb{\bar{P}}_{\theta}$.

Appendix K. Matrix A from definition of Transformed Columns Distribution

Matrix A was randomly generated under constraint of having determinant 1, to keep the volume of sampled points the same. Its generated entries are:

Appendix L. Weights Uncorrelation and Gradient Similarity Space

In this appendix we will empirically demonstrate the relation between gradient similarity $g_{\theta}(X, X')$ and Euclidean distance d(X, X'), and how this relation changes along the optimization. Particularly, we show empirically that during first several thousand iterations of typical optimization the trend is achieved where high values of $g_{\theta}(X, X')$ are correlated with small values of d(X, X'). Further, this trend is preserved during the rest part of the optimization. This trend can be seen as an another motivation for kernel bandwidth analysis made in Section 5.5 - the shape of $r_{\theta}(X, X')$ has some implicit particular bandwidth.

Global Evaluation For this we apply PSO-LDE with $\alpha = \frac{1}{4}$ on a BD model for the inference of *Columns* distribution defined in Eq. (37), where at different optimization iterations we plot output pairs of $g_{\theta}(X, X')$ and d(X, X'). The plots are constructed similarly to Figure 8b. Specifically, we sample 500 points $D_U = \{X_i^U\}$ and 500 points $D_D = \{X_i^D\}$ from \mathbb{P}^U and \mathbb{P}^D respectively. For each sample from $D = D_U \cup D_D$ we calculated gradient $\frac{\partial f_{\theta}(X)}{\partial \theta}$. Further we calculated Euclidean distance and gradient similarity between

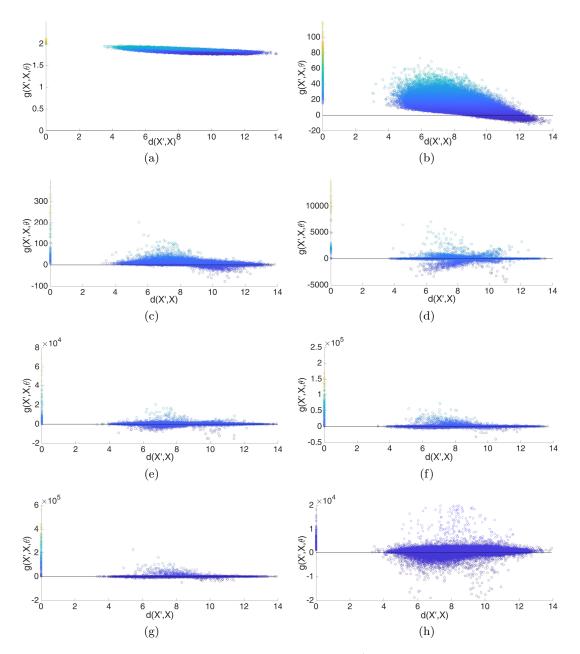


Figure 40: Relation between values of gradient similarity $g_{\theta}(X', X)$ and values of Euclidean distance d(X', X), along the optimization time t (iteration index). PSO-LDE with $\alpha = \frac{1}{4}$ is applied, where NN architecture is block-diagonal with 6 layers, number of blocks $N_B = 50$ and block size $S_B = 64$ (see Section 8.1). Each plot is constructed similarly to Figure 8b, see main text for more details. Outputs from both $g_{\theta}(X', X)$ and d(X', X) are demonstrated at different times; (a) t = 0, (b) t = 100, (c) t = 3200, (d) t = 3400, (e) t = 6000, (f) t = 100000 and (g) t = 200000. (h) Zoom-in of (g). As can be seen, self similarities $g_{\theta}(X, X)$, depicted at d(X', X) = 0, are high and increase during the optimization. The side similarities $g_{\theta}(X', X)$ for $X' \neq X$, depicted at d(X', X) > 0, are centered around zero at t = 200000 and are significantly lower than self similarities.

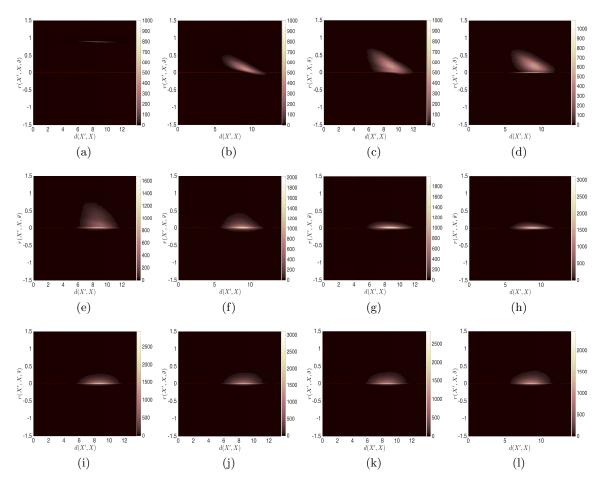


Figure 41: Histograms of the relative gradient similarity $r_{\theta}(X', X)$ and the Euclidean distance d(X', X) at different optimization times t, for the experiment in Figure 40. At each time t we calculate a relative side-influence $r_{\theta}(X_i, X_j)$ and a Euclidean distance $d(X_i, X_j)$ for 10^6 point pairs and depict a histogram of obtained $\{r_{\theta}(X_i, X_j)\}$ and $\{d(X_i, X_j)\}$. The optimization time is (a) t = 0, (b) t = 100, (c) t = 3200, (d) t = 3400, (e) t = 4000, (f) t = 6000, (g) t = 10000, (h) t = 29000, (i) t = 100000, (j) t = 150000, (k) t = 200000 and (l) t = 300000. As observed, after t = 10000 the relative gradient similarity between far away regions is much smaller than 1, implying that there is a insignificant side-influence over height $f_{\theta}(X)$ at point X from other points that are far away from X.

every two points within D, producing $\frac{1000 \cdot 1001}{2}$ pairs of distance and similarity values. These values are plotted in Figure 40.

Further, we also compute a relative side-influence $r_{\theta}(X, X')$, defined in Eq. (28), for each pair of points in D. In Figure 41 we construct a histogram of 10^6 obtained pairs of $\{r_{\theta}(X_i, X_j)\}$ and $\{d(X_i, X_j)\}$.

From the above figures we can see that during the first 100 iterations, gradient similarity obtains a form where its values are monotonically decreasing with bigger Euclidean distance between the points. During the next optimization iterations the self similarity $g_{\theta}(X, X)$ is growing by several orders of magnitudes. At the same time the side-similarity $g_{\theta}(X', X)$ for $X' \neq X$ is growing significantly slower and mostly stays centered around zero. In overall

values of $g_{\theta}(X, X)$ are much higher than values of $g_{\theta}(X', X)$ for $X' \neq X$, implying that self-influence forces are extremely stronger than side-influence forces. Furthermore, since side-similarity is centered around zero, theoretically side-influence forces may cancel each other, thus further improving the optimization performance. Likewise, from Figure 41 it is also clear that the self-influence of PSO is substantially stronger that the side-influence during the most part of the optimization process (i.e. after 10000 iterations in this experiment).

Local Evaluation Additionally, we performed a local evaluation of the above relation between gradient similarity and Euclidean distance. Particularly, after convergence we consider a path within a 20D input space, that starts at S = [-1, ..., -1] and ends at E = [1, ..., 1]. We evenly discretized this path into 1000 middle points with which we form an ordered point set $D = \{S, ..., E\}$, with |D| = 1000. Afterwards, we calculate θ gradients at each point in D and construct the Gramian matrix G, with $G_{ij} = g_{\theta}(X_i, X_j)$. Note that the index of each point expresses also its location within the chosen point path, and the index difference |i - j| also represents Euclidean distance between points X_i and X_j . In Figure 42a this matrix G is depicted, and here it can be observed that G's diagonal is very prominent. This again reasserts that self gradient similarity is significantly stronger than the side one.

Moreover, each row r_i inside G represents $g(X_i, \cdot, \theta)$ - side similarity between the point X_i and the rest of the points in D (i.e. the chosen path). Note that the i-th entry of r_i represents self similarity $g(X_i, X_i, \theta)$, while other entries represent the side-similarity from path points around X_i . Further, indexes of these other entries are related to the distance between the points and X_i , via the index difference |i-j|. Hence, first i-1 entries of r_i represent first i-1 points within the chosen path D before the i-th point, whereas the last 1000-i entries of r_i represent points at the end of the path. In Figures 42b-42d 11 different rows of G are depicted, where each row demonstrates gradient similarity around some path point X_i as a function of the second point index (and distance between two points). Here we can see that $g_{\theta}(X_i, X_j)$ typically has a peak at $X_i = X_i$, and further smoothly decreases as we walk away from point X_i in any of the two path directions (towards S or E). Thus, here we see that gradient similarity has a kernel-like behavior, returning high similarity for the same point and diminishing as the distance between the points grows. Yet, this kernel resemblance is not perfect, with some rows (e.g. 400-th in Figure 42c) having peaks outside of the i-th entry. Nevertheless, in context of PSO such local behavior allows us to conclude that when any training point is pushed by PSO loss, the force impact on the NN surface is local, centered around the pushed training point.

Further, in Figure 43 we also plot the normalized gradient similarity $\bar{g}(X_i, X_j, \theta) \triangleq \frac{\nabla_{\theta} f_{\theta}(X_i)^T \cdot \nabla_{\theta} f(X_j; \theta)}{\|\nabla_{\theta} f_{\theta}(X_i)\| \cdot \|\nabla_{\theta} f(X_j; \theta)\|} = \cos\left[\angle\left[\nabla_{\theta} f_{\theta}(X_i), \nabla_{\theta} f(X_j; \theta)\right]\right]$ for the same setting as in Figure 42. Here, we can see that $\bar{g}(X_i, X_j, \theta)$, which is cosine of the angle between θ gradients at points X_i and X_j , has a more symmetrical behavior w.r.t. $g_{\theta}(X_i, X_j)$. That is, $\bar{g}(X_i, \cdot, \theta)$ has a peak when the second argument is equal to X_i , and it is monotonically decreasing as the distance between the second argument and X_i is increasing. Moreover, the asymmetry that we observed in case of $g_{\theta}(X_i, X_j)$ (400-th and 600-th rows in Figure 42c) is caused actually by the difference in a gradient norm at different points X_i and X_j . Specifically, we can see that peak of 400-th row in Figure 42c is pushed towards the beginning of the path D, where X_{400} has neighbors with higher norm $\|\nabla_{\theta} f(X_j; \theta)\|$. In $\bar{g}(X_i, X_j, \theta)$ each gradient is

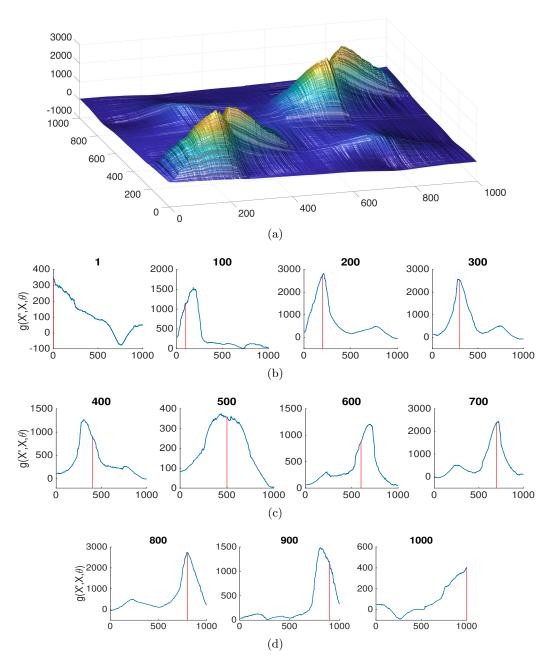


Figure 42: Local relation between values of gradient similarity $g_{\theta}(X',X)$ and values of Euclidean distance d(X',X) within BD architecture. The applied PSO method and model architecture are same as in Figure 40. After convergence, we calculate gradient $\frac{\partial f_{\theta}(X)}{\partial \theta}$ along path within input space, $[-1,\ldots,-1] \longrightarrow [1,\ldots,1]$, which is uniformly discretized via 1000 middle points. Afterwards, (a) the Gramian matrix G is constructed, with $G_{ij} = g_{\theta}(X_i, X_j)$ where X_i and X_j are i-th and j-th points along the path. Note that the index difference |i-j| also represents Euclidean distance between points X_i and X_j . Further, i-th row of G contains similarities $g(X_i, \cdot, \theta)$ between point i and rest of points. (a)-(c) 1-th, 100-th, ..., 900-th and 1000-th rows of G are shown. Red line indicates i-th entry of i-th row where self similarity $g(X_i, X_i, \theta)$ is plotted. See more details in the main text.

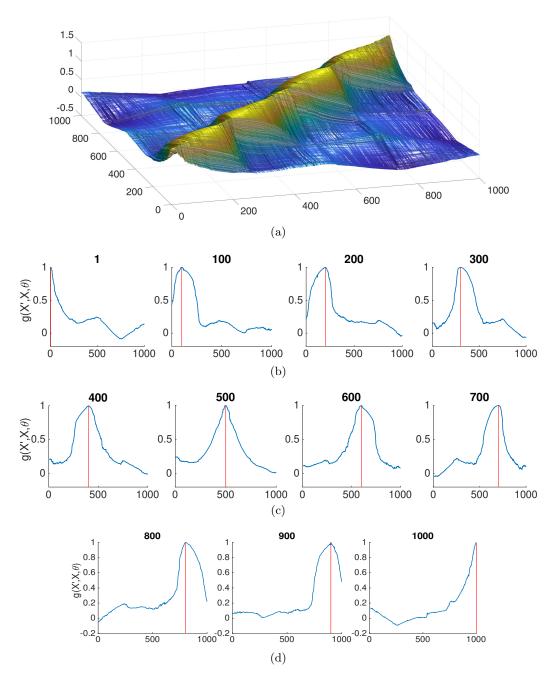


Figure 43: Normalized gradient results within BD architecture: same results from Figure 42, with Gramian matrix being normalized to $\bar{G}: \bar{G}_{ij} = \bar{g}(X_i, X_j, \theta) = \frac{\nabla_{\theta} f_{\theta}(X_i)^T \cdot \nabla_{\theta} f(X_j; \theta)}{\|\nabla_{\theta} f_{\theta}(X_i)\| \cdot \|\nabla_{\theta} f(X_j; \theta)\|}$. As observed, normalized gradient similarity $\bar{g}(X_i, X_j, \theta)$ is more symmetrical along both directions of a chosen path D than regular the gradient similarity $g_{\theta}(X_i, X_j)$ in Figure 42.

normalized to have a unit norm, which eliminates the above asymmetry as observed in Figure 43c. Hence, nearby points with a large gradient norm may affect the *gradient similarity* at a specific point and make it less symmetric/centered.

Note that in case the applied optimizer is GD, during the actual optimization the NN surface is pushed according to the $g_{\theta}(X_i, X_j)$ and not $\bar{g}(X_i, X_j, \theta)$. Therefore, various local asymmetries inside $g_{\theta}(X_i, X_j)$ may affect the optimization optimality. However, Adam optimizer (Kingma and Ba, 2014), used in our experiments, with its adaptive moment estimation and normalization per each weight implicitly transforms the actual similarity kernel of the PSO information flow. We speculate that the actual information kernel is more similar to the normalized gradient similarity. We shall leave a detailed investigation of the gradient similarity under Adam optimization update rule for future work.

Overall, our experiments show that NN weights undergo some uncorrelation process during the first few thousands of iterations, after which the gradient similarity obtains properties approximately similar to a local-support kernel function. Specifically, an opposite relation is formed between gradient similarity and Euclidean distance, where higher distance is associated with a smaller similarity. This uncorrelation can also be viewed as gradients (w.r.t. θ) at different training points are becoming more and more linearly independent along the optimization, which as a result increases angles between gradient vectors. Hence, these gradients point to different directions inside the parameter space $\mathbb{R}^{|\theta|}$, decreasing the side-influence between the training points. Furthermore, this uncorrelation process was observed almost in each experiment, yet the radius of local support for the kernel $g_{\theta}(X', X)$ (that is, how fast gradient similarity is decreasing w.r.t. d(X, X')) is changing depending on the applied NN architecture (e.g. FC vs BD) and on specific inferred density \mathbb{P}^{U} .

References

- David H Ackley, Geoffrey E Hinton, and Terrence J Sejnowski. A learning algorithm for boltzmann machines. *Cognitive science*, 9(1):147–169, 1985.
- Syed Mumtaz Ali and Samuel D Silvey. A general class of coefficients of divergence of one distribution from another. *Journal of the Royal Statistical Society: Series B* (Methodological), 28(1):131–142, 1966.
- T Amemiya. Asymptotic properties of extremum estimators. Advanced econometrics, Harvard university press, 1985.
- C. E. Antoniak. Mixtures of Dirichlet processes with applications to Bayesian nonparametric problems. *Annals of Statistics*, 2:1152–1174, 1974.
- Martin Arjovsky and Léon Bottou. Towards principled methods for training generative adversarial networks. arXiv preprint arXiv:1701.04862, 2017.
- Martin Arjovsky, Soumith Chintala, and Léon Bottou. Wasserstein gan. arXiv preprint arXiv:1701.07875, 2017.

- Leemon Baird, David Smalenberger, and Shawn Ingkiriwang. One-step neural network inversion with pdf learning and emulation. In 2005 IEEE International Joint Conference on Neural Networks, IJCNN'05, volume 2, pages 966–971. IEEE, 2005.
- James Vere Beck, Kevin David Cole, A Haji-Sheikh, and B Litkouhi. *Heat conduction using Green's functions*, volume 194. Hemisphere Publishing Corporation London, 1992.
- Ishmael Belghazi, Sai Rajeswar, Aristide Baratin, R Devon Hjelm, and Aaron Courville. Mine: mutual information neural estimation. arXiv preprint arXiv:1801.04062, 2018.
- Yoshua Bengio and Samy Bengio. Modeling high-dimensional discrete data with multi-layer neural networks. In *Advances in Neural Information Processing Systems (NIPS)*, pages 400–406, 2000.
- Yoshua Bengio and Jean-Sébastien Senécal. Adaptive importance sampling to accelerate training of a neural probabilistic language model. *IEEE Transactions on Neural Networks*, 19(4):713–722, 2008.
- Yoshua Bengio, Jean-Sébastien Senécal, et al. Quick training of probabilistic neural nets by importance sampling. In *In Proceedings of the Eleventh International Workshop on Artificial Intelligence and Statistics (AISTATS)*, pages 1–9, 2003.
- C.M. Bishop. Mixture density networks. Technical report, Aston University, Birmingham, 1994.
- Lev M Bregman. The relaxation method of finding the common point of convex sets and its application to the solution of problems in convex programming. *USSR computational mathematics and mathematical physics*, 7(3):200–217, 1967.
- Christian G Bucher. Adaptive sampling—an iterative fast monte carlo procedure. Structural safety, 5(2):119–126, 1988.
- Caffe. Caffe. caffe.berkeleyvision.org. URL caffe.berkeleyvision.org.
- Ciwan Ceylan and Michael U Gutmann. Conditional noise-contrastive estimation of unnormalised models. arXiv preprint arXiv:1806.03664, 2018.
- Richard Courant and David Hilbert. Chapter iv. the calculus of variations. *Methods of Mathematical Physics. New York: Interscience Publishers*, pages 164–274, 1953.
- Gustavo Deco and Wilfried Brauer. Higher order statistical decorrelation without information loss. In Advances in Neural Information Processing Systems (NIPS), pages 247–254, 1995.
- Laurent Dinh, David Krueger, and Yoshua Bengio. Nice: Non-linear independent components estimation. arXiv preprint arXiv:1410.8516, 2014.
- Laurent Dinh, Jascha Sohl-Dickstein, and Samy Bengio. Density estimation using real nvp. arXiv preprint arXiv:1605.08803, 2016.

- Xialiang Dou and Tengyuan Liang. Training neural networks as learning data-adaptive kernels: Provable representation and approximation benefits. arXiv preprint arXiv:1901.07114, 2019.
- Tarn Duong and Martin L Hazelton. Cross-validation bandwidth matrices for multivariate kernel density estimation. Scandinavian Journal of Statistics, 32(3):485–506, 2005.
- Shinto Eguchi. Information divergence geometry and the application to statistical machine learning. In *Information theory and statistical learning*, pages 309–332. Springer, 2009.
- Itzhak Fogel and Dov Sagi. Gabor filters as texture discriminator. *Biological cybernetics*, 61 (2):103–113, 1989.
- Mathieu Germain, Karol Gregor, Iain Murray, and Hugo Larochelle. Made: Masked autoencoder for distribution estimation. In *Intl. Conf. on Machine Learning (ICML)*, pages 881–889, 2015.
- Charles J Geyer and Elizabeth A Thompson. Constrained monte carlo maximum likelihood for dependent data. *Journal of the Royal Statistical Society. Series B (Methodological)*, pages 657–699, 1992.
- Xavier Glorot and Yoshua Bengio. Understanding the difficulty of training deep feedforward neural networks. In *Proceedings of the thirteenth international conference on artificial intelligence and statistics*, pages 249–256, 2010.
- Tilmann Gneiting and Adrian E Raftery. Strictly proper scoring rules, prediction, and estimation. *Journal of the American statistical Association*, 102(477):359–378, 2007.
- Ian Goodfellow, Jean Pouget-Abadie, Mehdi Mirza, Bing Xu, David Warde-Farley, Sherjil Ozair, Aaron Courville, and Yoshua Bengio. Generative adversarial nets. In *Advances in Neural Information Processing Systems (NIPS)*, pages 2672–2680, 2014.
- Dilan Görür and Carl Edward Rasmussen. Dirichlet process gaussian mixture models: Choice of the base distribution. *Journal of Computer Science and Technology*, 25(4):653–664, 2010.
- Arthur Gretton, Karsten M Borgwardt, Malte Rasch, Bernhard Schölkopf, and Alex J Smola. A kernel method for the two-sample-problem. In *Advances in neural information processing systems*, pages 513–520, 2007.
- Peter D Grünwald, A Philip Dawid, et al. Game theory, maximum entropy, minimum discrepancy and robust bayesian decision theory. the Annals of Statistics, 32(4):1367–1433, 2004.
- Ishaan Gulrajani, Faruk Ahmed, Martin Arjovsky, Vincent Dumoulin, and Aaron C Courville. Improved training of wasserstein gans. In *Advances in Neural Information Processing Systems (NIPS)*, pages 5769–5779, 2017.
- Michael Gutmann and Jun-ichiro Hirayama. Bregman divergence as general framework to estimate unnormalized statistical models. arXiv preprint arXiv:1202.3727, 2012.

- Michael Gutmann and Aapo Hyvärinen. Noise-contrastive estimation: A new estimation principle for unnormalized statistical models. In *Proceedings of the Thirteenth International Conference on Artificial Intelligence and Statistics*, pages 297–304, 2010.
- Michael U Gutmann and Aapo Hyvärinen. Noise-contrastive estimation of unnormalized statistical models, with applications to natural image statistics. *J. of Machine Learning Research*, 13(Feb):307–361, 2012.
- W Keith Hastings. Monte carlo sampling methods using markov chains and their applications. 1970.
- Kaiming He, Xiangyu Zhang, Shaoqing Ren, and Jian Sun. Deep residual learning for image recognition. In *IEEE Conf. on Computer Vision and Pattern Recognition (CVPR)*, pages 770–778, 2016.
- Nils-Bastian Heidenreich, Anja Schindler, and Stefan Sperlich. Bandwidth selection for kernel density estimation: a review of fully automatic selectors. AStA Advances in Statistical Analysis, 97(4):403–433, 2013.
- G.E. Hinton, S. Osindero, and Y. Teh. A fast learning algorithm for deep belief nets. Neural Computation, 18:1527–1554, 2006.
- Geoffrey E Hinton. Products of experts. 1999.
- Geoffrey E Hinton. Training products of experts by minimizing contrastive divergence. Neural Computation, 14(8):1771–1800, 2002.
- Jean-Baptiste Hiriart-Urruty and Claude Lemaréchal. Fundamentals of convex analysis. Springer Science & Business Media, 2012.
- Kurt Hornik. Approximation capabilities of multilayer feedforward networks. *Neural networks*, 4(2):251–257, 1991.
- P. Huber. Robust Statistics. John Wiley & Sons, New York, NY, 1981.
- Aapo Hyvärinen. Estimation of non-normalized statistical models by score matching. *Journal of Machine Learning Research*, 6(Apr):695–709, 2005.
- Aapo Hyvärinen. Some extensions of score matching. Computational statistics & data analysis, 51(5):2499–2512, 2007.
- Aapo Hyvarinen. Connections between score matching, contrastive divergence, and pseudo-likelihood for continuous-valued variables. *IEEE Transactions on neural networks*, 18(5): 1529–1531, 2007.
- Sergey Ioffe and Christian Szegedy. Batch normalization: Accelerating deep network training by reducing internal covariate shift. arXiv preprint arXiv:1502.03167, 2015.
- Arthur Jacot, Franck Gabriel, and Clément Hongler. Neural tangent kernel: Convergence and generalization in neural networks. In *Advances in Neural Information Processing Systems (NIPS)*, pages 8571–8580, 2018.

- Fred Jelinek, Robert L Mercer, Lalit R Bahl, and James K Baker. Perplexity a measure of the difficulty of speech recognition tasks. *The Journal of the Acoustical Society of America*, 62(S1):S63–S63, 1977.
- Jurgen Jost, Jürgen Jost, and Xianqing Li-Jost. *Calculus of variations*, volume 64. Cambridge University Press, 1998.
- Takafumi Kanamori, Shohei Hido, and Masashi Sugiyama. A least-squares approach to direct importance estimation. *Journal of Machine Learning Research*, 10(Jul):1391–1445, 2009.
- Takafumi Kanamori, Taiji Suzuki, and Masashi Sugiyama. Statistical analysis of kernel-based least-squares density-ratio estimation. *Machine Learning*, 86(3):335–367, 2012.
- Tero Karras, Timo Aila, Samuli Laine, and Jaakko Lehtinen. Progressive growing of gans for improved quality, stability, and variation. arXiv preprint arXiv:1710.10196, 2017.
- Rafail Khasminskii. Stochastic stability of differential equations, volume 66. Springer Science & Business Media, 2011.
- Diederik P Kingma and Jimmy Ba. Adam: A method for stochastic optimization. arXiv preprint arXiv:1412.6980, 2014.
- Pang Wei Koh and Percy Liang. Understanding black-box predictions via influence functions. In *Proceedings of the 34th International Conference on Machine Learning-Volume 70*, pages 1885–1894. JMLR. org, 2017.
- D. Kopitkov and V. Indelman. No belief propagation required: Belief space planning in high-dimensional state spaces via factor graphs, matrix determinant lemma and re-use of calculation. *Intl. J. of Robotics Research*, 36(10):1088–1130, August 2017.
- D. Kopitkov and V. Indelman. Deep PDF: Probabilistic surface optimization and density estimation. arXiv preprint arXiv:1807.10728, 2018a.
- D. Kopitkov and V. Indelman. Robot localization through information recovered from cnn classificators. In *IEEE/RSJ Intl. Conf. on Intelligent Robots and Systems (IROS)*. IEEE, October 2018b.
- Dmitry Kopitkov and Vadim Indelman. Neural spectrum alignment: Empirical study. arXiv preprint arXiv:1910.08720, 2019.
- Alex Krizhevsky, Ilya Sutskever, and Geoffrey E Hinton. Imagenet classification with deep convolutional neural networks. In *Advances in neural information processing systems*, pages 1097–1105, 2012.
- Matthieu Labeau and Alexandre Allauzen. Learning with noise-contrastive estimation: Easing training by learning to scale. In *Proceedings of the 27th International Conference on Computational Linguistics*, pages 3090–3101, 2018.

- Hugo Larochelle and Iain Murray. The neural autoregressive distribution estimator. In *Proceedings of the Fourteenth International Conference on Artificial Intelligence and Statistics*, pages 29–37, 2011.
- Y. LeCun, L. Bottou, Y. Bengio, and P. Haffner. Gradient-based learning applied to document recognition. *Proceedings of the IEEE*, 86(11):2278–2324, November 1998.
- Christian Ledig, Lucas Theis, Ferenc Huszár, Jose Caballero, Andrew Cunningham, Alejandro Acosta, Andrew Aitken, Alykhan Tejani, Johannes Totz, Zehan Wang, et al. Photo-realistic single image super-resolution using a generative adversarial network. arXiv preprint, 2016.
- Erich L Lehmann and George Casella. *Theory of point estimation*. Springer Science & Business Media, 2006.
- Zhibin Liao, Tom Drummond, Ian Reid, and Gustavo Carneiro. Approximate fisher information matrix to characterise the training of deep neural networks. *IEEE transactions on pattern analysis and machine intelligence*, 2018.
- Qiang Liu and Dilin Wang. Stein variational gradient descent: A general purpose bayesian inference algorithm. In NIPS, pages 2378–2386, 2016.
- Qiang Liu and Dilin Wang. Learning deep energy models: Contrastive divergence vs. amortized mle. arXiv preprint arXiv:1707.00797, 2017.
- S. N. MacEachern and P. Muller. Estimating mixture of dirichlet process models. *Journal of Computational and Graphical Statistics*, 7:223–238, 1998.
- Xudong Mao, Qing Li, Haoran Xie, Raymond YK Lau, Zhen Wang, and Stephen Paul Smolley. Least squares generative adversarial networks. In *Intl. Conf. on Computer Vision (ICCV)*, pages 2813–2821. IEEE, 2017.
- G.J. McLachlan and K.E. Basford. Mixture Models: Inference and Applications to Clustering. Marcel Dekker, New York, 1988.
- Aditya Menon and Cheng Soon Ong. Linking losses for density ratio and class-probability estimation. In *Intl. Conf. on Machine Learning (ICML)*, pages 304–313, 2016.
- Mehdi Mirza and Simon Osindero. Conditional generative adversarial nets. arXiv preprint arXiv:1411.1784, 2014.
- Takeru Miyato, Toshiki Kataoka, Masanori Koyama, and Yuichi Yoshida. Spectral normalization for generative adversarial networks. arXiv preprint arXiv:1802.05957, 2018.
- Andriy Mnih and Koray Kavukcuoglu. Learning word embeddings efficiently with noise-contrastive estimation. In *Advances in Neural Information Processing Systems (NIPS)*, pages 2265–2273, 2013.
- Andriy Mnih and Yee Whye Teh. A fast and simple algorithm for training neural probabilistic language models. arXiv preprint arXiv:1206.6426, 2012.

- Shakir Mohamed and Balaji Lakshminarayanan. Learning in implicit generative models. arXiv preprint arXiv:1610.03483, 2016.
- Youssef Mroueh and Tom Sercu. Fisher gan. In Advances in Neural Information Processing Systems (NIPS), pages 2510–2520, 2017.
- Alfred Müller. Integral probability metrics and their generating classes of functions. *Advances in Applied Probability*, 29(2):429–443, 1997.
- Hyunha Nam and Masashi Sugiyama. Direct density ratio estimation with convolutional neural networks with application in outlier detection. *IEICE TRANSACTIONS on Information and Systems*, 98(5):1073–1079, 2015.
- Amy Nesky and Quentin F Stout. Neural networks with block diagonal inner product layers. In *International Conference on Artificial Neural Networks*, pages 51–61. Springer, 2018.
- KW Newey and D McFadden. Large sample estimation and hypothesis. *Handbook of Econometrics*, IV, Edited by RF Engle and DL McFadden, pages 2112–2245, 1994.
- Jiquan Ngiam, Zhenghao Chen, Pang W Koh, and Andrew Y Ng. Learning deep energy models. In *International Conference on Machine Learning*, pages 1105–1112, 2011.
- XuanLong Nguyen, Martin J Wainwright, and Michael I Jordan. Estimating divergence functionals and the likelihood ratio by convex risk minimization. *IEEE Transactions on Information Theory*, 56(11):5847–5861, 2010.
- Sebastian Nowozin, Botond Cseke, and Ryota Tomioka. f-gan: Training generative neural samplers using variational divergence minimization. In *Advances in Neural Information Processing Systems*, pages 271–279, 2016.
- Thomas R Osborn. Fast teaching of boltzmann machines with local inhibition. In *International Neural Network Conference*, pages 785–785. Springer, 1990.
- Travis A O'Brien, Karthik Kashinath, Nicholas R Cavanaugh, William D Collins, and John P O'Brien. A fast and objective multidimensional kernel density estimation method: fastkde. *Computational Statistics & Data Analysis*, 101:148–160, 2016.
- George Papamakarios, Theo Pavlakou, and Iain Murray. Masked autoregressive flow for density estimation. In *Advances in Neural Information Processing Systems (NIPS)*, pages 2338–2347, 2017.
- Razvan Pascanu, Tomas Mikolov, and Yoshua Bengio. Understanding the exploding gradient problem. CoRR, abs/1211.5063, 2:417, 2012.
- Luis Perez and Jason Wang. The effectiveness of data augmentation in image classification using deep learning. arXiv preprint arXiv:1712.04621, 2017.
- Henning Petzka, Asja Fischer, and Denis Lukovnicov. On the regularization of wasserstein gans. arXiv preprint arXiv:1709.08894, 2017.

- Miika Pihlaja, Michael Gutmann, and Aapo Hyvarinen. A family of computationally efficient and simple estimators for unnormalized statistical models. arXiv preprint arXiv:1203.3506, 2012.
- Jose C Principe. Information theoretic learning: Renyi's entropy and kernel perspectives. Springer Science & Business Media, 2010.
- PyTorch. PyTorch. pytorch.org. URL pytorch.org.
- Alec Radford, Luke Metz, and Soumith Chintala. Unsupervised representation learning with deep convolutional generative adversarial networks. arXiv preprint arXiv:1511.06434, 2015.
- Danilo Jimenez Rezende and Shakir Mohamed. Variational inference with normalizing flows. arXiv preprint arXiv:1505.05770, 2015.
- Oren Rippel and Ryan Prescott Adams. High-dimensional probability estimation with deep density models. arXiv preprint arXiv:1302.5125, 2013.
- Tim Salimans, Ian Goodfellow, Wojciech Zaremba, Vicki Cheung, Alec Radford, and Xi Chen. Improved techniques for training gans. In *Advances in Neural Information Processing Systems (NIPS)*, pages 2234–2242, 2016.
- Saeed Saremi, Arash Mehrjou, Bernhard Schölkopf, and Aapo Hyvärinen. Deep energy estimator networks. arXiv preprint arXiv:1805.08306, 2018.
- David W Scott. Multivariate density estimation: theory, practice, and visualization. John Wiley & Sons, 2015.
- Jayaram Sethuraman and Ram C Tiwari. Convergence of dirichlet measures and the interpretation of their parameter. In *Statistical decision theory and related topics III*, pages 305–315. Elsevier, 1982.
- Georgy Shevlyakov, Stephan Morgenthaler, and Alexander Shurygin. Redescending mestimators. *Journal of Statistical Planning and Inference*, 138(10):2906–2917, 2008.
- Bernard W Silverman. Density estimation for statistics and data analysis. Routledge, 2018.
- Noah A Smith and Jason Eisner. Contrastive estimation: Training log-linear models on unlabeled data. In *Proceedings of the 43rd Annual Meeting on Association for Computational Linguistics*, pages 354–362. Association for Computational Linguistics, 2005.
- Paul Smolensky. Information processing in dynamical systems: Foundations of harmony theory. In D. E. Rumelhart and J. L. McClelland, editors, *Parallel Distributed Processing*, volume 1, page 194–281. The MIT press, Cambridge, MA, 1986.
- Nitish Srivastava, Geoffrey Hinton, Alex Krizhevsky, Ilya Sutskever, and Ruslan Salakhutdinov. Dropout: a simple way to prevent neural networks from overfitting. The Journal of Machine Learning Research, 15(1):1929–1958, 2014.

- Masashi Sugiyama, Taiji Suzuki, Shinichi Nakajima, Hisashi Kashima, Paul von Bünau, and Motoaki Kawanabe. Direct importance estimation for covariate shift adaptation. *Annals of the Institute of Statistical Mathematics*, 60(4):699–746, 2008.
- Masashi Sugiyama, Taiji Suzuki, and Takafumi Kanamori. Density-ratio matching under the bregman divergence: a unified framework of density-ratio estimation. *Annals of the Institute of Statistical Mathematics*, 64(5):1009–1044, 2012a.
- Masashi Sugiyama, Taiji Suzuki, and Takafumi Kanamori. Density ratio estimation in machine learning. Cambridge University Press, 2012b.
- Christian Szegedy, Wei Liu, Yangqing Jia, Pierre Sermanet, Scott Reed, Dragomir Anguelov, Dumitru Erhan, Vincent Vanhoucke, Andrew Rabinovich, et al. Going deeper with convolutions. In *IEEE Conf. on Computer Vision and Pattern Recognition (CVPR)*, 2015.
- Christian Szegedy, Vincent Vanhoucke, Sergey Ioffe, Jon Shlens, and Zbigniew Wojna. Rethinking the inception architecture for computer vision. In *IEEE Conf. on Computer Vision and Pattern Recognition (CVPR)*, pages 2818–2826, 2016.
- Christian Szegedy, Sergey Ioffe, Vincent Vanhoucke, and Alexander A Alemi. Inception-v4, inception-resnet and the impact of residual connections on learning. In *AAAI*, volume 4, page 12, 2017.
- TensorFlow. TensorFlow. www.tensorflow.org. URL www.tensorflow.org.
- George R Terrell, David W Scott, et al. Variable kernel density estimation. *The Annals of Statistics*, 20(3):1236–1265, 1992.
- Masatoshi Uehara, Takeru Matsuda, and Fumiyasu Komaki. Analysis of noise contrastive estimation from the perspective of asymptotic variance. arXiv preprint arXiv:1808.07983, 2018.
- Masatosi Uehara, Issei Sato, Masahiro Suzuki, Kotaro Nakayama, and Yutaka Matsuo. b-gan: Unified framework of generative adversarial networks. 2016.
- Benigno Uria, Iain Murray, and Hugo Larochelle. Rnade: The real-valued neural autoregressive density-estimator. In *Advances in Neural Information Processing Systems (NIPS)*, pages 2175–2183, 2013.
- Aaron Van Den Oord, Sander Dieleman, Heiga Zen, Karen Simonyan, Oriol Vinyals, Alex Graves, Nal Kalchbrenner, Andrew Senior, and Koray Kavukcuoglu. Wavenet: A generative model for raw audio. arXiv preprint arXiv:1609.03499, 2016.
- Cédric Villani. Optimal transport: old and new, volume 338. Springer Science & Business Media, 2008.
- Pascal Vincent. A connection between score matching and denoising autoencoders. *Neural computation*, 23(7):1661–1674, 2011.

DMITRY KOPITKOV AND VADIM INDELMAN

- Sebastien C Wong, Adam Gatt, Victor Stamatescu, and Mark D McDonnell. Understanding data augmentation for classification: when to warp? arXiv preprint arXiv:1609.08764, 2016.
- Saining Xie, Ross Girshick, Piotr Dollár, Zhuowen Tu, and Kaiming He. Aggregated residual transformations for deep neural networks. In *IEEE Conf. on Computer Vision and Pattern Recognition (CVPR)*, pages 5987–5995. IEEE, 2017.
- Makoto Yamada, Taiji Suzuki, Takafumi Kanamori, Hirotaka Hachiya, and Masashi Sugiyama. Relative density-ratio estimation for robust distribution comparison. In *Advances in Neural Information Processing Systems (NIPS)*, pages 594–602, 2011.
- Shuangfei Zhai, Yu Cheng, Weining Lu, and Zhongfei Zhang. Deep structured energy based models for anomaly detection. In *International Conference on Machine Learning*, pages 1100–1109, 2016.
- Junbo Zhao, Michael Mathieu, and Yann LeCun. Energy-based generative adversarial network. arXiv preprint arXiv:1609.03126, 2016.
- Zhiming Zhou, Yuxuan Song, Lantao Yu, Hongwei Wang, Weinan Zhang, Zhihua Zhang, and Yong Yu. Understanding the effectiveness of lipschitz-continuity in generative adversarial nets. arXiv preprint arXiv:1807.00751, 2018.